Advanced Ultrawideband Imaging Algorithms for Breast Cancer Detection

Tengfei Yin

A Thesis Submitted for the Degree of Doctor of Philosophy

School of of Engineering and Informatics

University of Sussex

September 2015

Declaration

I hereby declare that this thesis has not been submitted, either in the same or different form, to this or any other University for a degree and the work produced here is my own except stated otherwise.

Signature: _____

Tengfei Yin

September 2015

University of Sussex

Thesis Submitted in Fulfilment of the Requirements for the Degree of Doctor of Philosophy

Advanced Ultrawideband Imaging Algorithms for Breast Cancer Detection

By: Tengfei Yin

Summary

Ultrawideband (UWB) technology has received considerable attention in recent years as it is regarded to be able to revolutionise a wide range of applications. UWB imaging for breast cancer detection is particularly promising due to its appealing capabilities and advantages over existing techniques, which can serve as an early-stage screening tool, thereby saving millions of lives. Although a lot of progress has been made, several challenges still need to be overcome before it can be applied in practice. These challenges include accurate signal propagation modelling and breast phantom construction, artefact resistant imaging algorithms in realistic breast models, and low-complexity implementations. Under this context, novel solutions are proposed in this thesis to address these key bottlenecks.

The thesis first proposes a versatile electromagnetic computational engine (VECE) for simulating the interaction between UWB signals and breast tissues. VECE provides the first implementation of its kind combining auxiliary differential equations (ADE) and convolutional perfectly matched layer (CPML) for describing Debye dispersive medium, and truncating computational domain, respectively. High accuracy and improved computational and memory storage efficiency are offered by VECE, which are validated via extensive analysis and simulations. VECE integrates the state-of-the-art realistic breast phantoms, enabling the modelling of signal propagation and evaluation of imaging algorithms.

To mitigate the severe interference of artefacts in UWB breast cancer imaging, a robust and artefact resistant (RAR) algorithm based on neighbourhood pairwise correlation is proposed. RAR is fully investigated and evaluated in a variety of scenarios, and compared with four well-known algorithms. It has been shown to achieve improved tumour detection and robust artefact resistance over its counterparts in most cases, while maintaining high computational efficiency. Simulated tumours in both homogeneous and heterogeneous breast phantoms with mild to moderate densities, combined with an entropy-based artefact removal algorithm, are successfully identified and localised.

To further improve the performance of algorithms, diverse and dynamic correlation weighting factors are investigated. Two new algorithms, local coherence exploration (LCE) and dynamic neighbourhood pairwise correlation (DNPC), are presented, which offer improved clutter suppression and image resolution. Moreover, a multiple spatial diversity (MSD) algorithm, which explores and exploits the richness of signals among different transmitter and receiver pairs, is proposed. It is shown to achieve enhanced tumour detection even in severely dense breasts.

Finally, two accelerated image reconstruction mechanisms referred to as redundancy elimination (RE) and annulus predication (AP) are proposed. RE removes a huge number of repetitive operations, whereas AP employs a novel annulus prediction to calculate millions of time delays in a highly efficient batch mode. Their efficacy is demonstrated by extensive analysis and simulations. Compared with the non-accelerated method, RE increases the computation speed by two-fold without any performance loss, whereas AP can be 45 times faster with negligible performance degradation.

Acknowledgements

I would like to express my sincere and deepest gratitude to my supervisor Dr. Falah H. Ali for his supervision, guidance, encouragement, and support. The contributions of this thesis are the results of countless number of discussions with him. His professional and conscientious working manner deeply impressed me, and the thesis is significantly nourished and enhanced by his high-calibre knowledge and rich research experiences.

My thanks to Dr. Constantino C. Reyes-Aldasoro for his help and invaluable advice. It was a great privilege to work under his supervision in my first year of study, which laid a solid foundation and enriched the path towards research project completion.

I must extend my thanks to my wonderful colleagues and friends for their assistance and companionship. This is an incredibly rewarding experience, the innumerable interactions with them keep reminding me that how fortunate I was to be with such talented individuals. Some of them in no particular order are: Walid, Marwan, Saif, James, Bilal, Tom, Murtala, Ibrahim, Yu He, Guofeng, Weida, Nan, Xiaolin, Weifan, Guangfu, Yun, and Yanling.

Last but not least, I gratefully acknowledge my parents and family members for their great patience and selfless love. My motivation to succeed is founded on their incessant encouragement, which provided me with a lifetime of warmth and affection. I would not be able to reach this step without their support. I would like to dedicate this thesis to them and those who is always standing by me.

"It is not knowledge, but the act of learning, not possession but the act of getting there, which grants the greatest enjoyment."

Carl Friedrich Gauss (1808)

List of publications

- T. Yin, and F. H. Ali, "Adaptive Combining via Correlation Exploration for Ultrawideband Breast Cancer Imaging." *IEEE Antennas Wireless Propagat. Lett.*, vol. 14, pp 587-590, Feb. 2015.
- T. Yin, F. H. Ali, and C. C. Reyes-Aldasoro, "A Robust and Artifact Resistant Algorithm of Ultrawideband Imaging System for Breast Cancer Detection." *IEEE Trans. Biomed. Eng.*, vol. 62, no. 6, pp. 1514-1525, Jan. 2015.
- T. Yin, and F. H. Ali, "Three-dimensional Propagation Modeling and Simulation of Ultrawideband for Biomedical Applications", *Submitted to International Journal of RF and Microwave Computer-Aided Engineering*, Apr. 2015.

Table of contents

List of abbreviations

2-D Two-dimensional

3-D Three-dimensional

ABC Absorbing Boundary Conditions

ACR American College of Radiology

ADE Auxiliary Differential Equation

AIR Accelerated Image Reconstruction

AP Annulus Prediction

ASCII American Standard Code for Information Interchange

BER Bit Error Rate

CFL Courant-Friedrichs-Lewy

CMI Confocal Microwave Imaging

CPML Convolutional Perfectly Matched Layer

CPU Central Processing Unit

CS Compressing Sensing

CT Computed Tomography

DAS Delay and Sum

DCP Drude-Critical Point

DMAS Delay Multiply and Sum

DNPC Dynamic Neighbourhood Pairwise Correlation

EIRP Equivalent Isotropically Radiated Power

EM Electromagnetic

ETR Effective Tumour Response

FCC Federal Communication Commission

FDAS Filtered Delay and Sum

FDTD Finite-difference Time-domain

FEM Finite Element Method

FG Fibro-glandular

FIR Finite Impulse Response

FIT Finite Integration Technique

FMM Fast Multipole Method

FWHM Full-Width at Half Maximum

GPR Ground Penetrating Radar

GPU Graphics Processor Unit

HPC High Performance Computing

IARC International Agency for Research on Cancer

ID Identity Document

IEEE Institute of Electrical and Electronics Engineers

ITS Intelligent Transport Systems

LCE Local Coherence Exploration

LD Lorentz-Drude

LLNL Lawrence Livermore National Laboratory

MAMI Multistatic Adaptive Microwave Imaging

MGP Modulated Gaussian Pulse

MIMO Multi-input Multi-output

MoM Method of Moments

MRI Magnetic Resonance Imaging

MSD Multiple Spatial Diversity

MWDAS Modified Weighted Delay and Sum

NHSBSP NHS Breast Screening Programme

NHS National Health Service

NUFFT Nonuniform Fast Fourier Transform

OI Object of Interest

OR Operating Room

PC Personal Computer

PLRC Piecewise Linear Recursive Convolution

PML Perfectly Matched Layer

RAR Robust and Artefact Resistant

RC Recursive Convolution

RE Redundancy Elimination

RLS Recursive Least Squares

SAR Synthetic Aperture Radar

SCR Signal to Clutter Ratio

SMR Signal to Mean Ratio

SOI Signal of Interest

SVD Singular Value Decomposition

TLM Transmission Line Matrix

TR-MUSIC Time-reversal MUltiple SIgnal Classification

TRC Trapezoidal Recursive Convolution

TWI Through-wall Imaging

U.K. United Kingdom

U.S. United States

UPML Uniaxial Perfectly Matched Layer

URA Uniform Rectangular Array

USB Universal Serial Bus

US Ultra-sound

UWB Ultra-wideband

UWCEM University of Wisconsin Cross-disciplinary Electromagnetics Laboratory

VECE Versatile Electromagnetic Computational Engine

WBAN Wireless Body Area Network

WPAN Wireless Personal Area Network

XFDTD 3-D Electromagnetic Simulation Software from Remcom

List of figures

List of tables

Chapter 1

Introduction

1.1 Background and Motivations

Ultrawideband (UWB) radio technology received considerable attention in recent years due to its desirable characteristics, such as high-bandwidth communication, precise localisation, and strong penetrating capabilities. Along with its low system cost, low power consumption, and non-ionising features, UWB is poised to revolutionise a broad range of applications.

Different UWB applications in both military and civilian areas have been developed. In military area, two of the most popular ones are through-wall imaging (TWI) [1–3] and weapon detection [4]. In civilian area, UWB-based intelligent transport system (ITS) [5, 6], location of resource and asset [7–9], and indoor robot navigation [10, 11] have been investigated. Besides, the advantage of UWB being a physical layer mechanism in wireless personal area network (WPAN) [12–14] and wireless body area network (WBAN) [15–18] for short-range connectivity has been brought to the forefront.

UWB also holds a great promise for biomedical applications, and these include tracking of cardiac and respiratory motions [19], and high-speed data transmission for different recording systems [18, 20, 21]. Another applied category of UWB is the sensing and imaging [22, 23]. The imaging of biological systems such as human body enables the detection of various abnormalities [24], including unusual patterns, internal injuries, or even cancers. It has long been acknowledged that cancer imposes a great threat to human

health due to its complex pathology and adaptation to treatments [25], early detection is thus critical.

Among different cancers, breast cancer is the most common one among females [26], and one of the leading causes of death worldwide [27]. Although less common, detected incidences of breast cancer among males have been increasing recently [28]. Early diagnosis of breast cancer is one of the most challenging and important aspects for the management of the disease, as it may be possible to detect the cancer before it spreads [29]. Three common screening methods for breast cancer currently used are X-ray mammography [30], Ultrasound (US) [31], and magnetic resonance imaging (MRI) [32]. US is less popular than X-ray mammography because it has a higher rate of false-positive examination results [33], and MRI is usually recommended to be used in conjunction with mammography [34]. In spite of the many merits of mammography, its deficiencies are evident: low sensitivity [35], high false alarm rate [36], and radiation exposure from X-rays, which brings with it a potential threat of increasing the cancer risk [36, 37]. The shortcomings of existing approaches constitute a motivation for better alternatives.

UWB imaging is regarded as one of the most promising alternatives for breast cancer detection, and has attracted significant research interests [24, 38–52]. In spite of many advancements of UWB breast cancer imaging, several serious challenges still exist. One of the key issues is the construction of anatomically realistic breast models [53]. To validate the effectiveness of imaging techniques, rigorous models are needed, which should incorporate various attributes of the breast, including geometrical properties, spatial distribution of different constituent tissues, and dispersive property. The propagation of UWB signal and its interaction with breast tissues should also be accurately modelled, which discloses the fundamental principle of breast cancer detection. Another challenge is image formation algorithm [39, 45–52]. The image formation algorithm is expected to provide clear tumour identification, accurate positioning, and robust performance in a range of realistic scenarios. Last but not least, accelerated image reconstruction schemes are needed for obtaining results in a timely manner. For medical imaging which has a high requirement of resolution, computationally efficient strategies become particularly

desirable. Therefore, innovative techniques are required to address these key bottlenecks before the UWB breast cancer imaging can be applied in practice.

1.2 Research Aims and Objectives

The main objective of this thesis is to investigate and develop more effective and efficient imaging algorithms for UWB breast cancer detection, thereby bridging the gap between theory and practical application. To this end, the following objectives are defined:

- Investigate state-of-the-art techniques to construct accurate numerical breast models.
- Examine breast tissue response interacting with varied UWB signals.
- Simulate and model UWB signal and its propagation within breast tissues.
- Study multiple antenna propagation and its impact on signal acquisition.
- Design and develop robust UWB imaging algorithms for breast cancer detection.
- Explore low-complexity implementation mechanism for fast image reconstruction.

All of the above are based on the investigation and evaluation of existing research works. Systematic tests and extensive comparisons under a variety of realistic scenarios are carried out to validate the effectiveness of proposals.

1.3 Original Contributions

This thesis proposes solutions to further three aspects of UWB breast cancer detection, including accurate propagation modelling and simulation of UWB signal interacting with breast tissues, novel imaging algorithms with superior robustness, and accelerated image reconstruction schemes. The main contributions are summarised below.

1. In Chapter 3, 3-D propagation modelling of UWB signal and its interaction with tumour-free and tumour-bearing breast phantoms are investigated. A versatile electromagnetic computational engine (VECE) is proposed, which enables the characterisation of the impacts of UWB radiation and the capturing of valuable bioelectromagnetic information such as tumour response. To implement VECE in a accurate and efficient way, different techniques for modelling computational electrodynamics,

dispersive media, and absorbing boundary conditions are analysed and compared. The efficacy and accuracy of VECE are validated through comparisons with both analytical and simulated results across a range of appropriate metrics, which are in close agreement. Combined with MRI-derived 3-D breast phantoms, the interaction between non-ionising UWB pulses and breast tissues are simulated under different scenarios. Substantial results demonstrate the practicability of VECE to facilitate the development of diagnostic and therapeutic technologies for breast cancer, and great potential for related bio-imaging applications.

2. In Chapter 4, to overcome the vulnerability to artefacts of existing algorithms for UWB breast tumour imaging, a novel robust and artefact resistant (RAR) algorithm is proposed. Extensive analysis and simulations using backscattered signals received from 3-D anatomically realistic numerical breast models are conducted to validate the performance of RAR. The effectiveness of RAR is demonstrated under various scenarios, including different tumour positions in both homogeneous and heterogeneous breast phantoms with low to medium densities. For completeness, both ideal and practical artefact removal methods are considered. RAR is compared with four well-known algorithms, and it has been shown that RAR is able to overcome the adverse effect from both the early-stage artefact from skin-fat reflections, and the late-stage clutter from fibro-glandular tissues. Besides significantly improved performance, results also prove that RAR maintains a high computational efficiency as its comparisons, proving its strong potential for breast cancer screening.
3. In Chapter 5, to further improve tumour detectability in severely dense breasts, three new algorithms referred to as local coherence exploration (LCE), dynamic neighbourhood pairwise correlation (DNPC), and multiple spatial diversity (MSD) are proposed. Building upon the RAR algorithm, LCE and DNPC are designed via the exploration of diverse and dynamic correlation weighting factors, whereas MSD takes the advantage of multiple diversity of signals received from different transmitter and receiver pairs. Simulations in different challenging scenarios verify the effectiveness of these three algorithms. Their performance is also compared with

RAR, and further improved clutter rejection and image resolution are observed even in heterogeneously dense breasts.

4. In Chapter 6, to reduce the running time of UWB breast cancer detection, two accelerated image reconstruction mechanisms, namely, redundancy elimination (RE) and annulus prediction (AP) are proposed. The comparison between the proposed and conventional non-optimised methods is performed. Extensive analysis and simulations demonstrate that both RE and AP outperform the non-accelerated method with faster computation speed in all scenarios considered. In comparison to the non-accelerated method, RE can be twice faster with zero performance loss, whereas AP offers a 45 times speedup at the cost of graceful performance degradation. These two schemes can be applied in all UWB data-independent breast imaging algorithms in a straightforward way, which provides a valuable trade-off between imaging performance and reconstruction time.

1.4 Outline of the Thesis

The thesis is divided into seven chapters and organised as follows. Chapter 1 presents the background, motivations, and main objectives of this research project, the original contributions are also summarised.

In Chapter 2, related background of UWB technology, with focus on its imaging application for breast cancer detection is presented. The fundamentals of UWB are firstly introduced, followed by its characteristics and corresponding applications in three different fields, including data transmission, localisation, and imaging. Furthermore, the background of UWB breast cancer imaging is reviewed, which covers its significance, principle, and advantages. Lastly, the state-of-the-art technical advances and challenges in this area are introduced.

In Chapter 3, a versatile electromagnetic computation engine (VECE) for simulating UWB signal propagation within breast tissues is proposed. Specific literature review of related modelling and simulation work is firstly provided. Then the principle, design, and implementation of VECE are introduced. The efficacy of VECE is validated through both

theoretical analysis, simulations, and comparisons. The applicability of VECE is proved by extensive simulation results. Aside from the visualisation of breast phantoms and signal propagation, the capture of tumour response under varied scenarios are also simulated and analysed. Further potential applications of VECE are introduced in the last section of this chapter.

In Chapter 4, a robust and artefact resistant (RAR) algorithm for UWB breast cancer detection is proposed. Literature review on UWB imaging algorithms for breast cancer detection is first presented. Furthermore, related details of imaging system including signal parameter, antenna configuration, and medium compositions of breast models are provided. Then the rational and procedures of RAR are introduced. The robustness of RAR is verified through simulations and comparisons with four well-known algorithms over a wide range of scenarios, and related imaging results are discussed. Finally, the performance and complexity of RAR and comparative algorithms are analysed.

In Chapter 5, to further enhance tumour detection in severely dense breast, three new algorithms are proposed. Base on RAR, the diverse and dynamic weighting factor are firstly investigated, and two algorithms referred to as local coherence exploration (LCE) and dynamic neighbourhood pairwise correlation (DNPC) are presented. Then the multiple spatial diversity (MSD) algorithm, which utilises the richness possessed by multistatic signals, is introduced. The rational and procedures of these algorithms are presented, and their efficacy are examined in different scenarios. The performance of LCE, DNPC, and MSD is also cross-compared with RAR, which is accompanied with the discussion of their results. The difference of proposed algorithms, along with their strengths for different application scenarios are pointed out.

In Chapter 6, to speedup the process of breast tumour detection, two accelerated image reconstruction mechanisms called redundancy elimination (RE) and annulus prediction (AP) are proposed. Literature on existing fast imaging techniques is firstly reviewed. The complexity bottleneck of imaging algorithms is analysed, based on which the RE is developed. Detailed procedures of RE are then introduced, whose efficacy is validated in different scenarios. The rational and particulars of AP for fast computation is then

presented. Unlike RE which eliminates a huge number of redundant operations, AP utilises a novel annulus prediction to calculate the time delays of millions of pixels in a highly efficient manner. To verify the effectiveness of AP, extensive analysis and simulations are conducted. Besides examining different sizes of the imaging region, AP is also tested in scenarios combining two imaging algorithms. Both RE and AP are compared with its non-optimised counterpart, and results indicate that a valuable trade-off between imaging acceleration and performance loss is achieved.

In Chapter 7, the main achievements of the thesis are summarised, and possible areas and topics for future work are identified.

Chapter 2

Background of Ultrawideband (UWB) and Literature Review on UWB Breast Cancer Imaging

2.1 Introduction

This chapter provides the background of Ultrawideband (UWB) technology, with focus on its application for early-stage breast cancer imaging. Literature review on the UWB breast cancer imaging is given, and more specific literature review on technical challenges are presented in following contribution chapters.

The chapter is organised as follows. The fundamentals of UWB technology are given in Section 2.2, which includes its signal definition and system regulations. Section 2.3 is dedicated for the characteristics of UWB and corresponding applications. This includes high-speed data transmission, accurate localisation, and high-resolution imaging. Literature review on UWB imaging for early breast cancer detection is detailed in Section 2.4. It starts with the background of breast cancer, then the deficiencies of existing screening techniques for this disease are pointed out. Furthermore, the principles and advantages of UWB imaging for breast cancer screening are introduced. In Section 2.5, the state-of-the-art advances and existing technical challenges of UWB breast imaging system are identified,

which constitute the motivation and objectives of this thesis. Finally, chapter conclusions are summarised in Section 2.6.

2.2 UWB Fundamentals

2.2.1 Signal Definition

UWB is a radio technology which uses pulses to transmit high-bandwidth information at a low power level. The United States (U.S.) Federal Communication Commission (FCC) defined UWB operation in February 2002 with the following terms [54]:

- *Bandwidth* (*BW*) is the frequency range constrained by points that 10 dB below the peak radiated emission (see Fig. 2.1). *BW* is calculated based on (2.1), where f_H and f_L are the upper and lower frequencies, respectively.

$$BW = f_H - f_L. \tag{2.1}$$

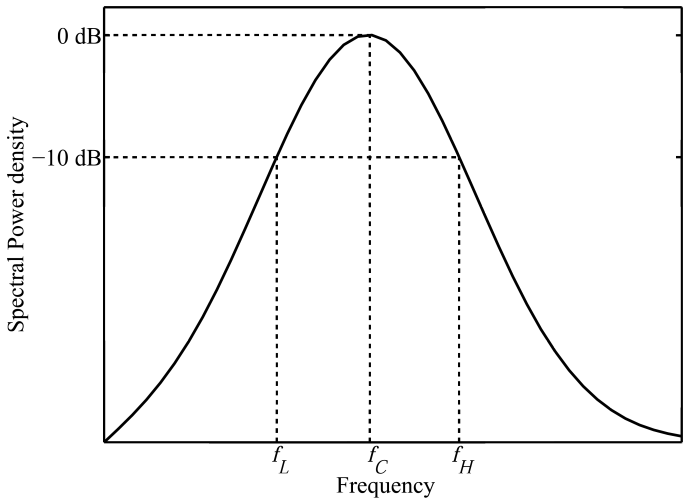

Fig. 2.1 Radiated spectral power density versus frequency in UWB definition.

- *Centre frequency* (f_C) is an arithmetic average of f_H and f_L, according to (2.2).

$$f_C = \frac{1}{2}\left(f_H + f_L\right). \tag{2.2}$$

- *Fractional bandwidth* (*bw*) is defined as the ratio of UWB bandwidth *BW* to the centre frequency f_C, which can be calculated through (2.3).

$$bw = \frac{BW}{f_C} = 2\frac{f_H - f_L}{f_H + f_L}. \tag{2.3}$$

- *UWB signal* has a fractional bandwidth *bw* equal or larger than 20%, or absolute bandwidth *BW* greater than 500 MHz. Radiators which are able to transmit such signals are regarded as UWB transmitters. Fig. 2.2 illustrates the comparison between narrowband and UWB signals in both time and frequency domains. Unlike conventional narrow-band signals [see Fig. 2.2(a)], UWB signal is impulse-like [see Fig. 2.2(b)]. Observing Fig. 2.2(c) and (d), the energy of UWB pulse is distributed across a broad range of frequency, thus its powder density is much lower in order of magnitude than a narrow-band signal.

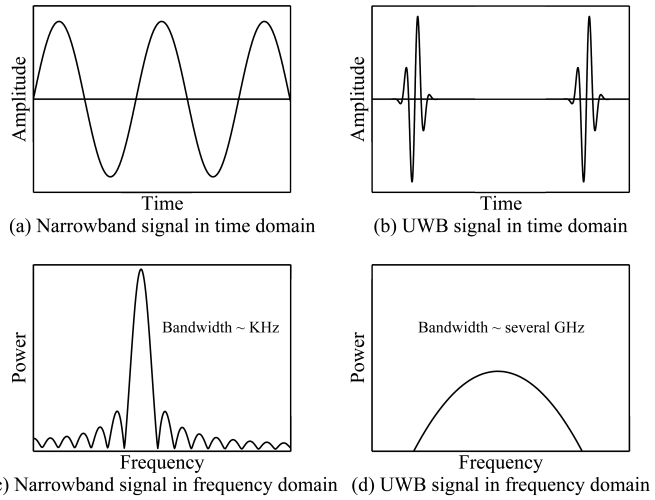

Fig. 2.2 Narrowband and UWB signals in time and frequency domains. (a) Narrowband signal in time domain. (b) UWB signal in time domain. (c) Narrowband signal in frequency domain. (d) UWB signal in frequency domain.

2.2.2 System Regulations

To protect existing radio services and avoid possible interference, the FCC authorised unlicensed use of spectrum for UWB devices. UWB devices have been classified into three categories: communication, imaging, and vehicular radar [55]. For each category, the authorised frequency range varies. For example, for wall imaging systems, they must be

operated below 960 MHz or in the frequency band 3.1 to 10.6 GHz, whereas the regulation for vehicular radar systems is in the range of 22 to 29 GHz. More details regarding authorised frequency range of UWB systems are provided in [54].

Besides frequency spectrum, the emission limit of UWB device is also applied, which is measured by equivalent isotropically radiated power (EIRP) or, alternatively, effective isotropically radiated power. The EIRP is defined as the product of the transmitter power output and the antenna gain in a given direction [56]. The transmission power output is the amount of power of radio frequency energy that a transmitter produces at its output. As for transmitting antenan, the antenna gain describes how well the antenna converts input power (transmitter power output) into radio waves. Depending on different application scenarios, the EIRP of UWB devices has been restricted, which are summarised in Table. 2.1.

Table 2.1 Emission limits for UWB devices in each operational frequency band [55].

	Application Categories		**Operation Band** (GHz)					
			0.96 to 1.61	1.61 to 1.99	1.99 to 3.1	3.1 to 10.6	10.6 to 22.0	22.0 to 29.0
EIRP (dBm)	Communications	Indoor	-75.3	-53.3	-51.3	-41.3	-51.3	-51.3
		Outdoor	-75.3	-63.3	-61.3	-41.3	-61.3	-61.3
	Imaging (mid-frequency)		-53.3	-51.3	-41.3	-41.3	-51.3	-51.3
	Vehicular Radar		-75.3	-61.3	-61.3	-61.3	-61.3	-41.3

According to Table 2.1, UWB communication systems have low average transmission power. With such low emission power, together with the discontinuous transmission [see Fig. 2.2(b)], UWB communication systems therefore have low probability of intercept and low probability of detection, making it suitable for secure and military applications [1]. The low transmit power also makes UWB an alternative physical layer mechanism for Institute of Electrical and Electronics Engineers (IEEE) 802.15 .15 wireless personal area network (WPAN) for short-range connectivity [12]. Aside from low power consumption, UWB also possesses merits such as high-bandwidth data communication and high-precision positioning. Therefore, besides serving military, UWB is also an ideal candidate for numerous civilian and medical applications, and these are introduced in the next section.

2.3 UWB Features and Related Applications

This section presents the features of UWB systems and corresponding applications, which include high-speed data transmission, precise localisation, and high-resolution imaging.

2.3.1 High-speed Data Transmission

Based on Shannon's formula [57] for the maximum capacity of information transmission, high data rate can be offered by UWB. For example, the multiband OFDM (orthogonal frequency-division multiplexing) alliance partitions the spectrum from 3 to 10 GHz into 528-MHz band and uses OFDM in each band to transmit data, with which the data rate can be as high as 480 Mb/s (see[58], Table 4.1). However, to achieve this as well as to make a trade-off between system performance and complexity, different UWB signal modulation schemes should be employed (see [59] and [60] and references therein).

The high-speed data transmission offers UWB an advantageous potential to support a variety of low-cost, low-power, short-range, and high-speed multimedia transport applications. UWB is a promising data transmission technique for WPAN, also known as in-home networks. In such a network, the real-time exchange of high-volume data, including message, audio, and video, between different file storage systems is critical. UWB is deemed as a promising physical layer alternative for WPAN because of its high-rate data transmission and high power efficiency [12, 13]. One of the applications is the wireless universal serial bus (USB) [14]. The wireless USB enables the transferring of data among devices, such as personal computers (PCs), digital television sets, digital cameras, video cassette recorders (VCRs), and portable media players.

Moreover, the gathering and exchanging data capability of UWB is highly desirable in sensor networks. The number of nodes, either static or mobile, in a sensor network can be huge; thus, to disseminate a wealth of sensory data in time can be difficult. Energy is normally restricted in sensor networks due to the nature of small-sized sensing devices and the difficulties of recharging their batteries. Thus, the low energy consumption of UWB communication becomes particularly attractive in such a network. Also because of the low transmission power and posing no harm to biological systems, UWB is popular in

WBAN [15], which enables reliable high-rate data communications on, near, and around the human body between sensors and the wearable centre [16, 17]. The integrated system structure of UWB with small-sized antenna is suitable for implanted medical devices as well. [18] evaluated the capacity of UWB wireless channel for neural recording systems. In [18], implanted sensors are deployed on the brain to capture neural responses. It was found that in a neural recoding system with multi-channels, the requirement of data rate was in excess of 100 Mb/s, which explains the necessity of UWB for this type of application thanks to its high-speed data transmission.

The feasibility of UWB for data communication in OR is also studied. [20] claimed that even in a dense multipath environment, UWB still showed strong robustness and had a great potential for applications such as wireless tracking for surgical navigation, and high data rate wireless telemetry of critical bio-signals (e.g. blood pressure, body temperature, etc.). A more advanced wireless communication system used in OR is presented in [21], which integrated the input, output, display, and control units.

It has been shown that the high-speed data transmission of UWB can serve various applications, from WPAN to WBAN, from civilian to medical fields. Another feature of UWB is localisation, which was initially used for military applications, and this is introduced in the next section.

2.3.2 Precise Localisation

Compared with conventional proximity and motion sensors, UWB-based sensing has the potential to offer an improved resolution [13]. Studies show that the positioning accuracy can be enhanced with increased signal bandwidth [61], considering the high-bandwidth signals (typically larger than 1 GHz) used in UWB systems, high-precision localisation can be obtained. Relying on the high ranging accuracy and object differentiation capability, different UWB sensing applications have been developed.

In [10] and [11], the indoor environment reconstruction based on UWB localisation is introduced. This application can be used to enable a navigating robot to sense its surroundings and concurrently to build up a map while navigating. The UWB localisation

for navigation is particularly useful in optically blurry scenarios, such as dark smog in disaster areas, where the camera-based vision system can barely work or suffer serious performance degradation.

UWB's positioning capability can also be applied in ITS. ITS aims to avoid or reduce traffic collisions, thereby realising a safe driving environment. For example, [5] presented a system scheme which integrated both UWB radar and data communication modules on one board. In this scheme, the distance between antenna transmitter and target vehicle is calculated according to propagation velocity and round trip time. With the aid of the extra communication module, an improvement of ranging precision was achieved. To avoid performance degradation of inter-vehicle communication, a successive interference cancellation technique was proposed in [6], which improved both the detection rate of signal and the bit error rate (BER) performance.

In industry, UWB positioning is mainly used for source tracking and asset locating. The tracking of resources such as people or equipment is necessary for safety. To this end, studies regarding different aspects of such tracking systems have been performed. [7] evaluated the performance of a commercially-available UWB tracking system. In [7], a static model for estimating position error as a function of receiver position is developed, which can be used as a guideline for practitioners. Another performance evaluation in more harsh environment was reported in [8]. In this study, a real-world construction setting combining field trials proved that a commercially-available UWB system is capable of proving sufficiently accurate real-time location data of construction resources, thereby assisting safe and efficient management of job sites. [9] optimised both monopole and dipole UWB antennas for asset tag location systems. This research proved that the time domain performance of antenna can be optimised based on the selected input pulse, whereas the improved frequency domain performance of antenna can be achieved by refining its geometry through genetic algorithms.

2.3.3 High-resolution Imaging

UWB imaging systems aim to sense and "see" the objects in a structure, which can be classified as ground penetrating radar (GPR), wall imaging, through-wall imaging (TWI), and biomedical imaging. The wide frequency range of UWB (3.1 to 10.6 GHz) ensures both through-the-interface penetrating capability and high resolution [62, 63].

The main electromagnetic (EM) properties of materials include permittivity and conductivity. The value of permittivity is related to the molecule's dipole moment per volume, whereas conductivity is associated with the free path length and speed of the electrons inside the material [64]. Depending on the EM properties of materials, their response (i.e. reflection, transmission, and absorption) to EM waves varies. Along the propagation path of EM wave, the inclusion of anomaly with different property compared with its surrounding can generate reflections. This reflected signals carry the information of the anomaly and can be captured by receiver antennas. Based on such reflected signals and combining appropriate algorithms, the construction of an image profile of the object under illumination can thus be achieved.

The advantages of UWB imaging including non-ionising radiation and low cost make it desired for surveillance systems, which can detect concealed weapons and plastic explosives [4]. These systems are normally deployed at major transportation hubs to enhance safety. By integrating with digital beamforming, such a system is capable of delivering high-resolution images in quasi-real time manner [65]. Another typical application of UWB is the TWI [2]. TWI is widely used in many areas, such as searching for alive people during earthquake's rescue operations, mine detection, and identifying and tracking of terrorist activities behind the wall [3].

UWB imaging also holds great potential for a variety of medical applications. Research demonstrated the feasibility of using UWB sensors to detect internal injuries of tissues, and non-contact imaging of human body [19]. Serving as a sensitive detector to identify possible abnormalities, UWB is able to image different human organs, such as brain [66], bone [67], and breast [39]. It was also used to detect myocardial ischemia and infarction

as introduced in [68–70]. As one of the most promising applications, UWB breast cancer imaging is elaborated in the next section.

2.4 Literature Review on UWB Imaging for Breast Cancer Detection

2.4.1 Significance

Breast cancer is the most common cancer among females [26], and one of the leading causes of death worldwide [27]. In United Kingdom (U.K.), it has been the most frequent cancer since 1997 in women, accounting 31% of new cases of cancer, and is the leading cause of deaths for women aged 34 to 54. Although less common in males, detected occurrence rate of breast cancer among males have been increasing recently [28]. This situation does not exist solely in U.K.. Each year in U.S. alone, approximately 182,000 female breast cancer cases are diagnosed [71]. Similar statistics of breast cancer in Canada [72] and Singapore [73] further confirmed the severity of this disease.

Early diagnosis of breast cancer is one of the most challenging and important aspects for the management of the disease, as it can detect the cancer when it is most likely to be treated or controlled [29]. Specifically, the 5-year survival rate of breast cancer patients in Stage 0 (earliest) and Stage IV (most serious) is 93% and 15%, respectively [74]. If we take U.K.'s statistic as an example, benefiting from the NHS (National Health Service) Breast Screening Programme (NHSBSP) launched in England, the International Agency for Research on Cancer (IARC) concluded that there was a 25% reduction in mortality in the trials of mammographic screening, and an estimated 1,400 lives were saved by NHSBSP each year in England [75].

2.4.2 Deficiencies of Existing Techniques

Three common screening methods for breast cancer currently used are Ultrasound (US) [31], magnetic resonance imaging (MRI) [32], and X-ray mammography [30]. The inherit lim-

itations of US and MRI make them less popular than mammography. US is unable to detect the early breast tumour with calcifications, since calcifications are invisible on US scans. Besides, poor image resolution and high rate of false-positive examination results of US further confine its practicability. As for MRI, its high cost makes it difficult to act as a screening tool with wide coverage. Additionally, MRI is unsuitable for patients with implanted devices. This is because MRI machines will interact with magnetic objects and can be damaged because of this interaction. Therefore, MRI is usually recommended to be used in conjunction with mammography [34].

Mammography is currently the standard modality for breast cancer screening. It uses low-energy X-rays to examine human breast and identifies the tumour based on the detection of characteristic masses and/or microcalcifications. The microcalcification can be distinguished due to its greater attenuation property compared with that of normal soft tissues [76]. Despite the merits of mammography, its deficiencies are evident. Firstly, the mammography has a low sensitivity in terms of accurate tumour detection [35, 77]. It might fail to detect malignant tumours and either false-negative or false-positive results can appear. False-negative results render the delay in treatment and give patients a sense of false security. False-positive results can be obtained when radiologists identify mammograms are abnormal but no actual tumour is present, resulting in unnecessary anxiety. Furthermore, the radiation exposure from mammography brings a potential threat of increasing cancer risk [37]. Although the amount of radiation exposure is low and under stringent federal regulation, repeatable screening could induce cancer. Based on the statistics in [78], 86 cancers and 11 deaths were predicted to happen out of 100,000 women who were screened annually from age 45 to 55 years and biennially thereafter to age 74 years, due to the radiation-induced breast cancer. Moreover, painful breast compression [79] and the variability of results interpretation [80, 81] in mammography also cause concerns.

2.4.3 Principle of UWB Breast Tumour Detection

The limitations of existing breast cancer screening methods constitute a motivation for better options. In the last few decades, different modalities of microwave imaging for

breast cancer detection, including passive, hybrid, and active approaches, have attracted considerable attention. The passive microwave imaging techniques seek to identify tumours based on the temperature differences between normal and cancerous breast tissues with the aid of radiometers [82, 83]. Hybrid approaches differentiate biological tissues by the acoustic waves radiated from thermoelastic expansion when tissues are under microwave illumination [84]. The active detection methods distinguish normal and malignant breast tissues based on the difference of their dielectric properties. The large dielectric property of malignant tumour leads to greater microwave scattering cross sections than that from normal tissues of comparable geometry with low dielectric property [85].

The passive microwave radiometry was not considered promising as stated in [86] and [87], whereas active microwave imaging has been continuously developed. Based on the reconstruction technique used, the active microwave imaging can be categorised into quantitative and qualitative methods. In quantitative techniques, based on the measured scattered field data, the unknown spatial distribution of dielectric constant and/or conductivity within an imaged object are iteratively calculated, and typically ill-posed, undetermined system of linear or nonlinear equations are solved [88]. To solve this, direct matrix inversion is needed, which can be computationally expensive especially when the size of problem is large. Iterative solvers are proposed to replace the direct inversion, thus quantitative imaging techniques are also referred to as forward iterative methods [89]. Another type of active microwave imaging is based on qualitative methods. In this technique, the qualitative profile of the hidden object is established through certain algorithms, such as time reversal, phase compensation, and back-migration. This imaging technique aims to identify the presence and location of strong scatterers or abnormalities, rather than quantitatively computing the distribution of dielectric properties, thus high computational efficiency in terms of processing time can be ensured.

As an active microwaving imaging technique, UWB breast cancer imaging is based on two fundamental aspects: physiological and technological. First, the dielectric contrast between malignant tumour and normal breast tissues under UWB frequency spectrum enables the differentiation. Research revealed that malignant tumours have the largest

microwave scattering cross sections among all breast tissues with comparable size, which is primarily determined by their varied water content. Malignant breast tumour tissue contains a higher number of water molecules than normal breast tissues [85]. Due to the polarity of water molecules, tissues with varied amounts of water molecules react microwave differently, rendering different levels of absorption and reflection ([90], Ch. 3, pp. 93). Therefore, tumour identification could be achieved by extracting their distinct microwave responses. Secondly, the attenuation of UWB signal in normal breast tissue is less than 4dB/cm up to 10 GHz, which permits the penetration depth up to 5 cm [85, 91, 92]. The depth of non-lactating, typical normal human breast is about 5 cm [93, 94], which allows UWB to cover the vast majority of tumours with decent sensitivity and dynamic range. These two reasons form the foundation of UWB breast imaging for tumour identification.

2.4.4 Advantages of UWB Breast Tumour Detection

As a promising complement for X-ray mammography, UWB breast imaging has several advantages. First, UWB can potentially offer an earlier tumour detection than mammography. UWB imaging distinguishes normal and cancerous tissues based on the dielectric contrast, whereas radiology density is used to discern different tissues by X-ray. Since the dielectric contrast of 2:1 is much higher than the few percent difference in radiographic density exploited in X-ray [41], improved sensitivity is expected in UWB breast imaging. UWB identifies tumour based on its high-water content [85] which is an early growth stage, whereas the detection of microcalcification used in mammogram scan is at an ageing stage [76]. Thus an earlier identification by UWB than mammography could be achieved, thereby offering a higher cure probability.

UWB imaging is a safe modality due to its non-ionising nature, in which the maximum radiated power spectral density of -41.3 dBm/MHz used is much lower than that from a mobile phone (see [95], Ch. 1.2.2.1). Furthermore, it is more comfortable than mammography. Unlike mammography [79], there is no breast compression needed in UWB imaging as the breast is illuminated with microwave signals radiated from antennas. The safety and

comfort enable the adoption of this technology for both frequent screening at early stage, and frequent monitoring of disease progression and response to therapy at later phases.

Equally important is that UWB imaging system can be economical. X-ray computed tomography (CT) can cost several hundred thousand to over million dollars. In comparison, the UWB sensor prototype developed at Lawrence Livermore National Laboratory (LLNL) costs only hundreds of dollars to manufacture [19]. Also due to the relatively simple system components, UWB imaging could be implemented as a hand-held device [19]. The low cost and portability permit a wide availability, making the serving for both personal healthcare and the in-field use by first responders feasible.

2.5 Technical Advances and Challenges of UWB Breast Cancer Imaging

Although numerous work has been conducted to advance the performance of UWB breast cancer imaging, several challenges still remain in the following areas.

2.5.1 Numerical Breast Phantom

To develop a system, modelling and simulation have been proved as one of the most effective ways to test hypotheses, thereby saving a significant amount of time and cost. As for microwave imaging for breast cancer detection, the interaction between breast tissues and EM waves is the first problem need to be addressed, which involves the construction of breast phantoms, and signal propagation modelling.

Reliable simulation results are based on accurate modelling. Realistic models should incorporate various attributes of the breast, including geometrical properties, spatial distribution of different tissues, and dispersive property. The fidelity of numerical breast model is mainly determined by the following factors.

- Model Dimension

  A numerical breast model is the basis of computational electromagnetics for microwave imaging. One of the most essential model measurements is the dimension.

The breast model can be either two-dimensional (2-D) or 3-D. The 2-D breast model was used as a benchmark in the seminal study in [85], which assumed that the structure being modelled extends to infinity in z-direction with no change in shape or position of its transverse cross section [53]. 2-D models can be used to analyse certain scenarios when the incident wave is uniform in z-direction, then all partial derivatives of the field components (e.g. electric field, magnetic field, etc.) with respect to z equal zero. However, this does not conform to practical imaging situation. Accordingly, 3-D breast models have been employed in studies such as [96] and the subsequent ones.

- Geometrical Property

  Geometry explains the relation of points, lines, surfaces, and volumes of an object. The geometry of an object directly affects the characteristics of the scattered fields when it interacts with microwave signals, which comprises the foundation of inverse scattering techniques for non-invasive imaging [97]. Based on related strategies such as contour parametrisation, the profile of the object-under-test can be established. Thus, quasi-human-breast shape is optimum for modelling and simulation. However, despite many studies employed 3-D models, the geometrical property of breast has been seriously neglected. For example, rectangular blocks were used to represent the breast in [50, 96] and [51]. This cuboid-shaped breast model might be suitable for performance comparison of imaging algorithms; however, realistically shaped breast models should be constructed for further verification, considering the importance of model geometry.

- Tissue Composition

  In biology, tissue is the basic cellular organizational level intermediate between cells and an organ [98]. Organs such as breast can then be formed by the functional grouping of multiple tissues. Exactly mimicking the physiological property of all breast tissues can be extremely challenging. Therefore, three major aspects including structural heterogeneity, dispersive property, and density classifications of breast models are considered, which properly represent the composition of breast tissues.

The sparse breast model composed of two types of homogeneous tissues, including normal and malignant tissues, were used in [50, 51, 85, 96]. To capture the structural heterogeneity of normal breast tissue, the dielectric property was varied by ±10% around the selected mean value in [99], which was in line with the data from [100] and [101]. Further advance in terms of incorporating the dispersive property of breast tissues into the modelling was offered by [50]. This incorporation is pivotal because it enables the acquisition of backscattered signals from dispersive breast tissues rather than over-simplified nondispersive tissues, which is much more realistic. A series of advanced numerical breast phantoms with much improved accuracy were introduced in [102]. Besides heterogeneous structures and varied tissue types, the density classification was also considered. Derived from MRI-based data, the breast phantoms developed in [102] were both dielectrically and anatomically accurate.

- Tumour Modelling

  To aid the development of breast tumour detection approaches, varied tumour models are necessary to simulate different scenarios. In the database introduced in [103], tumours with different sizes are described. The size of tumour determines the magnitude of backscattered signals, which is critical for energy-based techniques to identify the existence and location of the tumour. Apart from size, the shape of tumour can be regular or irregular. Depending on the property of tumour, which can be either benign or malignant, different appearances and growing patterns have been observed. Benign tumours are usually compact and roughly elliptical, whereas malignant tumours show irregular appearance and have a blurry periphery. This distinct morphological appearance can be potentially useful for discrimination between benign and malignant anomalies [104, 105], which also indicates the importance of modelling tumours with different forms. The third aspect of tumour modelling is the position. Depending on the position of tumour, there can be ductal carcinomas which start at fibro-glandular regions [106] and the others which start from fatty tissue regions. Accordingly, various cases should be taken into account for complete examination of imaging techniques.

2.5.2 Modelling of Signal Propagation

To numerically explore microwave signal propagation within breast tissue, Maxwell's equations are needed to be solved as they state the fundamentals of electricity and magnetism. The major techniques to model computational electromagnetics include finite-difference time-domain (FDTD) [107], transmission line matrix (TLM) [108], finite element method (FEM) [109], finite-difference frequency-domain (FDFD) [110], method of moments (MoM) [111], and fast multipole method (FMM) [112]. Based on the way of solving Maxwell's equations in its differential or integral form, these methods can be classified into two categories as shown in Fig. 2.3.

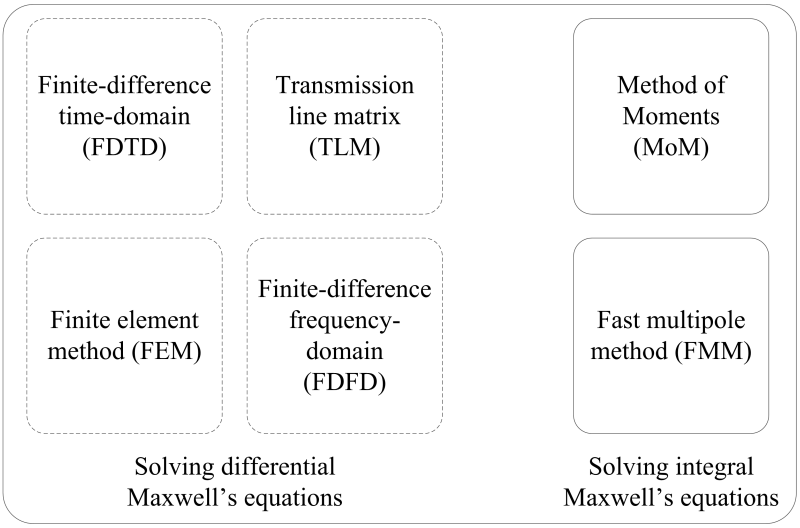

Fig. 2.3 Numerical techniques for solving Maxwell's equations.

- Finite-difference Time-domain (FDTD)

  FDTD is a time domain method that discretizes the Maxwell's curl equations using central-difference approximations to the space and time derivatives [107]. In this method, electric-field and magnetic-field vector components in a volume of space can be solved at alternate time steps. The process is repeated until the desired electromagnetic field is fully evolved. Since the FDTD technique allows the assignment of material property at all points within the computational domain, it enables the modelling of a variety of dielectric and magnetic materials. Additionally, FDTD is very suitable for transient analysis problems. Due to its time-domain basis, the

solutions of FDTD can cover a wide range of frequency with a single run, and treat linear and non-linear material problems in a natural way [113].

- Transmission Line Matrix (TLM)

  TLM is also a space and time discretizing method. It replaces the field problem by equivalent network, which is based on Huygen's model of wave propagation [108]. An analogous equivalence between the voltages and currents of transmission lines and electromagnetic fields is achieved through mapping the transmission line equations and the Maxwell's equations [114]. TLM analyses complicated structures with great flexibility because it incorporates the properties of EM fields, the material media, and their interaction with boundaries. However, this versatility is at the expense of extra memory requirement. Depending on the selected resolution of the mesh, large memory storage might be needed.

- Finite Element Method (FEM)

  FEM aims at finding approximate solutions for partial differential equations through dividing a large domain into subdomains. Each subdomain is called a finite element, and a set of element equations is used to represent the original problem. The recombination of all sets of element equations is required for final calculation. One advantage of FEM is its flexibility to analyse problems with complicated domains, such that each domain can be assigned with a varied resolution. However, this method is not well suited for modelling many electromagnetic interference problems, which is illustrated in [115].

- Finite-difference Frequency-domain (FDFD)

  FDFD has many similarities to FDTD, except it is a frequency-domain method. FDFD solves the Maxwell's equations in its time harmonic form, based on the finite-difference approximations of derivative operators. Although FDFD and FDTD share the same discretization constraints, their capabilities are different. FDFD has a preferable adaptability in defining composite structures (shape and type) in each defined sub-regions and extra memory saving than FDTD [116]; however, it is considerably more computational extensive for large-scale problems [117].

- Method of Moments (MoM)

  MoM is capable of solving the integral form of Maxwell's equations. This is accomplished by decomposing them into a system of linear equations, and the structure is discretized with planar and/or curvilinear triangular elements [118]. A matrix representation can then be established based on the number of segments. The distribution of problem structure can be calculated with different input parameters, such as near fields, far fields, and impedance. MoM is highly efficient when perfectly conducting wire scatterers are the types of problem, but limited for the analysis of complex heterogeneous geometries [115].

- Fast Multipole Method (FMM)

  FMM is a technique that was originally proposed to accelerate the computation of classical boundary value problems [119]. Later on, this method has been extended to solve acoustic and electromagnetic scattering problems [120]. FMM offers both reduced memory storage and computational complexity, thus it can expand the area of applying modelling techniques such as MoM to far greater problems which were previously impossible.

Since biological tissue in nature is frequency-dependent (also referred to as dispersion) when it interacts with EM waves [121], it is thus important to incorporate this for precise modelling. Different models for describing the dispersion of medium include Drude, Debye, and Lorentz [122], and Cole-Cole [123]. Another aspect for propagation modelling is the termination of computational domain by absorbing boundary conditions (ABCs). ABCs are needed for delimiting the area of interest for affordable computational burden and various proposals have emerged, and these include Mur's [124], Liao's [125], perfectly matched layer (PML) [126] and its variants include uniaxial perfectly matched layer (UPML) [127] and convolutional perfectly matched layer (CPML) [128].

Based on the review of these techniques, it is noted that each one has its capabilities, advantages, and limitations. Additionally, the propagation modelling of microwave signal within biological tissues can be highly complex. This is because it involves a large number of solving of differential/integral equations, which is known as the cruelty of computational

complexity in computer science. Therefore, depending on a particular task, it is of crucial importance to choose proper techniques and consider the combination of them as a whole to ensure the efficacy, accuracy, and computational and storage efficiency.

2.5.3 Image Reconstruction Algorithm

Another vital aspect of UWB imaging system is the imaging algorithm (also called image formation algorithm, or image reconstruction algorithm) due to its decisive significance to system output. As mentioned in Section 2.4.3, UWB imaging can be classified as quantitative and qualitative methods. Specifically, quantitative methods aim to recover the entire dielectric property profile of the breast, which is also called microwave tomography [129–131], whereas qualitative algorithms intend to identify and localise the abnormalities within normal tissues.

Qualitative UWB imaging techniques can be classified into two categories: data-dependent and data-independent. Data-dependent algorithms attempt to estimate the propagation channel based on the signals reflected from the object of interest (OI) [46, 48, 132–143], whereas data-independent methods employ an assumed channel model to compensate for path-dependent propagation effect [39, 41, 45, 50–52, 85, 144–147]. Data-dependent imaging algorithms account for some uncertainties during pre-processing steps, such as errors in amplitude compensation or non-ideal time delays, thus theoretically they can construct high-resolution images and offer stong interference rejection. However, this advantage relies on the assumed priori information that the array steering vector corresponding to the signal of interest (SOI) is accurately known. When this priori information is imprecise (as is often the case in practice), the performance of data-dependent methods may become worse than that of their data-independent counterparts [148]. Data-independent algorithms are free from this priori information and normally have a much more higher computational efficiency than data-dependent methods, but their interference rejection capability needs to be further enhanced.

Although many image reconstruction algorithms have been proposed, they have some shortages and limitations, which may seriously affect the applicability in realistic conditions, and these can be summarised as follows.

- Over-simplistic Imaging Scenario

  Some imaging algorithms were only examined in 2-D breast models [147]. Although encouraging results were obtained, their effectiveness in practical 3-D cases is arguable and further evaluation could be necessary. This is because in a 2-D modelling of computational electromagnetic, the third dimension is assumed to be infinitely long and all intensities (e.g. electric field, magnetic field, etc.) are invariant [46]. Therefore, the modelled tumour which has infinite dimension along the third axis can produce much more stronger backscattered signals. But these assumptions are invalid in 3-D imaging cases, thus the imaging algorithms may suffer severe performance reduction or totally fail. Furthermore, the breast models used for testing algorithms are over-simplistic. In many literature [50, 51, 146, 147, 149], only homogeneous breast models with few types of tissues were employed to validate the efficacy of proposed algorithms. Despite the promising results presented, it is essential to consider a broader range of more realistic scenarios. For example, it is acknowledged that the heterogeneously dense breast tissues would not only complicate the estimation of propagation channels, but also result in serious signal attenuation [52]. All of these can make the identification of small tumours much more challenging.

- Limited Detectability of Multiple Scatterers

  A range of imaging algorithms show decent tumour detection based on the significant dielectric contrast between adipose and malignant tissues, which represents the scenarios of mostly sparse breasts. However, the study in [150] pointed out that the dielectric contrast between fibro-glandular and malignant tissues is much less pronounced, making the detection of tumours in breasts with high-portion glandular tissues much more difficult. On one hand, the comparable dielectric property between tumour and glandular tissues raises a new sensitivity challenge for algorithm. In such

cases, the scattering from the tumour can easily get obscured by the scattering from glandular tissues. On the other hand, the presence of glandular tissues introduces significant amount of attenuation and dispersion, which can further complicate the estimation of propagation channels. Hence, it is necessary to develop effective techniques for tumour detection even in dense breasts.

- Vulnerability to Artefact Signals

  Another important aspect of UWB breast imaging is the removal of artefact signals [151]. The early-stage artefact is composed of incident signals, skin-fat reflection signals, and possible antenna reverberations. The artefact is typically orders of magnitude greater than desired tumour response which is the reflected signals from the tumour. Therefore, if the artefact cannot be removed, it could easily mask the tumour response and lead to the failure of imaging algorithms. Serving as a benchmark for performance analysis, the idealised artefact removal method is applied in many studies [39, 40, 50, 51, 152], in which the priori information obtained from tumour-free breast models is required. However, this ideal artefact removal is infeasible in practice, and a series of more practical solutions have been proposed [2, 40, 45, 145, 153–157]. These practical artefact removal methods employ adaptive or non-adaptive signal filtering techniques in either time or frequency domain, which can remove the majority of artefact. However, even the most advanced method is unable to perfectly remove all artefact signals. Thus, the imaging algorithm with high artefact resistance is particularly desired.

- Algorithm Complexity

  Besides robustness, the complexity of algorithm is of same importance as this directly determines the processing time of image reconstruction. This is especially prominent for constructing 3-D medical images that normally have a high requirement of resolution, which can be millions of pixels. This is because high resolution is a key for better understanding of the results, which can effectively remove the ambiguity of image interpretation [158]. Thus, enhancing the computational efficiency of imaging algorithms becomes critical. But most if not all existing studies only take

the effectiveness of algorithm into account, while improving their efficiency is not receiving enough attention it deserves.

2.5.4 Physical Breast Phantom and Antenna Design

Before applying an imaging system in clinical trial, the validation based on experimental test-bed is indispensable for reducing possible risks and unnecessary costs. Towards this end, physical breast phantoms and antennas are required.

To fabricate realistic physical breast phantom, tissue-mimicking materials with proper dielectric properties are used to represent different breast tissues, such as skin, fat, fibro-glandular, and tumour [159]. Additionally, the breast phantom should exhibit dispersive property and varied density classifications [160]. For example, the breast phantom based on 3-D printing was introduced in [161], which permits the preciseness of both exterior and interior breast structure and dielectric profile. The stability study of breast phantom over time and temperature, as well as their reproducibility for a given structure was performed in [162]. This study also suggested alternative materials which present similar dispersive property but with easier production and more flexible parameter settings.

Many efforts have also been addressed to design compact antennas for collecting signals from physical breast phantoms. Resistively loaded bowtie and dipole antenna were firstly introduced [163, 164], and the optimised Vee dipole with improved broadband behaviour was proposed in [165]. Unlike most antennas which are designed to observe co-polarised reflections from the target, target sensing with cross-polarised reflections using a bowtie antenna was explored in [166]. A modified prototype for resistively loaded bowtie antenna through modelling and genetic optimisation was presented in [38], the feasibility of which was validated by both simulated and measured results, achieving close agreement. A compact double-layer on-body matched bowtie antenna was presented in [167], which showed reduced size and fine range resolution. A hemispherical real-aperture antenna array was put forward in [42], and experimental results demonstrated the detection of small tumours with 4 mm and 6 mm in diameter in breast phantom.

As herein introduced, various breast phantoms and antennas have been designed, proposed, and optimised. However, few of them provided the experimental results which are based on both sufficiently accurate breast phantoms and effective antenna fabrications, therefore, further theoretical research and experimental validation are necessary.

2.6 Conclusion

This chapter introduces the background of UWB technology, and reviews the development of UWB imaging for breast cancer detection (more specific literature reviews are presented in following contribution chapters also). It starts with the overview of UWB, its fundamentals and a wide range of applications are introduced. Then UWB imaging for breast tumour identification is presented in detail, which is regarded as one of the most promising alternatives for breast cancer screening. The importance, principle, and advantages of UWB imaging for breast cancer detection are described. This is followed by a review of up-to-date advances and existing technical challenges, namely numerical breast phantom construction, signal propagation modelling, image reconstruction algorithm, physical breast phantom and antenna design.

This chapter identifies existing limitations and challenges which have fundamental impacts on the performance of UWB breast imaging system, upon which our contributions in Chapter 3 to 6 of this thesis are built.

Chapter 3

Propagation Modelling and Simulation of UWB Signals for Breast Tumour Detection

3.1 Introduction

To develop imaging algorithms and evaluate their effectiveness, accurate propagation modelling of UWB signals within realistic breast phantoms is critical. To this end, a new versatile electromagnetic computation engine (VECE) is proposed.

Based on the finite-difference time-domain (FDTD) technique, VECE provides the first implementation of its kind which combines auxiliary differential equations (ADE) and convolutional perfectly matched layer (CPML) for describing the Debye dispersive medium, and truncating the computational domain, respectively. The unique combination of ADE and CPML results in high accuracy, and improved computational and memory storage efficiency. Furthermore, realistic breast phantoms based on the state-of-the-art MRI-derived repository have been integrated, which enables the simulation of breast tissue response under microwave exposure conditions. The accuracy of VECE is validated via extensive simulations and comparisons, achieving excellent agreement across a range of appropriate metrics. VECE is capable of simulating a broad range of breast imaging

scenarios, such as varied input signals, breast models, tumour positions, and antenna configurations. These results show its strong practicability to facilitate the development of diagnostic and therapeutic technologies for breast cancer, and great potential for related bio-imaging applications.

The remainder of this chapter is organised as follows. Section 3.2 reviews existing numerical modelling techniques, boundary conditions, and different ways of integrating these techniques. Section 3.3 formulates the ADE-FDTD analysis for electromagnetic propagation in 3-D Debye dispersive medium. Section 3.4 introduces the theory of CPML boundary conditions which are used to truncate the FDTD lattices. Section 3.5 presents the design and implementation of VECE. Section 3.6 validates the effectiveness and accuracy of VECE through simulations and comparisons with the results obtained from Remcom's XFDTD commercial software [168]. Besides, the computational efficiency of VECE is discussed. Section 3.7 presents the visualisation of 3-D breast models and signal propagation. Simulation results for breast tumour detection under different scenarios are provided in Section 3.8. Section 3.9 introduces further potential application areas of VECE and concluding remarks are drawn in Section 3.10.

3.2 Literature Review

To simulate UWB imaging for breast cancer detection, two imperative aspects are the construction of breast phantoms, and the modelling of UWB signal propagation within breast tissues. The breast model should represent the dielectric properties of constituent tissues, and the highly correlated distribution of these tissues. The propagation modelling and simulation, on the other hand, should be effective, computationally efficient, and flexible for various scenarios. Building upon the state-of-the-art numerical breast phantoms established in UWCEM repository [103, 169, 170], this chapter mainly focuses on the propagation modelling of signals. To achieve this, three aspects need to be considered: numerical analysis techniques for computational electromagnetics, dispersive models to represent the biological entities, and absorbing boundary conditions (ABC) to attenuate the outgoing radiation. To implement each aspect above-mentioned, there are more options

than one. Therefore, appropriate selection and combination of these components can affect the efficacy and efficiency of the computation as a whole.

Several techniques are used for computational electrodynamics, including FEM [109], MOM [111], FIT [171], and FDTD [107]. Among these approaches, FDTD has been a preferred choice by virtue of its accuracy, robustness, and the capability to model a wide diversity of exposure conditions for anisotropic, non-linear, and dispersive media [172].

Rigorous models for describing the dispersion of medium include Drude, Debye, and Lorentz [122], whereas the Cole-Cole which is an empirical model also attracted noticeable interest in recent years [123]. Several approaches allow FDTD to incorporate frequency-dependent dielectric media include recursive convolution (RC) [173–175], trapezoidal recursive convolution (TRC) [176], piecewise-linear recursive convolution (PLRC) [177], Z-transform [178], and auxiliary differential equation (ADE) [179] [53].

The third aspect involves the termination of the computational domain by ABC and the necessity is twofold. First, the structure of interest should be enclosed in a limited area for the consideration of affordable computational burden. Second, boundary conditions are needed to truncate the mesh in a reflectionless way, which allows the analysis of electromagnetic interaction within the region of interest. Various ABCs have been developed, among which PML [126] and its variants include UPML [127] and CPML [128] have proven to be the most robust and efficient approaches for FDTD terminations [180].

FDTD with different dispersive models and ABCs have been investigated. In [181], the addition of CPML to 3-D FDTD simulations with dielectric and conducting objects was presented. [182] implemented a Cole-Cole model for biological tissues, which was delimited by the first-order Mur absorbing boundary. The analysis and implementation of FDTD for Debye dispersive media through PLRC with CPML boundary were provided in [172] and [183]. The simulation adopting Lorentz-Drude (LD) model in conjunction with ADE technique was introduced in [122] and [184], in which Mur and CPML boundary conditions were used, respectively. [185] presented the implementation of Drude-critical point (DCP) model for describing dispersive media through both PLRC and ADE approaches, and comparative analysis was elaborated.

Depending on selected techniques to implement different components of FDTD computation, the effectiveness and efficiency of the outcome can be vastly different. FDTD calculation can be computationally expensive with significant run-times, especially when accurate results of 3-D dispersive models are involoved. Despite the noticeable speedup offered by hardware accelerator approaches [172, 181, 184, 186, 187], the inherent complex computations still exist. The complexity mainly stems from two aspects: the way of simulating dispersion of host medium, and the selection of boundary conditions. The major two techniques which incorporate dispersion into FDTD are PLRC and ADE. ADE methods have the same second-order accuracy as PLRC. However, the time domain basis of ADE makes it particularly attractive for modelling arbitrary nonlinear dispersive media. Existing literature also demonstrated that the usage of ADE resulted in reduced computational amount compared to PLRC. This is because ADE does not involve complex-number arithmetic, thus it requires relatively fewer floating-point operations as compared to PLRC [185] [188]. Furthermore, ADE requires an equal or smaller number of unknowns to be stored, thereby reducing memory storage requirement and related processing time ([53], Ch. 9, pp. 361). Another concern is the selection of boundary conditions. For general media, the number of unknowns required for CPML is identical to PML and UPML [180]. To terminate a specific type of medium, such as isotropic, homogeneous, inhomogeneous, lossy, dispersive, anisotropic, and linear, unlike PML and UPML, CPML has exceptional flexibility since it does not require any further deformations. Moreover, CPML is highly absorptive for both propagating and evanescent waves, resulting in a significant memory saving [172]. The effective absorption of evanescent waves allows CPML layers to be placed fairly close to the host medium, whereas for PML and UPML, a sufficiently large distance is essential such that the evanescent waves have adequately decayed. Studies showed that this improvement of CPML has led to a four-fold reduction in memory space [189], which makes it a superior absorbing boundary for the analysis of complex geometries such as biological tissues.

The best attributes of ADE and CPML in terms of efficacy, computational efficiency, and memory saving over their counterparts are simultaneously integrated in the proposed

VECE. Computations were performed with low-complexity implementations on the high performance computing (HPC) Apollo Cluster (304 GB RAM) at University of Sussex. VECE is the first implementation of 3-D ADE-FDTD for modelling Debye dispersive media with CPML absorbing boundary, allowing for measuring and quantifying the biological effects arise from electromagnetic field radiation.

3.3 Auxiliary Differential Equation

In this section, the incorporation of Debye model to FDTD algorithm through ADE technique, describing the dispersion of main simulation area, is presented.

Starting by defining the permittivity $\varepsilon(\omega)$ of Debye model in frequency domain, which is expressed as ([53], Ch. 7, pp. 311)

$$\varepsilon(\omega) = \varepsilon_\infty + \sum_{p=1}^{P} \frac{\Delta\varepsilon_p}{1 + j\omega\tau_p} - j\frac{\sigma}{\omega\varepsilon_0} \tag{3.1}$$

where ω is angular frequency, ε_∞ is the permittivity at infinite frequency, $\Delta\varepsilon_p = \varepsilon_{s,p} - \varepsilon_{\infty,p}$ is the change in permittivity due to the pth dispersive pole of P, $\varepsilon_{s,p}$ and $\varepsilon_{\infty,p}$ are corresponding static permittivity and the permittivity at infinite frequency, respectively. τ_p is the relaxation time of the pth pole, σ is conductivity, ε_0 is free-space permittivity, and $j = \sqrt{-1}$. Ampere's law in frequency domain can be expressed as

$$\nabla \times \widetilde{H} = j\omega\widetilde{D} \tag{3.2}$$

where

$$\widetilde{D} = \varepsilon_0\varepsilon(\omega)\widetilde{E} \tag{3.3}$$

where ∇ is curl operator, H is magnetic field, E is electric field, D is electric flux density, and $\widetilde{H}$, $\widetilde{E}$, $\widetilde{D}$ are their corresponding Fourier transforms. Any function u (e.g. H, E, D, etc.) at a discrete point (i, j, k) of a 3-D space and at a discrete time n is denoted as

$$u(i\Delta x, j\Delta y, k\Delta z, n\Delta t) = u|^n_{i,j,k} \tag{3.4}$$

where i, j, k, n are integers, Δt is the time increment, and Δx, Δy, Δz are the space increments in x, y, and z coordinate directions, respectively.

By substituting (3.1) and (3.3) in (3.2), the following expression is obtained as

$$\nabla \times \widetilde{H} = \varepsilon_0 \varepsilon_\infty j\omega \widetilde{E} + \sigma \widetilde{E} + \sum_{p=1}^{P} \widetilde{J}_p \tag{3.5}$$

where $\widetilde{J}_p$ is the polarization current density with the pth dispersive pole given by

$$\widetilde{J}_p = \varepsilon_0 \Delta \varepsilon_p \big(\frac{j\omega}{1 + j\omega\tau_p}\big)\widetilde{E}. \tag{3.6}$$

Multiplying both sides of (3.6) by $(1 + j\omega\tau_p)$, which yields

$$\widetilde{J}_p + j\omega\tau_p \widetilde{J}_p = \varepsilon_0 \Delta \varepsilon_p j\omega \widetilde{E}. \tag{3.7}$$

Exploiting the differentiation theorem for the Fourier transform ([53], Ch. 7, pp. 362), the inverse Fourier transformation of each term of (3.7) is performed, which gives

$$J_p + \tau_p \frac{\partial J_p}{\partial t} = \varepsilon_0 \Delta \varepsilon_p \frac{\partial E}{\partial t}. \tag{3.8}$$

To implement (3.8) in FDTD, the semi-implicit scheme is adopted ([53], Ch. 7, pp. 362). In this strategy, the yet-to-computed field component at time-step $n+1$ is obtained based on a known field at time-step n, thereby creating an updating formula. Rewriting (3.8) in finite-difference expression, which centred at time-step $n + 1/2$ and can be expressed as

$$\big(\frac{J_p^{n+1} + J_p^n}{2}\big) + \tau_p \big(\frac{J_p^{n+1} - J_p^n}{\Delta t}\big) = \varepsilon_0 \Delta \varepsilon_p \big(\frac{E^{n+1} - E^n}{\Delta t}\big). \tag{3.9}$$

Solving (3.9) for J_p^{n+1}, we obtain

$$J_p^{n+1} = k_p J_p^n + \beta_p \big(\frac{E^{n+1} - E^n}{\Delta t}\big) \tag{3.10}$$

where

$$k_p = \frac{1-\Delta t/2\tau_p}{1+\Delta t/2\tau_p} \qquad \beta_p = \frac{\varepsilon_0 \Delta \varepsilon_p \Delta t/\tau_p}{1+\Delta t/2\tau_p} \tag{3.11}$$

To calculate E^{n+1}, $J_p^{n+1/2}$ is required, which can be obtained from (3.10) as

$$J_p^{n+1/2} = \frac{1}{2}\big(J_p^{n+1} + J_p^n\big) = \frac{1}{2}\big(1+k_p\big)J_p^n + \beta_p\big(\frac{E^{n+1}-E^n}{\Delta t}\big). \tag{3.12}$$

Similarly, we use semi-implicit scheme at time-step $n+1/2$ for the time-domain form of (3.5)

$$\nabla \times H^{n+1/2} = \varepsilon_0 \varepsilon_\infty \big(\frac{E^{n+1}-E^n}{\Delta t}\big) + \sigma\big(\frac{E^{n+1}+E^n}{2}\big) + J_p^{n+1/2}. \tag{3.13}$$

The explicit time-marching relation for E is solved as

$$E^{n+1} = C_a E^n + C_b \left[\nabla \times H^{n+1/2} - \frac{1}{2}\sum_{p=1}^{P}\big(1+k_p\big)J_p^n\right] \tag{3.14}$$

where C_a and C_b are auxiliary coefficients. Therefore, based on (3.14), the E-fields in x coordinate direction (E_x) with ADE for Debye medium can be obtained as

$$\begin{aligned} &E_x|_{i+1/2,j,k}^{n+1/2} \\ &= C_a|_{i+1/2,j,k} E_x|_{i+1/2,j,k}^{n-1/2} + C_b|_{i+1/2,j,k}\left[\frac{H_z|_{i+1/2,j+1/2,k}^n - H_z|_{i+1/2,j-1/2,k}^n}{\Delta y}\right. \\ &\left. - \frac{H_y|_{i+1/2,j,k+1/2}^n - H_y|_{i+1/2,j,k-1/2}^n}{\Delta z} - \frac{1}{2}\big(1+k_p\big)J_{p_x}|_{i+1/2,j,k}^{n-1/2}\right] \end{aligned} \tag{3.15}$$

where

$$\begin{aligned} C_a|_{i+1/2,j,k} &= \big(1-\frac{\sigma_{i+1/2,j,k}\Delta t}{2\varepsilon_{i+1/2,j,k}}\big)/\big(1+\frac{\sigma_{i+1/2,j,k}\Delta t}{2\varepsilon_{i+1/2,j,k}}\big) \\ C_b|_{i+1/2,j,k} &= \big(\frac{\Delta t}{\varepsilon_{i+1/2,j,k}}\big)/\big(1+\frac{\sigma_{i+1/2,j,k}\Delta t}{2\varepsilon_{i+1/2,j,k}}\big). \end{aligned} \tag{3.16}$$

Based on the formulations above-presented, it can be seen that modelling Debye medium with ADE-FDTD algorithm is a three-step fully explicit procedure. Starting with stored

fields include E^n, J_p^n, and $H^{n+1/2}$, the new E^{n+1} is first calculated through (3.14). Then J_p^{n+1} can be obtained based on J_p^n and the just-computed E^{n+1} according to (3.10). Lastly, $H^{n+3/2}$ can be calculated from known $H^{n+1/2}$ and E^{n+1} in a usual manner from the Yee cell realisation of Faraday's law [107], and the complete cycle starts again. It is noted that to model Debye medium through ADE technique, only P additional real variables related to polarisation current are required for each E component, which ensures a minimum extra computation cost.

3.4 Convolutional Perfectly Matched Layers

This section introduces the formulations of boundary conditions using CPML, which effectively truncate the main computational area of interest.

The tensor coefficient s_w (w indicates the axis direction, which can be x, y, or z) used in CPML is modified as follows ([53], Ch. 7, pp. 296)

$$s_w = k_w + \frac{\sigma_w}{\alpha_w + j\omega\varepsilon_0} \tag{3.17}$$

where k_w is a constructed nonunity real part, and σ_w is conductivity. Compared with the original form of s_w used in PML, the new term α_w is added to shift the pole off the origin into the upper-half complex plane, and this addition has been proven beneficial for reducing strong reflections at low frequencies [189, 190]. Additionally, with the purpose of absorbing both propagating and evanescent waves, spatial scaling is applied for α_w, such that it has a larger value at the truncation interface and decays to zero within CPML regions. s_w has been referred to as the complex frequency-shift (CFS) tensor coefficient of CPML. Denoting F^{-1} as the inverse Fourier transform operator, and define the following relation

$$\overline{s_w} = F^{-1}\left[\frac{1}{s_w(\omega)}\right] = \frac{\delta(t)}{k_w} - \zeta_w(t) \tag{3.18}$$

where

$$\zeta_w(t) = \frac{\sigma_w}{\varepsilon_0 k_w^2} e^{-\left(\frac{\sigma_w}{\varepsilon_0 k_w} + \frac{a_w}{\varepsilon_0}\right)t} u(t) \tag{3.19}$$

where $u(t)$ is the unit step function, and $\delta(t)$ is the unit impulse function. Based on Berenger's PML theory [189], the Ampere's law in frequency domain in complex-coordinate stretched space are expressed as

$$\nabla \times \widetilde{H} = \widehat{x}\Big(\frac{1}{s_y}\frac{\partial \widetilde{H_z}}{\partial y} - \frac{1}{s_z}\frac{\partial \widetilde{H_y}}{\partial z}\Big) + \widehat{y}\Big(\frac{1}{s_z}\frac{\partial \widetilde{H_x}}{\partial z} - \frac{1}{s_x}\frac{\partial \widetilde{H_z}}{\partial x}\Big) + \widehat{z}\Big(\frac{1}{s_x}\frac{\partial \widetilde{H_y}}{\partial x} - \frac{1}{s_y}\frac{\partial \widetilde{H_x}}{\partial y}\Big) \tag{3.20}$$

where the over-hat $\widehat{x}$, $\widehat{y}$, and $\widehat{z}$ denotes a phasor quantity. To obtain the time domain counterpart of (3.20), combining inverse Fourier transform and the reciprocal of tensor coefficient $\frac{1}{s_w}$ ($w = x, y, z$), which can yield ([53], Ch. 7, pp. 303)

$$\begin{aligned}\nabla \times H = \frac{\partial D}{\partial t} = \widehat{x}\Big(\overline{s_y} * \frac{\partial H_z}{\partial y} - \overline{s_z} * \frac{\partial H_y}{\partial z}\Big) + \widehat{y}\Big(\overline{s_z} * \frac{\partial H_x}{\partial z} - \overline{s_x} * \frac{\partial H_z}{\partial x}\Big) \\ + \widehat{z}\Big(\overline{s_x} * \frac{\partial H_y}{\partial x} - \overline{s_y} * \frac{\partial H_x}{\partial y}\Big)\end{aligned} \tag{3.21}$$

where "$*$" denotes the convolution. Noted that the right-hand side of (3.21) is independent of medium type since it only applies to the field intensities, which explains the capability of CPML for accommodating and truncating various host media. Expanding (3.21) by replacing $\overline{s_w}$ ($w = x, y, z$) in a more concise way

$$\begin{aligned}\nabla \times H = \frac{\partial D}{\partial t} = \widehat{x}\Big(\frac{1}{k_y}\frac{\partial H_z}{\partial y} - \frac{1}{k_z}\frac{\partial H_y}{\partial z} + \zeta_y * \frac{\partial H_z}{\partial y} - \zeta_z * \frac{\partial H_y}{\partial z}\Big) \\ + \widehat{y}\Big(\frac{1}{k_z}\frac{\partial H_x}{\partial z} - \frac{1}{k_x}\frac{\partial H_z}{\partial x} + \zeta_z * \frac{\partial H_x}{\partial z} - \zeta_x * \frac{\partial H_z}{\partial x}\Big) \\ + \widehat{z}\Big(\frac{1}{k_x}\frac{\partial H_y}{\partial x} - \frac{1}{k_y}\frac{\partial H_x}{\partial y} + \zeta_x * \frac{\partial H_y}{\partial x} - \zeta_y * \frac{\partial H_x}{\partial y}\Big).\end{aligned} \tag{3.22}$$

Transforming (3.5) from frequency domain to time domain for a single-pole Debye model [see (3.1) with P = 1], we obtain

$$\nabla \times H = \varepsilon_0 \varepsilon_\infty \frac{\partial E}{\partial t} + \sigma E + J_p. \tag{3.23}$$

Connecting the right-hand sides of (3.23) and (3.22), and taking the x-projection as an example

$$\varepsilon_0\varepsilon_\infty\frac{\partial E_x}{\partial t}+\sigma E_x+J_{p_x}=\frac{1}{k_y}\frac{\partial H_z}{\partial y}-\frac{1}{k_z}\frac{\partial H_y}{\partial z}+\zeta_y*\frac{\partial H_z}{\partial y}-\zeta_z*\frac{\partial H_y}{\partial z}. \tag{3.24}$$

To derive explicit updates for E-fields in x coordinate direction (E_x) from (3.24) in a computationally affordable manner, as well as for obtaining a time-marching equation, the recursive-convolution (RC) [174] technique is used. By using RC and the discrete time and space approximation employed in standard Yee scheme [107], E_x is obtained as

$$\begin{aligned}
&E_x|^{n+1/2}_{i+1/2,j,k}\\
&=C_a|_{i+1/2,j,k}E_x|^{n-1/2}_{i+1/2,j,k}+C_b|_{i+1/2,j,k}\Bigg[\frac{H_z|^n_{i+1/2,j+1/2,k}-H_z|^n_{i+1/2,j-1/2,k}}{k_{y_j}\Delta y}\\
&-\frac{H_y|^n_{i+1/2,j,k+1/2}-H_y|^n_{i+1/2,j,k-1/2}}{k_{z_k}\Delta z}+\psi_{E_{x,y}}|^n_{i+1/2,j,k}-\psi_{E_{x,z}}|^n_{i+1/2,j,k}\\
&-\frac{1}{2}\big(1+k_p\big)J_{p_x}|^{n-1/2}_{i+1/2,j,k}\Bigg]
\end{aligned} \tag{3.25}$$

where

$$\begin{aligned}
C_a|_{i+1/2,j,k}&=\big(1-\frac{\sigma_{i+1/2,j,k}\Delta t}{2\varepsilon_{i+1/2,j,k}}\big)/\big(1+\frac{\sigma_{i+1/2,j,k}\Delta t}{2\varepsilon_{i+1/2,j,k}}\big)\\
C_b|_{i+1/2,j,k}&=\big(\frac{\Delta t}{\varepsilon_{i+1/2,j,k}}\big)/\big(1+\frac{\sigma_{i+1/2,j,k}\Delta t}{2\varepsilon_{i+1/2,j,k}}\big)
\end{aligned} \tag{3.26}$$

and

$$\begin{aligned}
\psi_{E_{x,y}}|^n_{i+1/2,j,k}&=b_{y_j}\psi_{E_{x,y}}|^{n-1}_{i+1/2,j,k}+c_{y_j}\big(\frac{H_z|^n_{i+1/2,j+1/2,k}-H_z|^n_{i+1/2,j-1/2,k}}{\Delta y}\big)\\
\psi_{E_{x,z}}|^n_{i+1/2,j,k}&=b_{z_k}\psi_{E_{x,z}}|^{n-1}_{i+1/2,j,k}+c_{z_k}\big(\frac{H_y|^n_{i+1/2,j,k+1/2}-H_y|^n_{i+1/2,j,k-1/2}}{\Delta z}\big)
\end{aligned} \tag{3.27}$$

where

$$b_v=e^{-\left(\frac{\sigma_v}{\varepsilon_0 k_v}+\frac{a_v}{\varepsilon_0}\right)\Delta t}\qquad c_v=\frac{\sigma_v}{\sigma_v k_v+k_v^2\alpha_v}\big(b_v-1\big)\qquad (v=x_i,y_j,z_k). \tag{3.28}$$

J_{p_x} is updated following (3.10), which is the same as in main area. The ψ-arrays in (3.27) are called convolutional related coefficients. b_v and c_v are tensor related coefficients, which can be computed through (3.28) with scaled tensor parameters k_y, σ_y, and α_y defined in (3.17). Comparing (3.15) and (3.25), it is noted that the update for modelling Debye dispersive medium in main area with ADE and in boundary regions with CPML are identical, only with the exception of the additional coefficient k_w at the denominator of H update in (3.25), and the convolutional terms ψ-arrays in (3.25). This signifies that the iteration within the whole domain, including both main area and boundary regions, can be updated synchronously, thereby saving memory storage and improving efficiency.

For completeness, the update equations of E_y, E_z, H_x, H_y, and H_z using CPML to truncate the main area with Debye medium are deduced as follows. Corresponding updates in main area through ADE technique can be obtained in a straightforward way since there is only minor difference as explained above.

$$
\begin{aligned}
&E_y|^{n+1/2}_{i,j+1/2,k} \\
&= C_a|_{i,j+1/2,k} E_y|^{n-1/2}_{i,j+1/2,k} + C_b|_{i,j+1/2,k} \Bigg[\frac{H_x|^n_{i,j+1/2,k+1/2} - H_x|^n_{i,j+1/2,k-1/2}}{k_{z_k}\Delta z} \\
&- \frac{H_z|^n_{i+1/2,j+1/2,k} - H_z|^n_{i-1/2,j+1/2,k}}{k_{x_i}\Delta x} + \psi_{E_{y,z}}|^n_{i,j+1/2,k} - \psi_{E_{y,x}}|^n_{i,j+1/2,k} \\
&- \frac{1}{2}\big(1+k_p\big) J_{p_y}|^{n-1/2}_{i,j+1/2,k} \Bigg]
\end{aligned}
\tag{3.29}
$$

where J_{p_y} can be calculated through (3.10), and

$$
\begin{aligned}
\psi_{E_{y,z}}|^n_{i,j+1/2,k} &= b_{z_k} \psi_{E_{y,z}}|^{n-1}_{i,j+1/2,k} + c_{z_k} \Big(\frac{H_x|^n_{i,j+1/2,k+1/2} - H_x|^n_{i,j+1/2,k-1/2}}{\Delta z} \Big) \\
\psi_{E_{y,x}}|^n_{i,j+1/2,k} &= b_{x_i} \psi_{E_{y,x}}|^{n-1}_{i,j+1/2,k} + c_{x_i} \Big(\frac{H_z|^n_{i+1/2,j+1/2,k} - H_z|^n_{i-1/2,j+1/2,k}}{\Delta x} \Big).
\end{aligned}
\tag{3.30}
$$

and

$$
\begin{aligned}
&E_z|^{n+1/2}_{i,j,k+1/2} \\
&= C_a|_{i,j,k+1/2} E_z|^{n-1/2}_{i,j,k+1/2} + C_b|_{i,j,k+1/2} \Bigg[\frac{H_y|^n_{i+1/2,j,k+1/2} - H_y|^n_{i-1/2,j,k+1/2}}{k_{x_i}\Delta x} \\
&- \frac{H_x|^n_{i,j+1/2,k+1/2} - H_x|^n_{i,j-1/2,k+1/2}}{k_{y_j}\Delta y} + \psi_{E_{z,x}}|^n_{i,j,k+1/2} - \psi_{E_{z,y}}|^n_{i,j,k+1/2} \\
&- \frac{1}{2}\left(1+k_p\right) J_{p_z}|^{n-1/2}_{i,j,k+1/2} \Bigg]
\end{aligned}
\tag{3.31}
$$

where J_{p_z} can be calculated through (3.10), and

$$
\begin{aligned}
\psi_{E_{z,x}}|^n_{i,j,k+1/2} &= b_{x_i} \psi_{E_{z,x}}|^{n-1}_{i,j,k+1/2} + c_{x_i} \left(\frac{H_y|^n_{i+1/2,j,k+1/2} - H_y|^n_{i-1/2,j,k+1/2}}{\Delta x} \right) \\
\psi_{E_{z,y}}|^n_{i,j,k+1/2} &= b_{y_j} \psi_{E_{z,y}}|^{n-1}_{i,j,k+1/2} + c_{y_j} \left(\frac{H_x|^n_{i,j+1/2,k+1/2} - H_x|^n_{i,j-1/2,k+1/2}}{\Delta y} \right).
\end{aligned}
\tag{3.32}
$$

Corresponding updates for H-fields could be obtained through the same procedure as for E-fields, except no polarisation current is involved, and they are obtained as

$$
\begin{aligned}
&H_x|^{n+1}_{i,j+1/2,k+1/2} \\
&= H_x|^n_{i,j+1/2,k+1/2} + \frac{\Delta t}{\mu_0} \Bigg[\frac{E_y|^{n+1/2}_{i,j+1/2,k+1} - E_y|^{n+1/2}_{i,j+1/2,k}}{k_{z_k}\Delta z} \\
&- \frac{E_z|^{n+1/2}_{i,j+1,k+1/2} - E_z|^{n+1/2}_{i,j,k+1/2}}{k_{y_j}\Delta y} + \psi_{H_{x,z}}|^{n+1/2}_{i,j+1/2,k+1/2} - \psi_{H_{x,y}}|^{n+1/2}_{i,j+1/2,k+1/2} \Bigg]
\end{aligned}
\tag{3.33}
$$

where μ_0 is free space permeability, and

$$
\begin{aligned}
\psi_{H_{x,z}}|^{n+1/2}_{i,j+1/2,k+1/2} &= b_{z_{k+1/2}} \psi_{H_{x,z}}|^{n-1/2}_{i,j+1/2,k+1/2} + c_{z_{k+1/2}} \left(\frac{E_y|^{n+1/2}_{i,j+1/2,k+1} - E_y|^{n+1/2}_{i,j+1/2,k}}{\Delta z} \right) \\
\psi_{H_{x,y}}|^{n+1/2}_{i,j+1/2,k+1/2} &= b_{y_{j+1/2}} \psi_{H_{x,y}}|^{n-1/2}_{i,j+1/2,k+1/2} + c_{y_{j+1/2}} \left(\frac{E_z|^{n+1/2}_{i,j+1,k+1/2} - E_z|^{n+1/2}_{i,j,k+1/2}}{\Delta y} \right)
\end{aligned}
\tag{3.34}
$$

where b_{y_j} and c_{y_j} can be calculated through (3.28). H_y and H_z can be derived by permuting $(i,\ j,\ k)$ and $(x,\ y,\ z)$ as follows

$$\begin{aligned}
&H_y|^{n+1}_{i+1/2,j,k+1/2} \\
=&H_y|^{n}_{i+1/2,j,k+1/2} + \frac{\Delta t}{\mu_0}\left[\frac{E_z|^{n+1/2}_{i+1,j,k+1/2} - E_z|^{n+1/2}_{i,j,k+1/2}}{k_{x_i}\Delta x}\right. \\
&\left. - \frac{E_x|^{n+1/2}_{i+1/2,j,k+1} - E_x|^{n+1/2}_{i+1/2,j,k}}{k_{z_k}\Delta z} + \psi_{H_{y,x}}|^{n+1/2}_{i+1/2,j,k+1/2} - \psi_{H_{y,z}}|^{n+1/2}_{i+1/2,j,k+1/2}\right]
\end{aligned} \tag{3.35}$$

where

$$\begin{aligned}
\psi_{H_{y,x}}|^{n+1/2}_{i+1/2,j,k+1/2} &= b_{x_{i+1/2}}\psi_{H_{y,x}}|^{n-1/2}_{i+1/2,j,k+1/2} + c_{x_{i+1/2}}\left(\frac{E_z|^{n+1/2}_{i+1,j,k+1/2} - E_z|^{n+1/2}_{i,j,k+1/2}}{\Delta x}\right) \\
\psi_{H_{y,z}}|^{n+1/2}_{i+1/2,j,k+1/2} &= b_{z_{k+1/2}}\psi_{H_{y,z}}|^{n-1/2}_{i+1/2,j,k+1/2} + c_{z_{k+1/2}}\left(\frac{E_x|^{n+1/2}_{i+1/2,j,k+1} - E_x|^{n+1/2}_{i+1/2,j,k}}{\Delta z}\right).
\end{aligned} \tag{3.36}$$

and

$$\begin{aligned}
&H_z|^{n+1}_{i+1/2,j+1/2,k} \\
=&H_z|^{n}_{i+1/2,j+1/2,k} + \frac{\Delta t}{\mu_0}\left[\frac{E_x|^{n+1/2}_{i+1/2,j+1,k} - E_x|^{n+1/2}_{i+1/2,j,k}}{k_{y_j}\Delta y}\right. \\
&\left. - \frac{E_y|^{n+1/2}_{i+1,j+1/2,k} - E_y|^{n+1/2}_{i,j+1/2,k}}{k_{x_i}\Delta x} + \psi_{H_{z,y}}|^{n+1/2}_{i+1/2,j+1/2,k} - \psi_{H_{z,x}}|^{n+1/2}_{i+1/2,j+1/2,k}\right]
\end{aligned} \tag{3.37}$$

where

$$\begin{aligned}
\psi_{H_{z,y}}|^{n+1/2}_{i+1/2,j+1/2,k} &= b_{y_{j+1/2}}\psi_{H_{z,y}}|^{n-1/2}_{i+1/2,j+1/2,k} + c_{y_{j+1/2}}\left(\frac{E_x|^{n+1/2}_{i+1/2,j+1,k} - E_x|^{n+1/2}_{i+1/2,j,k}}{\Delta y}\right) \\
\psi_{H_{z,x}}|^{n+1/2}_{i+1/2,j+1/2,k} &= b_{x_{i+1/2}}\psi_{H_{z,x}}|^{n-1/2}_{i+1/2,j+1/2,k} + c_{x_{i+1/2}}\left(\frac{E_y|^{n+1/2}_{i+1,j+1/2,k} - E_y|^{n+1/2}_{i,j+1/2,k}}{\Delta x}\right).
\end{aligned} \tag{3.38}$$

3.5 Design and Implementation

This section introduces the design and implementation of VECE. For efficient execution and flexible scalability, the engine is divided into four modules: environment setting, memory initialisation, kernel iteration, and field output. The schematic flowchart of VECE is presented in Fig. 3.1.

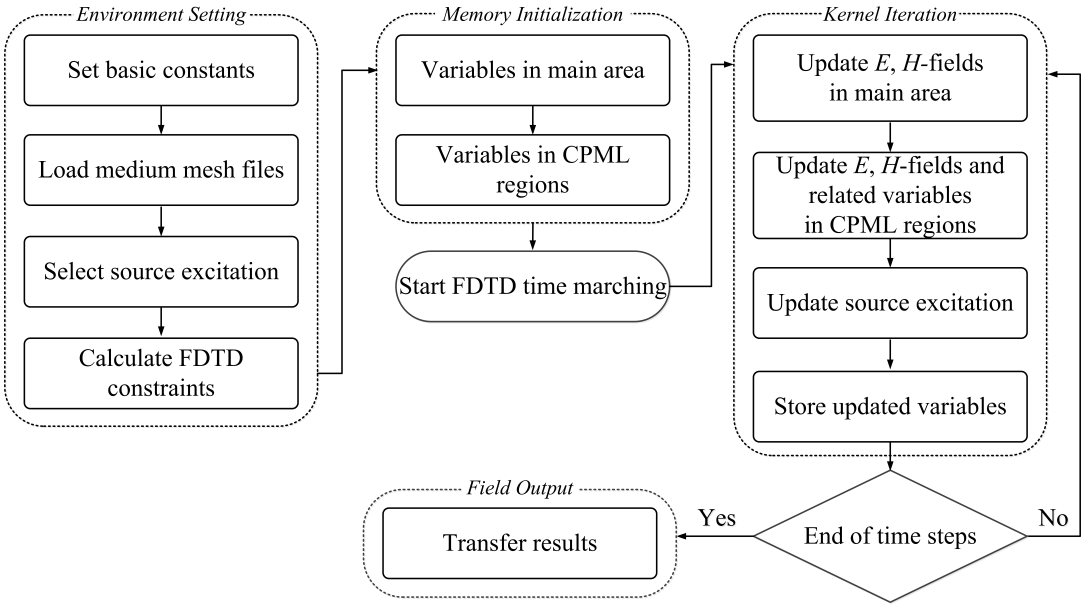

Fig. 3.1 Schematic flowchart of VECE.

3.5.1 Environment Setting

The environment parameters which should be preset include basic constants, user-defined medium mesh files, input source excitation, and FDTD simulation constraints.

The basic constants are free space related parameters, including the speed of light c_0, permittivity ε_0, permeability μ_0, and conductivity σ_0. For scalability, VECE accepts user-defined medium mesh files. VECE reads these files into a data structure, then it deduces relevant intermediate data from the geometry to prepare the construction of elemental matrices. For consistency and compatibility, imported files are transformed into a "*.txt*" format, and modifications of data structure are made where necessary.

VECE supports various input source excitations such as sinusoidal, modulated Gaussian pulse, and differentiated Gaussian pulse. Specifically, initial amplitude, initial time delay,

and frequency can be adjusted to suit specific environments. Furthermore, the position and number of source excitations are adjustable for simulating multi-antenna scenarios.

FDTD constraints include the size of entire simulation space (*imax*, *jmax*, *kmax*), the thickness of absorbing boundary (*n_xcpml*, *n_ycpml*, *n_zcpml*), cell size (*dx*, *dy*, *dz*), time step size (*dt*), and the maximum time steps (*tsteps*). Based on the size of imported models, VECE calculates an appropriate dimension for the entire simulation area, which is capable of containing user-defined models, and ensuring a minimum occupation of computation resources. Moreover, according to the selected type of source excitation, cell size and time step are computed based on the Courant-Friedrichs-Lewy (CFL) stability condition to make numerical dispersion error negligible [53]. These variables can be set in a step-by-step manner as follows:

1. Set basic constants (c_0, ε_0, μ_0, σ_0).
2. Load medium mesh files.
3. Set source excitation.
4. Calculate FDTD constraints (e.g., *imax*, *dx*, etc.).

3.5.2 Memory Initialisation

The memory initialisation of variables includes two parts: main computational area and CPML boundary regions. To implement ADE-FDTD in main area, VECE allocates and initialises the global memory and creates six 3-D arrays for E_x, E_y, E_z, H_x, H_y, and H_z field components, three 3-D arrays for polarisation current J_{p_x}, J_{p_y}, and J_{p_z}, four 3-D arrays for auxiliary medium-dependent coefficients, including k_p, β_p used in (3.11), and C_a, C_b used in (3.16). In order to update field components within each CPML region, corresponding convolutional coefficients expressed as ψ-arrays [last two items in (3.25)] are needed, and there are two parts involved: convolutional related coefficients and tensor related coefficients [in (3.27)].

3.5.2.1 Convolutional related coefficients

The convolution coefficients noted as ψ-arrays contained in (3.25) are discrete unknowns stored only in CPML regions. For each field component, four auxiliary coefficients are needed. Firstly, ψ-arrays are needed for corresponding normal interface boundaries, which include both sides of the CPML region. For example, for field component E_x, it requires $\psi_{E_{x,y}}$ and $\psi_{E_{x,z}}$ which represents the unknowns of ψ_{E_x} with y-normal and z-normal interface boundaries, respectively, and they are 3-D arrays corresponding to each 3-D boundary space. Secondly, for each $\psi_{E_{x,y}}$ and $\psi_{E_{x,z}}$, their subcomponents include $\psi_{E_{x,y1}}$ and $\psi_{E_{x,y2}}$, $\psi_{E_{x,z1}}$ and $\psi_{E_{x,z2}}$, which represent the bottom and top 3-D CPML regions, respectively. Therefore, for E_x, four coefficients are needed: $\psi_{E_{x,y1}}$, $\psi_{E_{x,y2}}$, $\psi_{E_{x,z1}}$, and $\psi_{E_{x,z2}}$. This applies for the other five field components (E_y, E_z, H_x, H_y, H_z) as well, thus twenty-four 3-D arrays are needed for all CPML regions.

3.5.2.2 Tensor related coefficients

To calculate each ψ-array, two tensor related coefficients b and c are needed as shown in (3.27). The discrete coefficients b and c are only non-zero with its corresponding normal interface boundaries, thus they are 2-D arrays. As shown in (3.27), for $\psi_{E_{x,y}}$, only b_y and c_y are needed (i.e. b_z or c_z is not needed). Coefficients b and c are computed using (3.28), with the scaled tensor coefficients k_w, σ_w, and α_w, where $w = x_i, y_j, z_k$. Therefore, for each field component such as E_x, ten tensor related parameters are needed, five among which are $b_{E_{x1}}$, $c_{E_{x1}}$, $k_{E_{x1}}$, $\sigma_{E_{x1}}$ and $\alpha_{E_{x1}}$, whereas the other five are $b_{E_{x2}}$, $c_{E_{x2}}$, $k_{E_{x2}}$, $\sigma_{E_{x2}}$ and $\alpha_{E_{x2}}$, which are for the other side of CPML region. Thus, there are sixty tensor related coefficients for all six field components, which all require memory allocation and initialisation before computation. This can be carried out in the following steps.

1. Allocate six 3-D arrays for field components (E_x, E_y, E_z, H_x, H_y, H_z).
2. Allocate three 3-D arrays for polarisation current (J_{p_x}, J_{p_y}, J_{p_z}).
3. Allocate four 3-D arrays for auxiliary medium-dependent coefficients used in main area (k_p, β_p, C_a, C_b).

4. Allocate twenty-four 3-D arrays for convolutional coefficients used in CPML regions (e.g., $\psi_{E_{x,y1}}$, etc.).
5. Allocate sixty 2-D arrays for tensor related coefficients used in CPML regions (e.g., $b_{E_{x1}}$, $c_{E_{x1}}$, $k_{E_{x1}}$, etc.)

3.5.3 Kernel Iteration

To improve computational efficiency, iterative coefficients such as C_a and C_b that are related to host medium are all precomputed prior to kernel iteration in VECE. This can extensively reduce the overall running time, especially considering the millions of unknowns associated with precise 3-D models. Each field component is updated in both main area and CPML boundary regions. In boundary regions, field components are updated for each side (top, bottom, left, right, front, back), along x, y, and z directions, respectively. To implement kernel iteration within each time step n, H and E are sequentially updated as follows.

Calculate H-fields in a step-by-step way:

1. H-fields in main area.
2. H-fields in boundary regions.

Calculate E-fields in a step-by-step way (corresponding to Pseudocode 3.1):

1. Update overlapped E-fields in both main area and boundary regions.
2. Update overlapped J_p in both main area and boundary regions.
3. Update separate E-fields in boundary regions only.
4. Add source excitation.
5. Store calculated variables at current time step.

Considering kernel iteration as the core computing process and for further clarification, a pseudocode segment illustrating the update of E_z within one time step n is presented in Pseudocode 3.1. The electric field E instead of magnetic field H is selected since it is more representative. Besides normal Yee formulations for E and H, additional polarisation current update is exclusively included in the iteration of E. E_z is selected since it is the variable that includes the calculation of source excitation. The update of its counterparts (E_x, E_y) could be implemented in a same way except the inclusion of source excitation.

In Pseudocode 3.1, the five steps are numbered from 1 to 5. (i, j, k) are indices for each 3-D array, which are limited by $(imax, jmax, kmax)$ in the entire simulation area that comprises main area and boundary regions, and by $(n\_xcpml, n\_ycpml, n\_zcpml)$ within boundary regions. C_a and C_b in Step 1 are medium-related auxiliary coefficients. For Debye medium, these two coefficients are computed with parameters ε_∞, ε_s, and τ through (3.16). den_E_x is the denominator of a variant of (3.25) for updating E_z, and it equals $1/(k_{x_i}\Delta x)$. $E_z(i, j, k)$ and $J_{p_z}(i, j, k)$ are the E_z and J_{p_z} at position (i, j, k) at current time step, whereas their counterparts at the previous time step at the same position are indicated by $E_{z\_prev}(i, j, k)$ and $J_{p_z\_prev}(i, j, k)$, respectively. Step 2 is the update of J_{p_z} in both main area and boundary regions. In Step 3, the update for E_z and J_{p_z} in boundary regions only are presented. It is worth mentioning that due to the partial update of E_z in boundary regions, J_{p_z} would be affected by this update. Thus J_{p_z} need to be updated through (3.10), corresponding to the third and sixth lines in Step 3. Observing Step 4, a dipole was used as a hard source excitation at position $(isrc, jsrc, ksrc)$, and $source(n)$ is the excitation waveform in discrete form. The pseudocode corresponds well with previous analysis, and this step-wise structure ensures VECE's readability while maintaining FDTD's simplicity.

3.5.4 Field Output

The last module of VECE transfers stored variables out of memory onto disk, allowing for the displaying, analysis, and calculations, and this can be done as follows.

1. Select the field components for export.
2. Name output files and specify storage locations.

3.6 Validation Study

This section validates the effectiveness and accuracy of VECE. Firstly its accuracy is demonstrated by analysing the results in both time and frequency domains across a range of appropriate assessment criteria. Furthermore, the results are compared with their

Pseudocode 3.1 Calculate E-fields in z coordinate direction E_z within one time step n

1: Update overlapped E_z in both main area and boundary regions [Equ. (3.31)]
$E_z(i,j,k) = C_a(i,j,k)E_z(i,j,k) + C_b(i,j,k)\big\{[H_y(i,j,k) - H_y(i-1,j,k)]den\_E_x(i)$
$+[H_x(i,j-1,k) - H_x(i,j,k)]den\_E_y(j) - 0.5[1 + k_p(i,j,k)]J_{p_z\_prev}(i,j,k)\big\}$

2: Update overlapped J_{p_z} in both main area and boundary regions [Equ. (3.10)]
$J_{p_z}(i,j,k) = k_p(i,j,k)J_{p_z\_prev}(i,j,k) + \beta_p(i,j,k)[E_z(i,j,k) - E_{z\_prev}(i,j,k)]/dt$

3: Update separate E_z in boundary regions only [two convolutional items in Equ. (3.31)]
/* Partial update along x axis */
$\psi_{E_{z,x}}(i,j,k) = b_{E_x}(i)\psi_{E_{z,x}}(i,j,k) + c_{E_x}(i)[H_y(i,j,k) - H_y(i-1,j,k)]/dx$ [Equ. (3.32)]
$E_z(i,j,k) = E_z(i,j,k) + C_b(i,j,k)\psi_{E_{z,x}}(i,j,k)$
$J_{p_z}(i,j,k) = k_p(i,j,k)J_{p_z\_prev}(i,j,k) + \beta_p(i,j,k)[E_z(i,j,k) - E_{z\_prev}(i,j,k)]/dt$

/* Partial update along y axis */
$\psi_{E_{z,y}}(i,j,k) = b_{E_y}(i)\psi_{E_{z,y}}(i,j,k) + c_{E_y}(i)[H_x(i,j-1,k) - H_x(i,j,k)]/dy$ [Equ. (3.32)]
$E_z(i,j,k) = E_z(i,j,k) + C_b(i,j,k)\psi_{E_{z,y}}(i,j,k)$
$J_{p_z}(i,j,k) = k_p(i,j,k)J_{p_z\_prev}(i,j,k) + \beta_p(i,j,k)[E_z(i,j,k) - E_{z\_prev}(i,j,k)]/dt$

4: Add source excitation
$E_z(isrc, jsrc, ksrc) = source(n)$

5: Store calculated variables at current time step
$E_{z\_prev}(:,:,:) = E_z(:,:,:)$
$J_{p_z\_prev}(:,:,:) = J_{p_z}(:,:,:)$

counterparts obtained from Remcom's XFDTD software package. The computational efficiency of VECE is analysed in the last subsection.

3.6.1 Measurements and Evaluation

To completely evaluate the accuracy of VECE, the output results are verified by three different metrics: convergence, relative reflection error, and dispersion.

3.6.1.1 Convergence

The propagation of an UWB pulse within 3-D FDTD lattice which hosts a Debye dispersive medium is simulated. The host medium is selected as fatty-median tissue [102], with a single-pole Debye parameters of ε_∞ = 3.11, σ_s = 0.05, τ_1 = 13.00 (ps), and ε_{s1} = 4.71. The

modulated Gaussian pulse (MGP) (see Fig. 3.2) is used as the excitation given by

$$G(t) = sin\left[\omega_c\left(t-b\right)\right] e^{-\left(\frac{t-b}{c}\right)^2} \tag{3.39}$$

where $\omega_c = 2\pi f_c$ is the centre angular frequency with centre frequency f_c = 6.85 GHz, the centre position of the Gaussian envelope b = 375 (ps), and c = 80.2 (ps) is the standard deviation which controls the width of Gaussian envelope. MGP is selected since it is considered to present better spectral control in practical use [191]. The input pulse width is 0.56 (ns), which has a full-width at half maximum (FWHM) bandwidth of 6.6 GHz. To discretize FDTD problem space, a rule of thumb to select the grid size is to keep it below one-tenth of the wavelength to make numerical dispersion error negligible [53]. Considering the broadband feature of input pulse, the permittivity of medium at f_c of 6.85 GHz is used to represent the entire frequency range, obtaining the wavelength is 21 mm. Thus, one-tenth of wavelength equals 2.1 mm. A smaller grid size of $\Delta x = \Delta y = \Delta z$ = 1 mm is employed for obtaining more accurate results. The time step Δt is determined by the CFL stability condition ([53], Ch. 4, pp. 154, Equ. 4.98), which equals 1.91 (ps) in this study.

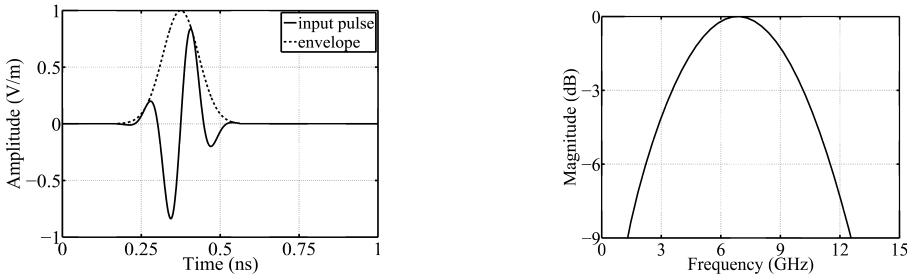

(a) MGP waveform (b) Spectrum of MGP

Fig. 3.2 Modulated Gaussian pulse (MGP) used as source excitation in FDTD simulations. (a) MGP waveform in time domain. (b) Spectrum of MGP.

The overall simulated FDTD space utilising a global coordinate system has a size of 49 mm × 124 mm × 24 mm [see Fig. 3.3(a)]. A 3-D space filled with fat-median medium [see Fig. 3.3(b)], which has a size of 29 mm × 104 mm × 4 mm, is simulated. The property parameters of fat-median is based on the study performed in [102]. Ten-layer CPML absorbing boundary conditions are placed around the volume of interest to attenuate

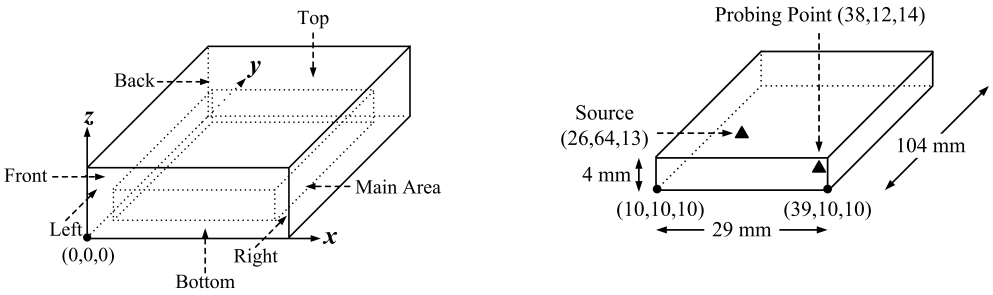

(a) Overall FDTD simulation space

(b) Main simulation area

Fig. 3.3 Three-dimensional FDTD simulation space. (a) Overall FDTD simulation space comprising main area and CPML boundary regions. The six surfaces of the main area are surrounded by corresponding 3-D boundary regions (top, bottom, front, back, left, and right). (b) Enlargement of main area, which is with fat-median medium and exposed to a z-polarised electric field. Ten-layer CPML absorbing walls are placed around the main area along each direction. The coordinate of the left-bottom point is (x, y, z) = (10, 10, 10), and coordinates of the source excitation and probing point are (x, y, z) = (26, 64, 13) and (38, 12, 14), respectively.

outgoing radiation. A z-polarised voltage source excitation is placed at (x,y,z) = (26, 64, 13), whereas a probing point is placed at (x,y,z) = (38, 12, 14). The probing point is very close to the lower right corner of the main area at (x,y,z) = (39, 10, 10) and the utility of this arrangement is twofold. First, the propagated signal received at this position can be used for observing its convergence and calculating the reflection error, thereby validating the correctness of CPML boundary. Second, the output results can be used for validating the propagation delay via the comparison with its theoretical counterparts. The time-stepping runs over 1500 iterations, well past the steady-state response. The z-component of electric field are recorded and plotted as the solid curve in Fig. 3.4, in which one can observe that no late-time reflection from boundary occurred and excellent convergence was achieved.

Besides CPML boundary's absorbing performance, the propagation delay of results produced by VECE is validated by comparing with theoretical results. The distance D is calculated based on the coordinates of source (26,64,13) and probing point (38,12,14), which is 53.4 mm. The propagation speed is calculated under the assumption that the medium has a constant relative permittivity at the centre frequency f_c of input pulse. The relative permittivity at f_c is chosen since it represents the majority of medium's permittivity across the whole frequency range. Related single-pole Debye parameters of fat-median medium can be found in [102], and the constant relative permittivity ε_r at f_c of 6.85 GHz

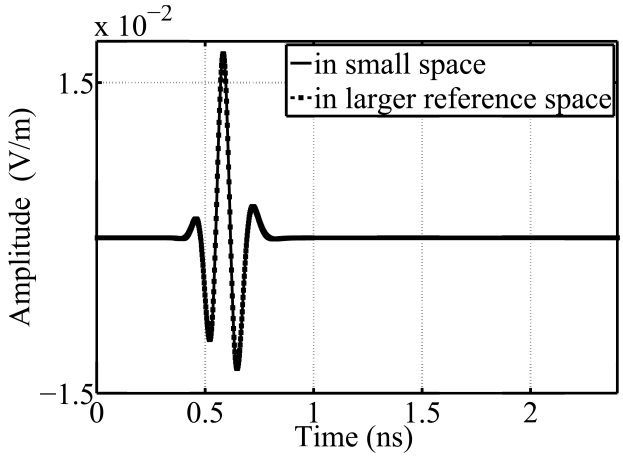

Fig. 3.4 E_z field at probing point offered by VECE, based on the model shown in Fig. 3.3. The amplitude of z-component of electric field (E_z) received at probing point. Solid and dash-dotted curves are the results at probing points in a small and larger reference simulation space, respectively.

is 4.34, which can be calculated through equation (3.1). Therefore, the propagation time pt equals 0.37 (ns) can be calculated as [192]

$$pt = D/v = D/(c_0/\sqrt{\varepsilon_r}) \tag{3.40}$$

where v is the propagation velocity in fat-median medium, and c_0 is the speed of light. By comparing the occurrence time of received pulse in Fig. 3.4 with the input pulse in Fig. 3.2(a), the time delay of the results offered by VECE is 0.38 (ns). Only a negligible relative error of 2.7% is observed, which could be caused by dispersion during propagation, and this indicates a very good agreement with the theoretical results.

3.6.1.2 Relative Reflection Error

To verify relative reflection error, the solution at a reference point $E_{ref}|^n_{i,j,k}$ with location (i, j, k) and at time step n is obtained using a larger simulation space equals 200 mm $\times$ 200 mm $\times$ 200 mm. In the larger reference space, an identical voltage and probing point which has the same position relative to source as in the small grid (see Fig. 3.3) are employed. The reference space is sufficiently large so that there are no reflections from its outer boundaries during the time-stepping span. This allows a relative error to be defined as

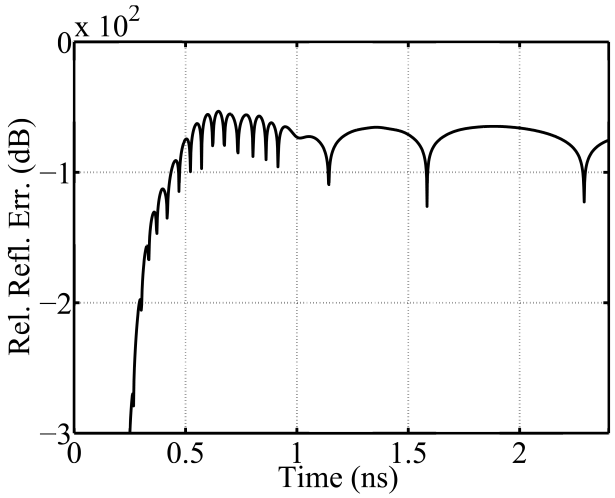

Fig. 3.5 Relative reflection error calculated according to (3.41) and measured in decibel, based on the model shown in Fig. 3.3.

([53], Ch. 7, pp. 314)

$$Rel.error|^n_{i,j,k} = \mid E|^n_{i,j,k} - E_{ref}|^n_{i,j,k} \mid / \mid E_{refmax}|^n_{i,j,k} \mid \tag{3.41}$$

where $E_{refmax}|^n_{i,j,k}$ is the maximum amplitude of the reference field as observed during the time-stepping span of interest. The output at reference point is plotted as dash-dotted line in Fig. 3.4, an almost perfect overlap with the result at the probing point of the small simulation space (solid line) is observed. Corresponding relative reflection error is calculated through (3.41) and plotted in Fig. 3.5. A quantitative analysis showed that the maximum relative reflection error is 0.002 (-53 dB). This is indeed an exceptionally low relative error level in comparison to the result of UPML with 0.02 (-30 dB) (see [53], Ch. 7, pp. 319, Fig. 7.7), of which an improvement of accuracy up to one full digit is achieved. This proves VECE's accuracy, which is highly desirable in numerical simulations.

3.6.1.3 Dispersion

To validate the efficacy of VECE to characterise medium's dispersion, two different types of dispersive media (fat-median and fat-high), and input MGP with two centre frequencies (6.85 and 3.0 GHz) are employed. For completeness, three different scenarios (S1 to S3) are considered. In S1, the propagation of pulse with f_c of 6.85 GHz in non-dispersive

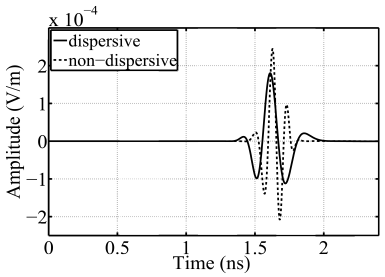

(a) In non-dispersive medium

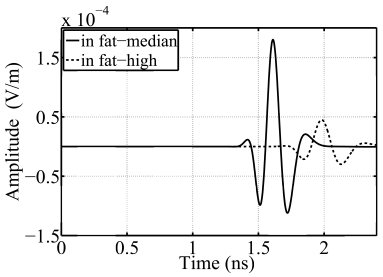

(b) In dispersive medium

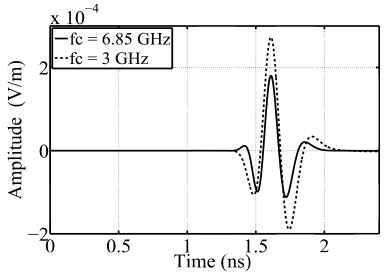

(c) Input pulse with different f_c

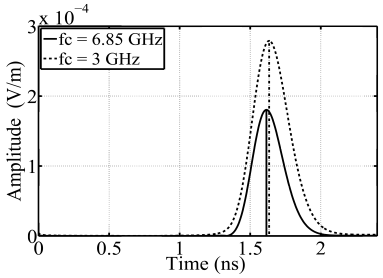

(d) Envelope of pulses in (c)

Fig. 3.6 Results offered by VECE in different scenarios, signals are represented by E_z at probing points. (a) Propagated pulses in non-disperisve medium (dotted) and in dispersive fat-median medium (solid), both using the input pulse shown in Fig. 3.2 with f_c = 6.85 GHz. (b) Solid and the dotted curves represent the propagated pulses in fat-median and fat-high medium, respectively, both using the same input pulse as in (a). (c) Propagated pulses in the same fat-median dispersive medium, using input pulses with f_c of 6.85 GHz and 3.0 GHz, respectively. (d) Envelope of signals shown in (c).

and disperisve media is compared. The dispersive medium is selected as fat-median tissue [102], whereas the non-dispersive medium has relative permittivity ε_r = 4.33 and conductivity σ_0 = 0.50 S/m. As shown in Fig. 3.6(a), compared with the non-dispersive case (dotted), obvious broadening effect is noted in the dispersive case (solid). In non-dispersive medium, all frequency components propagate at a same speed. In dispersive medium, however, each frequency component has its own phase velocity, the propagated pulse which contains all overlapping frequency components is therefore has a broadened pulse duration. Specifically, although the pulse has a f_c of 6.85 GHz, the components of higher or lower frequency than 6.85 GHz can propagate faster or slower, depending on the medium property. The dispersive effect is critical for breast imaging and there are two reasons. First, the dispersion can affect the amplitude of signals and thus reduce the contrast between tumour and non-tumour responses. Second, dispersion can result in

signal shape distortion. Both effects can make the detection of tumour more difficult, and the importance of incorporating dispersion was also emphasised in [193].

In S2, the same pulse with f_c of 6.85 GHz propagating in different media (fat-median and fat-high) is considered. Observing Fig. 3.6(b), stronger attenuation and larger time delay are observed when the pulse propagated in the denser fat-high tissue (dotted line). In comparison, the received pulse in fat-median tissue indicated by the solid line appeared earlier and had a much higher amplitude.

In S3, the same medium type with sources of different f_c are considered. As shown in Fig. 3.6(c), for the same dispersive fat-median medium, the behavior of signals with different f_c varies. After same iterations, the high-frequency pulse with f_c of 6.85 GHz attenuated more than the pulse with f_c of 3.0 GHz. This is shown by the obvious amplitude difference, which proves that the high-frequency components are more readily absorbed, leading to a larger attenuation. On the other hand, the different propagation velocity of these two pulses indicated by their envelopes could be observed in Fig. 3.6(d). It is noted that the pulse with f_c of 6.85 GHz (solid) appeared earlier than the pulse with f_c of 3 GHz (dotted). This is because the permittivity of fat-median tissue is a decreasing function of frequency (see [50], Fig. 3), thus the same medium exhibits a larger permittivity for the lower frequency components than that for the higher frequency components. According to (3.40), the pulse with a smaller f_c of 3.0 GHz has a larger propagation time delay and appeared late [see Fig. 3.6(d)]. The different propagation velocities of various frequency components expand the composite pulse envelope, and generate the broadening effect. Correspondingly, the propagated pulses in frequency domain would have a smaller centre frequency than that of the input pulse. Specifically, comparing the input pulse [see Fig. 3.2(a)] with the propagated pulse [see Fig. 3.6(c), f_c = 6.85 GHz], the FWHM of signal envelope increased from 0.14 (ns) to 0.25 (ns), whereas the f_c decreased from 6.85 to 4.0 GHz.

These scenarios illustrate the dispersive characteristics of single-layer biological tissues, and the combination of two and more tissues are investigated in the following sections.

3.6.2 Comparative Verification

In addition to analytical validation, the accuracy of VECE is further verified through comparing with the results produced by XFDTD 7.0 [168]. XFDTD is selected because it employs the same FDTD algorithm and is a widely acknowledged 3-D electromagnetic simulation software [172, 183].

Based on model shown in Fig. 3.7(a) and settings of Fig. 3.3, the results offered by VECE and XFDTD is compared. The only difference for these two engines is the different selection of absorbing boundary. In VECE, a ten-layer CPML is employed, whereas XFDTD utilised a ten-layer PML. PML is chosen in XFDTD since it does not offer CPML, and PML is the one most similar to CPML. Observing the normalised results in Fig. 3.7(b), it is noted that close agreement is achieved. The correlation coefficient between these two propagated pulses is 0.96, which demonstrates the high accuracy of VECE. Noted that the results of VECE outperform the one obtained from XFDTD by an improved boundary absorbing capability. Obvious fluctuation due to the reflection from boundary is observed in the XFDTD results within 1.0 (ns) to 1.5 (ns), whereas almost perfect absorbing is offered by VECE. This proves the superiority of CPML over PML in terms of effective absorption of propagating waves, which is similar to the observation made in [53]. The slight amplitude difference between these two propagated pulses is due to the different antenna modelling methods in VECE and XFDTD. In VECE, antenna is modelled as point source, whereas antennas with physical dimensions are employed in XFDTD.

To demonstrate VECE's accuracy in frequency domain, the reflection coefficient at the interface of two media are computed, as it is generally done [172] [183] [194]. The two media employed are fat-median and malignant breast tumour tissue as shown in Fig. 3.7(b). To model the frequency dependence of tumour tissue, Debye parameters of ε_∞ = 7.00, σ_s = 0.15, τ_1 = 7 (ps), and ε_{s1} = 54.00 are used [102]. During computation, the same spatial discretization of $\Delta x = \Delta y = \Delta z$ = 1 mm and Δt = 1.91 (ps) for both tools was chosen and the simulation was performed for 1500 time steps, achieving the steady-state condition. Results are recorded at the cell location (x, y, z) = (250, 25, 25), which is at the fat-tumour boundary. The incident field is subtracted from the total field for obtaining the

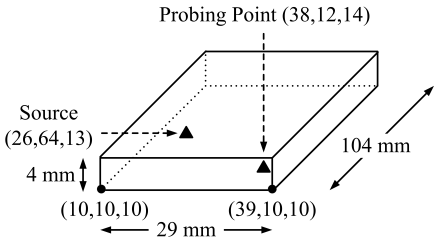

(a) Main simulation area

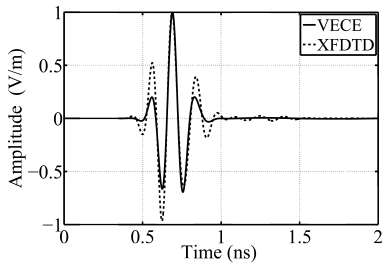

(b) Results by VECE and XFDTD

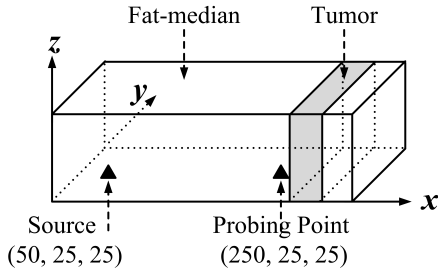

(c) Simulation space with two media

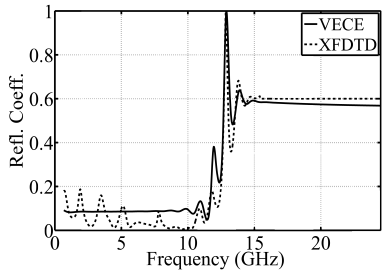

(d) Reflection coefficient

Fig. 3.7 Comparison of results produced by VECE and XFDTD. (a) Main simulation area. (b) Results by VECE and XFDTD based on model shown in (a) and settings of Fig. 3.3. (c) Simulation space with the combination of two dispersive media: fat-median and tumour. (d) Reflection coefficient frequency response calculated by VECE and XFDTD based on model shown in (c).

reflected field due to the material discontinuity. The reflection coefficient versus frequency is then calculated by normalising the Fourier transform of the reflected field divided by the Fourier transform of the incident pulse. Fig. 3.7(c) presents the results of VECE along with the comparison to the result obtained from XFDTD. It can be seen that a close agreement is achieved, which is indicated by the correlation coefficient of 0.99 between those two curves.

3.6.3 Computational Efficiency

Besides accuracy, the efficiency of VECE is achieved through three aspects, smaller number of arithmetic operations, less occupation of memory storage, and synchronous iteration in both main area and boundary regions.

Firstly, the reduced computational amount is achieved by ADE compared with its counterparts. Compared with PLRC, which is another widely used technique in FDTD for integrating the dipsersive property of materials, ADE requires relatively fewer floating-point

operations since there is no complex-number arithmetic involved [185] [188]. Secondly, the reduced storage of memory is achieved by both ADE and CPML techniques compared with their counterparts. Studies showed that an equal or smaller number of unknowns need to be stored in ADE than PLRC ([53], Ch. 9, pp. 361). As for CPML, since it is highly absorptive for both propagating and evanescent waves, CPML layers can be placed fairly close to the main simulation area. Study proved that this advantage of CPML led to a four-fold reduction in memory space occupation [189]. Therefore, the reduced number of unknowns need to be stored in both ADE and CPML over their counterparts contribute the memory saving and related reduction of processing time. Thirdly, the partial synchronous iteration in both main area and in boundary regions realised in VECE reduces the execution time. Comparing Equ. (3.15) and Equ. (3.25), which are the update for modelling Debye medium in main area by ADE and in boundary regions by CPML, the first two terms for these two equations are exactly the same, only with an additional coefficient k_w at the denominator of H update in (3.25). By pre-defining the denominator array for H update in main area and boundary regions in a proper way, the update for these two overlapped calculations can be accomplished in an uniform way throughout entire problem space, which is shown in Step 1 and 2 of Pseudocode 3.1. Considering the huge quantities of calculations involved, this is non-trivial and can save considerable computation resources.

3.7 Visualisation of Breast Model and Signal Propagation

In this section, the process of integrating and visualising 3-D realistic breast models through VECE is firstly presented. Then flexible setups for simulating clinical imaging scenarios are introduced. The propagation of UWB signal within breast tissues is also studied.

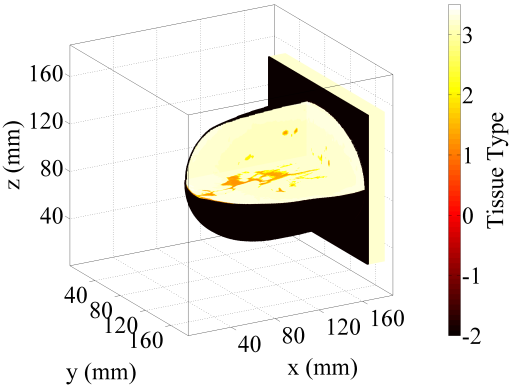

(a) Breast model by VECE

BREAST TISSUES TYPES AND PARAMETERS ASSUMED FOR THE SINGLE-POLE DEBYE MODEL

	ε_{∞}	ε_{s1}	τ_1 (ps)	σ_s (S/m)
Fat-High	3.9870	7.5318	13.0000	0.0803
Fat-Median	3.1161	4.7077	13.0000	0.0496
Fat-Low	2.8480	3.9521	13.0000	0.2514
Fibro-glandular High	14.2770	54.7922	13.0000	0.6381
Fibro-glandular Median	13.8053	49.351	13.0000	0.7384
Fibro-glandular Low	12.8485	37.4915	13.0000	0.2514
Skin	15.9300	39.7600	13.0000	0.8310
Malignant Tumor	20.2800	45.5000	13.0000	1.3000

(b) Breast tissue types

Fig. 3.8 Three-dimensional breast model and tissue compositions. (a) Breast model produced by VECE with raw data provided by UWCEM repository (breast ID = 071904). The categorised tissue types are represented by different values: fat-high(3.1), fat-median(3.2), fat-low(3.3), fibro-glandular (FG)-high(1.1), FG-median(1.2), FG-low(1.3), and skin(-2). (b) Breast tissue types and assumed parameters for a single-pole Debye model [102].

3.7.1 Breast Model Construction

For effective simulation and evaluation of imaging algorithms, high-fidelity numerical breast models are critical. In addition to dispersion, appropriate geometrical property, heterogeneity, and spatial distribution of different constituent tissues of breast are all expected to be incorporated. As shown in Fig. 3.8, to capture the physiological heterogeneity of breast, seven specific tissue categories are used, which are defined as: fat-high, fat-median, fat-low, transitional, fibro-glandular (FG)-high, FG-median, and FG-low. The Debye parameters for each tissue type inside the breast, along with those for skin and tumour, are presented in Fig. 3.8(b). Further details regarding the development of these breast tissues are available in [102].

The collection of breast phantoms offered by UWCEM database [169] is created in a representative sense. It captures the structural heterogeneity and dispersive dielectric properties of normal breast tissue, which ensures the phantom data is both anatomically and dielectrically accurate. Combining the raw ASCII files provided by this database, VECE can develop and visualise the 3-D breast models as shown in Fig. 3.8(a). After loading model files, VECE calculates the size of problem space according to the imported model. This size is determined by several factors. First it should be large enough to accommodate the entire model. Also a proper space between the model and boundary area

is needed for placing source excitations and probing points. The size, on the other hand, should be tailored to avoid redundant space. This is because even only a small increase of grid number along one dimension can cause huge extra computational cost, due to the millions of voxels of 3-D models. For example, the breast model shown in Fig. 3.8(a) is composed of 8,678,670 cubic voxels, which has a dimension of $x \times y \times z = 195$ (mm) $\times$ 238 (mm) $\times$ 187 (mm). If the x dimension increases from 195 to 205, the total voxel number would be 9,123,730, resulting in an extra 445,060 unknowns, which is a much more heavier computational burden. The visualisation can not only be used to observe and modify model, but also facilitates the positioning of excitation sources for simulations.

3.7.2 Breast Medium Types

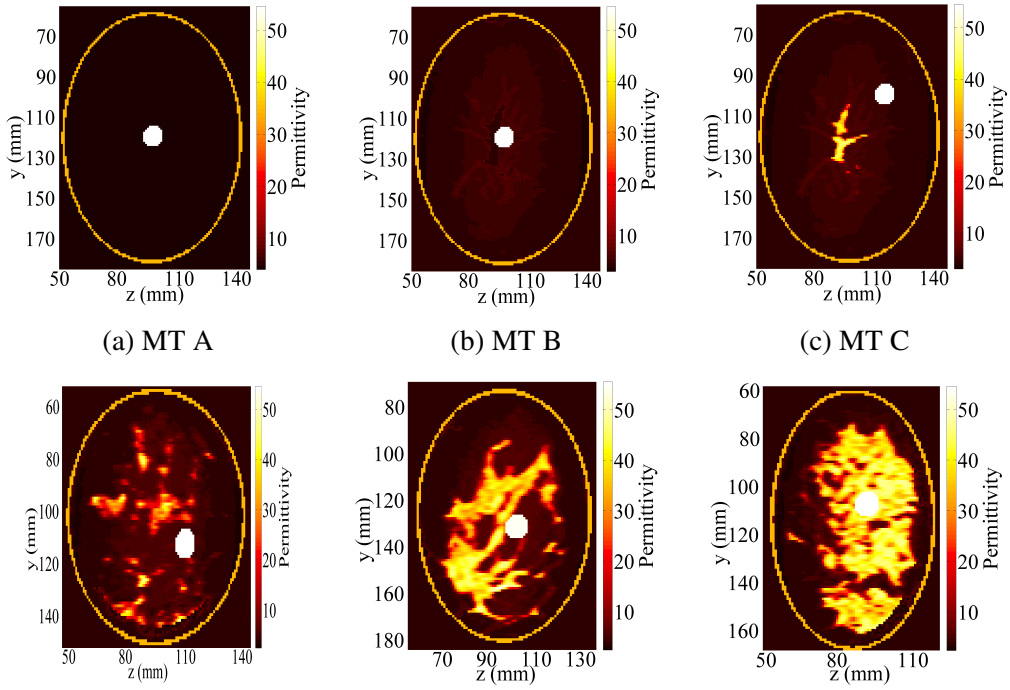

(a) MT A (b) MT B (c) MT C

(d) MT D (e) MT E (f) MT F

Fig. 3.9 Breast medium type (MT) represented by relative permittivity at 6.85 GHz. A tumour with 10 mm diameter is constructed as a sphere. The 2-D slices are taken at the x cross-sections of Fig. 3.8(a). (a) to (f) represent the six breast medium types, and details are described below.

To simulate various scenarios, VECE offers a flexible configuration of the imaging system. Derived from UWCEM repository, six breast medium types (MT) with different structures and radiographic density classifications are considered, which are shown in

Fig. 3.9. Tumours might have irregular shapes, but they are constructed as spheres with varied diameters in this study, which simulates different strengths of backscattered tumour response. Further reading about tumour modelling can be found in [103]. The density of breast is based on the definition of American College of Radiology (ACR) [195]. Details of these phantoms, including ACR type, Breast ID in UWCEM repository, and characteristics are listed as follows.

1. MT A: ACR-I-ID-071904, homogenous breast composed of fatty-median tissue only, all other tissues are replaced by the fatty-median tissue.
2. MT B: ACR-I-ID-071904, heterogeneous breast composed of three types of fatty tissues, all glandular tissues are replaced by the fatty-median tissue.
3. MT C: ACR-I-ID-071904, full heterogeneous breast composed of three types of fatty, and three types of glandular tissues with a percentage less than 25%.
4. MT D: ACR-II-ID-010204, full heterogeneous breast contain glandular tissues with a percentage ranging between 25% and 50%.
5. MT E: ACR-III-ID-070604PA2, full heterogeneous breast contain glandular tissues with a percentage ranging between 50% and 75%.
6. MT F: ACR-IV-ID-012304, full heterogeneous breast contain glandular tissues with a percentage over 75%.

3.7.3 Simulation Setup Variations

Studies showed that suitably-designed pulses may improve the imaging performance [196]. Therefore, varied pulses as shown in Fig. 3.10 are considered in VECE. Different input pulses could be set include sinusoidal, differentiated Gaussian, and modulated Gaussian. In this study, the modulated Gaussian pulse (MGP) is selected due to its better spectral control in practical use [191]. For MGP, besides centre frequency, pulse shape, pulse width, and pulse position are all able to be altered to suit specific simulation purpose.

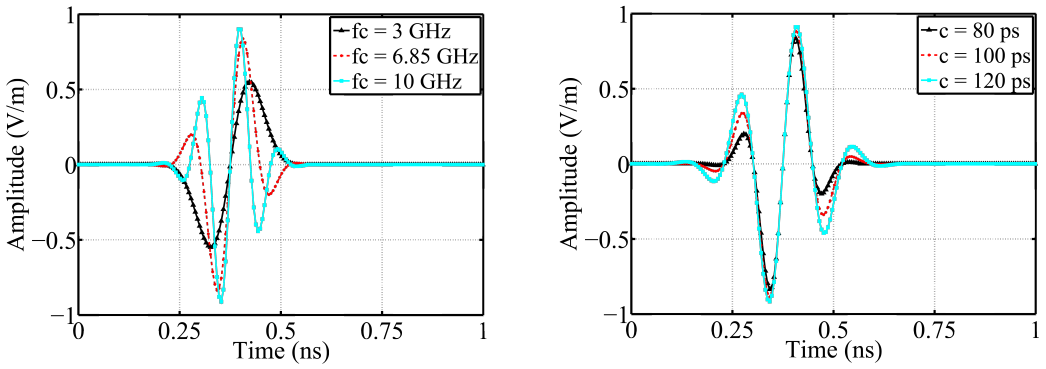

(a) Pulses with varied f_c (b) Pulses with varied c

Fig. 3.10 Variations of input pulses for UWB breast tumour detection. (a) Pulses with varied centre frequency f_c. (b) Pulses with shapes controlled by standard deviation c used in Equ. (3.39).

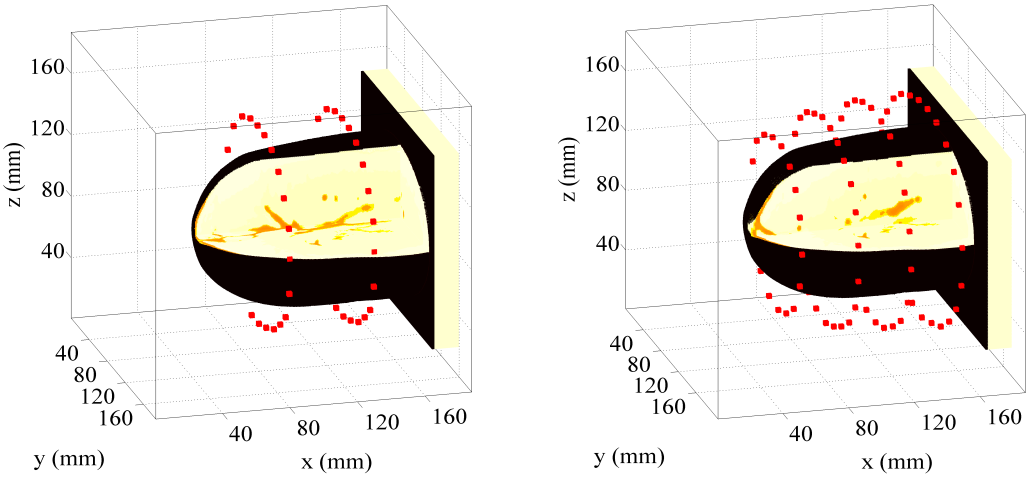

(a) Breast with cylindrical antenna array (b) Breast with hemispherical antenna array

Fig. 3.11 Alternative antenna arrays for UWB breast tumour detection. The small solid dots around the breast model show antenna positions to create the array. (a) Breast model and cylindrical antenna array. (b) Breast model and hemispherical antenna array.

In addition to breast model and input signal, another important aspect of UWB imaging system is the antenna configuration. Three commonly used types are planar [197], cylindrical [197], and hemispherical [42], the latter two are shown in Fig. 3.11. In a cylindrical antenna array [see Fig. 3.11(a)], two concentric rings of antennas are placed around the breast model, which are indicated by the solid dots. As for a hemispherical type [see Fig. 3.11(b)], four antenna rings with varied radiuses compromise the array. In the hemispherical array, in order to closely accommodate the breast, the further away the antenna ring from the chest wall, the smaller its radius is. For each type of antenna array,

depending on an applied scenario, the data collection can be realised through monostatic or multistatic to achieve the compromise between performance and complexity.

3.7.4 Visualisation of Signal Propagation

To clearly illustrate the interaction between UWB pulses and breast tissue, Fig. 3.12 illustrates the propagation of an UWB pulse within a breast at different instants of time.

The 2-D cross-section with z = 85 mm, and a relatively sparse breast model with MT B is selected for clear observation of radiation pattern. As shown in Fig. 3.12(a), the patient is assumed lying in a prone position. The dielectric properties of tissue distribution are obtained at 6.85 GHz. The excitation of MGP with f_c = 6.85 GHz is employed. Fig. 3.12(b) is the E_z field at time step of 120, in which the source is excited and initiates the radiation process. Strong reflection was generated at the skin-fat interface due to material discontinuity as shown in Fig. 3.12(c), in which a clear skin contour can be observed. During propagation, another strong scatterer the pulse encountered was the tumour. This is because tumour tissue has the largest permittivity among all comparably sized heterogeneous tissues under microwave frequencies, which is the physiological basis for microwave breast tumour detection. This is reflected in Fig. 3.12(d), an obvious backscattering occurred around tumour position of (x, y) = (78, 95) (mm). It is worth mentioning that in spite of attenuation during propagation, the backscattered signals

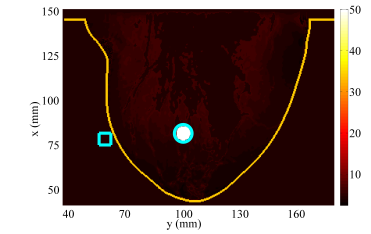

(a) Breast model and antenna

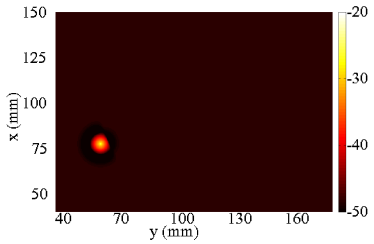

(b) Time step = 120

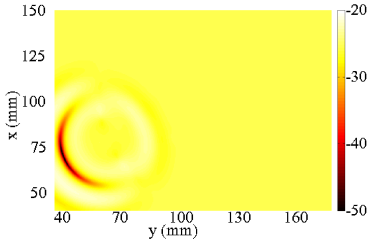

(c) Time step = 580

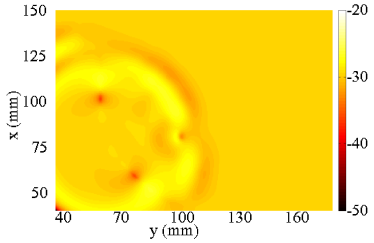

(d) Time step = 800

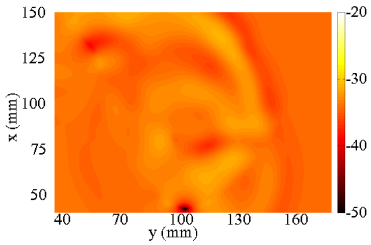

(e) Time step = 1240

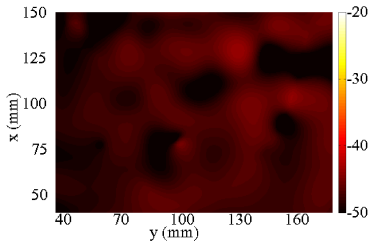

(f) Time step = 2500

Fig. 3.12 Radiation pattern visualisation between UWB pulse and breast model. (a) Breast model with tumour represented by the circle at $(x, y) = (78, 95)$ (mm) and antenna (transceiver) represented by the square at (75, 60) (mm). 2-D cross-section of breast phantom with MT B represented by relative permittivity at 6.85 GHz. (b)-(f) are the radiation patterns at different time steps along the propagation of pulse, which are represented by the electric field E_z in 10log10 logarithmic scale. (b) Time step = 120, pulse around source excitation. (c) Time step = 580, pulse around skin-fat interface. (d) Time step = 800, pulse around fat-tumour interface. (e) Time step = 1240, produce backscattered tumour response. (f) Time step = 2500, approaching steady-state.

resulted from the tumour could still have relatively larger amplitude than that from other tissues [see Fig. 3.12(e)]. Therefore, this backscattering could be collected and utilised for the sensing, identification, and localisation of tumours. A steady-state approached in Fig. 3.12(f), which is indicated by the small order of magnitude.

3.8 Simulation Results

To comprehensively simulate the interaction between UWB pulses and breasts with varied medium compositions, eight scenarios are considered and cross-compared.

To display simulation results in a compact way, each row represents a scenario (see Fig. 3.13). Within each row, the first column represents the selected input pulse. The second column illustrates the breast model and the antenna position. The antenna is represented by a square, which acts as both transmitter (excitation source) and receiver (probing point), unless otherwise stated. In VECE, the grid which is next to the excitation source grid is employed as the probing point to simulate such transceiver structure. The modelling of antenna as a point source is used in this study, i.e., it makes no distinction between various parts of the antenna such as feed region and the rest of the antenna structure. Depending on the level of discretization required, to accurately model the actual geometry in the feed region may be impractical, thus using a relatively simple model is often the case in FDTD analysis of an antenna, which can save significant computational resources [198]. Based on the input pulse and breast model, received pulses are plotted in the third column. Received pulses from both tumour-bearing and tumour-free breast models are plotted in the third column. The received pulse for the case without tumour employed the same breast model as shown in the second column, except there is no tumour present.

The acquisition of backscattered signals can be implemented by monostatic or multistatic method. In the monostatic approach, each element in antenna array transmits the pulse and receives backscattered signals from the breast model sequentially. In the multistatic method, each element in the antenna array takes a turn to transmit and the backscattered signals are recorded at all elements. The settings in the eight simulation scenarios are summarised in Table 3.1.

Table 3.1 Setting parameters in eight scenarios (S1 to S8). Input modulated Gaussian pulse with varied centre frequency (f_c) and standard deviation (c), breast models with different medium types (MT), different transmitter positions, and signal collection methods (monostatic or multistatic) are considered and compared.

	Input signal		Breast Model	Transmitter Position	Signal Collection
	f_c (GHz)	c (ps)			
S1	6.85	80.2	MT B	(x,y) = (80,60)(mm)	Monostatic
S2	6.85	80.2	MT D	(x,y) = (80,60)(mm)	Monostatic
S3	3.00	80.2	MT D	(x,y) = (80,60)(mm)	Monostatic
S4	10.0	80.2	MT D	(x,y) = (80,60)(mm)	Monostatic
S5	6.85	50.0	MT D	(x,y) = (80,60)(mm)	Monostatic
S6	6.85	120	MT D	(x,y) = (80,60)(mm)	Monostatic
S7	6.85	80.2	MT D	(x,y) = (50,125)(mm)	Monostatic
S8	6.85	120	MT D	(x,y) = (80,155)(mm)	Multistatic

3.8.1 Varied Breast Models

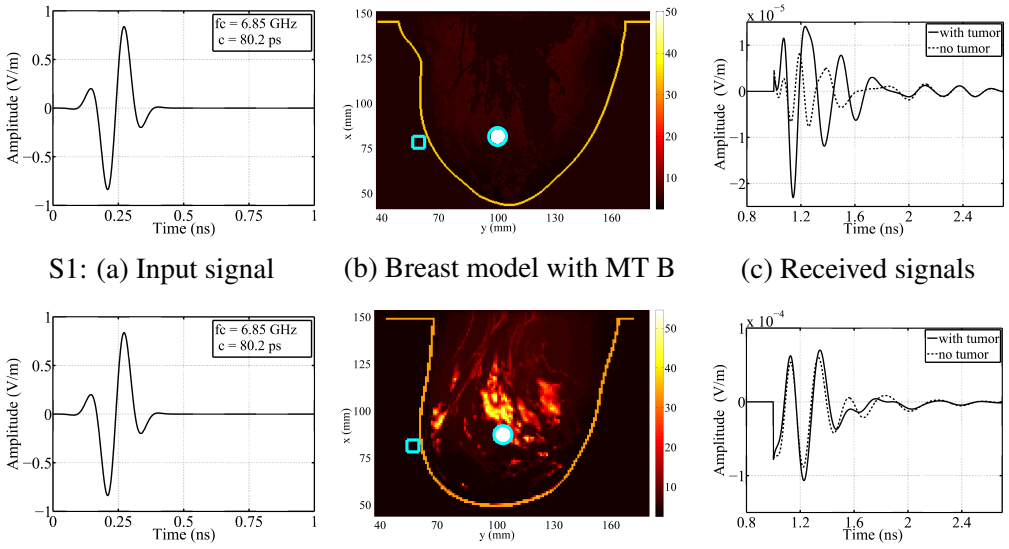

S1: (a) Input signal (b) Breast model with MT B (c) Received signals

S2: (d) Input signal (e) Breast model with MT D (f) Received signals

Fig. 3.13 Simulation results in S1 and S2 (setting details are introduced in Table 3.1), the breast models with MT B and D are used, respectively.

In S1 and S2, the input pulse described in Equ. (3.39) with f_c = 6.85 GHz and c = 80.2 ps is used [see Fig. 3.13(a) and (d)]. In S1, a breast model with MT B is used, whereas S2 selected a breast model with MT D. Observing Fig. 3.13(c), it is noticed that when there is tumour in breast [see Fig. 3.13(b)], the backscattered signal (solid) has an obvious peak around 1.2 (ns), compared with the no tumour case. This is due to the distinct dielectric

contrast between tumour and fatty tissues, a much higher dielectric property of cancerous tissue results in a stronger reflection, which is indicated by the higher signal amplitude.

In UWB breast imaging, the tumour response contained in received signals is the key data. Combining certain algorithms, this data could offer particularly useful information such as the existence, location, and size of tumours. Therefore, the effective tumour response (ETR) contained in raw received signals can be viewed as a crucial indicator. ETR is defined as the ratio between the maximum power of backscattered signals from tumour-bearing and tumour-free breasts within a time interval of interest [193], which can be calculated as

$$ETR = 10 \cdot \lg(P_{max\_with\_tumour} / P_{max\_tumour\_free}) \tag{3.42}$$

where $P_{max\_with\_tumour}$ is the maximum power of backscattered signal from a tumour-bearing breast model, whereas $P_{max\_tumour\_free}$ is the maximum power of backscattered signal from a tumour-free breast model. Higher ETR indicates higher quality of signal, which also indicates a higher chance of distinguishing tumour response from clutter signals.

For S1, observing the received signals in Fig. 3.13(c), assuming the ideal tumour response is within 0.8 (ns) and 1.6 (ns), the maximum absolute amplitudes for signal received from breast model with tumour and without tumour are 2.3e-5 and 8.1e-6 (V/m), respectively. Thus the $P_{max\_with\_tumour}$ and $P_{max\_tumour\_free}$ is 5.3e-10 and 6.6e-11 (W), respectively, and the ETR is obtained as 20.8 dB according to (3.42), which is a very large value. In S2, however, this value significantly reduced to 1.2 dB. This indicates that for denser breasts, the received tumour response is much more weaker than that from sparse breasts, due to the increased heterogeneity. Unlike MT B, the breast model with MT D used in S2 contains a higher portion of fibro-glandular tissues that can also generate strong reflections. This poses a serious challenge for the extraction of tumour response, due to the much smaller dielectric contrast between glandular and cancerous tissues, in comparison to the difference between fatty and cancerous tissues.

3.8.2 Signals with Varied Centre Frequencies

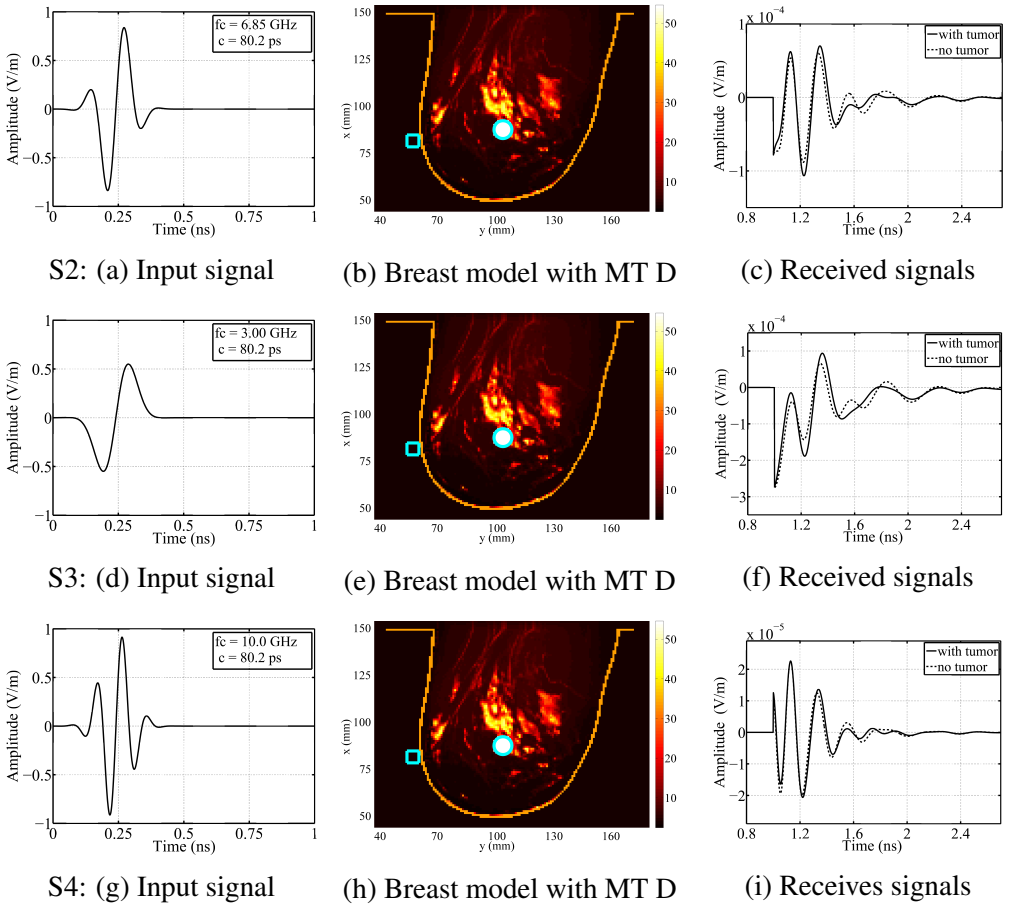

S2: (a) Input signal (b) Breast model with MT D (c) Received signals

S3: (d) Input signal (e) Breast model with MT D (f) Received signals

S4: (g) Input signal (h) Breast model with MT D (i) Receives signals

Fig. 3.14 Simulation results in S2, S3, and S4 (setting details are introduced in Table 3.1), the input signal with f_c of 6.85, 3.0, and 10.0 GHz are used, respectively.

To investigate the effect on tumour response from different signal frequencies, in S3 and S4, the pulses with different centre frequencies f_c than S2 are used. Considering UWB's frequency range regulated by Federal Communications Commission (FCC) is from 3.1 GHz to 10.6 GHz [19], in S3 and S4, f_c with 3.0 GHz and f_c with 10.0 GHz are employed, respectively. Observing the output of S3 [see Fig. 3.14(f)] and S4 [see Fig. 3.14(i)], signal shapes are different from that of S2. On the other hand, the ETR of S3 and 4 are 0.13 dB and 0.95 dB, respectively. It is noted that a lower frequency in S3 results in a smaller ETR of 0.13 dB, whereas in S2 and S4 with higher frequency, this value increased to 1.2 dB and 0.95 dB, respectively. This implies that a sufficiently high frequency is necessary to differentiate tumour and non-tumour responses.

3.8.3 Signals with Varied Pulse Widths

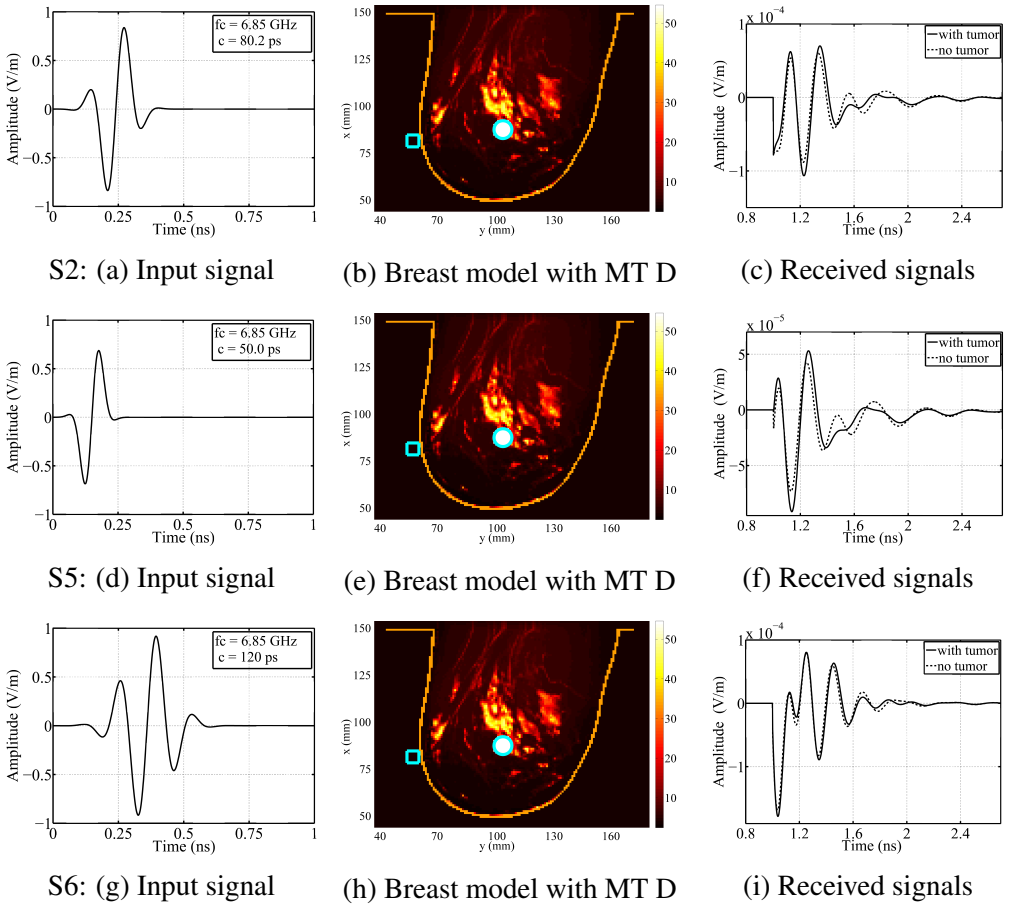

S2: (a) Input signal (b) Breast model with MT D (c) Received signals

S5: (d) Input signal (e) Breast model with MT D (f) Received signals

S6: (g) Input signal (h) Breast model with MT D (i) Received signals

Fig. 3.15 Simulation results in S2, S5, and S6 (setting details are introduced in Table 3.1). In S2, S5, and S6, the input signal with c of 80.2, 50, and 120 ps are used, respectively.

In S5 and S6, input pulses with different pulse widths controlled by the standard deviation c [see Equ. (3.39)] are considered. To preserve tumour response and reduce clutter signals, a time window which is comparable to input pulse width is employed in many tumour detection techniques [50], thus the effect on tumour response resulted from pulse width should be taken into account. Comparing Fig. 3.15(f) and (i) with Fig. 3.15(c), noted that the backscattered signals vary. The ETR of S2 is 1.2 dB, and this value decreased to 0.6 and 0.01 dB in S5 and S6, respectively. The pulse with a larger width (S6) obviously caused a serious decrease of effective tumour response, which is mainly due to the overlapping of backscattered signals from closely spaced heterogeneous tissues.

3.8.4 Signal Acquisition with Monostatic Method

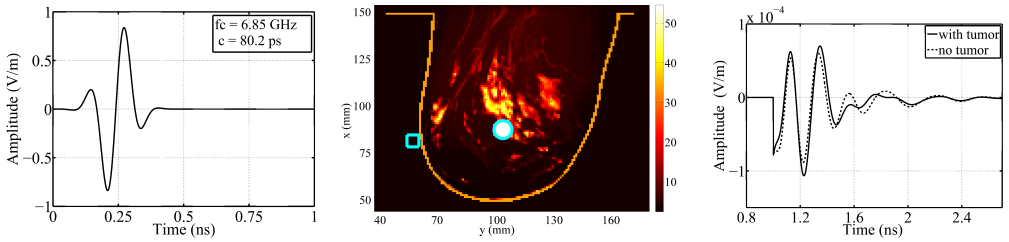

S2: (a) Input signal (b) Breast model with MT D (c) Received signals

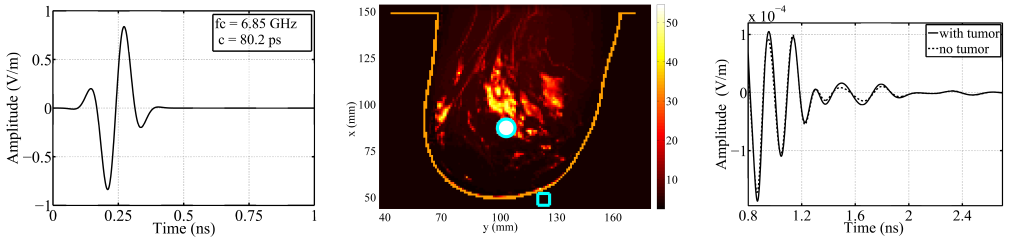

S7: (d) Input signal (e) Breast model with MT D (f) Received signals

Fig. 3.16 Simulation results in S2 and S7 (setting details are introduced in Table 3.1), transceiver (acts as both transmitter and receiver) at (x, y) = (80,60) and (125,50) are used, respectively.

The only difference in S7 [see Fig. 3.16(d)-(f)] compared with S2 is the antenna position. Due to the unknown distribution of heterogeneous tissues within breast, the useful tumour response received at different antennas varies. In S2, ETR is 1.2 dB, and this value reduced to 0.78 dB in S7. In spite of the same input pulse and selected breast model, it is noticed that the tumour response intensity can still be different, depending on the antenna-tumour distance and the medium composition of propagation channels. This reminds us that combining the collected signals from different propagation paths can be helpful to effectively extract tumour response, which also explains the necessity of using antenna array instead of one single antenna.

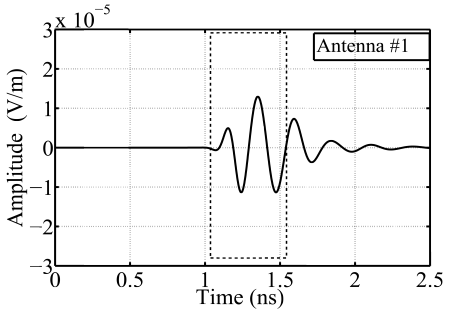

(a) Tumour response received at antenna 1

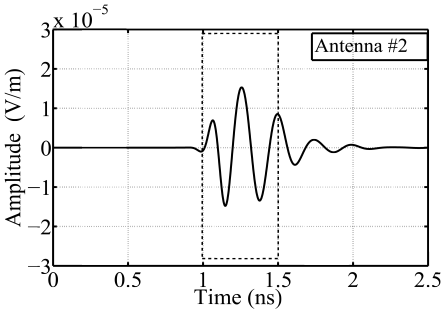

(b) Tumour response received at antenna 2

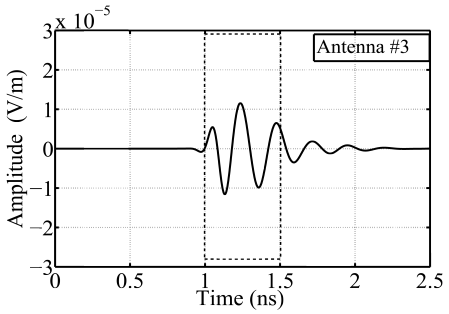

(c) Tumour response received at antenna 3

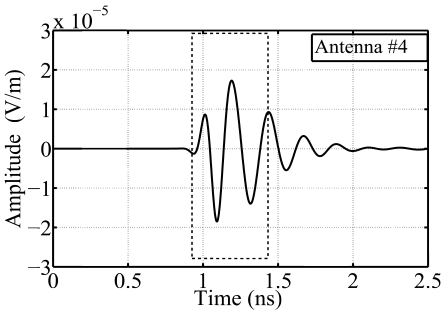

(d) Tumour response received at antenna 4

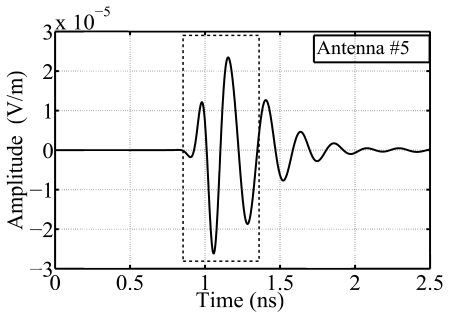

(e) Tumour response received at antenna 5

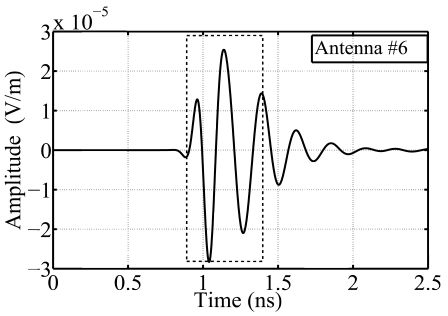

(f) Tumour response received at antenna 6

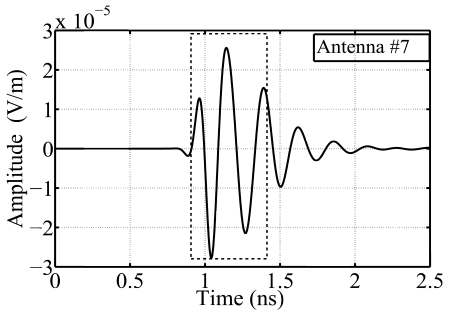

(g) Tumour response received at antenna 7

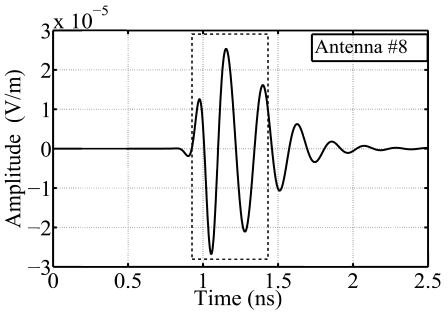

(h) Tumour response received at antenna 8

Fig. 3.17 Ideal tumour response received at different antennas. The antenna array shown in Fig. 3.11(a) is used, and monostatic data acquisition is employed. The antennas in Fig. 3.11(a) are numbered as follows: the outer ring of antennas is at x = 80 mm (antennas 1 to 24), and the inner ring (antennas 25 to 48) is at x = 130 mm, in which the position of both rings are related to the chest wall. The same yz plane coordinates for both rings of antennas are: (39, 101), (50, 120), (63, 140), (82, 153), (100, 158), (116, 159), (131, 158), (147, 154), (162, 145), (174, 132), (185, 116), (192, 97), (189, 74), (178, 56), (166, 47), (152, 39), (135, 34), (119, 32), (103, 31), (84, 38), (71, 44), (59, 55), (43, 69), and (37, 83). The ideal tumour response received at antennas 1 to 8 are displayed in (a)-(h).

However, all the scenarios above-presented are from only one antenna, and this can be easily repeated for each element in an antenna array such as the one shown in Fig. 3.11(a), then array signals can be obtained as displayed in Fig. 3.17. It is noted that useful tumour response from different propagation paths vary considerably. Specifically, the arising time of tumour response from different antennas is different, indicating a distinct propagation time delay which is determined by the distance between tumour and each antenna. In addition, the amplitude of tumour response differs, and this can be affected by varied distances, and propagation channels with different compositions.

3.8.5 Signal Acquisition with Multistatic Method

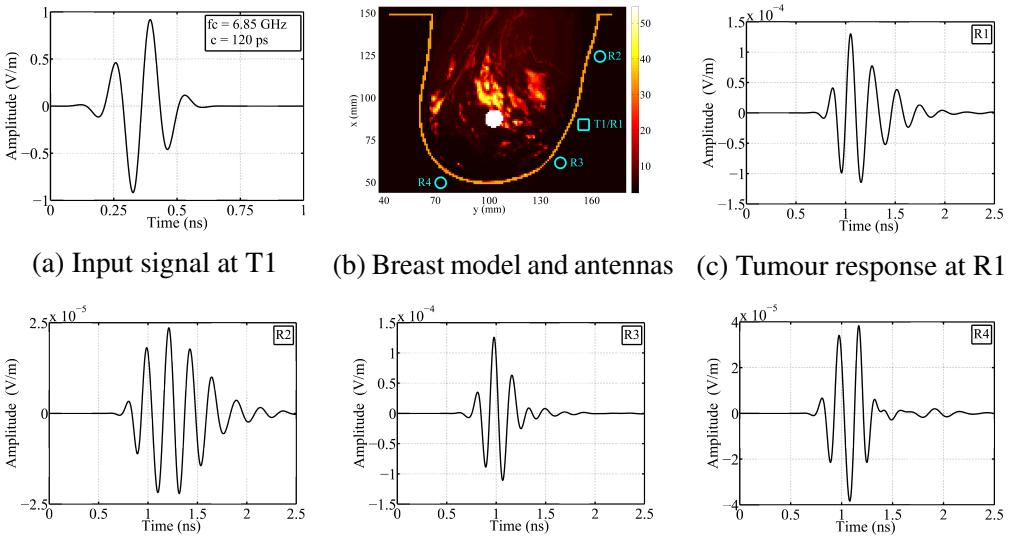

(a) Input signal at T1 (b) Breast model and antennas (c) Tumour response at R1

(d) Tumour response at R2 (e) Tumour response at R3 (f) Tumour response at R4

Fig. 3.18 Simulation setting and results of S8, signals are collected via multistatic method. Transmitter 1 (T1) and receiver 1 (R1) are both at (x, y) = (80,155) (mm), whereas receivers 2 to 4 (R2 to R4) are at (x, y) = (125,165), (65,140), and (50,70) (mm), respectively. Ideal tumour response received at R1 to R4 are shown in (c) to (f).

In S8, multistatic signal acquisition is used. In this method, each element in the antenna array takes a turn to transmit and the backscattered signals are recorded simultaneously at all antennas. Compared with monostatic method, multistatic can cause extra hardware cost and algorithm complexity, but it is able to gather multiple signals that propagate via different routes, accruing more information about the tumour. Since the propagation path between each transmitter and receiver pair varies in multistatic, to fairly evaluate

the received tumour response of each propagation channel, the ideal artefact removal method [50] is used.

As shown in Fig. 3.18(b), antenna 1 acted as both transmitter and receiver, whereas antennas 2 to 4 were used as receivers only. Specifically, transmitter 1 (T1) is the only excitation, and receivers 1 to 4 (R1 to R4) received backscattered signals at the same time. Observing and comparing the peak of the ideal tumour responses received at different receivers [see Figs. 3.18(c)-(f)], noted that the strongest backscattering from tumour is achieved at R1, which has a peak amplitude of 1.3e-4. When receivers are far away from transmitter, the received tumour reflection can be an order of magnitude smaller, which are the cases for R2 and R4 with the order of magnitude of 1e-5. Depending on propagation channel, the strength of these reflections varies. R2 and R4 have a similar distance from T1, due to the sparse medium between tumour and R4, slightly higher amplitude of signals with 4e-5 is obtained, in comparison to that of 2.5e-5 at R2. It is noted that the tumour response received at R3 is almost as strong as that at R1. This is because R3 is closer to T1, plus less attenuation is expected for the propagation path from tumour to R3 than to R1, because of the different tissue compositions and distributions of each path. The result of R3 explains the potential advantage of multistatic method over its monostatic counterpart. This implies that extra useful tumour information could be collected via multistatic, thereby improving the performance of tumour detection algorithms.

Based on the eight different scenarios, it is clear that collected tumour response can vary significantly, depending on input pulse, breast type, antenna position and signal acquisition method. However, these collected signals can hardly be used for tumour detection directly. But with the aid of certain imaging algorithms such as the one introduced in [42], tumour response can be effectively combined and extracted, thereby reconstructing a much more meaningful image indicating the existence and location of tumours. The ultimate tumour detection may largely depends on applied imaging algorithms and related configurations, and this will be investigated in succeeding chapters.

3.9 Further Applications

Considering the flexibility of VECE, besides breast cancer detection, VECE is potentially able to provide useful data for a wider diversity of bioelectromagnetic applications. For example, similar setting as used in Fig. 3.12 could be employed for dose absorbing calculation, which is particularly useful for establishing dose-response curves for nanosecond electromagnetic pulses [199], thereby determining the dosimetry for clinical efficacy and safety. Furthermore, through monitoring the small adjustment in dielectric properties caused by minor alterations of perfusion and internal pressure, the onset of ischemia of tissues could be detected [200]. Moreover, similar measurements could facilitate the development of biocompatible contrast agents that enhance the performance of diagnostic and therapeutic microwave breast imaging [201], and the development of microwave thermal therapies for brain tumours [202].

3.10 Conclusion

This chapter presented a new computational engine VECE, which enables the 3-D propagation modelling and simulation of UWB signals for breast cancer detection.

The novel implementation combining ADE and CPML, which is adopted for describing the dispersive medium and truncating the computational domain, respectively, is concurrently achieved in VECE. The ADE approach is adopted for integrating medium dispersion into FDTD, which has the great advantage in reducing computational complexity and memory storage requirement. The CPML, as a very robust absorbing boundary condition, significantly reduces the late-time reflections and offers improved efficiency and highly desirable flexibility for terminating the host medium. The efficacy and accuracy of VECE are validated in both time and frequency domain across a variety of assessment criteria. The results generated by VECE are in great agreement with the simulations results offered by commercial software.

The versatility of VECE is demonstrated through the modelling of UWB signal and its interaction with realistic breast phantoms, which simulated various breast imaging

scenarios for tumour detection. It is demonstrated that the tumour response is much more pronounced from relatively sparse breasts than that from heterogeneously dense breasts. The frequency of input signals will not cause significant effect on the strength of effective tumour response. Simulation results showed the clear practicability of VECE for facilitating the development of detecting techniques for breast cancer, and great potential for other bio-sensing and imaging applications.

It is revealed that received signals at distributed antennas contained vastly different tumour responses, due to the unknown heterogeneity within the breast, which indicated the importance of combining of signals from different propagation paths. Based on the collected tumour response and combined with certain algorithms, an image which shows the existence and location of tumour can be obtained. These images can not only be used for identifying tumour at its very early stage, monitoring it in subsequent growth stage, but also facilitate developing therapeutic techniques, which are of critical value, and related algorithms for forming such images is studied in subsequent chapters.

Chapter 4

A Robust and Artefact Resistant (RAR) Algorithm of UWB Imaging System for Breast Cancer Detection

4.1 Introduction

In this chapter, a novel robust and artefact resistant (RAR) imaging algorithm for early breast cancer detection is proposed. The chapter is organised as follows: in Section 4.2, the literature regarding UWB imaging algorithms for breast cancer detection are reviewed. In Section 4.3, configuration of the imaging system is introduced. Section 4.4 presents the proposed RAR algorithm for image reconstruction. The implementation of RAR is introduced in Section 4.5. Assessment criteria and simulation results of imaging algorithms under different scenarios are presented in Section 4.6. The robustness and complexity analysis of algorithm are provided in Section 4.7 and 4.8, respectively. Finally, Section 4.9 concludes this chapter.

4.2 Literature Review on UWB Breast Imaging Algorithms

In the last few decades, different modalities of microwave imaging for breast cancer detection, including passive, hybrid, and active approaches, have attracted considerable

attention. The passive microwave imaging techniques seek to identify tumours based on the temperature differences between normal and cancerous breast tissues with the aid of radiometers [82, 83]. Hybrid approaches differentiate biological tissues by the distinctive acoustic waves radiated from thermoelastic expansion when tissues are under microwave illumination [84]. The active detection methods distinguish normal and malignant breast tissues based on the contrast of dielectric properties at microwave frequencies [85]. Based on the reconstruction technique used, active detection methods can be categorised into microwave tomography and UWB radar-based imaging. In microwave tomography, the spatial distributions of dielectric constant and/or conductivity within the breast are iteratively calculated; thus, nonlinear inverse scattering problems are involved. More details on tomographic imaging can be found in [129, 203]. UWB radar-based methods, on the other hand, aim to detect and localise strong scatterers such as tumours, instead of quantitatively computing the distribution of dielectric properties.

UWB imaging systems face several challenges for breast cancer detection, two of them is the antenna design, and the construction of realistic breast models. Another difficult challenge is image formation algorithm. The image formation algorithms are expected to provide superior identification ability, accurate positioning, strong robustness, and fast computation speed.

A variety of image formation algorithms have been proposed over the last decade. Hagness *et al.* [39, 45] first proposed the confocal microwave imaging (CMI) technique which adopted delay-and-sum (DAS) beamforming algorithm. Research on beamforming algorithms for CMI has evolved into two branches: data-dependent and data-independent. Some promising data-dependent beamforming algorithms that have been considered are multistatic adaptive microwave imaging (MAMI) [46], multi-input multi-output (MIMO) [47], and time-reversal multiple signal classification (TR-MUSIC) [48, 49]. Data-dependent algorithms can reconstruct high-resolution images when the array steering vector corresponding to the signal of interest (SOI) is accurately known, which is difficult in realistic imaging scenarios. In contrast, data-independent beamformers are free from this prior information and have been continuously developed. A number of data-independent algorithms

are proposed in recent years, including delay-multiply-and-sum (DMAS) [50], modified-weighted-delay-and-sum (MWDAS) [51], and filtered delay-and-sum (FDAS) [52]. Compared with the classical DAS algorithm, improved performance of clutter rejection is offered by DMAS and MWDAS. FDAS shows its capability of detecting multiple scatterers in dense breasts, where the presence of fibro-glandular tissue is considered. It is recognised that the increased heterogeneity of normal breasts introduced by glandular tissues constitutes a big challenge for tumour detection. There are two reasons for this: first, although there is a large dielectric contrast between adipose and cancerous tissues, the difference between glandular and cancerous tissues is much less pronounced. Also the glandular tissue introduces a significant amount of attenuation and dispersion in backscattered signals, making it more difficult to detect any small tumours present. Despite the strengths of these algorithms, all of them are only examined in scenarios assuming an ideal artefact removal method is applied. However, this assumption is oversimplified and infeasible in a real set-up. Because the artefact is typically several orders of magnitude greater than the reflections from tumours within the breast, even a very small amount of residual artefact can easily mask the desired tumour response, which may result in the failure of existing algorithms to identify any tumours present.

In this study, focus is placed on data-independent algorithms due to its independence of priori knowledge, strong robustness, and computational efficiency. Existing data-independent UWB breast imaging algorithms are firstly examined and evaluated. Simulation results showed that although these methods show satisfactory tumour detection capabilities with an idealised artefact removal method, their performance suffer significant deterioration or completely fail when the early-stage artefact, including incident signals and skin-fat interface reflections, cannot be perfectly removed.

Accordingly, a new robust and artefact resistant (RAR) image formation algorithm is proposed. Extensive simulations and analyses using backscattered signals received from 3-D anatomically realistic MRI-derived numerical breast models were conducted to validate the performance of the proposed algorithm. Results showed that RAR offered superior tumour identification, accurate localisation, and strong artefact resistance over existing

data-independent algorithms. The robustness of RAR was demonstrated under various scenarios: homogenous and heterogeneous breast structures, varied density classifications, tumour sizes and positions, and in cases considering both ideal and practical artefact removal methods.

4.3 Backscattered Signal Acquisition

4.3.1 Breast Model

Realistic models are expected to incorporate various attributes of the breast, including geometrical properties, spatial distribution of different constituent tissues, and the dispersive property. Based on the proposed computational engine VECE introduced in Chapter 3, 3-D anatomically accurate FDTD-based breast models are developed and employed, and the raw data is obtained from UWCEM MRI breast phantoms repository [169]. In addition to skin layer and malignant tumour, the breast model is composed of three types of fatty tissues and three types of fibro-glandular tissues. The dielectric properties of skin, adipose, and fibro-glandular tissue used in the model are based on studies in [102, 150], whereas those representing malignant tumours are obtained from Bond *et al.* [40, 152]. The dispersive nature of tissues is incorporated into the FDTD model using the time-domain auxiliary differential equation (ADE) ([53], Ch. 9, pp. 311) for a single-pole Debye model. In the single-pole Debye model, the dielectric spectrum of a tissue sample is characterised by different dispersive regions or 'poles' at a range of frequencies. In each dispersive region there is a relaxation time, which describes the time needed for electron polarisation to relax towards a new equilibrium when there is an applied electric field. The relaxation time is regarded as a constant in the simplest form. The dispersion in frequency domain through Debye model can be described as [188]:

$$\varepsilon_r(\omega) = \varepsilon_\infty + \frac{\varepsilon_{s1} - \varepsilon_\infty}{1 + j\omega\tau_1} - j\frac{\sigma_s}{\omega\varepsilon_0} \tag{4.1}$$

where $\varepsilon_r(\omega)$ is calculated relative permittivity at a certain angular frequency ω (in radians per second), $\omega = 2\pi f$, f (in Hz) is the frequency of input UWB pulse, ε_∞ is the permittivity at infinite frequency, σ_s is static conductivity (in siemens per second), ε_0 is free-space permittivity (8.854 pF/m), ε_{s1} is the permittivity at static frequency of the dispersive pole, $j = \sqrt{-1}$, and τ_1 is the relaxation time of the dispersive pole (in picoseconds). Debye parameters for each tissue type [102] are summarised in Table 4.1.

Table 4.1 Tissue parameters (3-10 GHz) assumed for a single-pole Debye model [102].

	ε_∞	ε_{s1}	τ_1(ps)	σ_s(S/m)
Fat-High	3.9870	7.5318	13.0000	0.0803
Fat-Median	3.1161	4.7077	13.0000	0.0496
Fat-Low	2.8480	3.9521	13.0000	0.2514
Fibro-glandular High	14.2770	54.7922	13.0000	0.6381
Fibro-glandular Median	13.8053	49.3510	13.0000	0.7384
Fibro-glandular Low	12.8485	37.4915	13.0000	0.2514
Skin	15.9300	39.7600	13.0000	0.8310
Malignant Tumour	20.2800	45.0500	13.0000	1.3000

Fig. 4.1 illustrates the 3-D breast phantom and antenna configuration used in simulation. To focus on breast tissue response and avoid possible interference, the chest wall is not included as assumed in [49] and [52]. Two concentric rings of antennas are positioned around the skin layer, which has a thickness of 1.5 mm, with a 10 mm spacing to the skin surface. Each antenna is modelled as a point source with horizontal polarisations (x-directed). The outer ring of antennas is at x = 80 mm (antennas 1 to 24), and the inner ring (antennas 25 to 48) is at x = 130 mm, in which the position of both rings are related to the chest wall. The same yz plane coordinates for both rings of antennas are: (39, 101), (50, 120), (63, 140), (82, 153), (100, 158), (116, 159), (131, 158), (147, 154), (162, 145), (174, 132), (185, 116), (192, 97), (189, 74), (178, 56), (166, 47), (152, 39), (135, 34), (119, 32), (103, 31), (84, 38), (71, 44), (59, 55), (43, 69), and (37, 83).

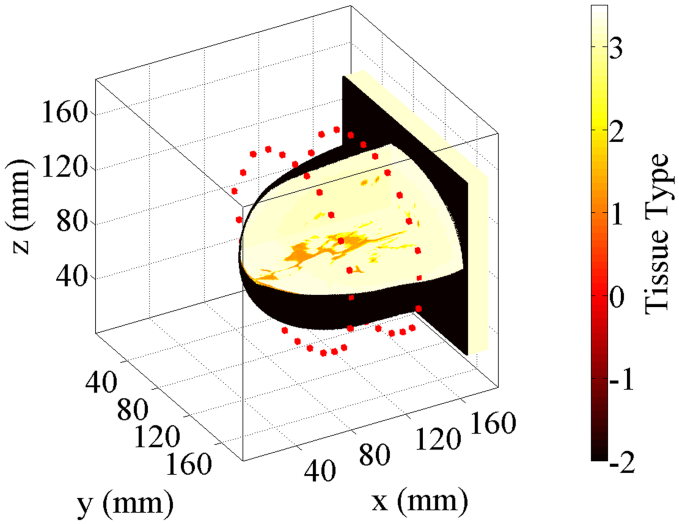

Fig. 4.1 Three-dimensional FDTD breast model with two concentric rings of 24 antennas (indicated by solid dots) surrounding the breast. The categorised tissue types are represented by different values: fat-high(3.1), fat-median(3.2), fat-low(3.3), fibro-glandular (FG)-high(1.1), FG-median(1.2), FG-low(1.3), and skin(-2).

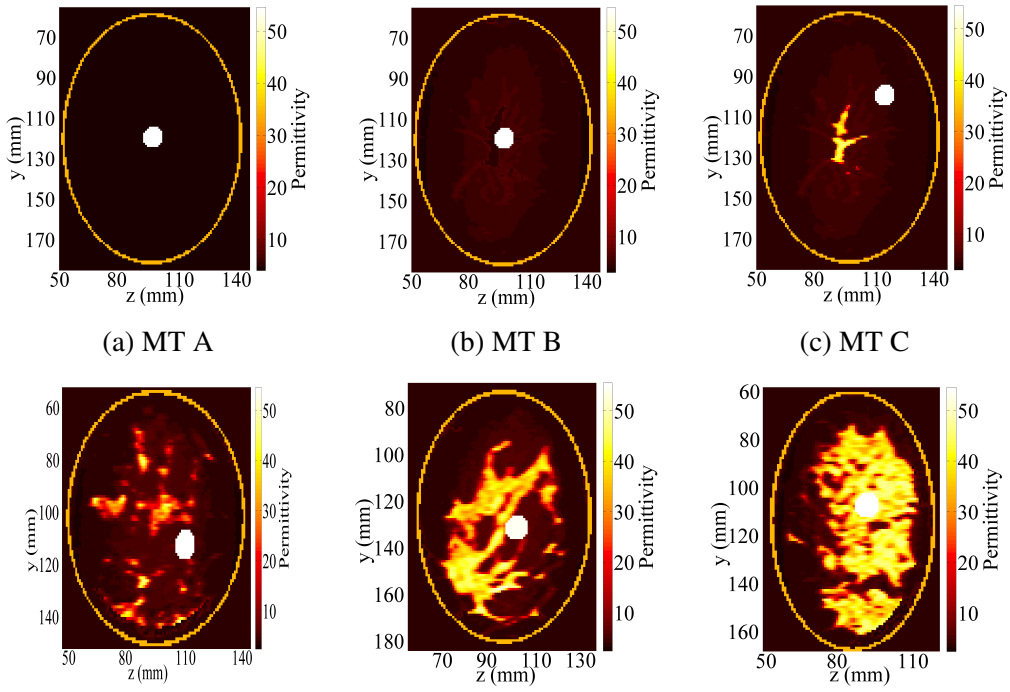

(a) MT A (b) MT B (c) MT C

(d) MT D (e) MT E (f) MT F

Fig. 4.2 Breast medium type (MT) represented by relative permittivity at 6.85 GHz [169]. A tumour with 10 mm diameter is constructed as a sphere. The 2-D slices are taken at the $x = 95$ cross-sections of Fig. 4.1. (a) to (f) represent the six breast medium types, and details are described below.

For completeness, six breast medium types (MT) with various structures and radiographic density classifications are used to evaluate the proposed algorithm. Medium types

are selected from UWCEM database [169] and are shown in Fig. 4.2. The density follows the definition of the American College of Radiology (ACR) [195] and details of each MT is described as follows (ACR type, Breast ID in UWCEM repository, characteristics): 1) MT A: ACR-I-ID-071904, homogeneous breasts composed of fatty-median tissue only, all other tissues are replaced by fatty-median tissues; 2) MT B: ACR-I-ID-071904, heterogeneous breasts composed of three types of fatty tissues, all fibro-glandular tissues are replaced by fatty-median tissues; 3) MT C: ACR-I-ID-071904, full heterogeneous breasts composed of three types of fatty, and three types of fibro-glandular tissues with a percentage less than 25%; 4) MT D: ACR-II-ID-010204, full heterogeneous breasts contain glandular tissues with a percentage ranging between 25% and 50%; 5) MT E: ACR-III-ID-070604PA2, full heterogeneous breasts contain glandular tissues with a percentage ranging between 50% and 75%; 6) MT F: ACR-IV-ID-012304, full heterogeneous breasts contain glandular tissues with a percentage over 75%.

Although tumours have irregular shapes, for this study they are constructed as spheres with varied radiuses, which can simulate different strengths of backscattered tumour response. Without losing generality, the tumour is placed at three different positions: 1) close to the centre of the outer ring; 2) at the centre between the two antenna rings; and 3) off-centre between the two antenna rings. Position 1 at (x, y, z) = (80, 119, 94) represents tumour locations on different x cross-sections and are close to one of the antenna rings. Position 2 at (x, y, z) = (95, 119, 94) is representative for those which are between two antenna rings and centre at the yz plane with different x cross-sections, whereas those off-centre at the yz plane with different x cross-sections and close to the skin surface are represented by Position 3 at (x, y, z) = (95, 99, 112). In addition, since a high proportion of breast cancers are invasive ductal carcinomas, which start at fibro-glandular regions [106], tumours which are located within fatty and glandular tissues are both considered. To mitigate the strong reflections from the skin-fat interface, the model and antenna array are considered to be positioned inside an immersive liquid with the same permittivity as that of fat-median tissue at the centre frequency of the input pulse, as it is generally done [50, 51].

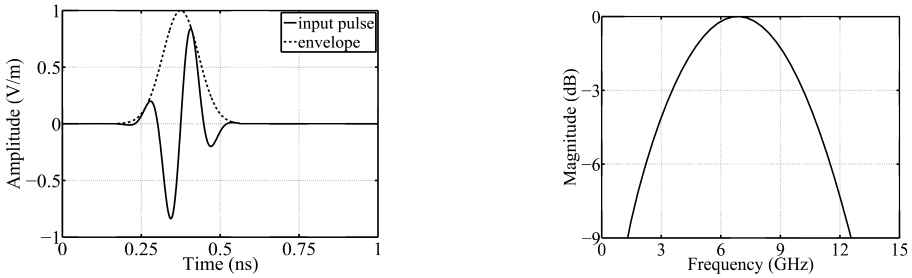

(a) MGP waveform (b) Spectrum of MGP

Fig. 4.3 Modulated Gaussian pulse (MGP) used as source excitation in FDTD simulations. (a) MGP waveform in time domain. (b) Spectrum of MGP.

4.3.2 Simulated Model Setup

The antenna is excited with a modulated Gaussian pulse (MGP) (see Fig. 4.3), which is given by

$$G(t) = sin\left[\omega_c\left(t-b\right)\right] e^{-\left(\frac{t-b}{c}\right)^2} \tag{4.2}$$

where $\omega_c = 2\pi f_c$ is the centre angular frequency with centre frequency f_c = 6.85 GHz, the centre position of Gaussian envelope b = 0.375 (ns), and c = 0.0802 (ns) is the standard deviation which controls the width of Gaussian envelope. MGP is selected since it is considered to present better spectral control in practical use [191]. The input pulse width is 0.56 (ns), which has a full-width at half maximum (FWHM) bandwidth of 6.6 GHz. The acquisition of backscattered signals can be implemented by monostatic or multistatic method. In the monostatic approach, each antenna is used to transmit the pulse and receive the backscattered signal from the breast model sequentially. In the multistatic method, each antenna takes a turn to transmit and the backscattered signals are recorded at all antennas. Despite the advantage of multistatic approach in terms of capturing more information about the target, its disadvantages are obvious, such as additional hardware cost and high algorithm complexity. Monostatic method is employed for signal acquisition in this study.

To discretize FDTD problem space, a rule of thumb to select grid size is to keep it below one-tenth of wavelength, with the purpose of making numerical dispersion error negligible [204]. Assuming the breast is mainly composed of fatty-median tissue, and using the centre frequency of input pulse as a baseline, obtaining the wavelength is 21

mm, thus one-tenth of wavelength is 2.1 mm. A smaller grid size of $\Delta x = \Delta y = \Delta z = 1$ mm is employed for capturing the response from small sized tumours and adapting possible smaller wavelengths in dense breasts. The time step represented by Δt is determined by the Courant-Friedrichs-Lewy (CFL) stability condition ([53], Ch. 4, pp. 154, Equ. 4.98), which equals 1.91 (ps). Ten-layer convolutional perfectly matched layer (CPML) [128] absorbing boundary conditions are placed around the computational domain to attenuate outgoing radiation.

4.4 Breast Cancer Detection with RAR

4.4.1 Pre-processing for Artefact Removal

Recorded backscattered signals consist of two parts: the early-stage and the late-stage. The majority of early-stage parts consist of incident signals and strong reflections from skin-fat interface, whereas the late-stage parts include tumour response, fibro-glandular tissue response, fatty tissue response, and the multi-reflections between these tissues. Tumour, fibro-glandular, and fatty responses refer to the signals directly reflected from these tissues. For identification purpose, only tumour response is needed, thus all other signals are regarded as interferences, which can be categorised as the early-stage artefact and the late-stage clutter. The late-stage clutter mainly includes fibro-glandular and fatty tissues responses, which are mixed with tumour response and should be suppressed for tumour detection. The early-stage artefact, which includes incident signals and skin-fat reflections, can be several orders of magnitude greater than the desired tumour response, and there are two reasons. Firstly, the skin layer is the first strong scatterer that the EM wave encounters when it still has large magnitude, thus the backscattering is stronger than later-time response. Secondly, skin has larger permittivity than fatty tissue and comparable permittivity as tumour tissue (see Table 4.1). Thus even with the same incident EM wave, the backscattering from the skin layer can be very strong. Therefore, these artefact signals must be removed before applying any image reconstruction algorithms.

Ideal removal of the early-stage artefact is realised with the aid of *a priori* information generated from a tumour-free breast model. The ideal tumour response from the ith transceiver in a discrete form denoted as $S_i(n)$ can be obtained by

$$S_i(n) = S_{i\_with\_tumour}(n) - S_{i\_tumour\_free}(n) \tag{4.3}$$

where $n = 1, 2, ..., K$, and K is the number of signal sampling points, $S_{i\_with\_tumour}(n)$ is the backscattered signal received at the ith transceiver from the breast model with tumour, and $S_{i\_tumour\_free}(n)$ represents the backscattered signal received at the same transceiver from a breast model which is exactly the same as the previous one except that there is no tumour present. $S_{i\_with\_tumour}(n)$ is composed of early-stage artefact, tumour response, glandular tissue response, fatty tissue response, and the multi-reflections between heterogeneous tissues, whereas $S_{i\_tumour\_free}(n)$ comprises similar level of early-stage artefact, glandular tissue response, fatty tissues response, and multi-reflections between these tissues, thus $S_i(n)$ is the signal dominated by tumour response. This method not only removes the early-stage artefact, but also the glandular tissue response, fatty tissue response, and the multi-reflections between tissues. This is not feasible in practice; however, it could serve as a useful benchmark of the best performance of algorithm possible and clearly illustrate the effect of heterogeneity on imaging results.

A number of more practical artefact removal algorithms have been developed, these can be classified as adaptive and non-adaptive techniques. Adaptive methods include Wiener filter [40], recursive least squares (RLS) filter [153], and singular value decomposition (SVD) [2], whereas some other promising techniques that have been considered are average subtraction [45], rotation subtraction [145], frequency domain pole splitting [154], and entropy-based time window [155]. Robustness to local variations of skin thickness and differences in the antenna-skin distance is observed in adaptive filtering methods; however, varied levels of distortion to tumour response is introduced. Considering both the capability of preserving tumour response and the effectiveness of removing artefact, the best results are offered by Wiener filter and entropy-based time window methods [151].

The performance of image reconstruction algorithms closely depends on the outcome of artefact removal. When the artefact cannot be effectively removed, the residual artefact could easily mask the useful tumour response. For completeness and fairness, it is thus essential to evaluate imaging algorithm in cases with both ideal and practical artefact removal, under the same conditions.

4.4.2 Algorithm Rationale

The block diagram depicted in Fig. 4.4 shows the RAR algorithm to reconstruct the intensity value of each pixel in the breast model. Let l represent the lth location of a pixel within the imaging region of a constructed image L. For each location, RAR explores and exploits the cross-correlation of time-shifted signals. To time-shift each signal, an estimated average velocity for all propagation channels, between transmitter to scatterer and back to receiver, is assumed to be sufficiently close to the actual speed and could well represent the characteristics of propagation channels. Considering the larger dielectric property of tumour than other comparably sized tissues, tumour response is the dominant part of received signals within a certain time widow, in most if not all cases. Thus, after being time-shifted, signals received at neighbouring antenna pairs should have a higher correlation between tumour responses resulted from the same strong scatterer, compared with those signals from other heterogeneous breast tissues. The enhancement of tumour detection is achieved by rewarding this correlation. To calculate the intensity value of l, three steps are involved.

Step 1: Each pre-processed $S_i(n)$ is time-shifted based on the corresponding round-trip time delay at a location l. The time-shifted signals are expressed as $S_i(n+\tau_{il})$, where $n = 1,2,\ldots,K$, and τ_{il} is the round-trip travel time from the ith transceiver to a specific location l within the imaging region. Propagation distance is calculated based on relevant space coordinates in the constructed model. The propagation speed of signal is calculated under the assumption that each traversed medium, including immersive liquid, skin layer, and underlying breast tissue, has a constant relative permittivity at the centre frequency of the input pulse. The relative permittivity at centre frequency is chosen since

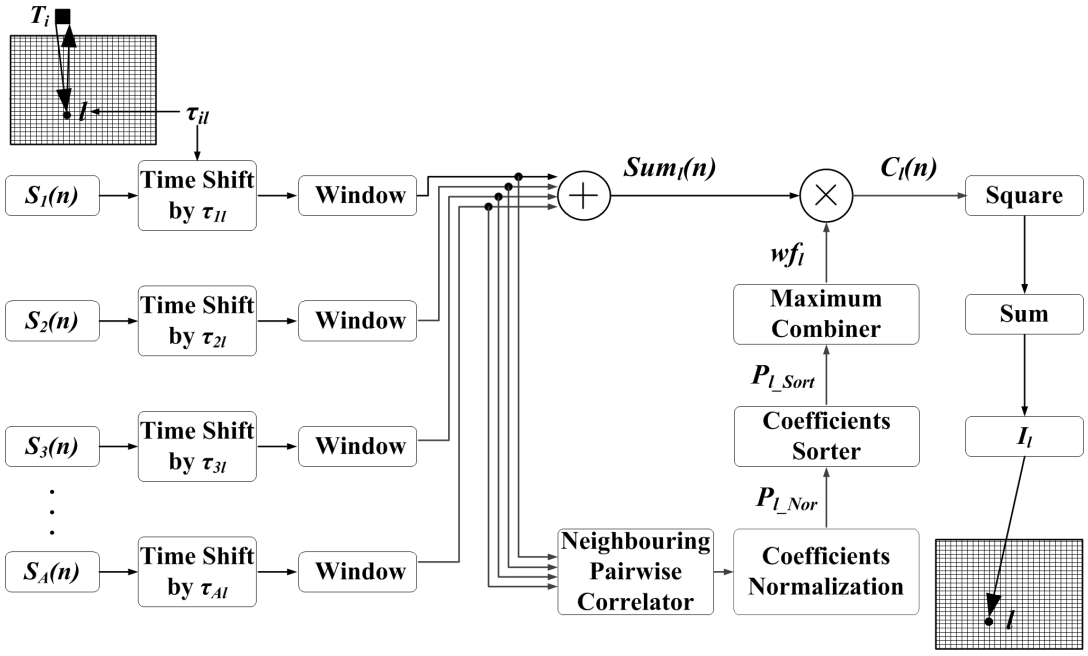

Fig. 4.4 Block diagram illustrating the RAR algorithm used to calculate the intensity of the lth pixel I_l in imaging region indicated by the mesh area.

it represents the majority of tissues' permittivity across the frequency range of input pulse. The average dielectric property of underlying breast tissue is assumed to be established through an appropriate patient-specific dielectric property estimation algorithm such as the one developed by Winters *et al.* [205].

Prior to further processing, a time window truncation for each time-shifted signal is applied. The utility of time window truncation is twofold. First, it only preserves the desired tumour response. Second, it reduces the algorithm complexity since only truncated signals are needed in the following steps. The time window is represented as W_α, where $W_\alpha = \alpha\Delta t$. α is an integer value and Δt is the time step used in FDTD, which equals 1.91 (ps) as explained previously. W_{294} which represents a length $294\Delta t$ = 562 (ps), equals to the input pulse is used as a default time window, unless otherwise specified. The selection of this window length is because backscattered signals from dispersive biological tissue are a distorted version of the excitation pulse as frequency-dependent tissues broaden the duration of input pulse. Studies showed that this broadening effect is directly proportional to tumour size [40]. The aim of this research is to detect early-stage breast cancer when tumour is small, thus a short-length time window, which is comparable to the input pulse width, is selected. Larger or smaller time windows could result in either high clutter

or tumour location bias. Thus, the time-shifted signal after truncation with W_α can be represented as $S_i(n+\tau_{il})$, where $n = 1,2,\ldots,\alpha$.

Let A be the number of antennas. After artefact removal, A sets of signals containing tumour response are collected in a monostatic way as explained in Ch. 4.3.2. Thus, for every single location l, there are A sets of time delays corresponding to each transceiver. Let $Sum_l(n)(n = 1,2,\ldots,\alpha)$ denote the sum of all time-shifted signals at the lth location given by

$$Sum_l(n) = \sum_{i=1}^{A} S_i(n+\tau_{il}). \tag{4.4}$$

Step 2: To enhance tumour response and suppress the adverse effect resulted from both early-stage artefact and late-stage clutter, a weight factor wf_l for the lth location is introduced. The Pearson's correlation coefficient r_{i,j_l} between neighbouring pair of time-shifted signals is calculated as

$$r_{i,j\_l} = \frac{\sum_{n=1}^{\alpha} X_i(n)X_j(n)}{\sqrt{\sum_{n=1}^{\alpha}[X_i(n)]^2 \sum_{n=1}^{\alpha}[X_j(n)]^2}} \tag{4.5}$$

where $X_i(n) = S_i(n+\tau_{il})$ and $X_j(n) = S_j(n+\tau_{jl})$ with $j = i+1$ (or $j = i-1$), are the time-shifted signals at location l from the ith and $(i+1)th$ transceiver, respectively. Correlation coefficient r_{i,j_l} measures the degree of coherence between time-shifted signals of neighbouring antenna pairs. High positive correlation between shifted signals received at neighbouring antenna pairs is expected at tumour locations, considering all time-shifted signals are a broadened version of the same input pulse, after reflection from the same strong scatterer. Based on (4.5), the neighbourhood pairwise correlation coefficients vector P_l composed of $(A-1)$ elements for l is obtained (the first and the last antenna are excluded since they are far away from each other, all the neighbouring antenna pairs between them are considered), where A is the total number of antenna. Thus, P_l can be expressed as

$$P_l = [r_{12\_l}\ r_{23\_l}\ \ldots\ r_{(A-1)A\_l}]. \tag{4.6}$$

Considering r_{i,j_l} is in the range of [-1, 1], all coefficients are linearly normalised to the range of [0, 1], avoiding negative coefficients generating a high weight

$$P_{l\_Nor} = \frac{(P_l + 1)}{2}. \tag{4.7}$$

Let P_{l_Sort} be the sorted P_{l_Nor} in a descending order and R_{i_l} be the sorted coefficients, $i = 1, 2, \ldots, (A-1)$. Therefore,

$$P_{l\_Sort} = [R_{1\_l}\ R_{2\_l}\ \ldots\ R_{(A-1)\_l}] \tag{4.8}$$

where $R_{1\_l} > R_{2\_l} > \ldots > R_{(A-1)\_l}$. The associated weighting factor for the lth location wf_l is introduced as

$$wf_l = \prod_{i=1}^{i=\frac{A-1}{2}} R_{i\_l} \tag{4.9}$$

which is the product of the first half elements of the sorted correlation coefficients vector P_{l_Sort}. The neighbourhood pairwise correlation ensures that the correlation between two antennas for each location is measuring the reflection from the same scatterer, because of the short distance between two neighbouring antennas. The distance between neighbouring antenna of 20 ± 5 mm is used, which offers a trade-off between effective performance and algorithm complexity. If this distance is too small, more antennas will be needed to accommodate the entire breast model (see Fig. 4.1). Accordingly, more signals will needed to be processed, increasing algorithm complexity as a result. If this distance is too large, the signals received at neighbouring antennas might be dominated by the backscattering from different scatterers in heterogeneous dense breast, which could suppress the efficacy of pairwise neighbourhood correlation measurement.

Considering the useful tumour response contained in signals from different propagation channels varies, depending on tumour locations, skin thickness variations, differences in antenna-skin distances, and interfering response from other tissues, the selective multiplication of the maximum half coefficients is used. This mechanism implements an adaptive combination of antenna pairs, which guarantees the introduced weight can focus on those

strongest scatterers, regardless of their positions. Considering malignant tumours's higher scattering cross-sections relative to comparably sized heterogeneity in normal breast tissue [40], wf_l adaptively rewards potential tumour locations with a high weighted value, thereby enhancing tumour identification in most if not all cases.

Step 3: The last step calculates the intensity for the lth location. Although the maxima of coherent addition of time-shifted signals may no longer exactly correspond to tumour location in dense breast, the sum still has a relatively high value at tumour locations, since signals from some, if not all antennas, are still able to add coherently. The constructed signal $C_l(n)$ in RAR is therefore

$$C_l(n) = wf_l \cdot Sum_l(n). \tag{4.10}$$

Let I_l denote the intensity of location l within a desired imaging area, and it is given by

$$I_l = \sum_{n=1}^{\alpha} [C_l(n)]^2. \tag{4.11}$$

The procedure is repeated for every location within imaging region as shown in Fig. 4.4, and L loops in total are required. The distribution of intensity at each location I_l is displayed as an image. The pairwise correlation in the proposed RAR algorithm measures the backscattered energy intensity from scatterers at each location. The combination of neighbouring antennas ensures that the strong reflection received at each neighbourhood antenna pair is from the same strong scatterer, considering possible multi-scatterer cases. The maximum combining of correlation coefficients implements an adaptive selection of neighbourhood paired antennas, only those that have high correlation can contribute to the weight factor, yielding a flexible beamforming. The efficacy and robustness of RAR are demonstrated under a variety of challenging scenarios, where non-perfect artefact removal and in breasts with varied levels of fibro-glandular tissues are considered, and these are presented in the following sections.

4.5 Software Environment and Implementation

4.5.1 Software Environment

RAR is implemented in Matlab R2014a on a PC with Intel (R) Core (TM) 2 Duo CPU E7500 2.93 GHz (2 CPUS). As a widely used high-level scientific computing language, Matlab enables a range of matrix and vector computations with great flexibility. Additional convenience is offered by its integrated visualised development environment. In the simulation, 48 signals with 1500 sampling points in each signal are processed, where a time window length α of 294 is employed. Thus, $A = 48$, $K = 1500$, and $\alpha = 294$. The pseudocode as well as Matlab code for implementing RAR are given in next subsection.

4.5.2 Implementation

Three modules are involved in RAR's implementation, including environment initialisation, pre-processing for artefact removal, and kernel calculation of pixel intensity for forming imaging matrix. This is illustrated in Pseudocode 4.2 and Matlab code in Fig. 4.5 and Appendix A, and details are explained as follows.

Module 1: Environment initialisation. In this module, the time delay of all antenna-pixel pairs are computed, which is used for time-shifting signals. To this end, antenna coordinates, estimated average dielectric property of breast, and the limit of desired imaging region are needed. The antenna coordinate is stored in variable *ant_pos_cor*, and there are 48 antennas in total. The average dielectric property of breast ε_{r_ave} is estimated by an appropriate patient-specific dielectric property estimation algorithm such as the one developed by Winters *et al.* [205]. The desired imaging area is composed of L pixels, and the intensity of each pixel will be computed. The time delay τ_{il} between each antenna and pixel is calculated based on their space coordinates and the estimated propagation velocity with the breast. The Matlab code of this module is displayed in Fig. 4.5(a).

Module 2: Pre-processing for artefact removal. This module loads the collected signals $S_{i\_raw}(n)$ and applies certain method to remove the early-stage artefact. The artefact can be removed through the ideal method [see Equ. (4.3)] or more practical algorithms as

Pseudocode 4.2 Calculate the intensity of pixel I_l (l=1,2,...,L) with RAR

1: *Module 1: Environment initialisation*

2: Set *ant_cor_mat* % Antenna coordinate matrix
3: Calculate ε_{r_ave} % Estimate average permittivity of breast
4: Set L % Number of pixels of desired imaging area
5: Calculate τ_{il} % Time delay of all antenna-pixel pairs

6: *Module 2: Pre-processing for artefact removal*

7: Obtain $S_{i\_raw}(n)$, where $n = 1, ..., K$ % Load A sets of collected signals
8: Obtain $S_i(n)$, where $n = 1, ..., K$% Obtain A sets of artefact-removed signals

9: *Module 3: Kernel calculation of pixel intensity for forming imaging matrix*

10: Obtain $S_i(n+\tau_{il})$, where $n = 1, \ldots, \alpha$ % Time-shifting and windowing of signals
11: for l = 1 to L do % lth pixel of L
12: for i = 1 to A do % ith signal of A
13: $r_{i,j\_l} = corr[X_i(n), X_j(n)]$ % Pairwise correlation coefficient (4.5)
14: $P_l(i) = r_{i,j\_l}$ % Coefficient vector (5.11)
15: end for i % End of iteration of signal
16: $P_{l\_Nor} = (P_l + 1)/2$ % Normalised vector (4.7)
17: $P_{l\_Sort} = [R_{1l}\, R_{2l}\, ...\, R_{(A-1)\_l}]$ % Sorted vector (5.15)
18: $wf_l = \prod_{i=1}^{i=\frac{A-1}{2}} R_{i\_l}$ % Weight factor at l (5.16)
19: $Sum_l(n) = \sum_{i=1}^{A} S_i(n+\tau_{il})$ % Sum of time-shifted signals (4.4)
20: $C_l(n) = wf_l \cdot Sum_l(n)$ % Weighted sum of shifted signals (5.17)
21: $I_l = \sum_{n=1}^{\alpha} [C_l(n)]^2$ % Intensity at l (5.18)
22: end for l % End of iteration of pixels
23: Store: $I_1, I_2, ..., I_L$ % Store intensity of all pixels

introduced in [151]. The artefact-removed signals are denoted as $S_i(n)$, where $i = 1, ..., A$. The Matlab code of this module is displayed in Fig. 4.5(b), and the entropy-based artefact removal [155] is used in the example provided.

Module 3: Calculate and store pixel intensity for forming imaging matrix. This module calculates the intensity of each pixel within the imaging area. Firstly, signals are time-shifted for phase compensation. The time-shifted signal is then truncated by time window W_α, obtaining $S_i(n+\tau_{il})$, where $n = 1, \ldots, \alpha$. The correlation of time-shifted signals for neighbourhood pairwise antennas is calculated through (4.5), which is shown in line 13 of the pseudocode. The coefficient vector $P_l(i)$ is then be normalised and sorted for maximum combining. The product of half number of those highest correlation coefficients is used as the weight factor wf_l (line 18). Based on the weighted sum of time-shifted signals (line 20

of pseudocode), the intensity of pixel I_l is calculated through (5.18). In the last step (line 23), the intensity of each pixel I_l is stored for further analysis, and corresponding Matlab code for this module is shown in Fig. 4.5(c).

```
function [ output_args ] = Untitled( input_args )
%%% ********[Environment initialisation]********
%********[Antenna coordinate]********
ant_pos_cor(1,1) = {[80,39,101]};ant_pos_cor(1,2) = {[80,50,120]};ant_pos_cor(1,3) = {[80,63,140]};ant_pos_cor(1,4) = {[80,82,153]};
ant_pos_cor(1,5) = {[80,100,158]};ant_pos_cor(1,6) = {[80,116,159]};ant_pos_cor(1,7) = {[80,131,158]};ant_pos_cor(1,8) = {[80,147,154]};
ant_pos_cor(1,9) = {[80,162,145]};ant_pos_cor(1,10) = {[80,174,132]};ant_pos_cor(1,11) = {[80,185,116]};ant_pos_cor(1,12) = {[80,188,97]};
ant_pos_cor(1,13) = {[80,186,74]};ant_pos_cor(1,14) = {[80,178,56]};ant_pos_cor(1,15) = {[80,166,47]};ant_pos_cor(1,16) = {[80,152,39]};
ant_pos_cor(1,17) = {[80,135,34]};ant_pos_cor(1,18) = {[80,119,31]};ant_pos_cor(1,19) = {[80,103,31]};ant_pos_cor(1,20) = {[80,84,38]};
ant_pos_cor(1,21) = {[80,71,44]};ant_pos_cor(1,22) = {[80,59,55]};ant_pos_cor(1,23) = {[80,49,69]};ant_pos_cor(1,24) = {[80,45,83]};
ant_pos_cor(1,25) = {[130,39,101]};ant_pos_cor(1,26) = {[130,50,120]};ant_pos_cor(1,27) = {[130,63,140]};ant_pos_cor(1,28) = {[130,82,153]};
ant_pos_cor(1,29) = {[130,100,158]};ant_pos_cor(1,30) = {[130,116,159]};ant_pos_cor(1,31) = {[130,131,158]};ant_pos_cor(1,32) = {[130,147,154]};
ant_pos_cor(1,33) = {[130,162,145]};ant_pos_cor(1,34) = {[130,174,132]};ant_pos_cor(1,35) = {[130,185,116]};ant_pos_cor(1,36) = {[130,192,97]};
ant_pos_cor(1,37) = {[130,189,74]};ant_pos_cor(1,38) = {[130,178,56]};ant_pos_cor(1,39) = {[130,166,47]};ant_pos_cor(1,40) = {[130,152,39]};
ant_pos_cor(1,41) = {[130,135,34]};ant_pos_cor(1,42) = {[130,119,31]};ant_pos_cor(1,43) = {[130,103,31]};ant_pos_cor(1,44) = {[130,84,38]};
ant_pos_cor(1,45) = {[130,71,44]};ant_pos_cor(1,46) = {[130,59,55]};ant_pos_cor(1,47) = {[130,43,69]};ant_pos_cor(1,48) = {[130,37,83]};
%********[Setting and time delay calculation]********
M = 48;                          % Number of antennas;
vfreespace = 2.99792458e11;      % Speed of light in free space,millionmeter/s;
immer_epsr = 4.3284; skin_epsr = 34.08; % Fatty-2 = immesive liquid, the epsr at center freq (6.85 GHz);
vbre = vfreespace/sqrt(immer_epsr);vskin = vfreespace/sqrt(skin_epsr); % Propagation velocity of EM wave in breast and skin tissues;unit: mm/s;
skin_time = 2*1.5/vskin; basistimeslot = 1.9066e-12; TotalTimeDelay = cell(1,M);% Number of time delay group; for Mono-static;
cro_sec_cor_x = 95;imagerow = 130; imagecol = 100;% 2D Cross-section imaging area;
img_row_start = 55;img_row_end = 184;img_col_start = 45;img_col_end = 144;timedelay = zeros(imagerow,imagecol);% Limits of imaging area;
for cur_ant = 1 : M              % Calculate the 48 sets of theoretical time delay, between the desired imaging plane and each antenna;
    ant_pos_cell = ant_pos_cor(1,cur_ant);ant_pos_mat = cell2mat(ant_pos_cell);
    Tx = ant_pos_mat(1,1);Ty = ant_pos_mat(1,2);Tz = ant_pos_mat(1,3);
    for i = img_row_start:img_row_end
        for j = img_col_start:img_col_end
            d = 2*sqrt((cro_sec_cor_x - Tx)^2 + (i - Ty)^2 + (j - Tz)^2);temptimedelay = (d - 2*1.5)/vbre;%Round-trip time delay;
            tempx = i - 54;tempy = j - 44;timedelay(tempx,tempy) =  temptimedelay + skin_time;
        end
    end
    TotalTimeDelay(1,cur_ant) = {timedelay};%Store time delay matrix;
end
```

(a) Environment initialisation

```
%%% ********[Pre-processing for artefact removal]********
TimeWindowNum_pusewidth = round(0.56e-9/basistimeslot);
Ratio_TimeWindow_Pulsewidth = 1;
TimeWindowNum1 = Ratio_TimeWindow_Pulsewidth*TimeWindowNum_pusewidth;
TimeWindowUsing = TimeWindowNum1;
for i = 1 : M
    rawdata_name = ['output/A',num2str(i), '_with_E_sig','.txt'];RawData = load(rawdata_name); TotalRawData(1,i) = {RawData};
end
[RawDataRowNum,b] = size(RawData);alltime =  RawData(:,1);
Ideal_sign = 0;%"1": Ideal; "0":Entropy, Choose code running mode;
if(Ideal_sign == 1)
    run_mode = 'Ideal';TotalRawData = TotalRawData;
else
    run_mode = 'Entropy';
%********[Entroy-based artefact removal]********
entropy_truncate_time1 = 0.66*1e-9;entropy_truncate_time2 = 0.66*1e-9;
for i = 1:M
    if(i > 24)
        truncate_time = entropy_truncate_time2;
    else
        truncate_time = entropy_truncate_time1
    end
    truncate_time_mat_start(1,i) = truncate_time;
end
for i = 1:M
    data = TotalRawData{1,i};truncate_time = truncate_time_mat_start(i); truncate_num = round(trucate_time/basistimeslot);
    val = data(:,2);val(1:truncate_num) = 0;data(:,2) = val; TotalRawData(1,i) = {data};
end
end
```

(b) Pre-processing for artefact removal

```
%%% ********[Kernel calculation of pixel intensity for forming the imaging matrix]********
Intensity1 = zeros(imagerow,imagecol);% Memory allocation;
for i = 1: imagerow
    for j = 1: imagecol
        shifted_sig_mat = zeros(TimeWindowUsing,M);SumofShiftedData = zeros(TimeWindowUsing,1);% Zeroing clearing;
        for k = 1:M
            timedelaygroup = TotalTimeDelay{1,k};timedelay = timedelaygroup(i,j);% Get the desired focal point's time delay;
            RawData = TotalRawData{1,k};res = mytimeshift(RawData,timedelay,basistimeslot);
            s1 = res(:,2);s_truncated = s1(1:TimeWindowUsing);shifted_sig_mat(:,k) = s_truncated;
        end
        SumofShiftedData = sum(shifted_sig_mat,2); % Sum of all time-shifted signals;
        %*********[Neighbourhood pairwise correlation]*********
        pair_nei_ind = 1;% Index initialisation;
        for k = 1: M-1
            s1 = shifted_sig_mat(:,k);s2 = shifted_sig_mat(:,k+1);
            the_cor = mycoreff(s1,s2,TimeWindowUsing);pair_neibour_cor_mat_all(1,pair_nei_ind) = the_cor;pair_nei_ind = pair_nei_ind + 1;
        end

        pair_neibour_cor_mat_all = (pair_neibour_cor_mat_all + 1)/2;% Normalise coefficients;
        pair_neibour_cor_mat_all_sort = sort(pair_neibour_cor_mat_all,'descend');% Sort coefficients;
        %*********[Maximum combining]*********
        num = 0.5*length(pair_neibour_cor_mat_all_sort);pair_neibour_cor_mat_all_sort_using = pair_neibour_cor_mat_all_sort(1:num);
        prod_pair_nei = prod(pair_neibour_cor_mat_all_sort_using);SumofShiftedData_weighted = prod_pair_nei*SumofShiftedData;
        Intensity1(i,j) = sum(SumofShiftedData_weighted.^2);
        %************************************************END
    end
end
%********[Store imaging matrix]********
save('S6_RAR.mat','Intensity1');

end
```

(c) Calculate and store pixel intensity

Fig. 4.5 Matlab Code for implementing RAR. (a) Environment initialisation. (b) Pre-processing for artefact removal. (c) Calculate pixel intensity for forming imaging matrix.

4.6 Imaging Results and Discussion of RAR and Comparisons

In this section, algorithm performance is analysed in depth. The superiority of RAR is demonstrated via comparisons with four techniques, including DAS, DMAS, MWDAS, and FDAS. For completeness, all algorithms were evaluated in breast models with varied structures, density classifications, and tumour positions.

Serving as benchmark of best algorithm performance, the ideal artefact removal (see Fig. 4.6) for obtaining clear tumour response was applied. Noted that the tumour response indicated by the dotted box in Fig. 4.6(c), which exists in later time, is totally obscured in received signals in Fig. 4.6(a). This is due to its small order of magnitude, especially compared with that of incident signals and skin reflections appear earlier. The small order of magnitude for tumour response peak with 1e-5 is a relative value (rather than absolute value) compared to the input signal peak of an order magnitude of 1, obtaining the peak energy ratio of tumour response with -100 dB (input signal magnitude is used as a reference point). The magnitude of tumour response can be affected by various factors such as input signal magnitude, breast density, transmitting and receiving antenna position, and tumour size and position. To ensure such weak tumour response can be effectively captured, increase transmitting power (under regulated power limit) and/or improve receiver sensitivity should be considered in practice.

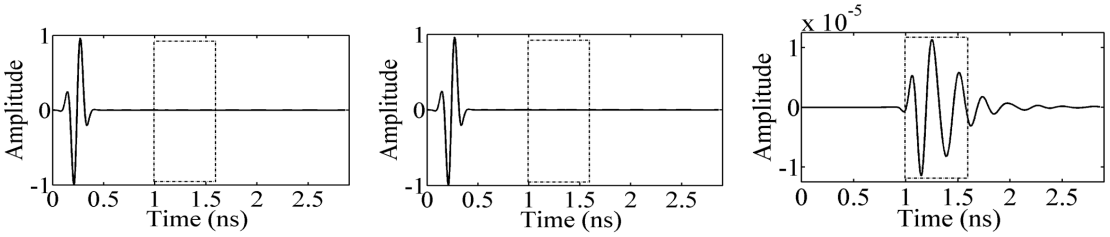

(a) From tumour-bearing breast (b) From tumour-free breast (c) Tumour Response

Fig. 4.6 Illustration of ideal artefact removal. (a) Signal recorded at antenna 4 of Fig. 4.1. A tumour with a 10 mm diameter is placed at (x, y, z) = (95, 99, 112). (b) Signal recorded at antenna 4 from a tumour-free reference breast model. (c) Pure tumour response obtained by subtracting (b) from (a).

All constructed images were normalised to the maximum intensity value of the 3-D volume, and same datasets were applied for all algorithms. To assess algorithm performance, two quantitative metrics were applied, which are signal-to-clutter ratio (SCR) and signal-to-mean ratio (SMR) [50]. SCR was defined as the ratio of the maximum tumour response to the maximum clutter response in a same image, whereas SMR was defined as the ratio of the mean tumour response to the mean response of the whole image. The maximum or mean tumour response was assumed to be the peak or average energy of an area defined by twice the physical extent of the tumour [50], whereas the clutter response was those outside this area. SCR defines the difference between tumour and clutter response, whereas SMR indicates the image contrast between tumour and non-tumour areas.

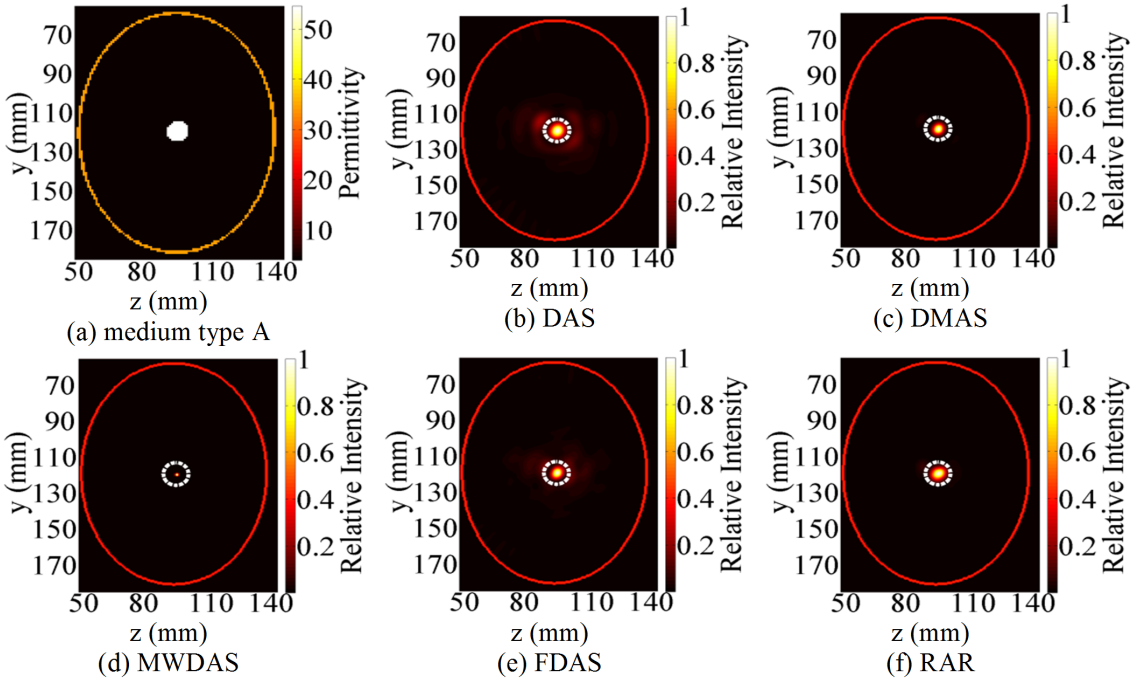

Fig. 4.7 (a) 2-D slice of breast model with MT A. (b)–(f) Results of imaging algorithms with ideal artefact removal. Tumour's actual position is indicated by dotted circles.

Fig. 4.7 presents the constructed images produced by the five techniques, representing a distribution of energy resulted from each voxel within the breast model. The peak of this image is usually regarded as the tumour, which has the strongest reflection among all heterogeneous breast tissues with a comparable size [40]. It can be seen that the embedded 10 mm diameter tumour is clearly identified and accurately localised by all approaches. However, the clutter rejection capability of these techniques varies due to the

different weighting mechanisms employed. Specifically, the image constructed by DAS [see Fig. 4.7(b)] is filled with the strongest level of clutter, which is indicated by the smallest SCR of 7.0 dB (see Table 4.2). This shows its limited capability for discriminating against clutter since it does not account for any dispersive propagation effect. The result of FDAS [see Fig. 4.7(e)] is slightly cleaner than that of DAS, which validates the effectiveness of the filtering process, but its performance is still inferior to the other three algorithms. It is observed that DMAS, MWDAS, and the proposed RAR algorithm provided almost clutter-free images [see Fig. 4.7(c), (d), and (f)]. Assuming perfect tumour response could be captured, the cross multiplying of weighted tumour response from all channels in MWDAS forms particularly high weights [see Fig. 4.7(d)], which achieved the strongest clutter rejection with a SCR of 415.6 dB in this case.

4.6.1 Breast of Medium Type A and B with Ideal Artefact Removal

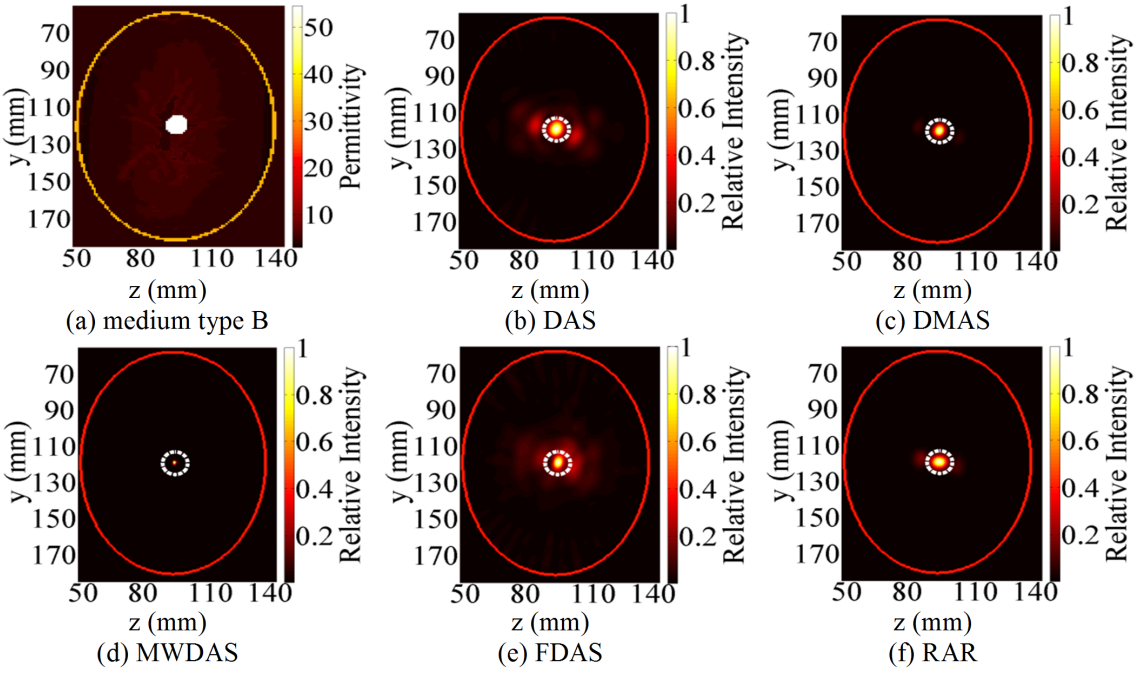

Fig. 4.8 (a) 2-D slice of breast model with MT B. (b)–(f) Results of imaging algorithms with ideal artefact removal. Tumour's actual position is indicated by dotted circles.

Imaging results presented in Fig. 4.8 employs the same ideal artefact removal method as in Fig.4.7, but the breast medium type is changed from homogeneous fatty to heterogeneous fatty [see Fig. 4.8(a)], in which three different types of adipose tissues, fatty-low, fatty-

Table 4.2 SCR and SMR of algorithms in different scenarios. "Ave" abbreviates for average, which is the arithmetic mean of SCR and SMR values in ten different scenarios. Best results of each case are highlighted in **Bold**.

	Fig. 4.7	Fig. 4.8	Fig. 4.10	Fig. 4.11	Fig. 4.12	
			SCR(dB)			
(b)DAS	7.0	5.0	-11.9	-2.3	-3.6	
(c)DMAS	14.9	10.8	-25.9	-4.6	-5.6	
(d)MWDAS	**415.6**	**403.3**	-728.1	-78.5	-107.5	
(e)FDAS	11.4	6.8	-17.9	1.3	-4.2	
(f)RAR	14.0	8.5	**5.3**	**4.8**	**4.0**	
			SMR(dB)			
(b)DAS	17.2	17.0	-1.9	7.6	7.0	
(c)DMAS	20.8	20.3	-12.4	7.3	7.1	
(d)MWDAS	**21.1**	**21.1**	-705.3	-56.5	-90.0	
(e)FDAS	17.2	16.5	-2.9	11.6	9.0	
(f)RAR	21.0	20.7	**20.1**	**17.1**	**14.3**	
	Fig. 4.13	Fig. 4.14	Fig. 4.15	Fig. 4.16	Fig. 4.17	Ave
			SCR(dB)			
(b)DAS	-6.5	-1.8	-2.5	-0.7	-2.8	-2.0
(c)DMAS	-12.3	-0.5	-4.6	-2.45	-5.3	-3.5
(d)MWDAS	-306.5	-40.1	-87.2	-17.9	-129.5	-67.6
(e)FDAS	-11.9	0.1	-1.6	-0.3	-0.5	-1.7
(f)RAR	**3.9**	**0.5**	**0.1**	**0.05**	**-0.3**	**4.1**
			SMR(dB)			
(b)DAS	2.6	9.5	7.0	9.1	5.6	8.1
(c)DMAS	-3.1	11.1	6.6	11.1	5.5	7.4
(d)MWDAS	-285.3	-61.8	-65.0	-3.3	-114.1	-133.9
(e)FDAS	1.1	10.7	9.2	11.0	8.3	9.2
(f)RAR	**18.2**	**11.4**	**16.0**	**17.3**	**9.2**	**16.5**

median, and fatty-high are included. With increased heterogeneity, more dispersion of received signals is expected, due to the increased propagation behaviour difference of frequency components among various tissues. Furthermore, the estimated average propagation velocity might not as well represent the actual speed as in the homogeneous case, leading to a mismatch between estimated and the actual propagation time delay. This is reflected by the results. Compared with Fig. 4.7(b) and Fig. 4.8(b), which are both the results of DAS, more clutter outside the circle is observed, corresponding to a 2.0 dB decrease of SCR. The same trend applies for all the algorithms considered. Although with

a slight degradation in terms of clutter suppression, the embedded tumour is noticeably recognised and accurately localised in all images constructed by the five techniques. This also indicates certain fault tolerance of these algorithms for inaccurate propagation time delay estimation.

4.6.2 Breast of Medium Type B with Entropy Artefact Removal

Previous results show that all algorithms present decent tumour identification and localisation capabilities, regardless of homogeneous or heterogeneous breasts, assuming the tumour response could be ideally extracted. However, perfect artefact removal is unlikely in practical situations, it is thus critical to test algorithm performance in scenarios applying more realistic artefact removal methods. In this section, combining one of the most effective practical artefact removal methods, the performance of imaging algorithms are tested in mildly, moderately, and severely dense breast models, respectively.

The artefact is a mixed signal composed of incident signals and skin-fat interface reflections, thus pure tumour response can be difficult to recover. Even the state-of-the-art artefact removal algorithm is unable to completely remove this interference. However, desired tumour response could be easily obscured by the artefact, which has a much higher order of magnitude, especially when tumour has a relatively small size. All these poses a great challenge to imaging algorithms.

Based on the latest review study provided in [151], which evaluated seven different artefact removal methods, the best two are the Wiener Filter [40] and entropy-based window truncation [155]. The correlation measurement between recovered tumour response by these two techniques and perfect tumour response are 0.66 and 0.60 (ranging from 0 to 1), respectively. In Wiener Filters, the artefact in each propagation channel is estimated as a filtered combination of the signals from all other channels, then the estimated artefact is subtracted from the signal received at the chosen channel. Wiener Filter can remove most of artefact signals. However, this method requires the prior knowledge of the time interval in which only artefact is included. Moreover, distortion is introduced to tumour response, which might result in tumour location bias. By contrast, the entropy-based

method introduces zero distortion to tumour response, has higher computational efficiency, and does not require any prior information. Hence, given both efficacy and efficiency, the entropy-based artefact removal method is chosen as for the following study as in [206, 207]

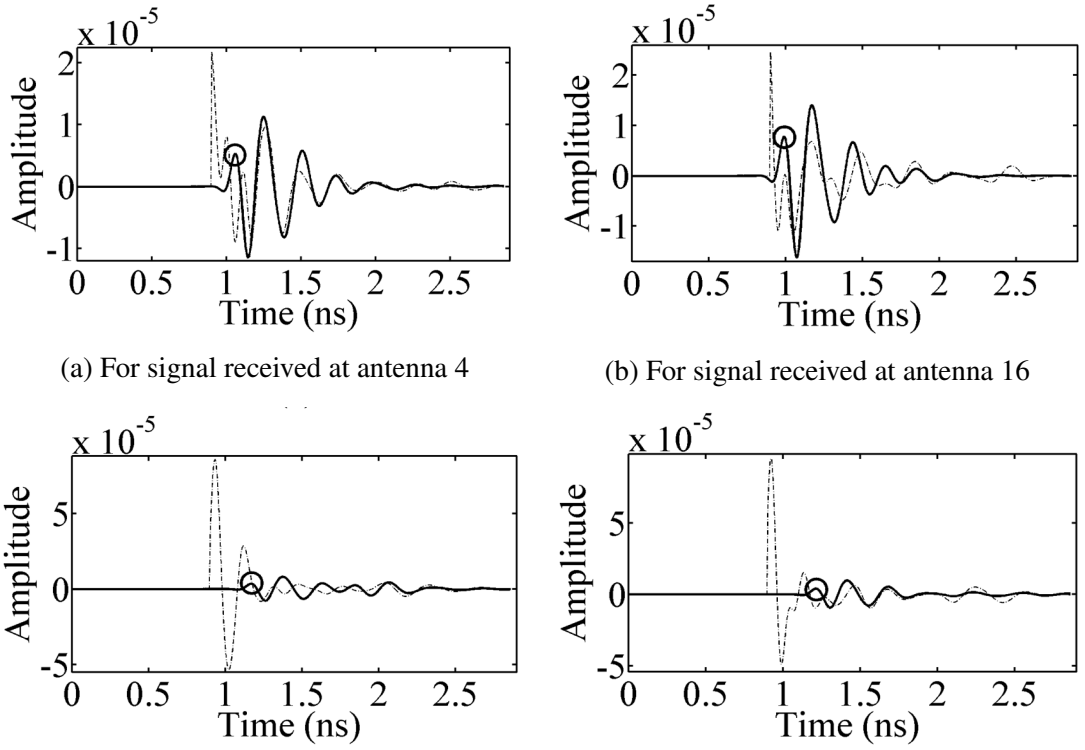

(a) For signal received at antenna 4

(b) For signal received at antenna 16

(c) For signal received at antenna 33

(d) For signal received at antenna 46

Fig. 4.9 (a)-(d) represent the pre-processed signals received at antenna 4, 16, 33, and 46 as numbered in Fig. 4.1, exemplifying the performance difference between artefact removal methods. The solid and dotted curves are the results based on ideal and entropy-based method for artefact removal, respectively. The circle indicates where tumour response is expected to appear. A tumour with 10 mm diameter is placed at (x, y, z) = (95, 99, 112) of the model shown in Fig. 4.1.

Fig. 4.9 illustrates the entropy-based time window truncation for artefact removal. The ideal tumour response at antenna 4 is shown as the solid curve in Fig. 4.9(a). Comparing the actually received signal [see Fig. 4.6(a)] with the entropy-truncated signal shown as the dotted curve in Fig. 4.9(a), it is noted that this method removes the majority of the early-stage artefact composed of incident signals and skin-fat reflections, which have several higher orders of magnitude than the tumour response. As shown in Fig. 4.6(a), the tumour response that has an order of magnitude of 1e-5 is completely overwhelmed. This effectiveness can also be noticed at antenna 16 [see Fig. 4.9(b)], where almost all artefact is removed and no obvious distortion is imported, compared with the ideal tumour response

within the time period of 1.0 to 1.5 (ns). However, for antenna 33 and 46 [see Fig. 4.9(c) and (d)], there is still a large amount of residual artefact with high amplitude. This is because one truncation time window with the same length is used for the signals received at all antennas [155]. Hence, depending on the tumour-antenna distance, truncated signals of different antennas could contain varied percentages of useful tumour response versus residual artefact, which could potentially lead to location bias in constructed images.

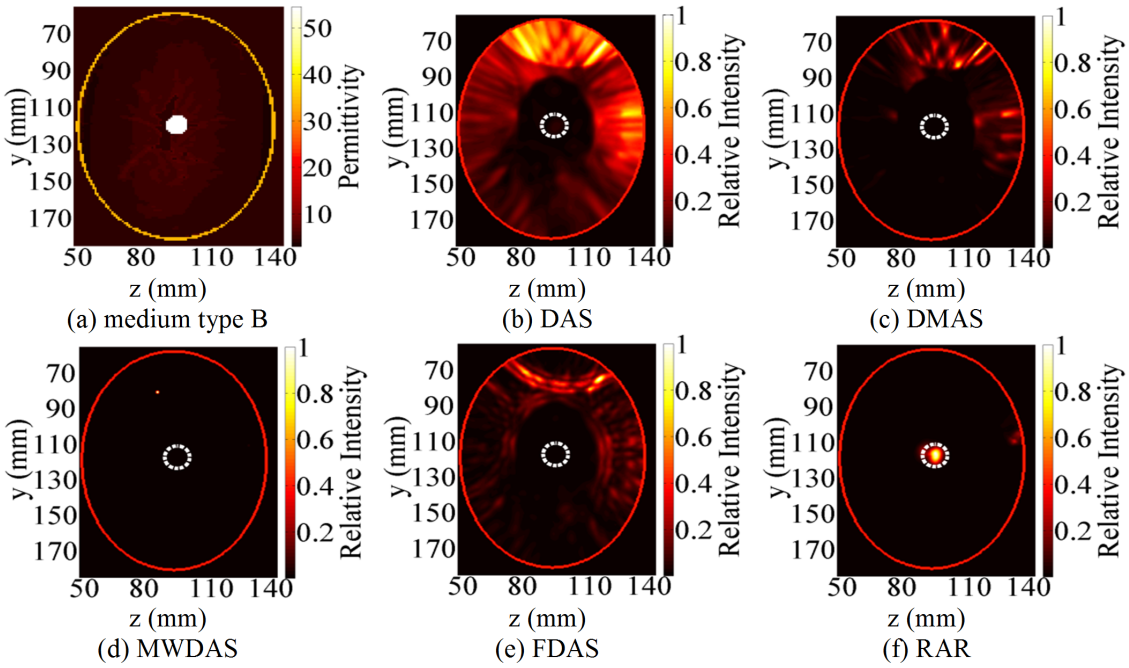

Fig. 4.10 (a) 2-D slice of breast model with MT B. (b)–(f) Results of imaging algorithms with entropy artefact removal. Tumour's actual position is indicated by dotted circles.

Fig. 4.10 displays the imaging results where using the same MT B as in Fig. 4.8. However, instead of using ideal artefact removal, entropy-based method is applied. Compared with Fig. 4.8, it is noticed that the performance of DAS, DMAS, MWDAS, and FDAS suffers significantly. The result of DAS [see Fig. 4.10(b)] is seriously unrecognisable, only an area with high intensity is observed. However, none of these high-intensity positions reveal the actual tumour location, which is indicated by the dotted circle. Although the results of DMAS, MWDAS, and FDAS [see Fig. 4.10(c)-(e)] only show limited focused areas, the peaks of these images are all far away from the actual tumour position. In contrast, the tumour is conspicuously shown at correct location in the image constructed by RAR [see Fig. 4.10(f)]. This demonstrates the robust performance of RAR even if the

artefact cannot be removed faultlessly. Specifically, the SCR of DAS, DMAS, MWDAS, FDAS, and RAR are -11.9, -25.9, -728.1, -17.9, and 5.3 dB, respectively. The positive SCR of RAR signifies that it is the only algorithm reveals the tumour with correct location, which illustrates its clear advantage of excellent artefact resistance. These results also prove that the effective artefact removal is vital for producing useful imaging results, even for breasts with relatively low heterogeneity.

The reason behind RAR's robustness lies in the fact that except RAR, all other algorithms simply exploit the amplitude information of time-shifted signals, expecting that the maximum coherent addition or multiplication could occur at tumour locations. According to previous results, this is indeed the case when tumour response can be perfectly extracted, and all algorithms can perform well. Nevertheless, when artefact cannot be removed effectively, it is very likely that at some non-tumour positions, only the artefact from one propagation channel can be greater than the coherent sum of tumour responses from all other channels, due to the different orders of magnitude between artefact and tumour response. For RAR, in addition to utilising coherent addition of tumour response from various propagation channels, it also explores the phase coherence between signals.

The introduced adaptive weight control mechanism of RAR ensures its robustness on two aspects. First, the neighbourhood pairwise correlation between all antennas measures the average coherence, which is less likely to be distorted by one or two artefact signals with abnormally large amplitude. This is because phase coherence is independent of signal amplitude, only the linear relationship between signal shapes affects correlation coefficients. Second, the maximum combining of pairwise correlation coefficients adaptively focuses on those position with large scattered energy. Considering the relatively high magnitude of scattered energy from tumours over other tissues, this maintains the capability of RAR in terms of localising tumours in most if not all cases with a much higher chance.

4.6.3 Breast of Medium Type C with Entropy Artefact Removal

Aside from artefact, it is agreed that fibro-glandular tissue forms another challenge for tumour detection. This is not only due to the substantial amount of attenuation and

dispersion to received signals introduced by glandular tissue, but also the small dielectric contrast between cancerous and glandular tissue could easily result in misidentification of glandular tissues as tumours. Thus, it is important to evaluate algorithm performance in such cases.

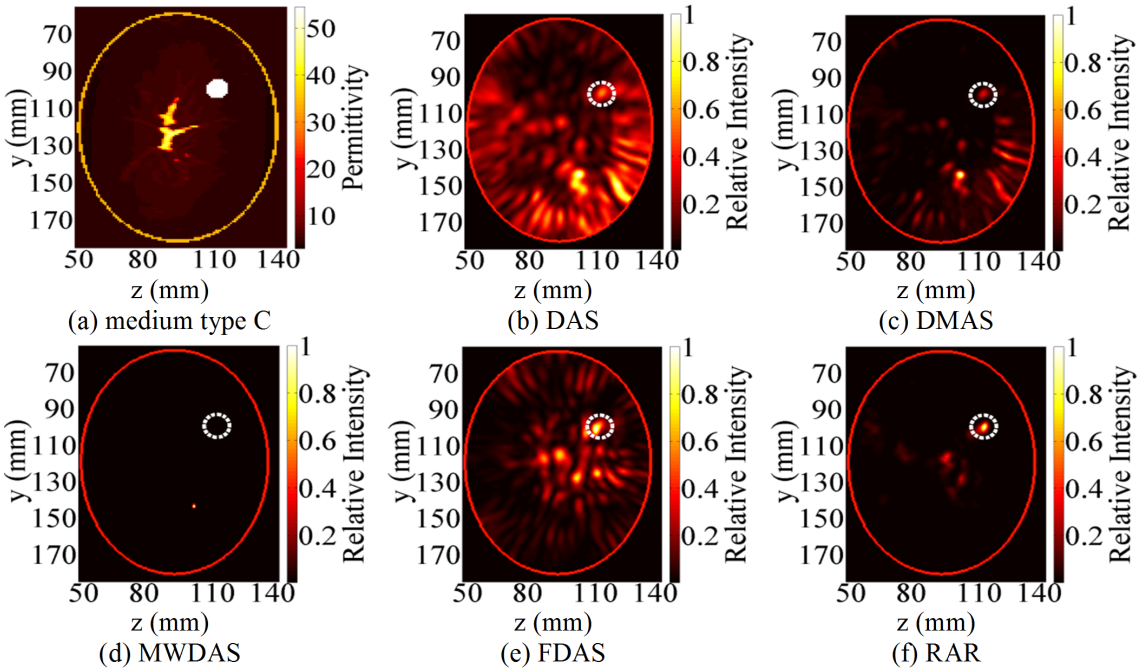

Fig. 4.11 (a) 2-D slice of breast model with MT C. (b)–(f) Results of imaging algorithms with ideal artefact removal. Tumour's actual position is indicated by dotted circles.

To independently assess algorithm performance for breast models with glandular tissues, the first case considered is assuming that the early-stage artefact is perfectly removed. Results shown in Fig. 4.11 are based on the collected signals from breast with MT C, where the same artefact removal used in [52] was applied, assuming the majority of early-stage artefact has been effectively removed. Results revealed that the presence of glandular tissue can seriously deteriorate the performance of algorithm, even assuming the early-stage artefact is perfectly removed. Compare Figs. 4.11(b) with Fig. 4.8(b), both using ideal artefact removal, it is observed that DAS failed to correctly localise the tumour in Fig. 4.11(b), where the presence of glandular tissues is considered. Although the actual tumour position indicated by the circle has a relatively high value, the peak of image no longer corresponds to tumour's position, which was the case in Fig. 4.8(b). This indicates limited detectability of DAS of separating the scattering from glandular

tissues and the scattering from the tumour. After combining signals from all propagation channels, the multi-reflections between tumour and glandular tissues could generate a higher intensity than those reflections from tumour or glandular tissues individually, which is indicated by the highest peak at bottom right of Fig. 4.11(b). Similar erroneous tumour locations are also offered by DMAS and MWDAS algorithms [see Fig. 4.11(c) and (d)]. Neither of them identified the tumour with correct location, indicating their vulnerability to the interference caused by glandular tissues. Despite clutter, the result of FDAS [see Fig. 4.11(e)] revealed the tumour correctly, which shows its advantage over DAS, DMAS, and MWDAS. This confirms the efficacy of compensating attenuation and dispersion provided by the filtering process used in FDAS. The result is consistent with its original presentation [52], whereas the slight difference is due to different percentages of glandular tissues contained in the breast models used. However, the best imaging result is provided by RAR [see Fig. 4.11(f)], which not only pinpoints the tumour accurately, but also provides the best clutter rejection. RAR ensures that high weights measured by correlation coefficients are obtained at tumour positions. After time-shifting signals at neighbouring antenna pairs for tumour and non-tumour positions, high correlation is obtained between tumour responses which resulted from the same strong scatterer, whereas low correlation is expected for those signals from other heterogeneous breast tissues. Thus, signals with high weights at tumour position generate larger intensities after being combined, thereby discriminating tumour response against glandular response. Comparing the results offered by FDAS and RAR [see Fig. 4.11(e) and (f)], although both identified the tumour, the clutter suppression capability varies considerably, and an improvement of SCR with 3.5 dB is offered by RAR. This is non-trivial, because the much more cleaner image offered by RAR can remarkably reduce the uncertainty of the existence of multi-tumours that are located near this region, which is greatly desirable in practice.

Undoubtedly, it is unrealistic to assume the early-stage artefact could be ideally removed, especially considering the enormous impact of artefact, which has been confirmed in the results displayed in Fig. 4.10. Therefore, combining entropy-based artefact removal method, the performance of algorithm for breasts with MT C is investigated and results

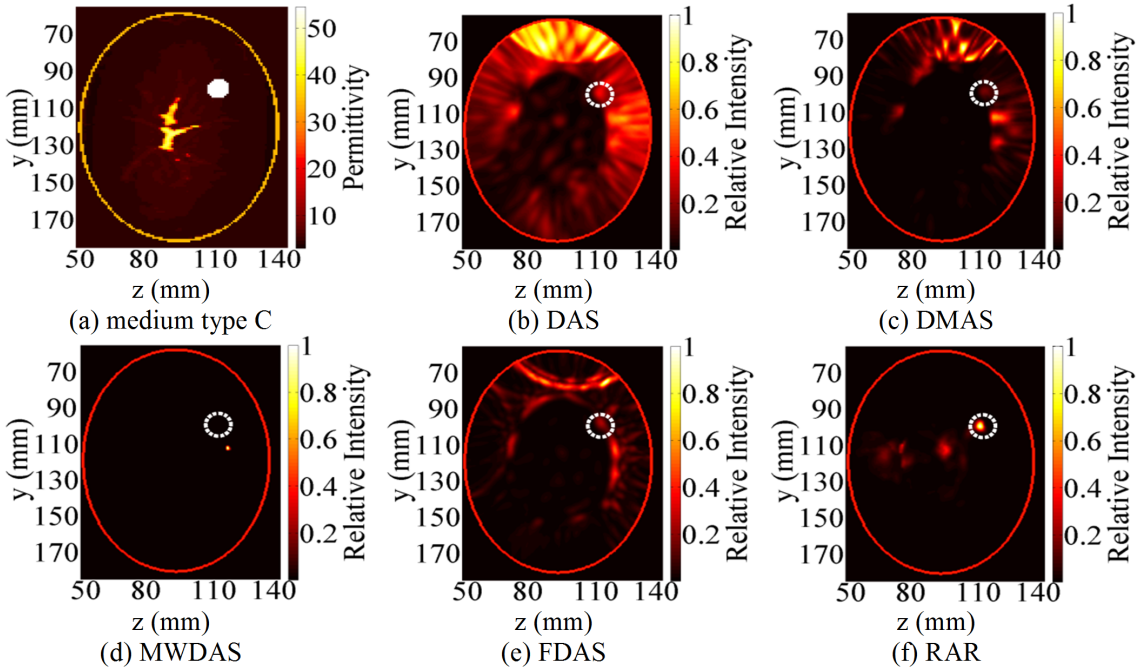

Fig. 4.12 (a) 2-D slice of breast model with MT C and a tumour away from glandular tissues. (b)–(f) Results of imaging algorithms with entropy artefact removal. Tumour's actual position is indicated by dotted circles.

are shown in Fig. 4.12. It is noticed that in this challenging scenario, RAR is the only algorithm reveals the tumour with correct location [see Fig. 4.12(f)], whereas with other four techniques, the tumour is either unidentifiable or with wrong estimated locations [see Fig. 4.12(b)-(e)]. Similar to results shown in Fig. 4.10, when the early-stage artefact cannot be effectively removed, the late-stage signals no matter tumour or glandular tissue response is totally masked by residual artefact, due to the vast difference of order of magnitudes. Even the filtering process introduced in FDAS is unable to be immune to this interference. This can be clearly illustrated by comparing Fig. 4.11(e) and Fig. 4.12(e), where ideal and entropy-based artefact removal methods are applied, respectively. These results once again confirm RAR's superiority over the other methods in terms of both strong artefact resistance and high detectability of distinguishing the scattering from tumour and from glandular tissues.

Since a high percentage of breast cancers are invasive ductal carcinomas, which start at fibro-glandular regions [106], it is worth testing algorithms in cases with tumours that are very close to or grow from glandular tissues. Fig. 4.13 shows a tumour located very close to glandular tissues. In the analysis of this case, the backscattered response from tumour

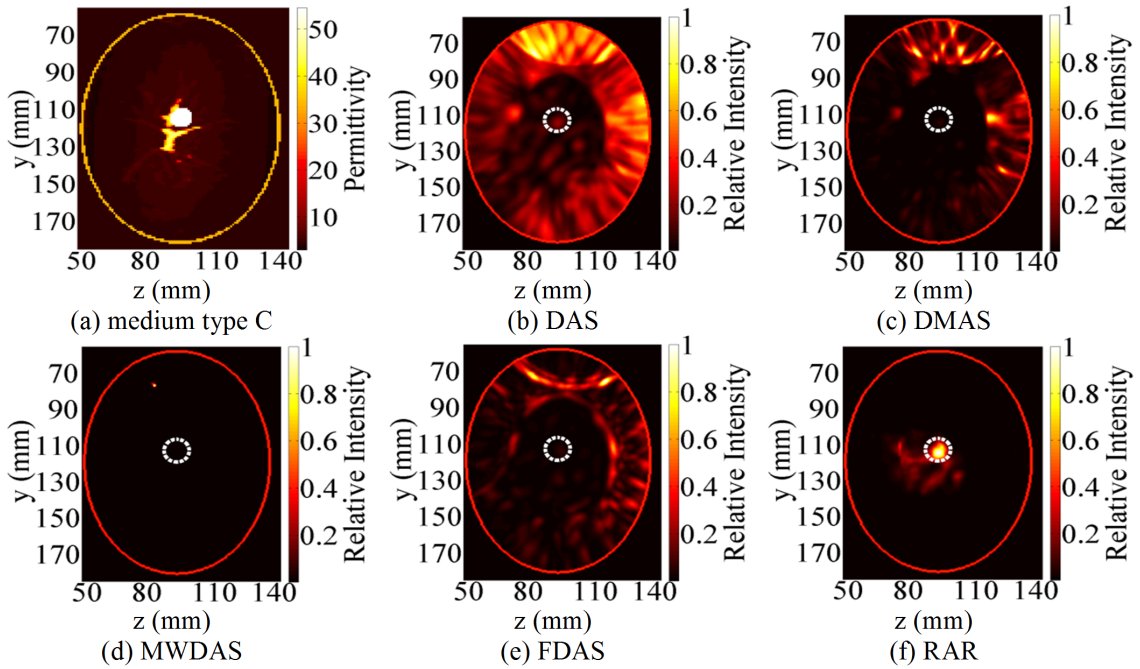

Fig. 4.13 (a) 2-D slice of breast model with MT C and a tumour close to glandular tissue. (b)–(f) Results of imaging algorithms with entropy artefact removal. Tumour's actual position is indicated by dotted circles.

and glandular tissue could easily overlap due to the small spacing, raising a challenge about the specificity of algorithms. Encouragingly, RAR is still able to localise the tumour correctly [see Fig. 4.13(f)], but with a decrease of SCR from 4.0 to 3.9 dB with respect to Fig. 4.12(f). The other four algorithms failed to do so, proving the efficacy of RAR for ductal carcinoma.

4.6.4 Breast of Medium Type D with Entropy Artefact Removal

So far, breasts with both homogeneous and heterogeneous structures and tumours at different positions have been considered. The breast models employed before are mildly dense, in which the fibro-glandular tissue is less than 25%. It should be considered that a high portion of fibro-glandular tissues could noticeably increase the density of breast and result in further signal attenuation. Therefore, for comprehensive analysis, moderately and severely dense breasts are used to test algorithms in following scenarios.

In Fig. 4.14, the breast model with MT D is employed. Although the percentage of glandular tissue for this type is normally between 25%-50%, which belongs to a moderately dense category, the randomly scattered glandular tissues could seriously reduce

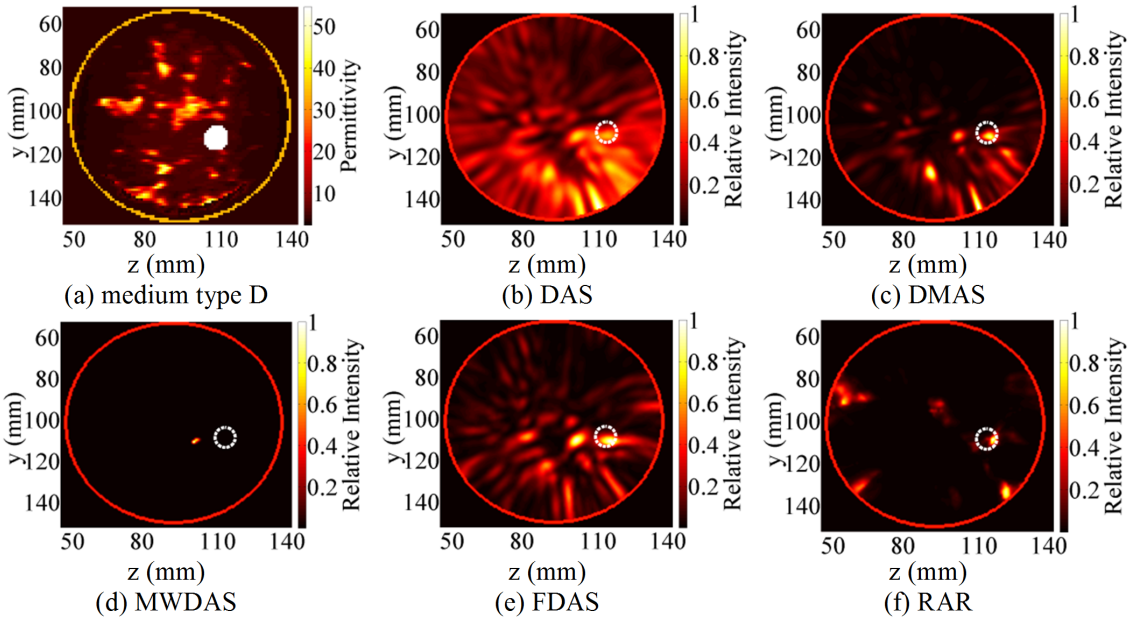

Fig. 4.14 (a) 2-D slice of breast model with MT D and an off-centre tumour. (b)–(f) Results of imaging algorithms with entropy artefact removal. Tumour's actual position is indicated by dotted circles.

the homogeneity of propagation channels and make the detection of tumour much more difficult. Based on the results shown in Fig. 4.14, it is clear that RAR is again the only method that correctly identified the tumour. However, strong scattered clutters are generated. Specifically, comparing Fig. 4.13(f) with Fig. 4.14(f), the SCR of RAR results

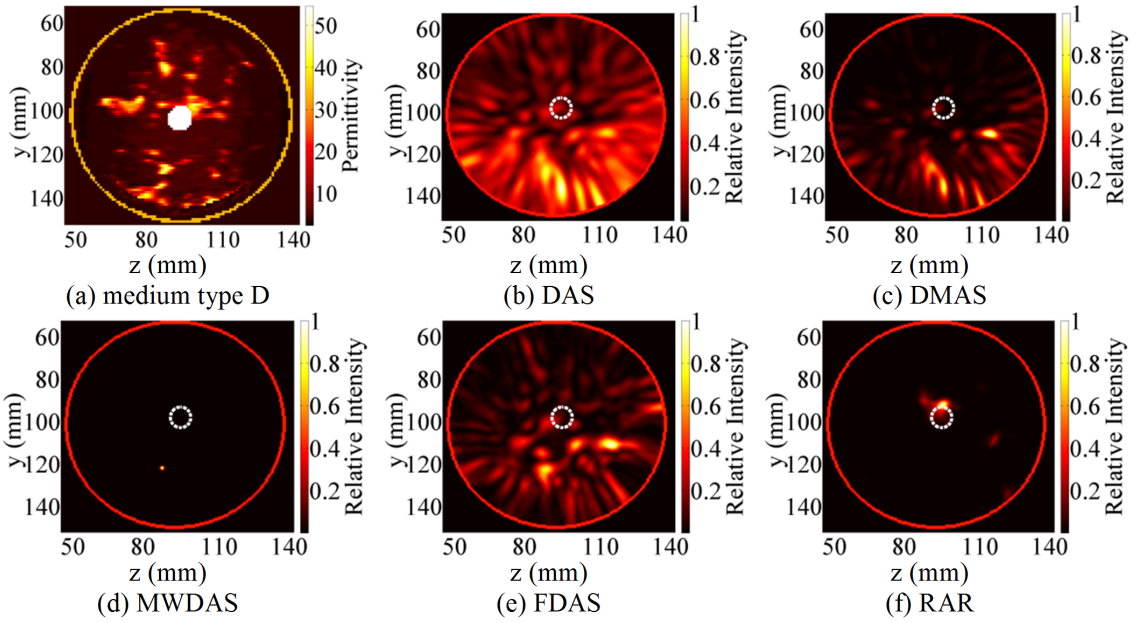

Fig. 4.15 (a) 2-D slice of breast model with MT D and an centre tumour close to glandular tissues. (b)–(f) Results of imaging algorithms with entropy artefact removal. Tumour's actual position is indicated by dotted circles.

dramatically decreased from 3.9 to 0.5 dB. This indicates that the increased glandular tissues not only cause the change of breast density and corresponding signal attenuation, it could also complicate the propagation channels, making the identification of strong scatterers such as tumours more difficult to be achieved.

The results shown in Fig. 4.15 employed the same breast model, but the tumour is moved within the scattered glandular tissues to simulate the invasive ductal carcinoma. In comparison to the results obtained in Fig. 4.14, the performance of algorithms in the scenario of Fig. 4.15 further degraded due to the further reduced uniformity of assumed propagation channel. Encouragingly, the proposed RAR algorithm in this case still kept its edge with a positive SCR of 0.1 dB (see Table 4.2), indicating its robustness to certain deviation between the assumed uniform propagation channel and the actual one.

4.6.5 Breast of Medium Type E and F with Entropy Artefact Removal

For completeness, the performance of algorithm in very dense breasts with MT E and F is also investigated. In Fig. 4.16, a tumour in breast model with MT E, which includes fibro-glandular tissues with percentage ranging from 50% to 75% is considered. It is noted that the result offered by RAR algorithm in Fig. 4.16(f) is the one with the highest SCR of 0.05 dB, whereas all others have a negative SCR, corresponding to poorer performance. Although the peak in the result of RAR does not exactly correspond to the actual tumour position indicated by the dotted circle, a relatively high intensity within the circle is observed. Also the peak generated by RAR is close to the actual tumour position, and this explains why RAR has a positive SCR value. However, when the breast model with MT F is considered (see Fig. 4.17), all algorithms failed, and none of them were able to provide images with discernible and correct tumour position. For both scenarios considered in Fig. 4.16 and Fig. 4.17, tumours located within fatty tissues instead of within glandular tissues are also tested. The results obtained were similar, which indicated the limited detectability of these algorithms for severely dense breasts.

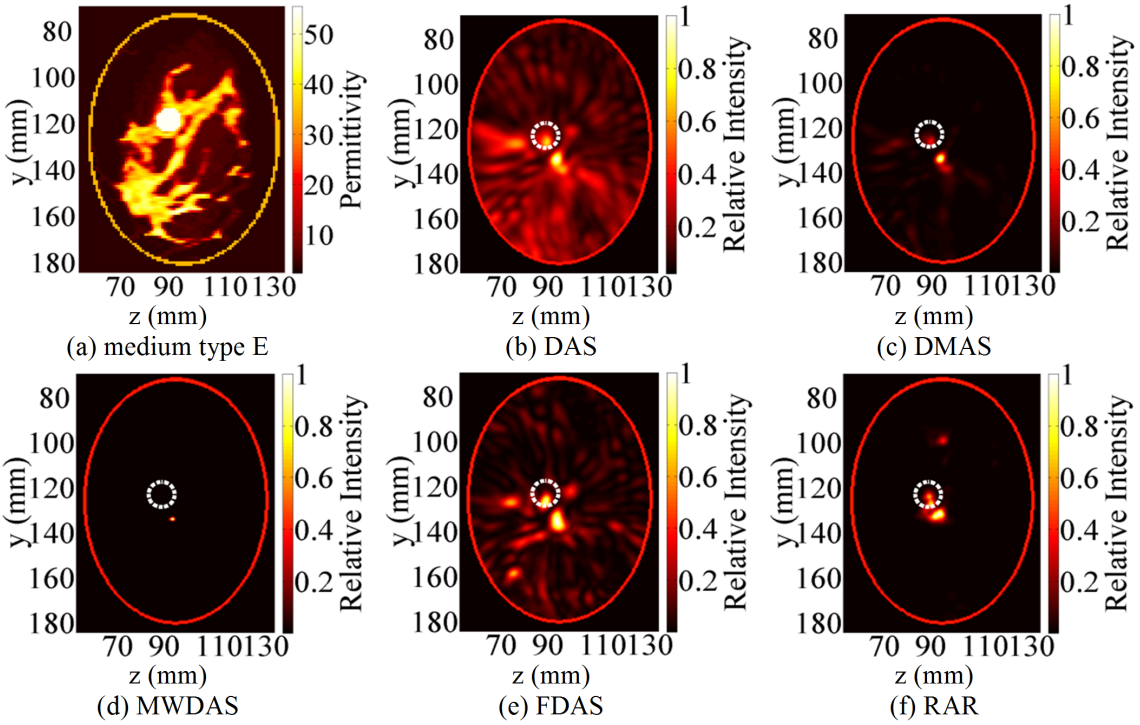

Fig. 4.16 (a) 2-D slice of breast model with MT E and a tumour in glandular tissues. (b)–(f) Results of imaging algorithms with entropy artefact removal. Tumour's actual position is indicated by dotted circles.

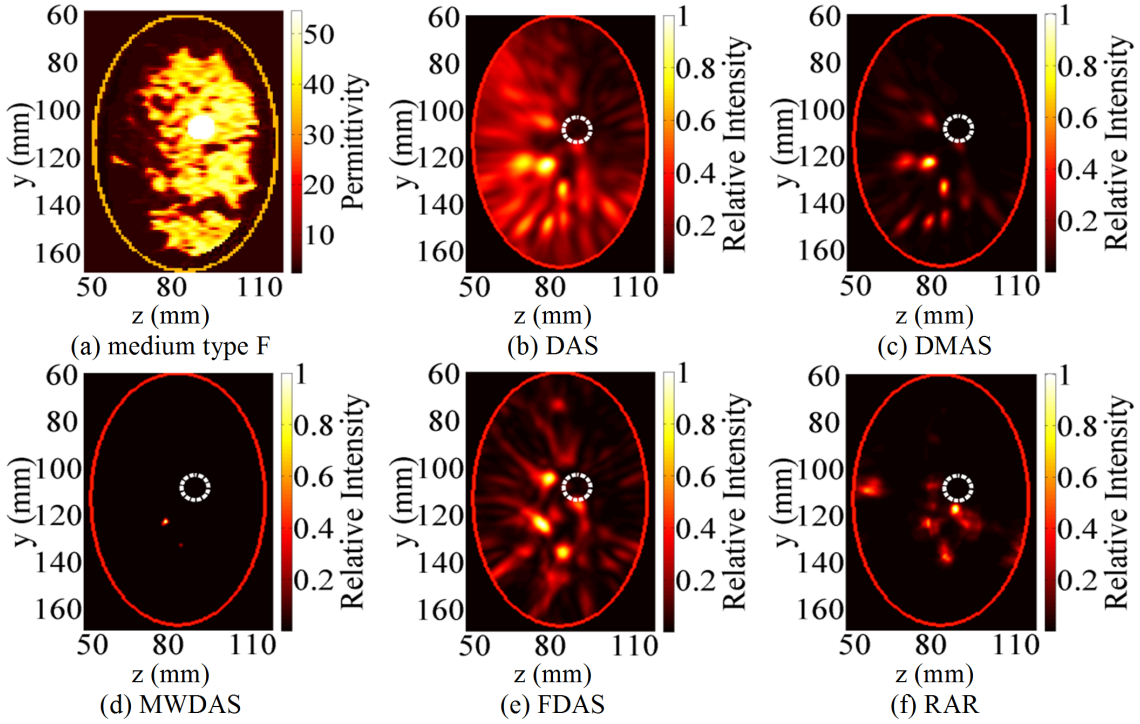

Fig. 4.17 (a) 2-D slice of breast model with MT F and a tumour in glandular tissues. (b)–(f) Results of imaging algorithms with entropy artefact removal. Tumour's actual position is indicated by dotted circles.

The poor performance of algorithm for severely dense breasts with MT E and F is mainly due to the following three reasons. 1) Dense breasts could considerably attenuate the propagated signals, resulting in very weak tumour response contained in backscattered signals. 2) The reflected energy from other scatterers such as glandular tissues might be equivalent or even larger than that from tumours, depending on the variability in adipose versus glandular tissue compositions. 3) For almost fully dielectrically heterogeneous ACR-III and ACR-IV breasts, the assumed uniform propagation channel would not be able to represent the actual one, and fatal inaccuracy of time delay estimation could occur, leading to incorrect localisation. Specifically, when the percentage of fibro-glandular tissue is higher than a certain threshold, the average estimated time delay of propagation path might be far from the actual one. The following solutions which could potentially alleviate these three problems are outlined. 1) Employ multistatic instead of monostatic acquisition to collect more useful backscattered signals from the tumour. 2) Enhance the contrast between tumour and its surrounding tissues through increasing the relative permittivity of tumour, such as using the contrast agent described in [106]. 3) Improve the accuracy of individual propagation channel estimation. These solutions will be considered in following studies.

The imaging with RAR from different view angles is also tested for completeness. The scenario considered in Fig. 4.12 with a tumour at (x, y, z) = (95, 99, 112) is selected as an example. On one hand, images are reconstructed at different x planes, where x = 85 mm, 95 mm, and 105 mm are selected. Fig. 4.18 shows the constructed images at different x planes, where x = 85 mm, 95 mm, and 105 mm are selected. This result illustrates that the largest intensity occurs on the plane of x = 95 mm, corresponding to the actual tumour position, which proves that RAR is able to accurately identify the plane which bears the tumour. On the other hand, the imaging results of y and z cross-sections by RAR are displayed in Fig. 4.19, where y = 99 mm and z = 112 mm are chosen, respectively. It is observed that the reconstructed images clearly identify the tumour in both cases, with accurate positioning and strong clutter suppression.

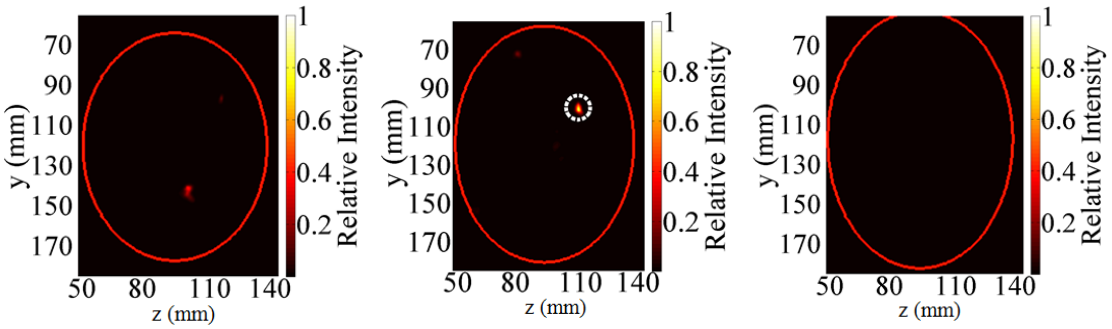

(a) $x = 85$ (b) $x = 95$ (c) $x = 105$

Fig. 4.18 Imaging results by RAR with entropy-based artefact removal for breast models with MT C on different x planes. (a) $x = 85$. (b) $x = 95$. (c) $x = 105$. Tumour position is $(x, y, z) = (95, 99, 112)$. Tumour's actual position is indicated by the dotted circle.

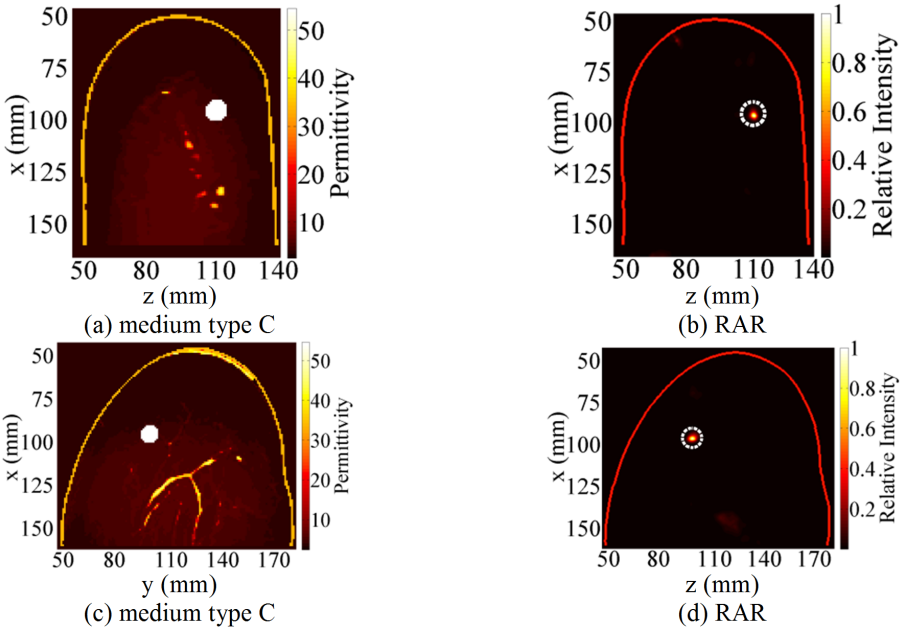

(a) medium type C (b) RAR

(c) medium type C (d) RAR

Fig. 4.19 Imaging results by RAR with entropy artefact removal for breast model with MT C from different view angles. (a) 2-D slice at $y = 99$ mm. (b) Imaging results. (c) 2-D slice at $z = 112$ mm. (d) Imaging results. Tumour's actual position is indicated by dotted circles.

4.7 Robustness Analysis of RAR and Comparisons

SCR and SMR statistics of algorithms are summarised in Table 4.2. Based on the calculated average in ten different scenarios, the proposed RAR algorithm achieves the highest SCR of 4.1 dB and SMR of 16.5 dB, respectively, indicating its excellent performance and strong robustness. It should be noted that RAR is the only algorithm which provided a

positive SCR in results shown in Fig. 4.12, Fig. 4.13, Fig. 4.15, and Fig. 4.16, proving its distinct advantage. On the other hand, MWDAS has the smallest SCR and SMR on average. In spite of its excellent clutter rejection with ideal artefact removal (see Figs. 4.7 and 4.8), this efficacy suffer significantly even with a small portion of residual artefact, indicating its limitation in more practical scenarios.

The second best technique is FDAS, although it is sensitive to artefact, results show that the filtering is beneficial since in most cases it outperforms the original DAS algorithm and achieves the second high SCR of -1.7 dB and SMR of 9.2 dB. Comparing DMAS with DAS, results revealed that the pure coherence-based algorithm DMAS is not always superior to DAS. In scenarios assuming the early-stage artefact could be perfectly removed, DMAS outperformed DAS without question (see Figs. 4.7 and 4.8), however, in scenarios which considered dense breasts and non-perfect artefact removal, DAS showed more robustness than DMAS. This is because the pair multiplication used in DMAS could lead to erroneous peaks in more complex medium which has less coherence among all propagation channels.

The performance of RAR with respect to tumour size was also studied. Combining entropy-based artefact removal, in breasts with MT A and B, tumours as small as 5 mm in diameter were successfully identified. However, in more dielectrically heterogeneous breasts with MT C, when the tumour size is less than 7 mm in diameter, the imaging results were quite blurry, which can hardly be used to identify the tumour. As for MT D, the smallest tumour that were successfully detected were with 10 mm diameter as shown in Figs. 4.14 and 4.15.

Additionally, the sensitivity of RAR to the error of average dielectric permittivity estimation is examined. Coupled with the entropy-based artefact removal, in mostly fatty breasts such as MT A and B, even when the relative error is up to 30%, only a minor reduction of SCR is observed. However, for fully heterogeneous breasts with low to medium density such as MT C and D, when the relative error is over 5%, the resulted images can rarely localise the tumour precisely. This reinforces the need to have an accurate average dielectric permittivity estimation. In this study, the collected signals are

assumed to be noiseless; in practice, however, possible measurement errors and noise need to be considered.

4.8 Complexity Analysis of RAR and Comparisons

Besides robustness, computational complexity of image formation algorithms is of great importance, especially considering the intensive computation for imaging high-resolution 3-D breast models.

In this section, the time complexity of algorithm is analysed. As described before, A sets of tumour response are collected in monostatic case; thus, A signals are needed to be processed. Let K refer to the signal sampling points and α be the window length, which is smaller than K. Both K and α are much larger than A, which determine the number of calculations for raw signals and truncated signals, respectively. The number of arithmetic operations (without distinguishing between addition and multiplication) required to calculate each pixel intensity is analysed. All algorithms considered in this paper require the same time-shifting module, thus only other different processes are compared.

To sum A time-shifted signals, DAS needs $(A-1)K$ additions. Then the summed signal is truncated by a time window with length α, and α and $\alpha-1$ operations for multiplication and addition are required for obtaining the energy of this signal. DAS thus has an asymptotic complexity of $O(K)$.

The first step in DMAS is generating C_A^2 sets of pairs from A signals for pair multiplication, and $[A(A-1)/2-1]K$ multiplications are involved. Step 2 sums $[A(A-1)/2-1]$ signals with K sampling points, which are $[A(A-1)/2-1]K$ additions. The last integration within a time window requires α and $(\alpha-1)$ operations for multiplication and addition, respectively. Ignoring small values in summed operations of all steps, DMAS has an asymptotic complexity of $O(K)$.

Unlike DAS and DMAS, MWDAS brings forward the windowing of signals; thus, for each signal, only α calculations are needed. Step 1 requires $(A-1)\alpha$ summations and one division to obtain the reference waveform. Step 2 involves weighting signals from A channels with the aid of the generated reference waveform, requiring $A\alpha$ multiplications.

Step 3 is the energy calculation of the weighted signals which calls for $(2\alpha - 1)$ operations. Last step multiplies signal energy from all propagation channels, where $(A - 1)$ multiplications are needed. Thus MWDAS requires $(4A\alpha - 1)$ operations in all and has a complexity of $O(\alpha)$.

Two additional parts are needed for FDAS in addition to that of DAS. First is the collection of distance-dependent reference waveforms for filter design, and second is the filtering process. Since the gathering of reference signals could be precomputed, the main extra computational burden of FDAS lies in the filtering process when calculating each pixel intensity. For K sampling points, $K(NK)$ multiplications are required to implement the finite impulse response (FIR) filtering in time domain, where N is the selected filter length. Combined with extra DAS operations and ignore small values, FDAS therefore has a complexity of $O(K^2)$.

In the proposed RAR, the windowing of signal is brought forward; thus, only α calculations is involved for each signal. Step 1 involves $(A - 1)$ calculation of neighbourhood pairwise correlation coefficients, which requires $6\alpha(A - 1)$ operations following equation (4.5). Then, the normalisation needs $2(A - 1)$ operations. Step 3 sorts the $(A - 1)$ normalised correlation coefficient for the maximum combining. For a sorting algorithm with $(A - 1)$ numbers, the time complexity is up to $O(A^2)$. To generate the weighted value, which is the product of the first half number of sorted correlation coefficients, $[(A - 1)/2 - 1]$ multiplications are involved. Step 4 weights the signal and α multiplications are required. Last step calculates the energy and needs $(2\alpha - 1)$ operations. Accordingly, ignoring small values in summed operations, RAR has an asymptotic complexity of $O(\alpha)$.

Simulation results on a PC with Intel (R) Core (TM) 2 Duo CPU E7500 2.93 GHz (2 CPUS) combined with Matlab R2014a software confirmed the computation overhead of algorithms. 48 signals with 1500 sampling points in each signal are processed, where a time window length of 294 is employed. Thus, A = 48, K = 1500, and α = 294. The calculated processing time employs the mean of three replicates to reduce random errors.

Algorithm	Time Complexity
DAS	$O(K)$
DMAS	$O(K)$
MWDAS	$O(\alpha)$
FDAS	$O(K^2)$
RAR	$O(\alpha)$

(a) Time complexity of algorithms

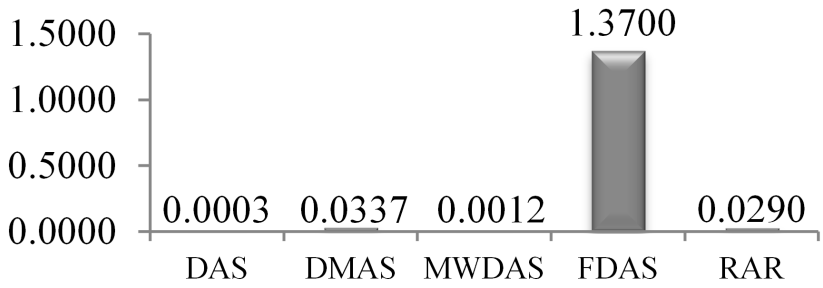

(b) Processing time

Fig. 4.20 (a) Time complexity of algorithms, where K is the length of sampled signal, and α is the time window length. K = 1500 and α = 294 are used in our simulations. (b) Processing time (unit: second) to calculate each pixel intensity by different algorithms.

Fig. 4.20 compares the complexity and processing time to calculate one pixel intensity required by each algorithm. Simulation results verified the time complexity analysis. As can be seen, the complexity is mainly determined by the number of points needed to be processed in each signal, which can be K or α in different algorithms. A much higher computation burden than other algorithms is observed in FDAS, which requires the longest processing time of 1.37 (s), whereas DAS only needs 0.0003 (s). In addition, the same linear growth is observed in DAS, DMAS, MWDAS, and RAR, whereas FDAS has an exponential tendency. This demonstrates that RAR maintains the same level of computational efficiency, even compared with the simplest DAS algorithm.

4.9 Conclusion

A novel imaging algorithm for early breast cancer detection entitled RAR is proposed. The efficacy of RAR is verified under a number of scenarios, using FDTD-based 3-D breast models with various structures and densities.

Simulation results showed that the performance of imaging algorithms is more sensitive to the early-stage artefact, compared with the late-stage clutter, due to the different orders of magnitude of these two types of interference. Results with superior performance and robustness were provided by RAR in comparison to other algorithms, including DAS, DMAS, MWDAS, and FDAS. In the four out of the six challenging scenarios (see Figs. 4.12, 4.13, 4.15, and 4.16), RAR was the only algorithm which clearly identified and accurately localised the tumour. These scenarios considered practical artefact removal, various tumour positions, and breasts ranging from mildly to moderately density classifications. Simulations also demonstrated the computational efficiency of RAR, which has the same asymptotic complexity as DAS, DMAS, and MWDAS. The significant improvement provided by RAR is only at the expense of negligible increased computational effort. These results show a high potential of RAR for early cancer detection in breasts with low to medium densities. The investigation of RAR's performance for further enhancement will be involved in next chapter.

Chapter 5

Improved Algorithms via Weighting Factor and Spatial Diversity Exploration

5.1 Introduction

The proposed RAR algorithm in Chapter 4 offered significantly improved performance over existing methods, and achieved excellent tumour detection capability in mildly and moderately dense breasts. To enhance tumour detectability in severely dense breasts, based on the exploration of weighting factor and spatial diversity, three new imaging algorithms are proposed in this chapter, which is organised as follows. In Section 5.2, two algorithms referred to as local coherence exploration (LCE) and dynamic neighbourhood pairwise correlation (DNPC) are presented. In Section 5.3, the multiple spatial diversity (MSD) algorithm is introduced. Differ from previous algorithms building upon the monostatic signal acquisition, multistatic signals are evaluated and exploited in MSD. The imaging results of LCE, DNPC, and MSD in various scenarios are presented and discussed in Section 5.4. Section 5.5 provides comparative analysis of proposed algorithms, and conclusions are drawn in Section 5.6.

5.2 Diverse and Dynamic Weighting Factor Exploration

5.2.1 Monostatic Signal Acquisition

For consistent comparison, the same antenna configuration and monostatic signal acquisition for RAR [see Fig. 5.1(a)] is used in this section. In monostatic method, the same antenna is used to transmit signal and receive the backscattered signal from the breast, which functions as as a transceiver, while all other antennas are turned off. Then this process is repeated sequentially for every antenna in the antenna array. The received signal in monostatic is uniformly denoted as $S_i(n)$, representing the received signal at the ith antenna while itself acts as the transmitting antenna. As exemplified in Fig. 5.1(b), four monostatic signals $S_1(n),...,S_4(n)$ are collected, where $n = 1,2,...K$, and K is the number of signal sampling points.

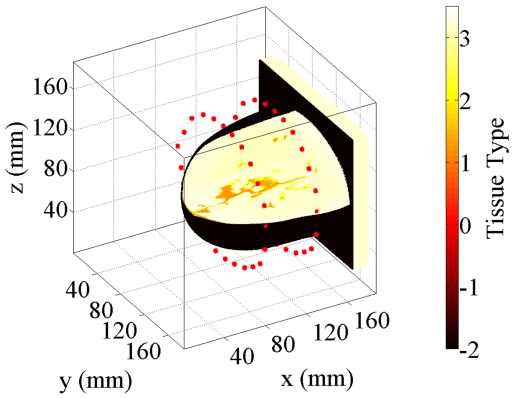

(a) Breast model and antenna array

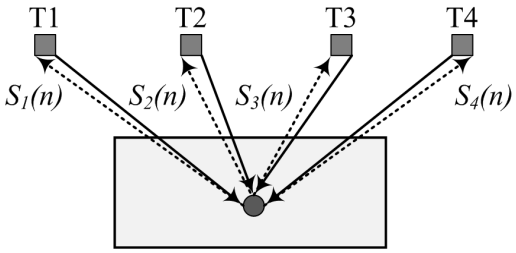

(b) Monostatic signal collection

Fig. 5.1 Breast model, antenna configuration, and illustration of monostatic signal collection. (a) Breast model with two concentric rings of 24 antennas (indicated by solid dots) surrounding the breast. (b) Illustration of monostatic signal collection. Four antennas are represented by squares, which are labelled as T1 to T4. Solid arrows provide a reference of the propagation path of transmitted signals, and dotted arrows provide a reference of the propagation path of received signals.

5.2.2 Local Coherence Exploration (LCE)

This section details the proposed LCE imaging algorithm and its novelty is threefold. First, the correlation is used to quantify the consistency of relative phase change between backscattered signals. Second, adjacent antennas are grouped, and related backscattered

signals are utilised to generate a local coherence reference signal for each group. This is critical because the strongest reflection received at different antennas may originate from different scatterers, this regional correlation measurement ensures the robustness in both single- and multi-scatterer cases. Third, the signals exhibit high correlation are adaptively selected and combined, reducing the algorithm sensitivity to data anomalies and ensuring a high chance of localising the tumour.

Let l be the lth location of a pixel within a constructed image L. Let A be the number of antennas, and A signals are collected in a monostatic way. Let $S_i(n)$ be the artefact-removed signal at ith antenna in discrete form, where $n = 1,2,\ldots,K$, and K is number of signal sampling points. To compute the intensity at each l, three steps are involved in LCE.

Step 1: Signals received from all antennas are time-shifted at l. The ith signal after being time shifted is denoted as $S_i(n+\tau_{il})$, where τ_{il} is the two-way travel time from the ith antenna to l. Signal propagation speed is calculated assuming that each traversed medium, including immersive liquid, skin layer, and underlying breast tissue, has a constant permittivity. The average dielectric property of underlying breast tissue is assumed to be established through an appropriate patient-specific estimation algorithm such as the one developed in [205]. This step is needed in all UWB data-independent imaging algorithms for compensating propagation time delay.

Step 2: Time-shifted signals at adjacent antennas are grouped with a size of G. The reference signal for calculating correlation is generated by averaging the signals within each group, which is a representative of the local coherence. For the ith shifted signal $S_i(n+\tau_{il})$, its group members include $S_j(n+\tau_{jl})$, where $j = i+1, i+2, \ldots,$ and $i+G-1$. The reference signal $R(n)$ is thus obtained as

$$R(n) = \frac{1}{G}\sum_{j=i}^{j=i+G-1} S_j(n+\tau_{jl}). \tag{5.1}$$

The correlation coefficient c_{il} between the ith shifted signal and its intragroup reference signal within a time window W_α is obtained as

$$c_{il} = \frac{\sum_{n=1}^{\alpha} X_i(n)R(n)}{\sqrt{\sum_{n=1}^{\alpha}[X_i(n)]^2 \sum_{n=1}^{\alpha}[R(n)]^2}} \tag{5.2}$$

where $X_i(n) = S_i(n+\tau_{il})$, and α is an integer defines the time window. $W_\alpha = \alpha\Delta t$, and Δt is the time step used in FDTD. Time window W_{294} is used, which is equivalent to input pulse width, since it is proved to be effective for detecting small tumours [50]. The procedure is repeated for every signal, thus A correlation coefficients are obtained. This coefficient represents the conformity of each signal with its proximity peers. High correlation is expected at tumour locations, since all shifted signals should be a broadened version of the same input pulse, after backscattering from the same strong scatterer.

Step 3: The intensity of location l is obtained through the combining of selected signals. Let P_l be the correlation coefficients vector at l, which can be expressed as

$$P_l = [c_{1l}\ c_{2l}\ ...\ c_{Al}]. \tag{5.3}$$

All c_{il} are linearly normalised from the range of [-1, 1] to [0, 1], avoiding negative coefficients generating a high weight

$$P_{l\_Nor} = \frac{(P_l + 1)}{2}. \tag{5.4}$$

Let P_{l_Sort} be the sorted P_{l_Nor} in a descending order and C_{il} be the sorted coefficients. P_{l_Sort} can thus be expressed as

$$P_{l\_Sort} = [C_{1l}\ C_{2l}\ ...\ C_{Al}] \tag{5.5}$$

where $C_{1l} > C_{2l} > ... > C_{Al}$. Let I_l be the intensity of l

$$I_l = \sum_{n=1}^{\alpha} [wf_l \cdot Sum_l(n)]^2 \tag{5.6}$$

where

$$wf_l = \prod_{i=1}^{A/2} C_{il} \tag{5.7}$$

is weight factor, equals to the product of the first half elements of P_{l_Sort}, and

$$Sum_l(n) = \sum_{i=1}^{A/2} S_i(n+\tau_{il}) \tag{5.8}$$

is the sum of signals, corresponding to those selected largest coefficients. Simulation results showed that selecting the best half of signals with the highest coefficients is sufficient to offer effective performance in most if not all cases. This procedure is repeated for each l, and L loops are needed as shown in Pseudocode 5.3. A group size (G) of 6 is used since it provides an effective tumour detection as verified by simulation results. The distribution of I_l is displayed as an image. For comparison and consistency, the imaging results of LCE are presented in subsequent sections.

Pseudocode 5.3 Calculate the intensity of pixel I_l (l=1,2,...,L) with LCE

```
INPUT: S_i(n), i = 1,2,...,A.          % A monostatic signals
Obtain S_i(n+τ_il), where n = 1,...,α % Time-shifting and windowing of signals
for l = 1 to L do                      % lth location of L
    for i = 1 to A do                  % ith signal of A
        c_il = corr[S_i(n+τ_il)R(n)]   % Local correlation coefficient (5.2)
        P_l(i) = c_il                  % Coefficient vector (5.3)
    end for i                          % End of iteration of signal
    P_l_Nor = (P_l + 1)/2              % Normalised vector (5.4)
    P_l_Sort = [C_1l C_2l ... C_Al]    % Sorted vector (5.5)
    wf_l = ∏_{i=1}^{A/2} C_il          % Weight factor at l (5.7)
    Sum_l(n) = Σ_{i=1}^{A/2} S_i(n+τ_il) % Sum of selected signals (5.8)
    I_l = Σ_{n=1}^{α} [wf_l · Sum_l(n)]^2 % Intensity at l (5.6)
end for l                              % End of iteration of pixels
OUTPUT: I_1, I_2, ..., I_L             % Intensity of all pixels
```

5.2.3 Dynamic Neighbourhood Pairwise Correlation (DNPC)

This section presents the DNPC imaging algorithm. DNPC is based on the RAR algorithm, and two modifications are added for further robustness. First, it changes the way of calculating the neighbourhood pairwise correlation between signals. Second, instead of the equal weighting of signals used in RAR, a dynamic weighting of signals for combining is exploited in DNPC.

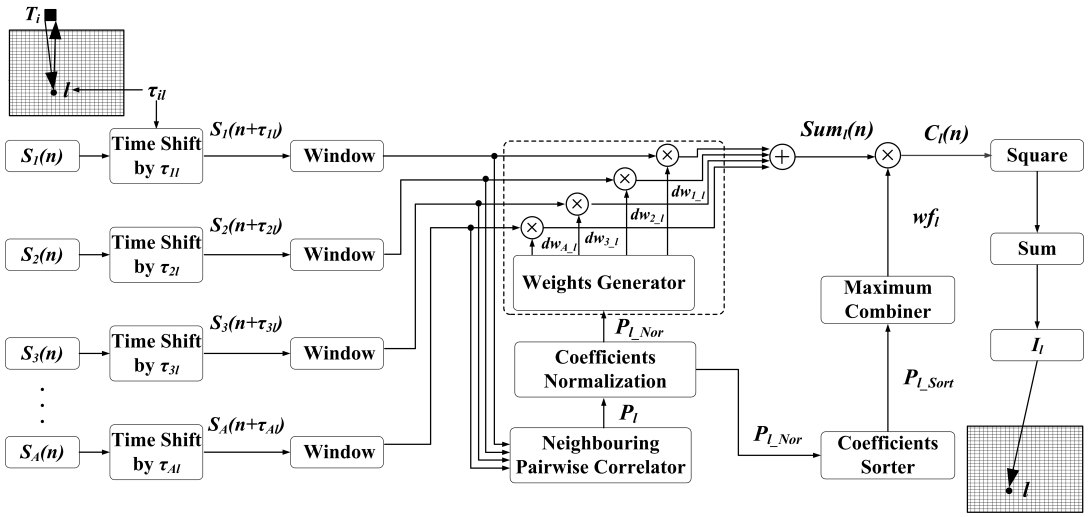

Fig. 5.2 Block diagram illustrating the DNPC algorithm to calculate the intensity of the lth pixel I_l in the imaging region indicated by the mesh area.

The block diagram depicted in Fig. 5.2 shows DNPC to calculate the intensity value of each pixel in the breast model. Let l represent the lth location of a pixel within a constructed image L. The whole process is composed of four steps.

Step 1: Time shifting and windowing of signals. Each pre-processed $S_i(n)$ is time-shifted based on the corresponding round-trip time delay at a location l. The time-shifted signals are expressed as $S_i(n+\tau_{il})$, where $n = 1,2,\ldots,K$, and τ_{il} is the two-way travel time from the ith transceiver to a specific location l within the imaging region. Moreover, a window truncation for each time-shifted signal is applied. The time window is represented as $W_\alpha = \alpha\Delta t$, where α is an integer and Δt is the time step used in FDTD, which equals 1.91 (ps) as explained in Cha. 4.3.2. $W_{294} = 294\Delta t$ = 562 (ps) is used as a default time window, unless otherwise specified.

Step 2: Modified calculation of neighbourhood pairwise correlation. To generate consistent weight for each signal, and considering the distance between the two rings of antenna array, the correlation coefficients between signals received at each antenna ring is calculated separately. Let A represent the number of antennas. The first ring includes antenna $1,2,...,A/2$, and the second ring includes antenna $A/2+1,,...,A$. In the model shown in Fig. 5.1(a), $A = 48$, and this process is illustrated in Fig. 5.3.

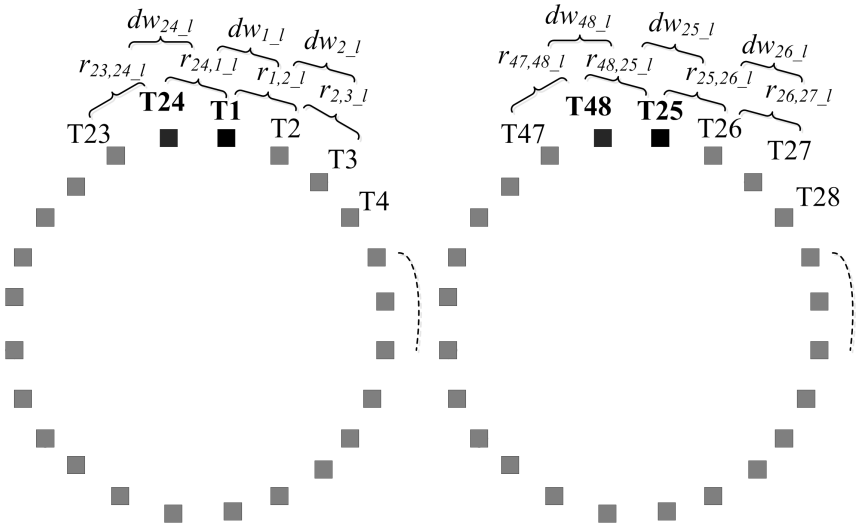

Fig. 5.3 Correlation and weighting coefficients calculation in DNPC. The antenna (T) is represented by solid squares. The left-side Ring 1 contains T1 to T24, and the right-side Ring 2 contains T25 to T48. r_{i,j_l} is the neighbourhood pairwise correlation coefficients in each antenna ring at l, and dw_{i_l} is the dynamic weight for the ith shifted signal at l.

For signals received at antennas which are within the two rings (see Fig. 5.3), the neighbourhood pairwise correlation coefficient r_{i,j_l} is calculated as:

$$r_{i,j\_l} = \frac{\sum_{n=1}^{\alpha} X_i(n)X_j(n)}{\sqrt{\sum_{n=1}^{\alpha}[X_i(n)]^2 \sum_{n=1}^{\alpha}[X_j(n)]^2}} \tag{5.9}$$

where $X_i(n) = S_i(n+\tau_{il})$ and $X_j(n) = S_j(n+\tau_{jl})$ with $j = i+1$, are the shifted signals at location l from the ith and $(i+1)th$ antenna, respectively, where i = 1,..., 23; 25,..., 47.

For the correlation between signals received at end antennas (see Fig. 5.3), including T24 and T48, their neighbourhood pairwise correlation is calculated also following (5.9), but with $i = 24, j = 1$, and $i = 48, j = 25$, respectively. These two additional sets of correlation coefficients for the signals received at end antennas were not included in RAR. Accordingly, the neighbourhood pairwise correlation coefficients vector P_l in DNPC composed of A elements for l is obtained as

$$\begin{aligned} P_l =& [r_{1,2\_l}\ r_{2,3\_l}\ \ldots\ r_{A/2,1\_l}\ r_{A/2+1,A/2+2\_l}\ \ldots\ r_{A-1,A\_l}\ r_{A,A/2-1\_l}] \\ =& [r_{1,2\_l}\ r_{2,3\_l}\ \ldots\ r_{24,1\_l}\ r_{25,26\_l}\ \ldots\ r_{47,48\_l}\ r_{48,25\_l}]. \end{aligned} \tag{5.10}$$

Considering r_{i,j_l} is in the range of [-1, 1], all r_{i,j_l} are linearly normalised to the range of [0, 1], avoiding negative coefficients generating a high weight

$$P_{l\_Nor} = \frac{(P_l + 1)}{2}. \tag{5.11}$$

Based on the normalised r_{i,j_l}, the dynamic weight dw_{i_l} for the ith signal at location l, where i = 2,..., 23; 26,..., 47, is giving by

$$dw_{i\_l} = (r_{i-1,i\_l} + r_{i,i+1\_l})/2 \tag{5.12}$$

which is the average of the two neighbourhood pairwise coefficients the ith signal involved, including the $i-1$ antenna and the $i+1$ antenna. For those two end antennas, including T1, T24, T25, and T28, corresponding dw_{i_l} are calculated as: $dw_{1\_l} = (r_{24,1\_l} + r_{1,2\_l})/2$, $dw_{24\_l} = (r_{23,24\_l} + r_{24,1\_l})/2$, $dw_{25\_l} = (r_{25,26\_l} + r_{48,25\_l})/2$, and $dw_{48\_l} = (r_{47,48\_l} + r_{48,25\_l})/2$, which are illustrated in Fig. 5.3.

Step 3: Generate dynamic weights for combining signals. Unlike the equal weighting in RAR, DNPC exploits a dynamic weighting for combining signals.

In RAR, the same weighting coefficient of 1 is applied for all signals (4.4):

$$\begin{aligned} Sum_l(n) &= \sum_{i=1}^{A} S_i(n + \tau_{il}) \\ &= 1 \cdot S_1(n + \tau_{1l}) + 1 \cdot S_2(n + \tau_{2l}) + ... + 1 \cdot S_A(n + \tau_{Al}) \end{aligned} \tag{5.13}$$

where $Sum_l(n)$, $n = 1, 2, \ldots, \alpha$, is the sum of all time-shifted signals within the time window W_α at the lth location. $S_i(n)$ is artefact-removed signal from the ith antenna, τ_{il} is the two-way travel time from the ith transceiver to a specific location l within the imaging region, and $S_i(n + \tau_{il})$ is the time-shifted signal.

In DNPC, each signal is weighted by its corresponding dynamic weight dw_{i_l}, and the sum of dynamic-weighted signals is calculated as

$$\begin{aligned} Sum_l(n) =& \sum_{i=1}^{A} dw_{i\_l} \cdot S_i(n+\tau_{il}) \\ =& dw_{1\_l} \cdot S_1(n+\tau_{1l}) + dw_{2\_l} \cdot S_2(n+\tau_{2l}) + ... + dw_{A\_l} \cdot S_A(n+\tau_{Al}). \end{aligned} \tag{5.14}$$

Each neighbourhood pairwise correlation coefficient measures the likelihood of carrying effective tumour response, a larger dw_{i_l} signifies a higher quality of this propagation channel. An increased tumour response can be obtained in the summed signal by weighting each signal based on its quality level, thereby achieving an enhancement of tumour detection.

Step 4: Pixel intensity calculation through maximum combining. Let P_{l_Sort} be the sorted P_{l_Nor} in a descending order and R_{i_l} be the sorted coefficients, $i = 1, 2, \ldots, A$,

$$P_{l\_Sort} = [R_{1\_l}\ R_{2\_l}\ ...\ R_{A\_l}] \tag{5.15}$$

where $R_{1\_l} > R_{2\_l} > ... > R_{A\_l}$. The weighting factor for the summed signal at the lth location is introduced as

$$wf_l = \prod_{i=1}^{i=\frac{A}{2}} R_{i\_l} \tag{5.16}$$

which is the product of the first half elements of P_{l_Sort}.

To calculate the intensity at l, the combined signal $C_l(n)$ is calculated as

$$C_l(n) = wf_l \cdot Sum_l(n). \tag{5.17}$$

where $Sum_l(n)$ is the weighted summed signal calculated in (5.14). Let I_l denote the intensity of pixel l within the desired imaging area, and it is given by

$$I_l = \sum_{n=1}^{\alpha} [C_l(n)]^2. \tag{5.18}$$

The procedure is repeated for every pixel within the imaging region (see Fig. 5.2), and L loops are required in total. The distribution of intensity at each location I_l is displayed as an image. For comparison and consistency, the imaging results of DNPC are presented in subsequent sections.

5.3 Multiple Spatial Diversity (MSD) Algorithm

5.3.1 Multistatic Signal Acquisition

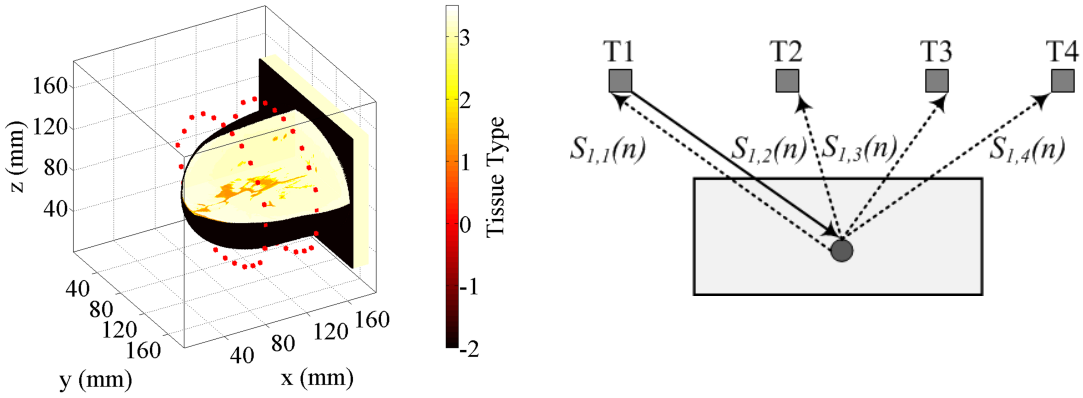

(a) Breast model and antenna array

(b) Multistatic signal collection

Fig. 5.4 Breast model, antenna configuration, and multistatic signal collection. (a) Breast model with two concentric rings of 24 antennas (indicated by solid dots) surrounding the breast. (b) Diagram illustrating multistatic signal collection. Four antennas are represented by squares, which are labelled as T1 to T4. T1 is selected as the transmitter and all antennas record the backscattered signals. $S_{1,2}(n)$ denotes the backscattered signal received at T2 while T1 is acting as the transmitter. $S_{1,1}(n), S_{1,3}(n)$, and $S_{1,4}(n)$ follow the same rule. The solid arrow provides a reference of the propagation path of transmitted signal, and the dotted arrows provide a reference of the propagation path of backscattered signals.

As opposed to monostatic, another signal acquisition method is multistatic. In multistatic, each antenna takes a turn to transmit and the backscattered signals are recorded at all antennas simultaneously. This process is illustrated in Fig. 5.4(b). As an example, an antenna array composed of four elements (T1 to T4) is used. The received signal in multistatic is uniformly denoted as $S_{i,j}(n)$, representing the received signal at the jth antenna while the ith antenna acts as the transmitter. Therefore, signal $S_{i,i}(n)$ which refers to the received signal at the ith antenna while itself acts as the transmitter, which is the same as $S_i(n)$ defined in monostatic mode. For clarity, in the following study, $S_{i,i}(n)$ is

called monostatic signal, $S_{i,j}(n)$ is called multistatic signal. In particular, $S_{i,j}(n)$, when $j = i+1$ or $j = i-1$, is called neighbouring multistatic signal, which is the signal received at the ith antenna while the $(i+1)th$ or $(i-1)th$ antenna is the active transmitter.

As shown in Fig. 5.4(b), T1 is selected as the transmitter and all antennas record the backscattered signals. $S_{1,2}(n)$ denotes the backscattered signal received at T2 while T1 is acting as the transmitter. $S_{1,1}(n), S_{1,3}(n)$, and $S_{1,4}(n)$ follow the same rule. Compared with the monostatic method, a much higher number of signals can be obtained in multistatic. Let A represent the number of antennas. A signals are collected in monostatic, whereas $A(A+1)/2$ independent signals can be acquired in multistatic [145], through which one order of magnitude higher number of signals than monostatic can be collected.

Compared with monostatic, multistatic-based algorithms have several advantages. Firstly, the diversity of multiple angles can improve the probability of target detection due to a higher number of available signals [208]. Moreover, it can mitigate clutter effectively. In monostatic UWB breast imaging, the direct reflection path always suffer from the greatest skin reflection, whereas in multistatic, extra paths containing less reflection could be employed for extracting useful tumour response while suppressing clutter signals [42]. Therefore, in the proposed MSD algorithm, besides monostatic signals, extra signals via multistatic propagation paths are taken into account, and the details are introduced in next section.

5.3.2 Algorithm Rationale

Based on the simulation of UWB breast imaging with multistatic signals presented in Chapter 3.8.5, two important indications were given. First, backscattered signals received at antennas which act as transceivers (i.e. monostatic signals) have the maximum strength of effective tumour response in most if not all cases. Second, signals received at neighbouring receiving antennas (relative to transmitting antenna) tend to possess higher portion of effective tumour response than those received at antennas which are far away from the transmitting antenna, due to the small distance from a transmitting antenna to tumour and back to its neighbouring receiving antenna, assuming all antennas are equally placed.

Accordingly, in MSD algorithm, besides monostatic signals [e.g. $S_{1,1}(n), S_{2,2}(n)$, etc.], only neighbouring multistatic signals [e.g. $S_{1,2}(n), S_{2,3}(n)$, etc.] are employed, and the benefits are twofold. First, the neighbourhood pairwise correlation between monostatic signals indicates the probability that the dominant part of these two signals are from the same strong scatterer, the efficacy of which has been proved by the results of RAR algorithm. Signals received at transmitter/receiver pairs which are far away from each other could be dominated by different scatterers, such as tumour and glandular tissue. Thus those signals are less reliable to evaluate the quality of propagation channels. Second, a much high computational efficiency can be achieved by employing the neighbourhood multistatic signals only. Assuming there are 48 (A) antennas, the number of all independent multistatic signals would be 1176 [$A(A+1)/2$], including $S_{1,1}(n), S_{1,2}(n), ...S_{1,48}(n), S_{2,2}(n), S_{2,3}(n), ...S_{2,48}(n), ..., S_{48,48}(n)$. For neighbourhood multistatic signals only, including $S_{1,1}(n), S_{1,2}(n), ..., S_{47,48}(n), S_{48,48}(n)$, this number reduces to 96, which leads to a 91.8% reduction of the number of signals. This ensures a high algorithm efficiency by choosing those most usable signals.

Let l represent the lth location of a pixel within the imaging region of a constructed image L. To calculate the intensity value of l, three steps are included in MSD: time shifting and windowing, signal quality evaluation, and adaptive combining.

Step 1: Time Shifting and Windowing of Signals. Each pre-processed (for artefact removal) monostatic and neighbouring multistatic signal $S_{i,j}(n)$ is time-shifted based on the corresponding round-trip time delay at a location l. This is for phase compensation as used in all data-independent imaging algorithms. The time-shifted signals are expressed as $S_{i,j}(n+\tau_{i,j\_l})$, where $n = 1, 2, \ldots, K$, and τ_{i,j_l} is the travel time from the ith transmitter to a specific location l within the imaging region and back to the jth receiver. The same propagation velocity is assumed for both propagation trips, from transmitter to l and from l back to receiver. Propagation distance is calculated based on relevant space coordinates in the constructed model. The propagation speed of the signal is calculated under the assumption that each traversed medium has a constant relative permittivity at the centre frequency of input pulse. The permittivity at centre frequency is chosen since it can be

regarded as an average value across the frequency range of input pulse. This average dielectric property of underlying breast tissue is assumed to be established through an appropriate patient-specific dielectric properties estimation algorithm such as the one developed by Winters *et al.* [205].

Prior to further processing, a window truncation for each time-shifted signal is applied. The time-shifted signal after truncation with a time window W_α can be represented as $S_{i,j}(n+\tau_{i,j\_l})$, where $n = 1,2,\ldots,\alpha$, and α is the window length. The time window is represented as $W_\alpha = \alpha\Delta t$, where α is an integer and Δt is the time step used in FDTD, which equals 1.91 (ps) as explained in Cha. 4.3.2. W_{294} equals $294\Delta t$ = 562 (ps) is used as a default time window, unless otherwise specified. Let A be the number of antennas, and $2A$ monostatic and neighbouring multistatic signals are employed in MSD algorithm.

Step 2: Signal Quality Evaluation. Considering the high amplitude of monostatic signals, including $S_{1,1}(n), S_{2,2}(n), ..., S_{48,48}(n)$, only monostatic signals are used to evaluate the quality of each propagation channel. Due to the distance between the two rings of antenna array, the correlation coefficients between signals received at each antenna ring is calculated separately. The first ring includes antenna $1,2,...,A/2$, and the second ring includes antenna $A/2+1,,...,A$. In the following simulation, $A = 48$, which is illustrated in Fig. 5.3.

For signals received at antennas which are within the antenna ring (see Fig. 5.3), the neighbourhood pairwise correlation coefficient is calculated as

$$r_{i,j\_l} = \frac{\sum_{n=1}^{\alpha} X_i(n)X_j(n)}{\sqrt{\sum_{n=1}^{\alpha}[X_i(n)]^2 \sum_{n=1}^{\alpha}[X_j(n)]^2}} \tag{5.19}$$

where $X_i(n) = S_{i,i}(n+\tau_{i,i\_l})$ and $X_j(n) = S_{j,j}(n+\tau_{j,j\_l})$ with $j = i+1$, are shifted signals at location l from the ith and $(i+1)th$ antenna, respectively, where i = 1,..., 23; 25,..., 47, are antennas 1 to 23 on ring 1 and antennas 25 to 47 on ring 2.

For signals received at end antennas (see Fig. 5.3), including T24 and T48, their neighbourhood pairwise correlation is calculated also following (5.19), but with $i = 24$, $j =$ 1, and $i = 48$, $j = 25$, respectively. Accordingly, the neighbourhood pairwise correlation

coefficients vector for P_l for the lth pixel in MSD is composed of A elements as following

$$P_l = [r_{1,2\_l}\ r_{2,3\_l}\ ...\ r_{A/2,1\_l}\ r_{A/2+1,A/2+2\_l}\ ...\ r_{A-1,A\_l}\ r_{A,A/2-1\_l}]. \tag{5.20}$$

Considering r_{i,j_l} is in the range of [-1, 1], all r_{i,j_l} are linearly normalised to the range of [0, 1], avoiding negative coefficients generating a high weight

$$P_{l\_Nor} = \frac{(P_l + 1)}{2}. \tag{5.21}$$

Let P_{l_Sort} be the sorted P_{l_Nor} in a descending order and R_{i_l} be the sorted coefficients, $i = 1, 2, \ldots, A$. Therefore,

$$P_{l\_Sort} = [R_{1\_l}\ R_{2\_l}\ ...\ R_{A\_l}] \tag{5.22}$$

where $R_{1\_l} > R_{2\_l} > ... > R_{A\_l}$.

Step 3: Adaptive Combining. To exploit the extra useful information contained in neighbourhood multistatic signals, the high-quality (indicated by high R_{i_l}) transceiver-related monostatic and neighbouring multistatic signals are combined. R_{i_l} measures the degree of coherence between time-shifted signals. High correlation between signals received from neighbouring antenna pairs is expected at tumour locations, considering all time-shifted signals are a broadened version of the same input pulse, after reflected from the same strong scatterer. Thus, a larger R_{i_l} indicates that this position could have a higher possibility of being the tumour.

The intensity of location l is represented by I_l, which can be obtained through the combining of selected signals.

$$I_l = \sum_{n=1}^{\alpha} [wf_l \cdot Sum_l(n)]^2 \tag{5.23}$$

where wf_l is weight factor given by

$$wf_l = \prod_{i=1}^{A/2} R_{i\_l} \tag{5.24}$$

equals to the product of the first half elements of P_{l_Sort}, and $Sum_l(n)$ is the sum of monostatic and neighbouring multistatic signals, corresponding to those selected largest coefficients, which is given by

$$Sum_l(n) = \sum_{i=1}^{A/2} [S_{i,i}(n+\tau_{i,i\_l}) + S_{i,j}(n+\tau_{i,j\_l})] \tag{5.25}$$

where $j = i+1$. Provided that the selected high-quality signals are $S_{1,1}(n), S_{3,3}(n), ..., S_{5,5}(n)$, then $Sum_l(n) = [S_{1,1}(n+\tau_{1,1\_l}) + S_{1,2}(n+\tau_{1,2\_l}) + S_{3,3}(n+\tau_{3,3\_l}) + S_{3,4}(n+\tau_{3,4\_l}) + ... + S_{5,5}(n+\tau_{5,5\_l}) + S_{5,6}(n+\tau_{5,6\_l})]$. Simulation results showed that selecting the half number of signals with the highest coefficients is sufficient to offer effective performance in most if not all cases. This procedure is repeated for each l, and L loops are needed as shown in Pseudocode 5.4.

Pseudocode 5.4 Calculate the intensity of pixel I_l (l=1,2,...,L) with MSD

1: INPUT: $S_{i,i}(n), S_{i,j}(n), i = 1, ..., A, j = i+1$. % $2A$ input signals
2: Obtain $S_{i,j}(n+\tau_{i,j\_l})$, where $n = 1, \ldots, \alpha$ % Time-shifting and windowing of signals
3: for l = 1 to L do % lth location of L
4: for i = 1 to A do % ith monostatic signal of A
5: $r_{i,j\_l} = corr[X_i(n)X_j(n)] (j = i+1)$ % Correlation coefficient (5.19)
6: $P_l(i) = r_{i,j\_l}$ % Coefficient vector (5.20)
7: end for i % End of iteration of signals
8: $P_{l\_Nor} = (P_l + 1)/2$ % Normalised vector (5.21)
9: $P_{l\_Sort} = [R_{1\_l}\ R_{2\_l}\ ...\ R_{A\_l}]$ % Sorted vector (5.22)
10: $wf_l = \prod_{i=1}^{A/2} R_{i\_l}$ % Weight factor at l (5.24)
11: $Sum_l(n) = \sum_{i=1}^{A/2} [S_{i,i}(n+\tau_{i,i\_l}) + S_{i,j}(n+\tau_{i,j\_l})]$ % Sum of selected signals (5.25)
12: $I_l = \sum_{n=1}^{\alpha} [wf_l \cdot Sum_l(n)]^2$ % Intensity at l (5.23)
13: end for l % End of iteration of pixels
14: OUTPUT: $I_1, I_2, ..., I_L$ % Intensity of all pixels

Observing line 1 of Pseudocode 5.4, both monostatic and neighbourhood multistatic signals are used in MSD, which enables the exploration of richness of signals via different propagation routes. In line 5, the correlation coefficients r_{i,j_l} between shifted neighbouring

monostatic signals are used as a quality indicator. A higher r_{i,j_l} indicates that the position l has a higher chance of being the tumour, considering these two time-shifted signals can be both dominated by the reflection from the same strong scatterer, assuming time-shifting can well compensate the phase of backscattered signals. Due to the largest dielectric property of tumour among all comparably sized breast tissues, the weighting which is based on such a quality evaluation can localise the tumour with a high chance in most if not all cases. After the quality evaluation of propagation channels, high r_{i,j_l} and related both monostatic and neighbourhood multistatic signals are combined to calculate the intensity of pixel l, corresponding to the line 10, 11, and 12, respectively.

The quality measurement and selective combining of monostatic and neighbouring multistatic signals are concurrently used in MSD, which implements an adaptive selection of those most usable signals. In MSD, only signals with high chance of possessing effective tumour response can contribute to the weight factor, and only high-quality propagation channel-related multistatic signals would be used for the combining of signals, which yields a flexible beamforming. The robustness of MSD is demonstrated under a variety of challenging scenarios, where non-perfect artefact removal, along with multi-density breast models are considered, and these are presented in the next section.

5.4 Imaging Results and Discussion

For completeness, the proposed algorithms are evaluated in ten scenarios (S1 to S10), in which breast models with both homogeneous and heterogeneous structures, different density classifications, and varied tumour positions are considered. For fair cross-comparisons, the same conditions used for RAR are applied.

Both ideal and the entropy-based artefact removal methods are applied to assess algorithm performance, considering the serious impact of artefact signals. The entropy-based artefact removal method is selected since it introduces zero distortion to tumour response, does not require any prior information, and has high computational efficiency [206, 207]. This also allows the direct performance comparison between RAR and the newly proposed techniques.

All reconstructed images were normalised to the maximum intensity value of the 3-D volume. Same datasets were applied for all algorithms. To quantify algorithm performance, two metrics were applied, which are signal-to-clutter ratio (SCR) and signal-to-mean ratio (SMR) [50].

5.4.1 Breast of Medium Type A and B with Ideal Artefact Removal

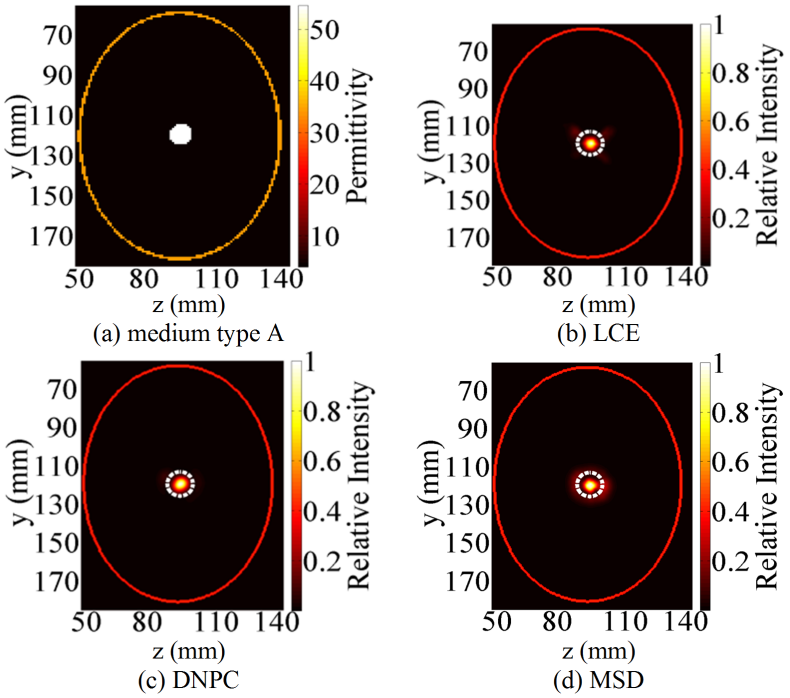

Fig. 5.5 S1: (a) 2-D slice of breast model with medium type (MT) A. (b)-(d) Imaging results of LCE, DNPC, and MSD with ideal artefact removal. Tumour's actual position is indicated by dotted circles.

To assess the best performance of algorithm and serve as benchmark, ideal artefact removal and sparse breast with medium type (MT) A was used in S1. As shown in Fig. 5.5(a), the malignant tumour (white area) is constructed as a sphere with a diameter of 10 mm. In this study, the focus is placed on different tumour sizes and positions, which represent different orders of magnitude of backscattered tumour response, thereby enabling the performance evaluation of imaging algorithm. It is aware that tumour can have different shapes and properties (benign or malignant), and these factors will be considered in future work.

The imaging results offered by LCE, DNPC, and MSD algorithms are shown in Fig. 5.5(b) to (d), which represent a distribution of energy resulted from each voxel within

the breast model. The peak intensity of the reconstructed image (white area) is regarded as the tumour position, which has the strongest reflection among all heterogeneous breast tissues with a comparable size [40]. For clarity, the actual tumour position in constructed images is indicated by dotted circles [see Fig. 5.5(b)-(d)]. It can be seen that in this case, the embedded tumour is clearly identified and accurately localised by all three methods.

In S2 (see Fig. 5.6), the same ideal artefact removal is applied as in S1, but the breast model has been changed from single-layer homogeneous fatty (MT A) to the three-layer heterogeneous fatty (MT B). All three methods offered images with correct tumour localisation. However, compared with S1, the image resolution decreased due to the increased heterogeneity. Specifically, the SCR of LCE reduced from 11.8 to 9.2 dB (see Table 5.1), whereas for DNPC, this value reduced from 13.6 to 7.5 dB.

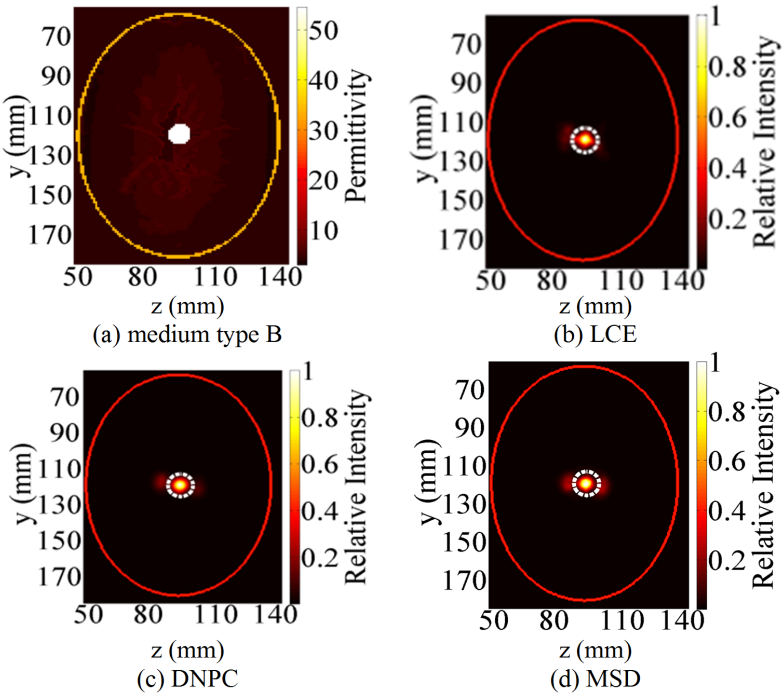

Fig. 5.6 S2: (a) 2-D slice of breast model with MT B. (b)-(d) Imaging results of LCE, DNPC, and MSD with ideal artefact removal. Tumour's actual position is indicated by dotted circles.

Table 5.1 SCR and SMR of LCE, DNPC, and MSD algorithms in ten scenarios (S1 to S10). The ten scenarios correspond to Figs. 5.5 to 5.14(b)-(d). For comparison, the results of RAR algorithm are included, corresponding to Figs. 4.7(f) and 4.8(f), Figs. 4.10(f) to 4.17(f). "Ave" abbreviates for average, which is the arithmetic mean of SCR and SMR values in ten different scenarios. Best results of each case are highlighted in **Bold**.

	S1	S2	S3	S4	S5	S6	S7	S8	S9	S10	Ave
						SCR(dB)					
RAR	**14.0**	8.5	5.3	4.8	4.0	**3.9**	0.5	0.1	0.1	-0.3	4.1
LCE	11.8	**9.2**	6.7	5.1	3.8	0.5	-4.7	-1.0	-1.9	-1.0	2.9
DNPC	13.6	7.5	6.5	4.0	3.9	4.0	1.1	1.2	0.3	**-0.3**	4.2
MSD	10.5	6.4	**6.9**	**6.5**	**4.4**	3.1	**1.9**	**2.9**	**1.2**	-1.3	**4.3**
						SMR(dB)					
RAR	**21.0**	**20.7**	20.1	17.1	14.3	18.2	11.4	16.0	17.3	9.2	16.5
LCE	20.8	20.7	19.6	16.0	15.7	14.1	9.8	14.4	15.4	15.3	16.2
DNPC	21.0	20.6	20.4	17.3	15.3	18.4	12.9	**17.6**	18.4	11.5	17.3
MSD	20.8	20.6	**20.5**	**19.2**	**19.5**	**20.5**	**17.8**	17.3	**18.4**	**15.6**	**19.0**

5.4.2 Breast of Medium Type B with Entropy Artefact Removal

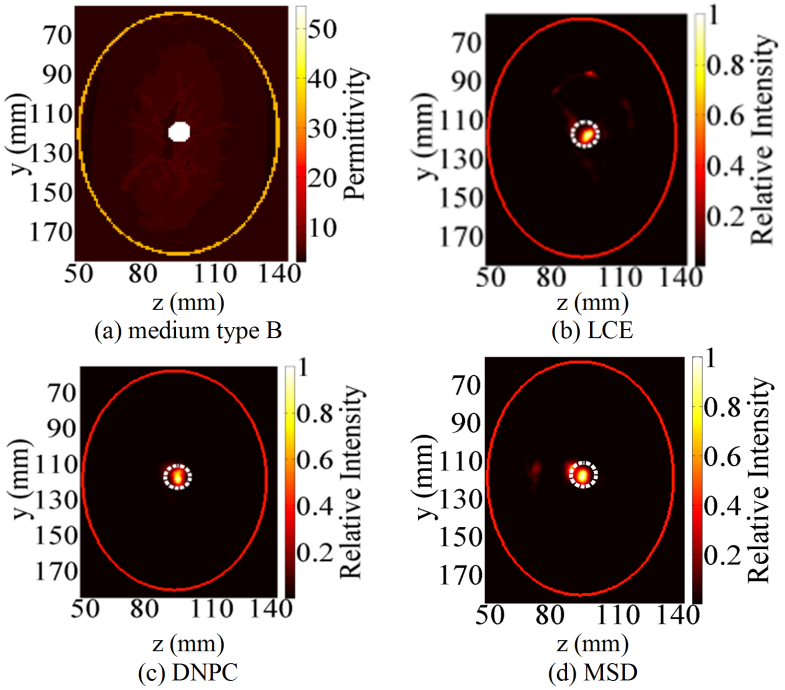

Fig. 5.7 S3: (a) 2-D slice of breast model with MT B. (b)-(d) Imaging results of LCE, DNPC, and MSD with entropy artefact removal. Tumour's actual position is indicated by dotted circles.

In S3 (see Fig. 5.7), the same breast model with S2 is used, but the entropy-based artefact removal rather than the ideal method is applied. As previously shown in Chapter 4.5.3, the

residual artefact signals seriously degraded the performance of all existing data-independent algorithms, making all of them failed to identify the tumour (see Fig. 4.10). Observing Fig. 5.7(b)-(d), all three newly proposed algorithms showed encouraging results, the tumour was accurately positioned and clearly identified. The SCR of LCE, DNPC, and MSD algorithms are 6.7, 6.5, and 6.9 dB, respectively. The positive SCR value indicates the correct localisation of tumour, which proves their strong artefact resistance than existing algorithms, including DAS, DMAS, MWDAS, and FDAS, all of which completely failed to localise the tumour [see Fig. 5.7(b)-(e)].

5.4.3 Breast of Medium Type C with Entropy Artefact Removal

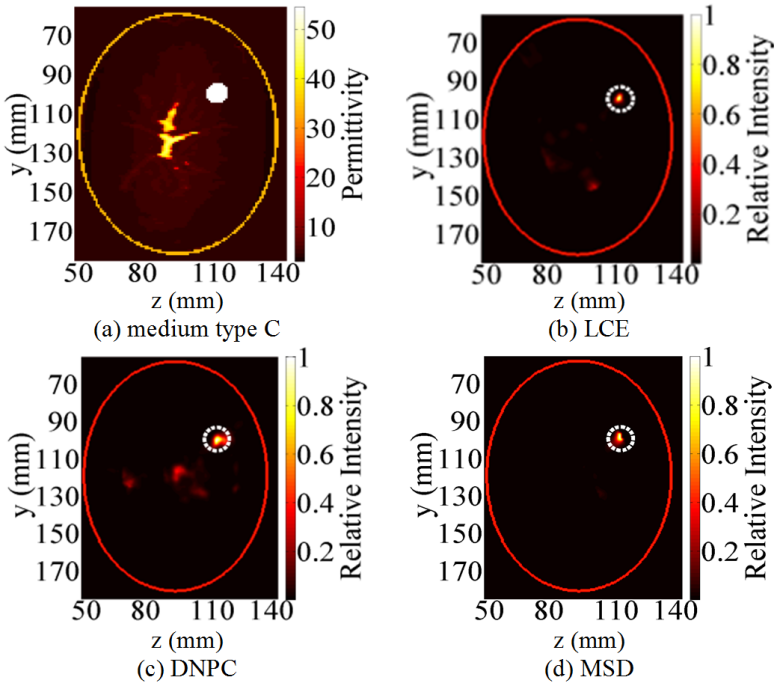

Fig. 5.8 S4: (a) 2-D slice of breast model with MT C. (b)-(d) Imaging results of LCE, DNPC, and MSD with ideal artefact removal. Tumour's actual position is indicated by dotted circles.

The performance of these techniques in breast models with fibro-glandular tissue was investigated in S4 (see Fig. 5.8). To independently investigate the effect brought by glandular tissues, S4 assumes that all artefact signals have been ideally removed. Compared with S2 (see Fig. 5.6), which did not consider the glandular tissue, it can be seen that the performance of three methods suffered due to the signal attenuation and dispersion

introduced by glandular tissues. In spite of reduced image sharpness, the three methods located the tumour with a high accuracy, whose peak intensity precisely corresponded to the dotted circle. Specifically, the decrease of SCR from S2 to S4 of LCE, DNPC, and MSD are 4.1, 2.5, and 0.1 dB, respectively. The smallest degradation was observed in MSD, which demonstrated the strength of utilising multiple spatial diversity. The best clutter rejection and overall image resolution are achieved by MSD in this case, which has the highest SCR of 6.5 dB, and SMR of 19.5 dB. In comparison, a small portion of clutter can be observed in the result of DNPC [see Fig. 5.8(c)] at position (y,z) = (120, 95) (mm), which has a SCR of 4.0 dB and is the smallest value among all algorithms in this scenario.

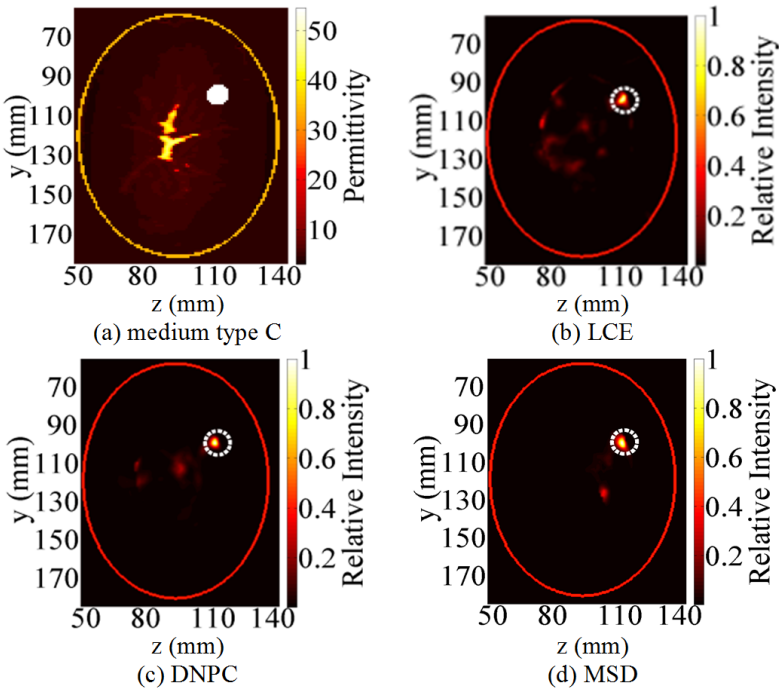

Fig. 5.9 S5: (a) 2-D slice of breast model with MT C and a tumour in fatty tissue. (b)-(d) Imaging results of LCE, DNPC, and MSD with entropy artefact removal. Tumour's actual position is indicated by dotted circles.

In S5 (see Fig. 5.9), the same breast model in S4 but with the entropy-based artefact removal method was considered. In this case, both glandular response and residual artefact signal can have adverse effect on tumour detection. Despite the challenge, fairly clear images with correct tumour localisation were provided by all three techniques, which proved their capability of distinguishing the scattering from tumour and that from glandular tissues. However, this comes with further increased clutter in the constructed

images. Compared with S4, the SCR of LCE, DNPC, and MSD decreased from 5.1 to 3.8, 4.0 to 3.9, 6.5 to 4.4 dB, respectively.

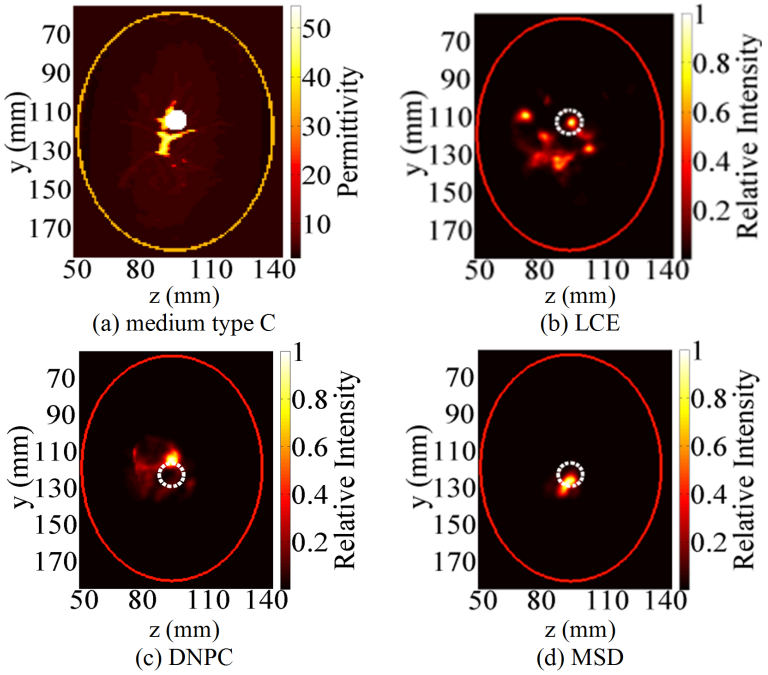

Fig. 5.10 S6: (a) 2-D slice of breast model with MT C and a tumour close to glandular tissue. (b)-(d) Imaging results of LCE, DNPC, and MSD with entropy artefact removal. Tumour's actual position is indicated by dotted circles.

Since a high percentage of breast cancers are invasive ductal carcinomas, which start at fibro-glandular regions [106], it is worth testing algorithm in cases considering tumours are very close to or grow from the glandular tissues. This new case is simulated in S6 (see Fig. 5.10), which can be challenging for algorithm to discriminate the easily overlapped tumour and glandular responses. Comparing Fig. 5.10(b) with Fig. 5.9(b), the performance of LCE deteriorated drastically. In this case, the backscattered signal from tumour and glandular tissues overlap seriously due to the small spacing, the local-region coherence-based reference waveform used in LCE can be a mixture of backscattered signals from heterogeneous tissues, resulting in serious clutter around the tumour. In contrast, the neighbourhood pairwise correlation-based weighting factor used in DNPC offers a much more improved clutter rejection [see Fig. 5.10(c)].

This scenario clearly illustrates the significance of properly designing the reference waveform. LCE uses the average of local signals as the reference signal to calculate the cross-correlation coefficients. When there is residual artefact, the average of signals could

be dominated by the artefact signal due to its much higher order of magnitudes than tumour response. With this distorted reference signal, which is no longer dominated by tumour response, the calculated weights at tumour positions could be comparable or even smaller than other positions, resulting in tumour location bias. In comparison, all the reference signal used for calculating neighbourhood pairwise correlation for RAR, DNPC, and MSD is the actually received signal at each antenna. This reference signal represents a single propagation path between the target and the antenna, which is independent from other antennas, thus it is less likely to be deformed. After calculating the correlation based on this reference signal with high robustness, high weights are more likely to be produced at tumour positions.

The imaging results confirmed the above analysis. For LCE, the SCR is 0.5 dB, whereas this value of DNPC and MSD are 4.0 and 3.1 dB, which offer much improved performance than LCE. This illustrates the stability of DNPC and MSD. For DNPC, the neighbourhood pairwise correlation measurement is more robust than the local group coherence used in LCE. Also its dynamic weighting can further suppress clutter signals. The selective combining of signals in MSD ensures the robustness and reduce the sensitivity to data abnormality. Furthermore, the adoption of multiple spatial diversity is achieved through exploiting those applicable neighbouring multistatic signals.

5.4.4 Breast of Medium Type D with Entropy Artefact Removal

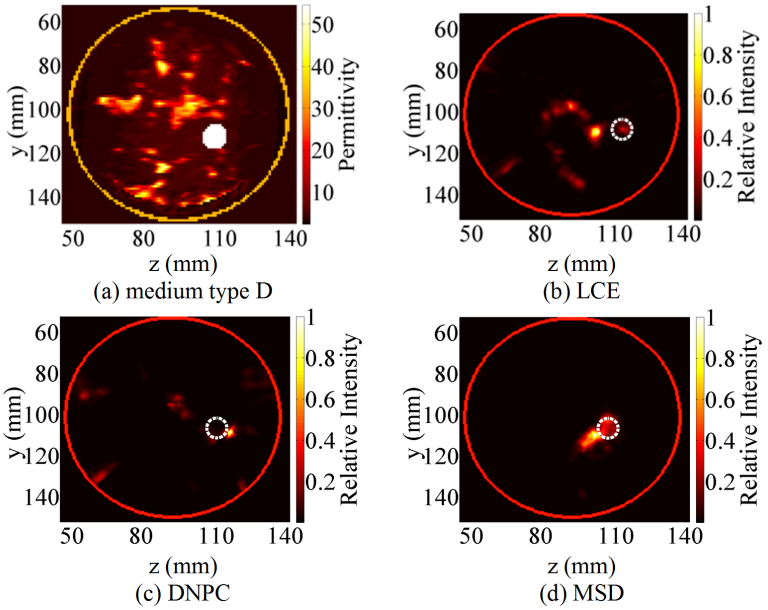

Fig. 5.11 S7: (a) 2-D slice of breast model with MT D and an off-centre tumour. (b)-(d) Imaging results of LCE, DNPC, and MSD with entropy artefact removal. Tumour's actual position is indicated by dotted circles.

The breast model with increased glandular tissues is considered in S7 [see Fig. 5.11(a)]. The percentage of glandular tissue in previous breast models is below 25%, whereas for this MT D, 25% to 50% among all are glandular tissues, which belongs to a denser category. The imaging results in S7 further verified the advantage of DNPC and MSD over LCE. Observing Fig. 5.11(b), LCE failed to localise the tumour, whereas DNPC and MSD still positioned the tumour properly [see Fig. 5.11(c)-(d)]. This scenario also showed the advantage of MSD over DNPC in terms of enhanced image readability. Although both DNPC and MSD identified the tumour, the image offered by MSD is clearer than that offered by DNPC. The three strong clutters in the result of DNPC [see Fig. 5.11(c)] at position (y, z) = (90, 55), (y, z) = (100, 95), (y, z) = (130, 60) (mm) are all diminished in the result offered by MSD [see Fig. 5.11(d)]. This is greatly desired in practice, which can help radiologists make more informed decision of tumour identification.

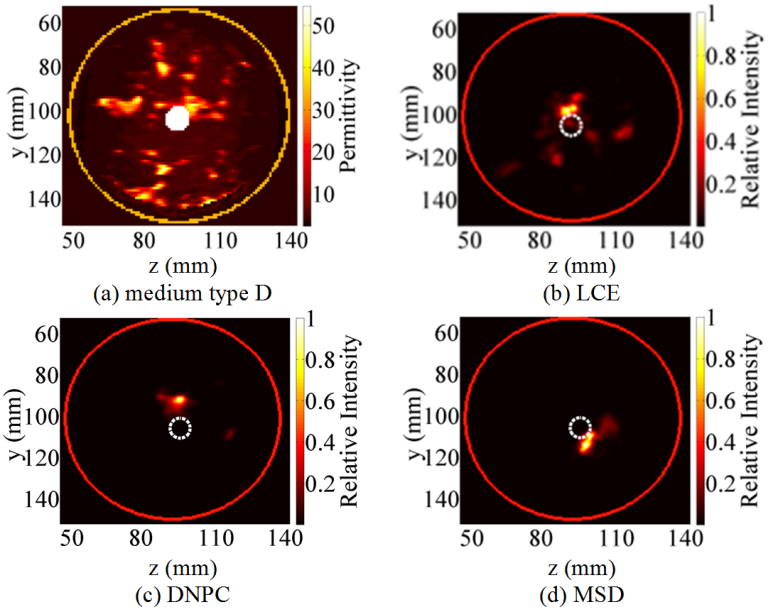

Fig. 5.12 S8: (a) 2-D slice of breast model with MT D and a tumour close to glandular tissues. (b)-(d) Imaging results of LCE, DNPC, and MSD with entropy artefact removal. Tumour's actual position is indicated by dotted circles.

In S8 (see Fig. 5.12), the tumour is moved closer to glandular tissues to mimic the invasive ductal carcinomas. It is noted that the localisation accuracy of these algorithms decreases when the tumour is surrounded by scattered glandular tissues. These sporadic glandular tissues considerably reduces the uniformity between different propagation channels, which leads to a huge mismatch between the assumed uniform and actually non-uniform channels. This can be observed by comparing the results of S6 (see Fig. 5.10) with that of S8 (see Fig. 5.12). In both cases, the tumour is located in the centre of breast, but with different distributions of the glandular tissues. From S6 to S8, the SCR of LCE, DNPC, and MSD dropped from 0.5 to -1.0, 4.0 to 1.2, 3.1 to 2.9 dB, respectively. Although all three imaging results do not exactly correspond to the tumour position, the peak of the reconstructed image by these algorithms are not far from the tumour, which can be used as a reference for tentative diagnosis.

5.4.5 Breast of Medium Type E and F with Entropy Artefact Removal

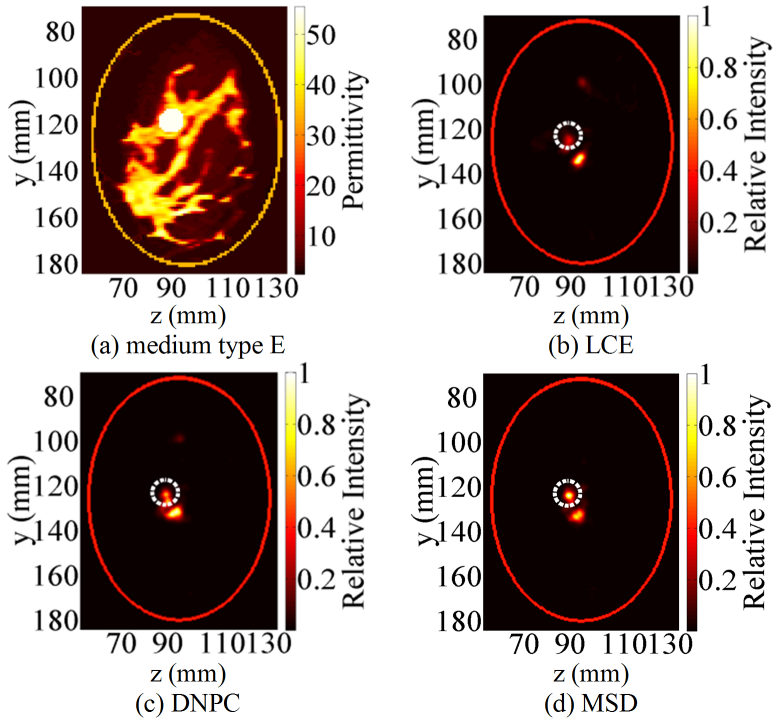

Fig. 5.13 S9: (a) 2-D slice of breast model with MT E and a tumour in glandular tissues. (b)-(d) Imaging results of LCE, DNPC, and MSD with entropy artefact removal. Tumour's actual position is indicated by dotted circles.

In S9, the breast with MT E is considered [see Fig. 5.13(a)]. Breast with MT E represents the severely dense category, and the percentage of glandular tissue in breast is between 50% to 75%. Without doubt, much more attenuation of backscattered signals is expected in this type of breast. Observing the results shown in Fig. 5.13(c)-(d), in spite of relatively clear images, the SCR of all three methods further decreased. From S8 to S9, a reduction of SCR with 0.8, 0.9, and 1.7 dB of the three methods is observed. Interestingly, all three images have strong clutters around the correct tumour position [see Fig. 5.13(b)-(d)], which is outside the dotted circle. But only the peak in the image offered by MSD corresponding to the correct tumour position, which explains its highest SCR of 1.2 dB. This again confirms the superiority of MSD algorithm over its monostatic counterparts.

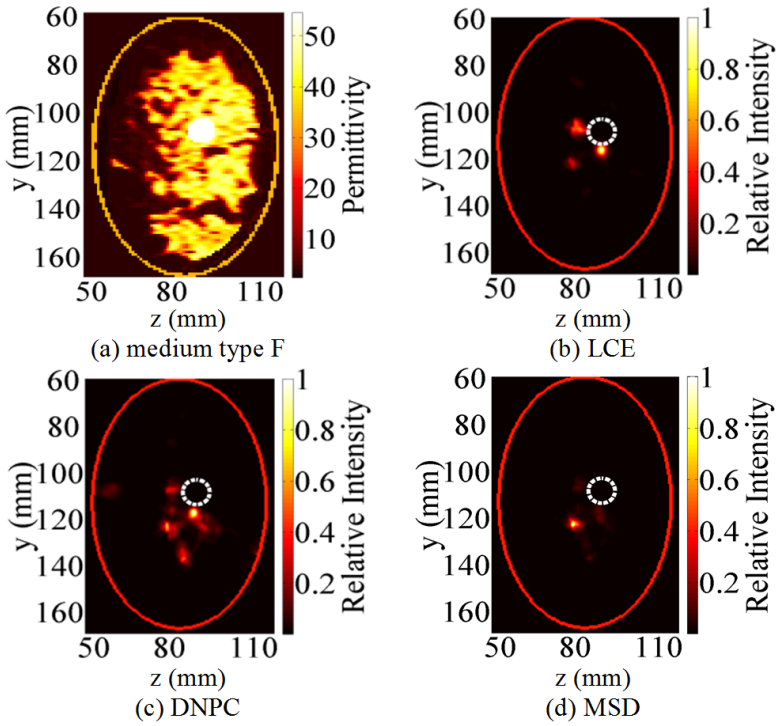

Fig. 5.14 S10: (a) 2-D slice of breast model with MT F and a tumour in glandular tissues. (b)-(d) Imaging results of LCE, DNPC, and MSD with entropy artefact removal. Tumour's actual position is indicated by dotted circles.

In S10 (see Fig. 5.14), the breast with MT F is applied, in which the glandular tissue percentage can be over 75% among all tissues. For this extremely dense breast, none of the proposed algorithms is able to position the tumour correctly. In this case, the large mass fibro-glandular tissue could generate the backscattering which is as strong as that from the tumour. Additionally, the seriously damaged uniformity of propagation channel makes it challenging to identify the tumour correctly solely based on the reflected energy. The difference among propagation channels, i.e., from transmitter to a scattering point in breast and back to receiver, can be caused by the variance of skin thickness and the compositions of heterogeneous tissues along each path, and the later one is the key factor. In sparse breasts which are mainly composed of fatty tissues, the propagation channels are relatively uniform and thus an assumed average propagation velocity could closely represent the characteristics of actual propagation channels. With significantly increased heterogeneity mainly caused by fibro-glandular tissues, however, this assumption used in the imaging algorithm no long holds, rendering the malfunction of these techniques. To address this

challenge, potential solutions such as contrast agent-based tumour detection [106, 209], and morphology-dependent lesion differentiation [105] could be considered.

5.5 Comparison and Analysis of Proposed Algorithms

5.5.1 Algorithm Comparison

In this section, the difference between proposed algorithms are analysed and compared. For clarity, the first proposed RAR algorithm is used as a benchmark.

For LCE algorithm, its first difference from RAR is the way of generating weighting factors. Specifically, the selected reference signal for calculating correlation coefficient is different. RAR uses the neighbourhood pairwise correlation, whereas LCE employs a local grouping averaged signal. Secondly, LCE utilises a two-step maximum combining, in which both the most usable signals and weights are selected based on their correlation coefficients, whereas RAR only employs one-step maximum combining which only selects highest weights, and uses all shifted signals for calculating the intensity of pixels.

The first difference between DNPC and RAR is the modified calculation of neighbourhood pairwise correlation. For each antenna ring, the correlation is calculated separately in DNPC. The new correlation between signals received at end-to-end antenna elements are also included for producing consistent weighting coefficients. Additionally, the dynamic weighting of signals for effective combining is applied in DNPC, whose efficacy and superiority were confirmed by simulation results.

As for MSD, its first difference from RAR is its signal quality evaluation procedure for selective combining. This ensures only high-quality signals that possess a higher portion of effective tumour response can be used for computing the intensity of pixel. Furthermore, besides monostatic signals, extra signals which bear useful tumour response collected through multistatic method are exploited. These two extra modules in MSD secures the effectiveness and desirable detectability, which is particularly effective for tumour detection in severely dense breasts.

5.5.2 Performance Analysis

SCR and SMR statistics of algorithms are summarised in Table 5.1. For comparison, the performance statistics of RAR are also listed.

Based on the calculated average in ten different scenarios, MSD performs best among all, which has the highest SCR and SMR on average. This proves the effectiveness of using multiple spatial diversity of signals. Despite that LCE provides decent tumour detectability in S1 to S6, its imaging performance deteriorate seriously for dense breasts, which results in its smallest SCR and SMR.

DNPC method is superior to RAR algorithm in general. Specially, in eight out of ten scenarios, the SMR of DNPC outperforms RAR (S3 to S10); and in five out of ten scenarios (S3, S6 to S9), the SCR of DNPC is higher than that of RAR. With an improved SMR, the non-tumour area is overshadowed by DNPC, thereby highlighting the tumour and reducing the chance of misidentification. This confirms the efficacy of dynamic weighting, which strengthens the overall image readability.

For fairness, it should be mentioned that the improved performance of DNPC and MSD over RAR is at the expense of increased algorithm complexity. For DNPC, this is caused by the additional dynamic weighting of signals. For MSD, from the shifting of multistatic signals to signal quality evaluation and combining, more processing steps than RAR are required. Therefore, depending on the specific application scenario, DNPC and MSD can be used in cases with high-robustness requirement, whereas RAR can be applied in cases call for fast image reconstruction or with limited computing power.

5.6 Conclusion

In this chapter, three new algorithms, namely, LCE, DNPC, and MSD, are proposed. The examination of these algorithms under a variety of challenging scenarios is conducted, which is followed by discussion and analysis. Strong artefact resistance of the proposed algorithms over existing data-independent methods is observed. In these proposed algorithms, both monostatic and multistatic signal acquisition, static and dynamic weighting,

selective and non-selective signal combining are investigated. RAR offers an optimum trade-off between performance and complexity. The best performance was achieved by MSD, which exploited selective combining of neighbouring multisatic signals, and offered strong robustness even in heterogeneously dense breasts.

Besides robustness, the computational efficiency of image reconstruction algorithms is of crucial importance, as it can significantly reduce the processing time, and this will be studied in next chapter.

Chapter 6

Accelerated Image Reconstruction Mechanisms

6.1 Introduction

Motivated by the high complexity of UWB imaging algorithms, the accelerated image reconstruction (AIR) mechanism for UWB breast cancer detection is investigated. Two AIR schemes are proposed in this chapter, which is organised as follows. Literature review on fast image forming techniques are presented in Section 6.2. In section 6.3, a redundancy elimination (RE) scheme is proposed, of which the effectiveness is validated by theoretical analysis and simulations. In section 6.4, a novel annulus predication (AP) scheme is proposed. Extensive analysis and simulation results demonstrate the strong accelerating capability of AP. The performance of imaging algorithms with and without AP is examined, and a remarkable speedup is offered by AP at the expense of graceful performance degradation. A comparative analysis of the proposed AIR schemes is provided in Section 6.5, which is followed by the conclusions in Section 6.6.

6.2 Literature Review

Besides improving the robustness of UWB detection and imaging techniques, another obstacle need to be overcome is computational complexity. Fast image reconstruction is

desired for almost all applications, and is particularly critical for scenarios which require real-time results [210]. Several factors can restrict the speed of UWB imaging, including the size of imaging scene, the number of collected signals, sampling number of signals, and image resolution requirement. To reduce the processing time of image reconstruction, two strategies can be employed: 1) hardware enhancement, such as the use of high performance computing (HPC) or graphics processing units (GPUs); and 2) introduction of accelerated calculation approaches. The second strategy is the focus of this study.

Fast image reconstruction has attracted much attention and various techniques have been developed, which can be divided into quantitative and qualitative categories. Quantitative imaging is based on the inverse scattering, through which the retrieval of geometry and/or constitutive parameters of the target can be achieved. To reduce computational burden, a range of strategies have been exploited. For example, [112] proposed a fast multipole method (FMM), which accelerated the volumetric target reconstruction without compromising accuracy. In FMM, the matrix inversion was not required, and the calculation speed was improved by 40 times. As for qualitative UWB SAR imaging, the main complexity stems from matrix–vector multiplications which is inevitable in compressing sensing (CS) theory. This multiplication is both time-consuming and requires a large memory for variable storage. To reduce complexity, a segmented reconstruction method for CS-based SAR is proposed in [211]. This method splits the large-scale imaging area into small pieces and then combine all pieces back for final reconstruction. In spite of improved computational and memory storage efficiency, this approach may lead to serious reconstruction error with the increased number of segmented pieces. Another way to speed up the matrix-vector multiplication is through the non-uniform fast Fourier transform (NUFFT) as presented in [212] and [213], whose efficacy of NUFFT for fast and accurate imaging was verified, while restricting the introduced error within a low level. Another promising method for fast imaging was realised by the employment of uniform rectangular array (URA) [213]. Both theoretical analysis and experimental results for TWI application demonstrated the validity of URA, which offered a 60 times speed up than the approach without using URA.

However, none of these acceleration techniques are designed for UWB breast imaging, rendering the application of these methods inappropriate or infeasible. Even the URA method which is developed for UWB TWI is inapplicable for UWB breast imaging, and there are three reasons. First, URA is only suitable for uniform rectangular planar antenna arrays. The planar antenna, however, has limited tumour detection capability compared with the circular antenna array, which has been studied and reported in [197]. Second, the assumption made in URA that the spacing of pixel should be equal to that of antenna array elements cannot be met in UWB breast imaging. This is due to the widely different resolution requirements in TWI and breast imaging. For TWI, is normally human body and centimetre-level spacing of image pixels is sufficient, whereas for breast cancer detection, target is the early-stage tumour and a millimetre imaging resolution is a minimum. Third, URA only considered the cross-range imaging resolution, whereas the down-range resolution is not taken into account, which further limited its practicability.

Therefore, novel accelerating techniques for UWB breast cancer imaging are needed. In this study, two schemes for accelerating data-independent UWB breast imaging algorithms are proposed, namely, redundancy elimination (RE) and annulus prediction (AP), and their rationale and details are introduced in following sections.

6.3 Redundancy Elimination (RE) for Fast Computation

6.3.1 Complexity Bottleneck

UWB imaging is a pixel-based method, which is opposed to the boundary extraction imaging techniques such as the one introduced in [214]. Therefore, the intensity of each pixel within imaging area need to be calculated. For clear target identification, high-resolution images have been favourable as a large number of pixels of the reconstructed image is vital for reliable distinction between target and its surroundings [213]. This is because certain target may only occupy several cross-range cells or be confined to a single resolution cell [215]. Hence, the complexity of algorithm can be gravely large, leading to a lengthy image reconstruction process.

Table 6.1 Time complexity of DAS imaging algorithm.

Number of signals (A)	Signal sampling points (K)	Pixel number (L)	Complexity
4.8e1	1.5e3	6.4e6	$O(AKL)$

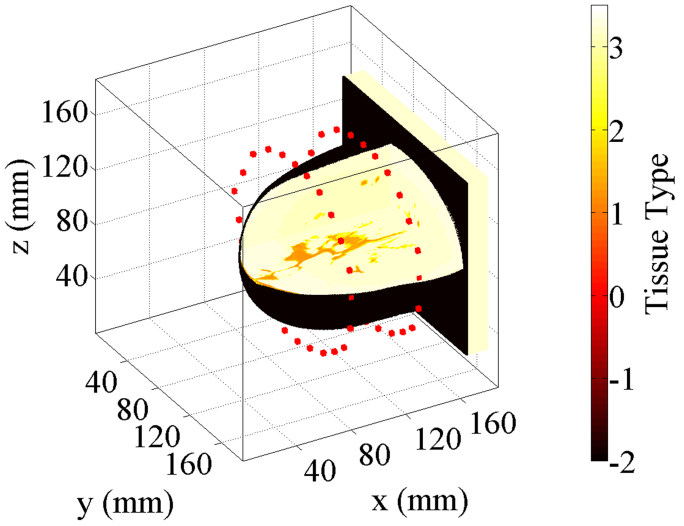

Fig. 6.1 Breast model with two concentric rings of 24 antennas (indicated by solid dots) surrounding the breast. The categorised tissue types are represented by different values: fat-high (3.1), fat-median (3.2), fat-low (3.3), fibro-glandular (FG)-high (1.1), FG-median (1.2), FG-low (1.3), and skin (-2). The outer ring of antennas is at x = 80 mm (antennas 1 to 24), and the inner ring (antennas 25 to 48) is at x = 130 mm, in which the position of both rings are related to the chest wall. The same yz plane coordinates for both rings of antennas are: (39, 101), (50, 120), (63, 140), (82, 153), (100, 158), (116, 159), (131, 158), (147, 154), (162, 145), (174, 132), (185, 116), (192, 97), (189, 74), (178, 56), (166, 47), (152, 39), (135, 34), (119, 32), (103, 31), (84, 38), (71, 44), (59, 55), (43, 69), and (37, 83).

The complexity of algorithm is measured by the number of arithmetic operations, which is determined by different aspects of inputs. For UWB imaging algorithm, three aspects which determine the complexity are the number of signals, signal sampling points, and the number of pixels. The number of signals varies depending on the number of antennas, and the selected signal collection method, which can be monostatic or multistatic. The signal sampling points decide the arithmetic number for each signal, and the pixel number is determined by the size of imaging area and required resolution. Take the monostatic DAS algorithm as an example, its asymptotic complexity is $O(AKL)$, in which A is the number of signals, K is signal sampling points, and L is pixel number of imaging area. The value s of A, K, and L are summarised in Table 6.1, which is for imaging the breast model shown in Fig. 6.1. It is noted that pixel number L is the decisive one among all three

factors, which is three orders of magnitude higher than signal sampling points K, and five orders of magnitude higher than the signal number A. Accordingly, exploring an efficient way to reduce the complexity of pixel-related operations can significantly alleviate the overall computational burden.

6.3.2 Redundancy Classification

As analysed in Chapter 4.7, all UWB data-independent imaging algorithms share the same time-shifting module for signal phase compensation. This module calculates the propagation time delay between each pixel and antenna based on their space coordinates, then the signal is shifted by the estimated time delay for each pixel sequentially, and the process is illustrated in Fig. 6.2.

Assuming a monostatic signal collection is applied, thus A signals can be collected from A antennas. Let $S_i(n)$ be the ith received signal from antenna $\mathrm{T_i}$, where $n = 1, 2, ..., K$, K is the number of signal sampling points. Let L be the total number of pixel of imaging area [see Fig. 6.2(a)]. For clear illustration, an enlargement of partial imaging area with numbered pixels is provided in Fig. 6.2(b). The estimated propagation time delay for the ith antenna at the lth pixel is expressed as τ_{i_l}, which is the two-way travel time from the ith antenna to pixel l. As shown in Fig. 6.2(b), for $\mathrm{T_1}$, corresponding time delays include $\tau_{1\_1}, \tau_{1\_2}, ..., \tau_{1\_20}$, whereas for $\mathrm{T_2}$, corresponding time delays include $\tau_{2\_1}, \tau_{2\_2}, ..., \tau_{2\_20}$. Propagation distance is calculated based on their coordinates, and the propagation speed of signal is calculated under the assumption that the medium has a

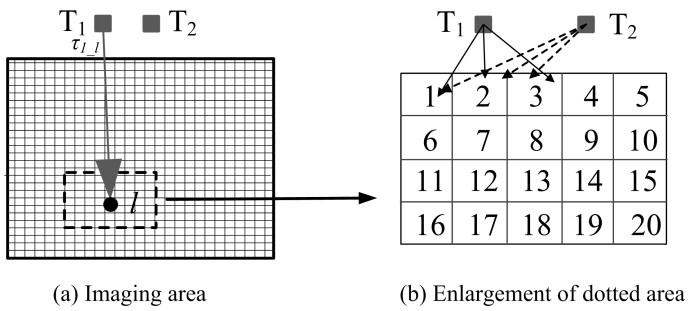

Fig. 6.2 Propagation time delay calculation between antenna and pixel in UWB data-independent imaging algorithms. (a) Antenna $\mathrm{T_1}$, $\mathrm{T_2}$ and imaging area composed of L pixels. (b) Enlargement of partial imaging area of (a) with numbered pixels.

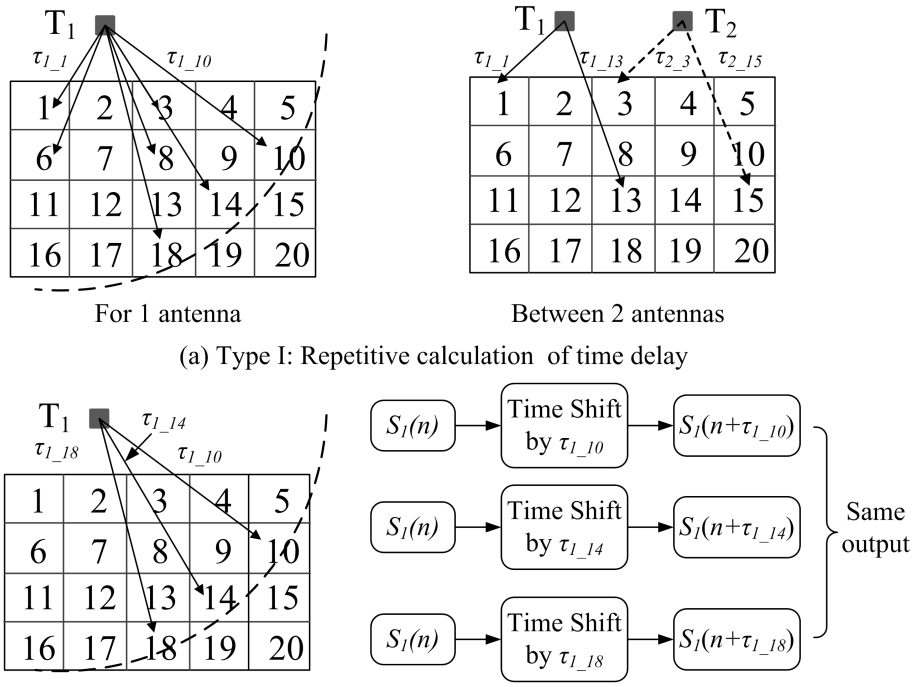

Fig. 6.3 Classification of redundancies in non-optimised UWB data-independent algorithms for obtaining shifted signals between antenna-pixel pairs. (a) Type I: Repetitive calculation of time delays. (b) Type II: Repetitive operation of time shifting signals.

constant relative permittivity. Therefore, *AL* time delays and corresponding time-shifted signals are needed for all pixel-antenna pairs. As for the example shown in Table 6.1, this involves 3.1e8 calculations, which is the product of *A* and *L*. This is a huge number of computations, which can be extremely time- and resource-consuming. However, it is observed that plentiful redundant operations exist in this process, which can be classified into two categories (see Fig. 6.3).

The first type of redundancy (Type I) is the repetitive calculation of time delays. This is performed for each antenna, and for those antenna-pixel pairs with the same relative distance. As shown in Fig. 6.3(a), for antenna T_1, all pixels that have a same distance to T_1 will be assigned a same time delay. All pixels are equally spaced, since pixel 1, T_1, and pixel 3 are equally space along the horizontal direction, thus time delay τ_{1_1} and τ_{1_3}, τ_{1_6} and τ_{1_8} are exactly the same. τ_{1_10}, τ_{1_14}, and τ_{1_18} are also equivalent, because these three pixels have a same distance to T_1, which form the circle indicated by a dotted arc. Additionally, because time delay is determined by the relative distance between antenna

and pixel, there can be numerous time delays with same value between different antennas. This can be seen in the right-hand sub-figure of Fig. 6.3(a). τ_{1_1} and τ_{2_3}, τ_{1_13} and τ_{2_15} are exactly the same due to their same relevant spacing. Since all time delays are needed for time-shifting signals, these repeated computations can cause a huge waste and slow the computing process.

The second type of redundancy (Type II) is the actual operation of time-shifting of each signal by the estimated time delay. As shown in Fig. 6.3(b), for pixel 10, 14, and 18, due to their same time delay, for the signal S_1 received at T_1, the output of time-shifted signals at these three pixels, namely, $S_1(n+\tau_{1\_10})$, $S_1(n+\tau_{1\_14})$, $S_1(n+\tau_{1\_18})$, are exactly the same. Therefore, these three time-shifting operations are repeated.

Type II redundancy can consume more computing power than Type I. In Type I redundancy, to calculate time delay τ, only the distance D between two points and estimated velocity v are needed, then the time delay can be obtained through basic arithmetic operations such as summation and multiplication, and this can be illustrated as

$$\tau = D/v = \sqrt{(x_1-x_2)^2+(y_1-y_2)^2+(z_1-z_2)^2}/v \tag{6.1}$$

where (x_1,y_1,z_1) and (x_2,y_2,z_2) are the coordinates of antenna and pixel, respectively. v is the estimated average propagation velocity in breast, and it can be calculated as [192] $v = c_0/\sqrt{\varepsilon_{r\_ave}}$, where c_0 is the speed of light and ε_{r_ave} is the estimated average dielectric property of breast through an appropriate patient-specific dielectric property estimation algorithm such as the one developed by Winters *et al.* [205]. Without distinguishing between addition and multiplication, the number of arithmetic operations in (6.1) is 8, in which square root is regarded as 1 basic operation. In Type II redundancy, the time-shifted signal $S_i(n+\tau_{i\_l})$ can be obtained through a discrete filter. The filtering process adds a single delay to the input signal, and the signal is shifted by the number of samples. This process can be expressed as

$$S_i(n+\tau_{i\_l}) = \text{filter}[S_i(n), \tau_{i\_l}] \tag{6.2}$$

which has an asymptotic complexity of $O(FK^2)$, where $K = 1500$ is signal sampling points, and F is the filter length. Obviously, Type II has a much higher complexity than Type I and more execution time is expected.

Therefore, to improve computational efficiency, a new redundancy elimination (RE) mechanism to accelerate image formation is proposed.

6.3.3 Redundancy Elimination

The proposed RE scheme employs an uniform computing and indexing of time-shifted signals for all antenna-pixel pairs, which avoids both repetitive time delay calculation and the operation of time-shifting signals. Due to the enormous quantity of pixels, the overall running time can be effectively shortened. Let l be the lth pixel of L, $S_i(n)$ be the ith signal

Pseudocode 6.5 Calculate time-shifted signals without RE

```
1: INPUT: S_i(n), i = 1,...,A          % A input signals
2: for i = 1 to A do                   % ith signal of A
3:     for l = 1 to L do               % lth pixel of L
4:         Calculate τ_{i_l}           % Calculate time delay for current antenna-pixel pair
5:         Shift S_i(n) by τ_{i_l}     % Obtain shifted signal
6:         Store S_i(n + τ_{i_l})      % Store shifted signal
7:     end for l                       % End of iteration of pixels
8: end for i                           % End of iteration of signals
9: OUTPUT: S_i(n + τ_{i_l}), i = 1,2,  % Shifted signal for all antenna-pixel pairs
   ...,A, l = 1,2,...,L
```

received from the ith antenna of A, where $n = 1,2,...,K$ and K is signal sampling points, τ_{i_l} be the time delay between the ith antenna and l, and $S_i(n+\tau_{i\_l})$ be the time-shifted signal for the ith signal at l. To calculate time-shifted signals for all antenna-pixel pairs, the implementation in methods with and without RE are presented in Pseudocode 6.5 and 6.6, respectively.

RE introduces a repetition-eliminating module which completely removes the two types of redundancies. Observing steps 5 to 11 in Pseudocode 6.6, for a certain signal $S_i(n)$, the time delay calculation and corresponding shifting signal operation will only be performed once throughout the whole computation. For a time delay, after comparing it with already calculated time delays, if the time delay exist, then corresponding time-shifted signal

Pseudocode 6.6 Calculate time-shifted signals with RE

```
INPUT: S_i(n), i = 1,...,A          % A input signals
for i = 1 to A do                   % ith signal of A
    for l = 1 to L do               % lth pixel of L
        Calculate τ_{i_l}           % Calculate time delay
    .....
        if τ_{i_l} exist then       % If this is an existing time delay
        Copy shifted signal         % Copy corresponding shifted signal
        end if                      % End of if
        if no τ_{i_l} exists then   % If this is a new time delay
        Shift S_i(n) by τ_{i_l}     % Obtain shifted signal
        Store τ_{i_l} & S_i(n+τ_{i_l}) % Store time delay and corresponding shifted signal
        end if                      % End of if
    .....
    end for l                       % End of iteration of pixels
end for i                           % End of iteration of signals
OUTPUT: S_i(n+τ_{i_l}), i = 1,2,    % Shifted signal for all antenna-pixel pairs
...,A, l = 1,2,...,L
```

will be indexed and copied. Only for the new time delays, corresponding shifted signals will be calculated. The comparison between the time delay of current pixel and existing time delays can be implemented by calculating their difference. If there is the outcome is zero, which means that current time delay already exists, then corresponding shifted signal will be copied and stored for this pixel. It is admitted that this indexing process will introduce new calculations, but it avoids a huge number of operations of shifting signals [see Fig. 6.3(b)]. For an imaging region composed of 13,000 pixels, simulation results showed the number of repeated time delays is 8,450, occupying 65% among all calculations. Considering the complexity of time-shifting signal as illustrated in (6.2), the extra complexity introduced by indexing is minor, thereby reducing the overall running time. All procedures involved in RE (Pseudocode 6.6) are fully implemented, and its effectiveness is proved by the simulation results shown in next section.

6.3.4 Simulation Results and Analysis

In this section, the following simulation parameters are used to assess the performance of RE: $A = 48$ and $K = 1500$. The methods with and without using RE for calculating time-shifted signals are implemented in Matlab R2014a. The testing environment is on a

PC with Intel (R) Core (TM) 2 Duo CPU E7500 2.93GHz (2 CPUS), and simulation results are displayed in Table. 6.2. To verify the performance in different scenarios, their running time as a function of imaging pixel number L is considered, which simulates different sizes of the imaging region.

Table 6.2 Running time (RT) of calculating time-shifted signals by different methods without and with RE measured in seconds. The speedup is measured by the ratio of running time of different methods, which is unitless.

Pixel Number (L)	Running Time (s)		Speedup = RT1/RT2
	Without RE (RT1)	With RE (RT2)	
10^2	20.3	18.7	1.1
20^2	78.4	62.8	1.2
30^2	172.9	135.6	1.3
40^2	307.2	212.0	1.4
50^2	512.6	300.1	1.7
60^2	731.1	422.3	1.7
70^2	984.9	492.6	2.0
80^2	1315.2	626.3	2.1
90^2	1659.2	790.1	2.1
100^2	1943.2	883.2	2.2

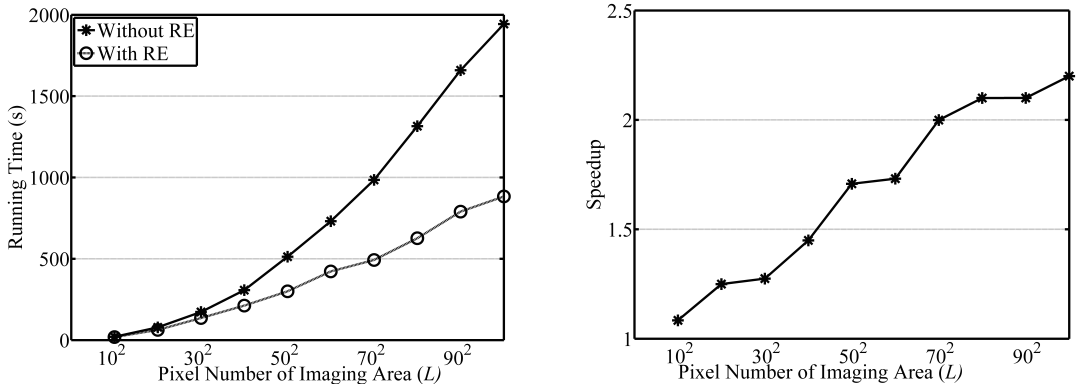

(a) Running time (b) Speedup offered by RE

Fig. 6.4 Running time comparison between methods with and without RE as a function of the pixel number of imaging area L. (a) Running time. (b) Speedup offered by RE.

Simulation results showed that the method with RE is faster than its counterpart without using RE in all cases with varied numbers of pixels, ranging from 100 to 10,000 (see Table 6.2). It is noted that when the imaging area is small, the running time of the two methods is comparable. Specifically, for an area composed of 100 pixels, the running times are 20.3 and 18.7 seconds, respectively, and the speedup is only 1.1. When the pixel

number of imaging area increases to 10,000, RE is 2.2 times faster, and 1060 seconds are saved. Observing Fig. 6.4(b), the exponentially increasing trend of speedup offered by RE is particularly encouraging, indicating an increased saving of time can be obtained for even larger imaging regions.

The favourable speedup offered by RE comes at zero performance loss, because its efficiency is accomplished by removing those purely repeated operations. The time-shifted signals through the method with RE is exactly the same as the outcome offered by the method without using RE. Furthermore, RE is flexible and has no application restricts. Unlike the URA method introduced in [213], RE is independent of antenna configurations and can be used for both planar and circular antenna arrays. RE does not require the same spacing of pixels and that of antenna elements, which is required in URA. RE also ensures both cross-range and down-range resolution since it transverses every single pixel in a row-by-row and column-by-column way, both horizontal and vertical directions are treated equally. Lastly, RE has a great applicability, which is suitable for a range of algorithms. For all data-independent UWB imaging algorithms which involve the time-shifting module, the RE mechanism can be applied in a straightforward way.

6.4 Annulus Prediction (AP) for Fast Computation

6.4.1 Rational

To further speedup the calculation of time-shifted signals, a novel annulus predication (AP)-based acceleration scheme is proposed in this section.

As mentioned in previous section, all signals need to be time-shifted for every single antenna-pixel pair. Thus, for a certain imaging area, there is a corresponding time delay matrix for each antenna, and each element in this matrix stores the time delay for each antenna-pixel pair and corresponding time-shifted signals. The time delay distribution of different antennas for the same imaging area are displayed in Fig. 6.5. It is noted that all time delay matrices show an uniform annulus pattern because of the same radius-based calculation. Considering the pixel spacing can be as small as 1 mm, the time

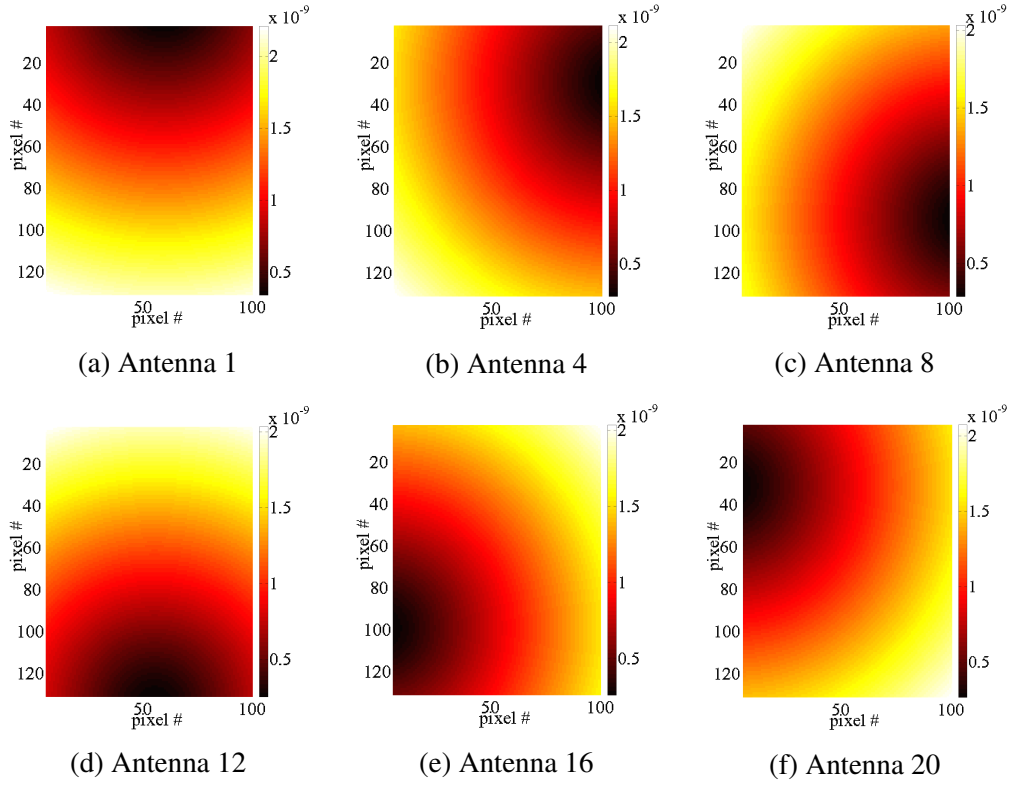

(a) Antenna 1 (b) Antenna 4 (c) Antenna 8

(d) Antenna 12 (e) Antenna 16 (f) Antenna 20

Fig. 6.5 Time delay (unit: second) matrices of different antennas for the cross-section x = 95 in the model shown in Fig. 6.1. (a) to (f) correspond to antenna 1, 4, 8, 12, 16, and 20, respectively, and the coordinate of numbered antennas is defined in caption of Fig. 6.1.

delay difference for adjacent pixels is very small. Therefore, an efficient annulus-based prediction of time delay over the whole imaging region is exploited.

In the proposed AP scheme, the same time delay is employed for all pixels which locate within the same annulus. This predicted scheme is flexible since the number of divided annulus zones can be varied. When the number of predicted annulus zones is large, each annulus would be fine enough to distinguish all pixels, which would produce the same output as original pixel-by-pixel computation. If the number of annulus decreases, one calculated time delay would represent an annulus area composed of certain number of pixels. Decreased accuracy is expected due to this approximative calculation of time delays, but this can lead to much faster computation. However, the number of annulus cannot be too small. If only very few annulus zones are used to represent the whole area, in spite of a much improved calculation speed, the inaccuracy caused by this prediction could be intolerant. Therefore, AP offers a trade-off between performance and complexity, and the detailed procedures of AP is introduced in next section.

6.4.2 Procedure

There are four steps involved in AP, including time delay range estimation, annulus zone division, calculation of time-shifted signals, and matching between pixels and predicted zones.

Step 1: Estimate the range of time delays. To divide the entire imaging area into several zones, the range of time delay for each antenna needs to be firstly estimated. This can be implemented by calculating the time delay of the first row and the last row pixels, which suffices the range estimation and introduces negligible computation. As illustrated in Fig. 6.6, the first row and last row pixels within the imaging region are pixel 1 to 5, and 16 to 20, respectively [see Fig. 6.6(a) and (b)]. The minimum and maximum time delay for the ith signal received at antenna Ti denoted by τ_{i_min} and τ_{i_max} can be obtained, which are the minimum among time delays of first row pixels, and the maxima among time delays of last row pixels, respectively [see Fig. 6.6(c)].

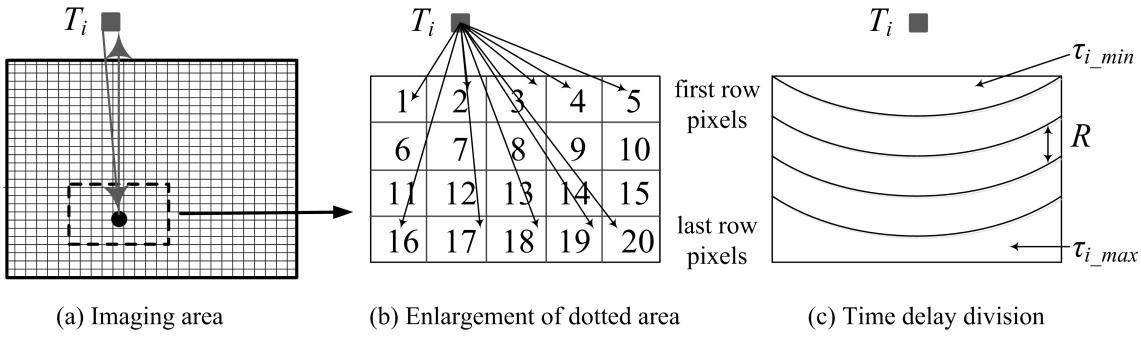

Fig. 6.6 Time delay range calculation. (a) Imaging area. (b) Enlarged partial imaging area with numbered pixels. (c) Predicted time delay matrix comprising divided annulus zones.

Step 2: Annulus zone-based time delay division. The whole imaging area is then linearly divided into N annulus zones with a width of R [see Fig. 6.6(c)]. Within each zone, the same time delay and corresponding shifted signal is applied for all pixels. The interval R represents the width of each annulus and it can be obtained as:

$$R = (\tau_{i\_max} - \tau_{i\_min})/(N-1). \tag{6.3}$$

Accordingly, the whole time delay matrix TD_i for the ith signal is composed of N time delays, corresponding to N annulus zones, which can be expressed as

$$\begin{aligned} TD_i =& [\tau_{i\_min}, \tau_{i\_min} + R, ..., \tau_{i\_min} + (N-1)R] \\ =& [TD_{i\_1}, TD_{i\_2}, ..., TD_{i\_N}]. \end{aligned} \tag{6.4}$$

N is a much smaller number than the total number of pixels L. For instance, L can be several millions, whereas N can be only several hundreds. Therefore, the annulus prediction-based calculation can offer a significant reduction of computation complexity.

Step 3: Calculate time-shifted signals for all annulus zones. For each annulus zone, time-shifted signals are calculated based on the estimated time delay. Specifically, for the first annulus zone with time delay TD_{i_1}, corresponding shifted signal is $S_i(n + TD_{i\_1})$, and this process repeats for all N annulus zones. Therefore, for N time delay zones, N shifted signals are obtained. The annulus-zone-based shifted signal vector ZS_i can be denoted as

$$ZS_i = [S_i(n + TD_{i\_1}), S_i(n + TD_{i\_2}), ..., S_i(n + TD_{i\_N})]. \tag{6.5}$$

Step 4: Match pixels to predicted time delays and obtain corresponding shifted signals. The match is conducted based on the minimum distance between the actual time delay of each pixel and the predicted time delays of annulus zones. Let τ_{i_l} be the time delay of the lth pixel. Firstly, the closest time delay in TD_i will be indexed for τ_{i_l}. This can be realised by calculating the difference between τ_{i_l} and each element in TD_i, which is a simple process since there are only N elements in TD_i. Secondly, after indexing the closest time delay, corresponding time-shifted signal will be copied for this pixel. Assume the xth element in TD_i is the closest predicted time delay for τ_{i_l}, where x can be $1, 2, ..,$ and N, then corresponding shifted signal $S_i(n + TD_{i\_x})$ will be copied and stored for this pixel. This process will go over all pixels, and all pixels will have their time-shifted signals, which can be used for subsequent steps involved in algorithms for image reconstruction.

The procedure of AP scheme is illustrated in Pseudocode 6.7. Depending on the selected number of annulus zones N, corresponding predicted time delay matrix TD_i would be different. The larger the N is, the higher accuracy can be ensured, whereas the

Pseudocode 6.7 Calculate all time-shifted signals with AP

INPUT: $S_i(n), i = 1,...,A$ % A input signals
for i = 1 to A do % ith signal of A
    Estimate τ_{i_min} and τ_{i_max} % Obtain time delay range
    Obtain TD_i % Obtain annulus-based predicted time delay
    Obtain ZS_i % Time shift the signal for each annulus
     for l = 1 to L do % lth signal of L
        Calculate τ_{i_l} % Calculate time delay for current pixel
        Match τ_{i_l} with TD_i % Match with predicted annulus zones
        Copy $S_i(n+TD_{i\_x})$ % Copy the matched time-shifted signal
    end for l % End of iteration of pixels
end for i % End of iteration of signals
OUTPUT: $S_i(n+\tau_{i\_l}), i = 1,2,...,A, l = 1,2,...,L$ % Shifted signal for all antenna-pixel pairs

smaller the N is, the predicted time delay matrix would have decreased accuracy. This may cause degradation of performance, but can produce a much faster computation speed. Specifically, for the same time delay matrix, depending on selected N, the predicted time delay matrix would have different levels of accuracy. As displayed in Fig. 6.7, five different values of N are used, including 112, 56, 28, 14, and 7. Obviously, when N is large enough [see Fig. 6.7(b)], each pixel will be treated individually and can be clearly differentiated, this offers the highest accuracy and matched degree with the original time delay matrix [see Fig. 6.7(a)]. If N is too small [see Fig. 6.7(f)], the divided zones will be too coarse to properly represent the original time delay matrix, which may lead to an unacceptable imaging result. Therefore, the number of annulus should be selected carefully to maintain a balance between performance reduction and increased computational efficiency, and corresponding results are presented in next section.

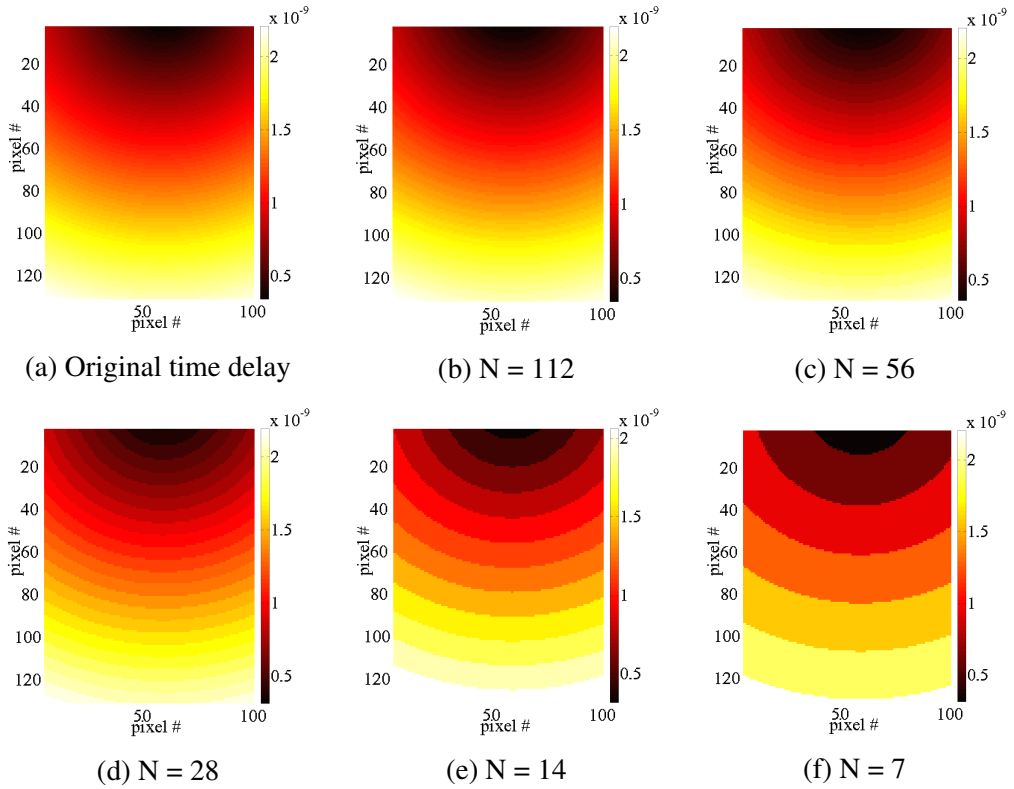

(a) Original time delay (b) N = 112 (c) N = 56

(d) N = 28 (e) N = 14 (f) N = 7

Fig. 6.7 Prediction of time delay (unit: second) matrix with different numbers of annulus zones N. (a) Original time delay. (b) to (f) are predicted time delays based on AP scheme, and N is selected as 112, 56, 28, 14, and 7, respectively.

6.5 Simulation Results and Analysis of AP

To comprehensively examine the effectiveness of AP acceleration scheme, three different testing scenarios are considered. First, the acceleration of AP as a function of the number of annulus is assessed. Second, the comparison of running time of methods with and without AP is conducted. Third, the performance of imaging algorithms combining AP is investigated.

6.5.1 Varied Numbers of Predicted Zones

In this section, the performance of AP as a function of the number of predicted annulus zones is examined. For consistent comparison, the same simulation environment used for RE in Section 6.3 is applied for AP.

The simulation is tested with following parameters: L = 13, 000, A = 48, and K = 1500. The running time required to calculate time-shifted signals for all antenna-pixel pairs is summarised in Table 6.3. The maximum number of annulus zone is chosen as 700, which is determined by the pixel resolution of the selected imaging area. Although there are 13,000 pixels, the maximum number of non-repeated time delays among all pixels is 708. This means that N should be less than 708, because even if N is larger than 708, no further improved resolution can be achieved. It is noted that by choosing different N, the running time varies considerably. Comparing the cases of N = 700 and 7, which takes 196.4 and 14.8 seconds, respectively. The latter case (N = 7) improved the speed by 13.3 times than the first case (N = 700), achieving the acceleration of one order of magnitude. This signifies that an appropriate selection of the number of annulus zones is critical for speeding the computation process.

Table 6.3 Running time of calculating time-shifted signals by AP as a function of annulus zones N measured in seconds. The number of signals A is 48, the signal sampling points K = 1500, and the pixel number of imaging area L = 13,000.

Annulus Number (N)	Running Time (s)
700	196.4
400	100.6
224	60.6
112	37.5
56	26.9
28	18.4
14	15.2
7	14.8

6.5.2 Computation Speed Comparison

In this section, the computation for obtaining shifted signals through methods with and without AP acceleration is examined and compared. In AP, N is selected as 56, which is a median value as shown in Table 6.3. For completeness, the running time as a function of the number of pixel L is considered. Different values of L represent different sizes of the imaging region, which is selected from 100 to 10,000. The maximum pixel number of

Table 6.4 Running time (RT) of calculating time-shifted signals by different methods with and without AP in seconds. The number of annulus number N of 56 is used in AP. The speedup is measured by the ratio of running time of different methods.

Pixel Number (L)	Running Time (s)		Speedup = RT1/RT2
	Without AP (RT1)	With AP (RT2)	
10^2	20.3	12.2	1.7
20^2	78.4	13.0	6.0
30^2	172.9	13.7	12.6
40^2	307.2	13.8	22.3
50^2	512.6	15.3	33.5
60^2	731.1	15.6	47.0
70^2	984.9	16.8	58.8
80^2	1315.2	18.9	69.6
90^2	1659.2	20.2	82.0
100^2	1943.2	21.6	90.0

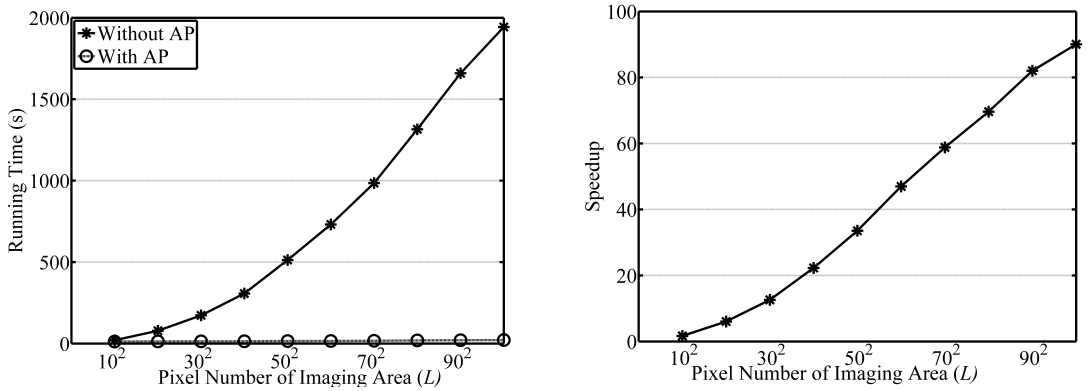

(a) Running time (b) Speedup offered by AP

Fig. 6.8 Running time comparison between methods with and without AP as a function of the number of pixels L. (a) Running time. (b) Speedup offered by AP.

10,000 can represent the widest zy cross-section in the breast model (see Fig. 6.1), and other zy cross-sections with different x coordinates can be computed in a same way following the same trend.

Corresponding results are displayed in Table 6.4, and the trend can be observed in Fig. 6.8. For a small imaging area which has 100 pixels, the running time of the methods without and with AP is comparable, which is 20.3 and 12.2 seconds, respectively. However, the running time of the method without using AP increased exponentially with the increase of pixel number, whereas AP still maintained a very low level [see Fig. 6.8(a)]. Specifically, when the image region has a 10,000 pixels, it takes the method without using AP 1943.2

seconds to calculate the shifted signals, whereas AP only needs 21.6 seconds, which is 90.0 times faster. Additionally, observing Fig. 6.8(b), the speedup offered by AP over its non-optimised counterpart shows an exponential trend, which means AP can offer an even stronger accelerating capability for larger imaging regions, proving its excellent scalability.

6.5.3 Algorithm with AP Acceleration

AP showed considerable speedup which can be up to 90 times faster than the non-optimised method with direct computation. However, this might cause performance loss of imaging algorithms due to the non-perfect prediction of time delays and corresponding time-shifted signals. Furthermore, the speedup of AP is associated with the number of annulus zones N, and the optimum compromise should be studied for practical use. To address these two problems, the performance of algorithms combining AP acceleration is examined in this section, and the key factors for optimum trade-off between performance and acceleration are pointed out.

Combined with the delay-and-sum (DAS) algorithm [39, 45], the accelerating capability of proposed AP scheme is evaluated. The performance of DAS without using AP is used as a benchmark, then combining AP, DAS performance is assessed with varied numbers of annulus zones N. The performance degradation is measured by the difference between the result of DAS with and without AP. Two metrics of SCR and SMR are used to measure the imaging results of DAS. The acceleration is measured by the ratio between running time for cases with and without AP, respectively. The breast model used is with medium type A, and ideal artefact removal is applied (the details of breast medium type and artefact removal technique are given in Chapter 4.3). The number of pixels in imaging area is 13,000.

The imaging results and metrics of DAS, and DAS with AP as a function of N are displayed in Fig. 6.9 and Table 6.5. Comparing Fig. 6.9(b) and (c), which are the results for DAS and DAS with AP of N = 700, there is no difference observed, but the DAS with AP is 14 times faster (see Table 6.6). Figs. 6.9(e) is the result of DAS with AP of N = 56. Compare this one with the original result of DAS [see Fig. 6.9(b)], a minor performance

degradation can be seen, which is reflected by the increased clutter around the peak. The SCR of this result is 6.8 dB, which is 0.2 dB smaller than the benchmark result offered

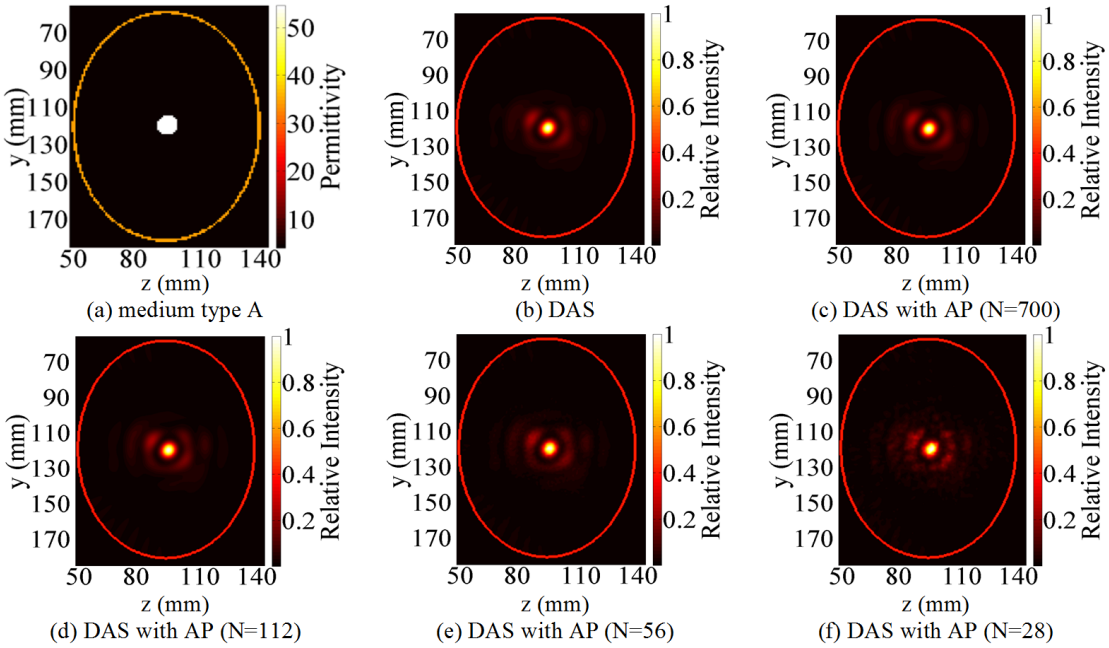

Fig. 6.9 Imaging results of DAS, and DAS with AP acceleration, different numbers of annulus N are applied. (a) Breast model with medium type A. (b) Imaging result by DAS. (c)-(f) Results by DAS with AP as a function of N, where N = 700, 112, 56, and 28, respectively.

Table 6.5 Performance of DAS, and DAS with AP as a function of number of annulus N.

DAS (Benchmark)	SCR (dB)	SMR (dB)
	7.0	17.2
DAS with AP		
Annulus Number (N)	SCR (dB)	SMR (dB)
700	7.0	17.2
400	7.0	17.2
224	7.0	17.2
112	7.0	17.2
56	6.8	17.0
28	5.4	16.6
14	3.9	15.1
7	0.3	12.4

by DAS without AP (see Table 6.5). But this case offers a speedup of 102.5 (see Table 6.6), which massively improved the computational efficiency. Observing Fig. 6.9(f), the number of annulus N of 28 is used. The imaged tumour in this scenario is more obscured in comparison to the original one [see Fig. 6.9(b)], and the clutter around the peak start to

Table 6.6 Running time of calculating shifted signals by AP with varied annulus numbers N for pixel number L of 13,000 (Corresponding to Fig. 6.9). The speedup is defined as the ratio between the running time of the two methods with and without AP.

	Running Time without AP (s)	
	2757.5	
Annulus Number (N)	Running Time with AP (s)	Speedup
700	196.4	14.0
400	100.6	27.4
224	60.6	45.5
112	37.5	73.5
56	26.9	102.5
28	18.4	149.5
14	15.2	181.3
7	14.8	186.9

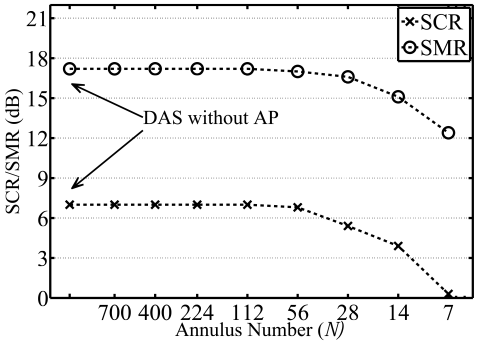

(a) DAS with AP

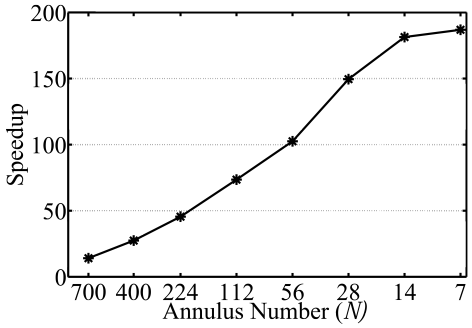

(b) Speedup offered by AP

Fig. 6.10 Performance of DAS with AP as a function of annulus zone number N. (a) Performance of DAS with AP. (b) Speedup offered by AP.

show an irregular pattern, which corresponds to a much lower SCR of 5.4 dB (see Table 6.5).

The trend of performance (see Table 6.5) and speedup (see Table 6.6) as a function of N are plotted in Fig. 6.10. Observing Fig. 6.10(a), with the decrease of N, the performance measured by SCR and SMR declines due to the increased inaccuracy between predicted and the original time delay matrix. Meanwhile, the speedup shows a steady increase [see Table 6.6 and Fig. 6.10(b)], from 14.0 to 186.9. These two figures indicate the trade-off between performance and computation speed. In practice, both high performance with extremely slow computation speed and fast calculation with seriously degraded performance should be avoided.

To examine the effectiveness of AP acceleration without affecting algorithm performance, two algorithms DAS and RAR [216] with AP are examined in ten different scenarios (S1 to S10), respectively. In these scenarios, different tumour positions in breast models with varied structures and densities are considered. The imaging results of non-accelerated DAS and RAR are shown in Figs. 4.7(b)(f) and 4.8(b)(f), Figs. 4.10(b)(f) to 4.17(b)(f), and the performance statistics of algorithms combining with AP are presented in Figs. 6.11 and 6.12, respectively. For each scenario, to accurately identify an appropriate trade-off between performance and acceleration, eight different annulus numbers of AP (N = 700, 400, 224, 112, 56, 28, 14, and 7) are used, which forms 160 simulation cases in total.

Observing Figs. 6.11 and 6.12, it can be seen that in all cases, the performance of both DAS and RAR degrades with the reduced N, which is due to the increased inaccuracy of predicted time delay matrices. Moreover, in most cases, when N is larger than 224, the performance degradation is fairly small, which is reflected by the gentle descending curves. Furthermore, when N is smaller than 56, a steep decline of performance can be observed. Meanwhile, abnormal increase of SCR and SMR can appear [see Fig. 6.11(d) and Fig. 6.12(d)].

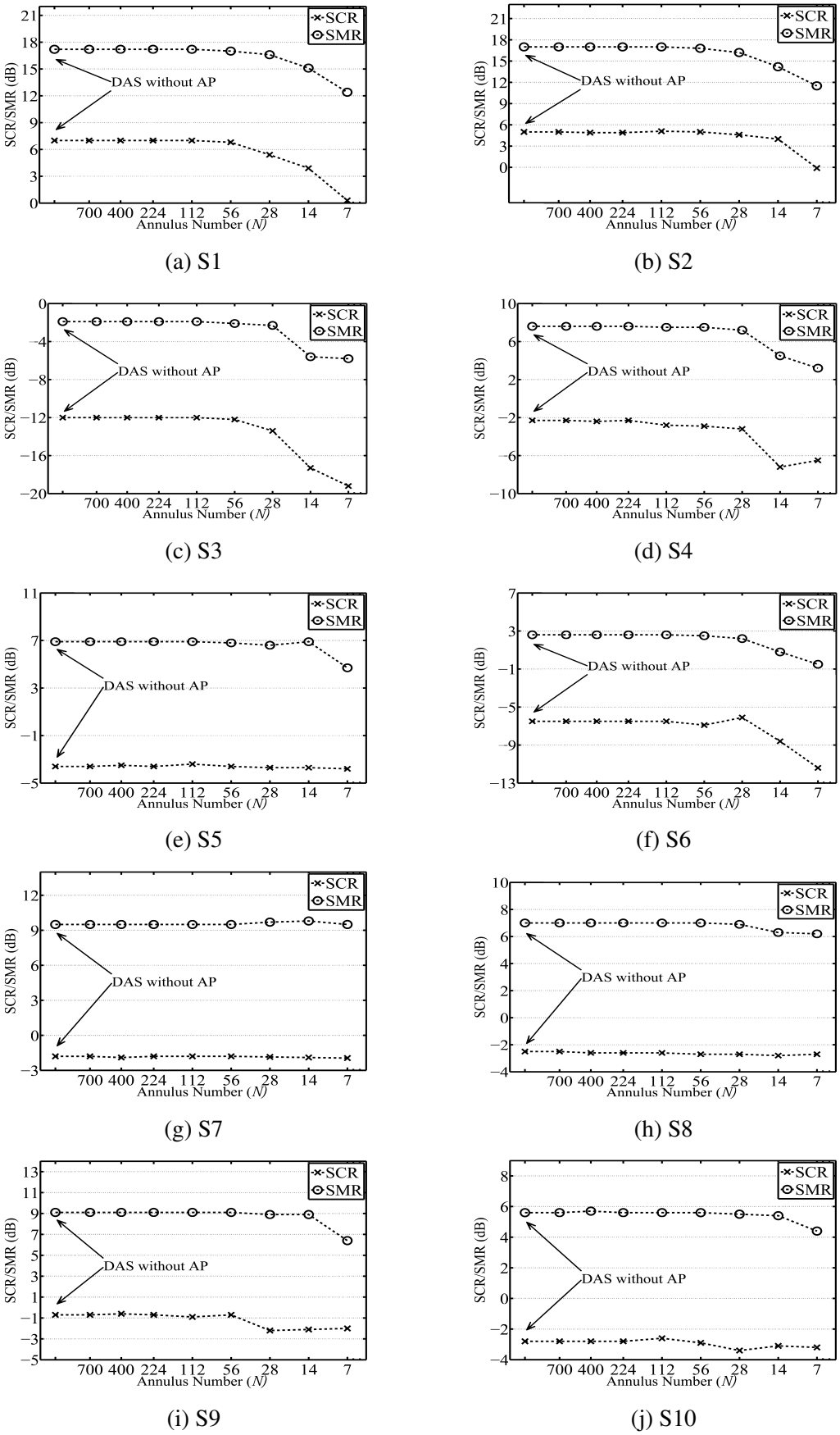

(a) S1 (b) S2

(c) S3 (d) S4

(e) S5 (f) S6

(g) S7 (h) S8

(i) S9 (j) S10

Fig. 6.11 Performance of DAS with AP as a function of the number of annulus N. (a) to (j) are the results in ten different scenarios (S1 to S10). DAS without AP is added as a benchmark.

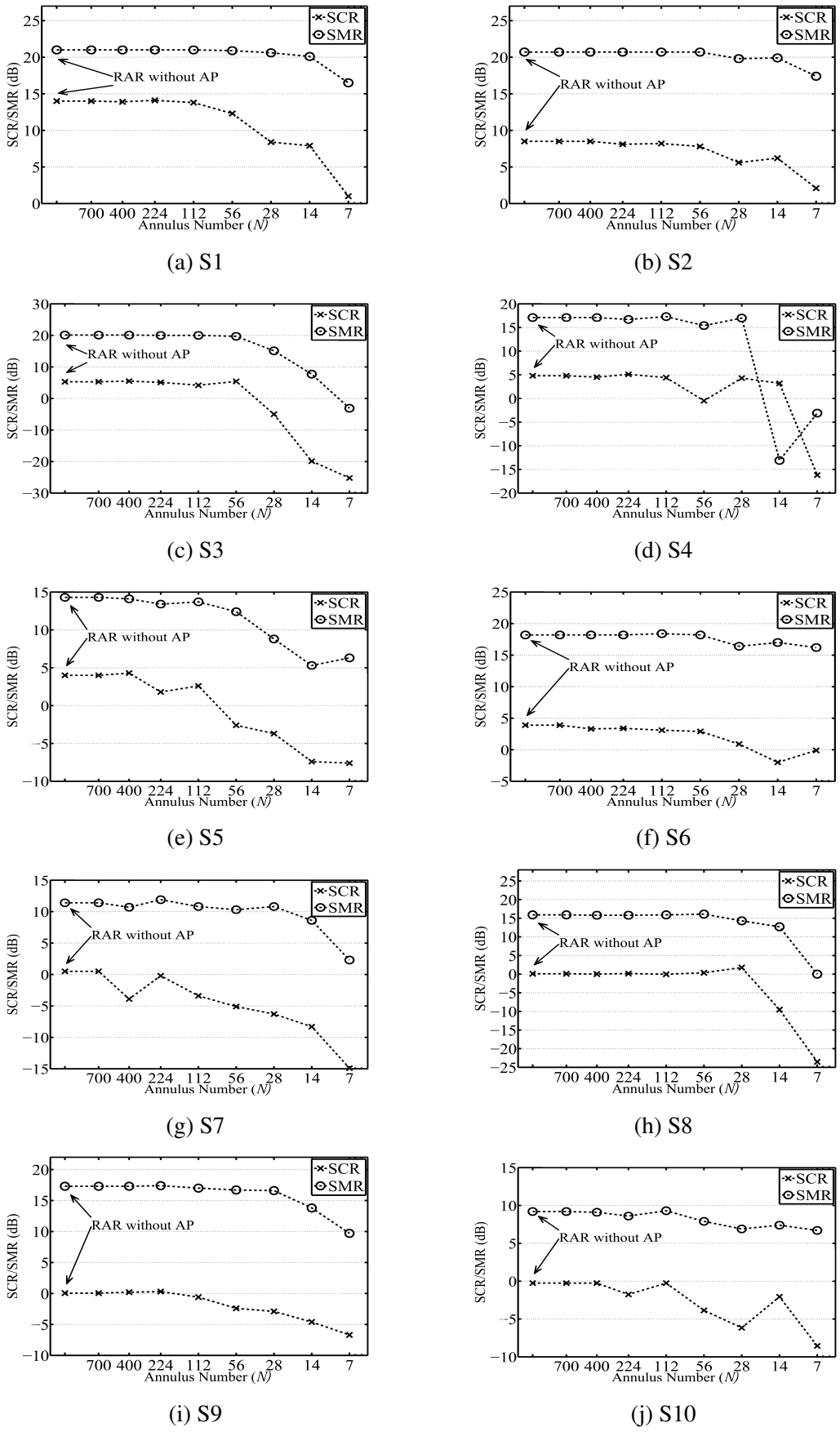

(a) S1 (b) S2

(c) S3 (d) S4

(e) S5 (f) S6

(g) S7 (h) S8

(i) S9 (j) S10

Fig. 6.12 Performance of RAR with AP as a function of the number of annulus N. (a) to (j) are the results in ten different scenarios (S1 to S10). RAR without AP is added as a benchmark.

Table 6.7 Performance loss of DAS and RAR as a function of the number of annulus N. For each N, the performance loss measured by SCR and SMR (unit: dB) is calculated by averaging the results in ten different scenarios. The speedup is measured by the ratio of running time of different methods, which is unitless.

Annulus Number (N)	700	400	**224**	112	56	28	14	7
Speedup	14.0	27.1	**45.5**	73.5	102.5	149.5	181.3	186.9
	DAS							
SCR Loss (dB)	0	0.02	**0.02**	0.03	0.17	0.45	1.86	3.03
SMR Loss (dB)	0	0	**0**	0.01	0.09	0.31	1.43	2.86
	RAR							
SCR Loss (dB)	0	0.48	**0.48**	0.89	2.66	4.4	7.7	14.1
SMR Loss (dB)	0	0.11	**0.15**	0.11	0.69	1.89	6.58	9.63

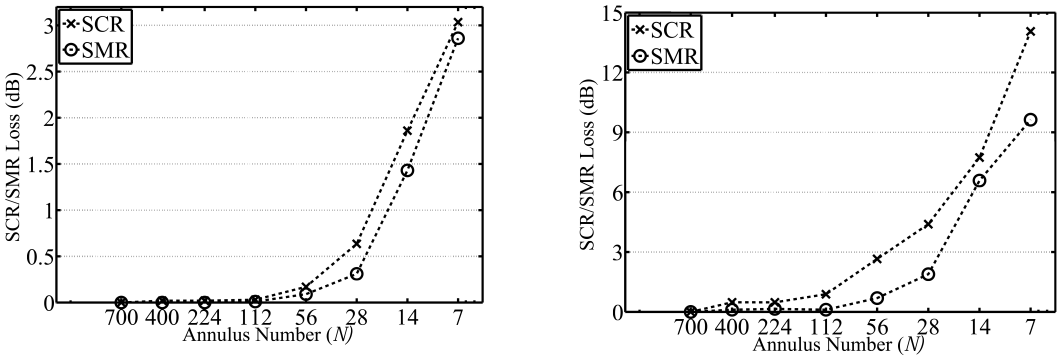

(a) DAS with AP

(b) RAR with AP

Fig. 6.13 Average performance loss of DAS and RAR as a function of the number of annulus N in different scenarios. (a) DAS. (b) RAR.

Based on the results shown in Table 6.7 and Fig. 6.13, it can be concluded that when N is large enough (e.g. $N = 700$), there is no performance loss caused, and a speedup factor of 14.0 can be offered by AP. Moreover, when N is slightly smaller (e.g. $N = 224$), a speedup of 45.5 can be offered by AP. Encouragingly, with such a high acceleration, only negligible performance loss is observed. Specifically, the average SCR and SMR loss of DAS is 0.02 and 0 dB, and these two values for RAR are 0.48 and 0.15 dB, respectively. With graceful performance degradation of less than 0.5 dB, the reconstructed images can still clearly show the location of tumours (see Fig. 6.9). With further decreased N (e.g. $N = 112$), in spite of a significantly improved acceleration, the performance loss can approach 1 dB on average, which is not advisable and should be employed with caution.

6.6 Comparative Analysis of RE and AP Mechanisms

Extensive analysis and simulation results proved that both RE and AP offered highly desired speedup over the non-optimised method. This speedup is particularly advantageous for large imaging area with millions of pixels, which is demonstrated by the exponentially increased trend of acceleration (see Fig. 6.4 and Fig. 6.8).

The proposed RE scheme removes a large number of repetitive operations of both time delay calculation and time-shifting signals. For an imaging region composed of 10,000 pixels, the acceleration ratio offered by RE over non-optimised method is 2.2, and no any performance degradation is observed. In comparison, AP exploits a novel annulus prediction to speed up the computation of time-shifted signals for millions of antenna-pixel pairs. In AP, the pixels that are close to each other are assigned with a same time-shifted signal, and results demonstrated that considerable acceleration is achieved by using this highly efficient batch computing. For a certain imaging region, depending on the selected number of predicted annulus, a flexible trade-off between imaging performance and speedup can be offered. On average, AP achieved a 45.5 speedup with a graceful performance degradation of less than 0.5 dB, which is a highly desirable trade-off for the vast majority of imaging scenarios.

Both RE and AP aim to speedup the calculation of time-shifting signals for antenna-pixel pairs, considering that this module is inescapable and one of the most time-consuming steps in all data-independent UWB breast cancer imaging algorithms. Although RE and AP are designed for accelerating image reconstruction for breast tumour detection, they can be directly applied for all UWB algorithms which involve time-shifting signals.

6.7 Conclusion

In this chapter, two mechanisms referred to as RE and AP are designed to reduce the complexity of UWB algorithms for accelerated imaging reconstruction. RE eliminates a massive number of redundant operations, whereas AP predicts the time delays of pixels

which are geographically close and belong to the same annulus zone with a width of R, thereby accomplishing the calculation in a highly efficient batch mode.

Extensive analysis and simulation results demonstrated the superiority of the proposed schemes. Without any performance loss, RE can be twice faster than its non-optimised counterpart. AP offers a valuable trade-off between imaging performance and reconstruction speed, which can be implemented by selecting appropriate number of predicted annulus zones. On average, AP is 45.5 times faster than the method without using AP, while restricting the performance loss less than 0.5 dB. Therefore, these techniques can speed up UWB imaging for breast tumour detection with remarkably reduced running time.

Chapter 7

Conclusions and Future Work

7.1 Conclusions

This thesis primarily focuses on UWB image reconstruction algorithm design for tumour detection. Idealised antenna modelling as point excitation source with single polarised field component is used. For completeness, both monostatic and multistatic signal acquisition methods were investigated. More practical antenna modelling will be considered in future work.

Several contributions have been made to improve UWB imaging algorithms for early breast cancer detection, and the main achievements are summarised in the following.

Chapter 2 reviewed the context of UWB technology and its existing and potential applications. This review was with a special emphasis on the UWB imaging for breast cancer detection, and conclusions from this review are: 1) UWB imaging is a promising technique for breast cancer screening, and hence it deserves wide attention from research communities; 2) Several challenges must be overcome before it can be deployed in practice. These include accurate propagation modelling of signals in realistic breast phantoms, and effective imaging algorithms with robust performance and affordable complexity. This review identified the major technical challenges in this area, which constituted the motivation and objectives of this thesis.

To address the challenges identified in Chapter 2, **Chapter 3** proposed a new computational engine entitled as VECE, which accurately simulated the propagation of UWB

signals in realistic breast tissues. The novel implementation combining ADE and CPML, which are adopted for describing the dispersive breast tissues and truncating the computational domain, respectively, is concurrently achieved in VECE. The ADE approach has great advantage in reducing computational complexity and memory storage requirement. The CPML, which is a very robust absorbing boundary condition, significantly reduces the late-time reflections and offers improved efficiency and flexibility for terminating various media. The accuracy of VECE was validated in both time and frequency domains across a variety of assessment criteria. The results generated by VECE were in great agreement with the outcome from commercial software. VECE's practicability for modelling and simulating UWB breast tumour imaging was clearly demonstrated through combining the state-of-the-art 3-D breast phantoms. In designed scenarios, the variation of input signals, breast models, and signal collection schemes were considered, which laid a solid foundation for developing imaging algorithms for following studies.

Considering the severe influence of artefacts on imaging results, a robust and artefact resistant algorithm of UWB imaging for breast cancer detection named as RAR was proposed in **Chapter 4**. A novel neighbourhood pairwise correlation of signals was utilised in RAR, which was proved to be very effective in mitigating the adverse effects from residual artefact signals. Furthermore, the maximum selection in RAR enabled the distinguishing of tumour response from the response from other strong scatterers such as fibro-glandular tissues. Based on 3-D anatomically and dielectrically accurate breast phantoms, extensive analysis and simulation results demonstrated the effectiveness and superiority of RAR, in which the comparisons with four well-known algorithms under a range of challenging scenarios were conducted. RAR exhibited substantially improved tumour identification capability and robust artefact resistance over existing techniques in the vast majority of cases considered. Based on the statistics of algorithm performance in ten different scenarios, compared with the other four methods, RAR offered both the highest SCR and SMR of 4.1 and 16.5 dB, respectively. These two metrics (SCR and SMR) of the second best algorithm FDAS were -1.68 and 9.17 dB. The performance difference

between RAR and FDAS showed a clear advantage and strong potential of RAR for breast cancer screening.

In **Chapter 5**, three new image reconstruction algorithms referred to as LCE, DNPC, and MSD have been designed, which further enhanced the performance in terms of clutter rejection and tumour detectability even in beasts with high density. To measure the local coherence among signals received at adjacent antennas, a grouping strategy was employed in LCE. Furthermore, unlike RAR which only selected the highest weighting coefficients, LCE adopted a two-step maximum combining, both the highest weighting coefficients and corresponding signals were combined for the calculation of pixel intensity. DNPC employed the dynamic weighting for different propagation channels according to their qualities. Differ from previous algorithms that were all based on monostatic signals, MSD explored and exploited the richness offered by the multistatics signals. Extra neighbouring multistatic signals were selected for acquiring extra tumour response. The efficacy of these algorithms were validated via extensive analysis and simulations. Encouragingly, compared with RAR, enhanced performance was observed in DNPC and MSD, which provided an average SCR of 4.2 and 4.3 dB in the ten scenarios considered, respectively, indicating a further improved tumour detection over the RAR algorithm.

In **Chapter 6**, two accelerated image reconstruction schemes, namely, RE and AP, have been proposed to speedup the imaging process for UWB breast tumour detection. This is motivated by the fact that medical imaging normally have high demand of resolution, in which millions of pixels can be involved. Therefore, RE and AP were designed to improve the efficiency of the pixel-based UWB breast cancer imaging algorithms. The substantial reduction of running time offered by these acceleration techniques could effectively speed up the overall imaging process. RE was implemented by removing of a huge number of repeated operations, whereas AP employed a novel predicted method to accomplish the pixel-related computations in a highly efficient batch mode. The effectiveness of RE and AP has been demonstrated through extensive analysis and simulations. Compared with the non-accelerated method, RE was two times faster with zero loss in imaging performance, whereas AP improved the speed by 45 times at the expense of performance degradation of

less than 0.5 dB for both SCR and SMR metrics, which provided efficient utilisation of computing resources and a valuable trade-off.

7.2 Future Work

This research primarily focuses on UWB image reconstruction algorithm design for tumour detection. To obtain the backscattered signals, idealised antenna (point source) modelling with single polarised field component was used, and more practical and extensive antenna modelling will be considered in future work. In addition, some other potentially productive areas and topics which are related to the work in this thesis are addressed as follows.

- **Extensive modelling.** First, different tumour modelling can be considered. In this study, the malignant breast tumour with varied positions and sizes were used to examine the imaging algorithms. All tumours were modelled as spheres but with varied diameters, which represented different strengths of backscattered energy from the tumour as widely used in existing studies. However, it is worthwhile to model the tumour with more realistic shapes, such as spiculate or lobulated. This could provide further insights regarding different tumour responses, thereby assessing and improving imaging algorithms in a wider range of scenarios. Second, alternative propagation modelling of UWB signal could be studied. The proposed computational engine VECE was designed for Debye model that well represented the dispersion of breast tissues. However, different dispersive models, such as Lorentz and/or Drude, might be more suitable for other types of biological tissues. Therefore, it is worth exploring a unified computational engine for generating heterogeneous families, which will enable a wide diversity of modelling, simulation, and imaging of different biological systems.
- **Further improved imaging algorithms.** The proposed algorithms in this thesis could potentially be improved, which can be achieved by combining them with other techniques, such as MIMO or signal filtering. Additionally, aside from the data-independent algorithms studied in this thesis, further investigation can be carried

out for data-dependent algorithms. These two types of methods have their own merits and demerits. Data-dependent algorithms potentially could be superior to their data-independent counterparts, assuming the required prior information is accurately known. Data-independent algorithms are free from this prior knowledge and have much higher computational efficiency than data-dependent techniques. For data-dependent algorithm, it is particularly interesting to test their performance in scenarios combining 3-D (rather than 2-D) breast models and practical (rather than ideal) artefact removal methods. This could be a challenge since in most existing literature, oversimplified breast models and artefact removal methods are being used. The elimination of these idealised assumptions could lead to more practical imaging scenarios. Furthermore, due to the high complexity of data-dependent algorithms, accelerated computation schemes could also be investigated.

- **Imaging algorithms for distinguishing different types of tumours.** Existing UWB breast tumour detection algorithms mainly aim to identify and localise the tumour. However, after the tumour is identified, none of these algorithms is able to distinguish the attribute of the tumour, such as benign or malignant. But this type of information is of great value for both screening and treatment, and it would be highly beneficial if this information could be retrieved by such UWB-based non-invasive imaging techniques.
- **Antenna and physical breast phantom design.** As an extension of this work, the antenna design for UWB breast cancer detection is suggested. Due to the limited space for accommodating antenna array, miniature UWB antennas are highly desirable. And this would involve innovative design, tuning, and validation of antennas. The performance of antenna will directly impact on the quality of collected UWB signals, which potentially could challenge existing algorithms. To enable the collection of signals, realistic physical breast phantoms are essential. Based on the combination of these two aspects, in conjunction with imaging algorithms, a prototype of UWB breast cancer imaging system could be established, thereby enabling further development of related diagnostic and therapeutic techniques.

References

[1] ECC, "Electronic Communication Committee (ECC) Decision 12(03): The harmonised conditions for UWB applications onboard aircraft," Available at: http://www.erodocdb.dk/docs/doc98/official/pdf/ECCDec1203.pdf, Nov. 2012 (Last accessed in Feb. 2015).

[2] P. K. Verma, A. N. Gaikwad, D. Singh, and M. Nigam, "Analysis of clutter reduction techniques for through wall imaging in UWB range," *Prog. Electromagn. Res. B Pier B*, vol. 17, pp. 29–48, 2009.

[3] Y. Wang and A. E. Fathy, "Advanced system level simulation platform for three-dimensional UWB through-wall imaging SAR using time-domain approach," *IEEE Trans. Geosci. Remote Sensing*, vol. 50, no. 5, pp. 1986–2000, May 2012.

[4] A. R. Al-Qubaa, A. Al-Shiha, and G. Y. Tian, "Threat Target Classification Using ANN and SVM Based on a New Sensor Array System," *Prog. Electromagn. Res. B Pier B*, vol. 61, pp. 69–85, 2014.

[5] H. Takahara, K. Ohno, and M. Itami, "A study on UWB radar assisted by inter-vehicle communication for safety applications," in *Vehicular Electronics and Safety (ICVES), 2012 IEEE International Conference on*, pp. 99–104, IEEE, Jul. 2012.

[6] H. Takahara, K. Ohno, and M. Itami, "A study on the iterative detection system using the SIC in the cooperative UWB radar and IVC system," in *ITS Telecommunications (ITST), 2013 13th International Conference on*, pp. 187–192, IEEE, Nov. 2013.

[7] K. S. Saidi, J. Teizer, M. Franaszek, and A. M. Lytle, "Static and dynamic performance evaluation of a commercially-available ultra wideband tracking system," *Automation in Construction*, vol. 20, no. 5, pp. 519–530, May 2011.

[8] T. Cheng, M. Venugopal, J. Teizer, and P. Vela, "Performance evaluation of ultra wideband technology for construction resource location tracking in harsh environments," *Automation in Construction*, vol. 20, no. 8, pp. 1173–1184, Aug. 2011.

[9] A. Dumoulin, M. John, M. J. Ammann, and P. McEvoy, "Optimized monopole and dipole antennas for UWB asset tag location systems," *IEEE Trans. Antennas Propagat.*, vol. 60, no. 6, pp. 2896–2904, May 2012.

[10] J. Seitz, M. Schaub, O. Hirsch, R. Zetik, T. Deissler, R. Thoma, and J. Thielecke, "UWB feature localization for imaging," in *Ultra-Wideband, 2008. ICUWB 2008. IEEE International Conference on*, vol. 2, pp. 199–202, IEEE, Sep. 2008.

[11] T. Deissler, M. Janson, R. Zetik, and J. Thielecke, "Infrastructureless indoor mapping using a mobile antenna array," in *Systems, Signals and Image Processing (IWSSIP), 2012 19th International Conference on*, pp. 36–39, IEEE, Apr. 2012.

[12] S. Roy, J. R. Foerster, V. S. Somayazulu, and D. G. Leeper, "Ultrawideband radio design: The promise of high-speed, short-range wireless connectivity," *Proc. IEEE*, vol. 92, no. 2, pp. 295–311, Feb. 2004.

[13] L. Yang and G. B. Giannakis, "Ultra-wideband communications: an idea whose time has come," *IEEE Signal Processing Mag.*, vol. 21, no. 6, pp. 26–54, Nov. 2004.

[14] F. Viani, L. Lizzi, R. Azaro, and A. Massa, "A miniaturized UWB antenna for wireless dongle devices," *IEEE Antennas Wireless Propagat. Lett.*, vol. 7, pp. 714–1, Jan. 2009.

[15] V. De Santis, M. Feliziani, and F. Maradei, "Safety assessment of UWB radio systems for body area network by the FD^2TD method," *IEEE Trans. Magn.*, vol. 46, no. 8, pp. 3245–3248, Aug. 2010.

[16] C.-H. Kang, S.-J. Wu, and J.-H. Tarng, "A novel folded uwb antenna for wireless body area network," *IEEE Trans. Antennas Propagat.*, vol. 60, no. 2, pp. 1139–1142, Feb. 2012.

[17] C.-P. Deng, X.-Y. Liu, Z.-K. Zhang, and M. M. Tentzeris, "A miniascape-like triple-band monopole antenna for WBAN applications," *IEEE Antennas Wireless Propagat. Lett.*, vol. 11, pp. 1330–1333, Dec. 2012.

[18] M. E. Khaled, H. Bahrami, P. Fortier, B. Gosselin, and L. A. Rusch, "Capacity of UWB wireless channel for neural recording systems," in *Engineering in Medicine and Biology Society (EMBC), 2014 36th Annual International Conference of the IEEE*, pp. 3965–3968, IEEE, Aug. 2014.

[19] C. N. Paulson, J. T. Chang, C. E. Romero, J. Watson, F. J. Pearce, and N. Levin, "Ultra-wideband radar methods and techniques of medical sensing and imaging," in *Optics East 2005*, pp. 60070L–60070L, Nov. 2005.

[20] M. R. Mahfouz and M. J. Kuhn, "UWB channel measurements and modeling for positioning and communications systems in the operating room," in *Biomedical Wireless Technologies, Networks, and Sensing Systems (BioWireleSS), 2011 IEEE Topical Conference on*, pp. 47–50, IEEE, Jan. 2011.

[21] V. Nambakam, J. Shen, J. Talbert, and A. Mahadik, "Wireless operating room communication system including video output device and video display," Oct. 15 2013. US Patent 8,558,880.

[22] X. Chen, H. Leung, and M. Tian, "Multitarget detection and tracking for through-the-wall radars," *IEEE Trans. Aerosp. Electron. Syst.*, vol. 50, no. 2, pp. 1403–1415, Jul. 2014.

[23] R. Chávez-Santiago and I. Balasingham, "Ultrawideband signals in medicine [Life Sciences]," *IEEE Signal Processing Mag.*, vol. 31, no. 6, pp. 130–136, Oct. 2014.

[24] N. Ghavami, G. Tiberi, D. J. Edwards, and A. Monorchio, "UWB microwave imaging of objects with canonical shape," *IEEE Trans. Antennas Propagat.*, vol. 60, no. 1, pp. 231–239, Jan. 2012.

[25] M. Duffy, "The war on cancer: are we winning?," *Tumor Biology*, vol. 34, no. 3, pp. 1275–1284, Apr. 2013.

[26] F. Bray, P. McCarron, and D. M. Parkin, "The changing global patterns of female breast cancer incidence and mortality," *childhood*, vol. 4, no. 5, Aug. 2004.

[27] A. Jemal, F. Bray, M. M. Center, J. Ferlay, E. Ward, and D. Forman, "Global cancer statistics," *CA-Cancer J. Clin.*, vol. 61, no. 2, pp. 69–90, Feb. 2011.

[28] V. Speirs and A. M. Shaaban, "The rising incidence of male breast cancer," *Breast Cancer Res. Treat.*, vol. 115, no. 2, pp. 429–430, May 2009.

[29] I. Schreer and J. Lüttges, "Breast cancer: early detection," in *Radiologic-Pathologic Correlations from Head to Toe*, pp. 767–784, Springer, 2005.

[30] A. Bleyer and H. G. Welch, "Effect of three decades of screening mammography on breast-cancer incidence," *N. Engl. J. Med.*, vol. 367, no. 21, pp. 1998–2005, Nov. 2012.

[31] H. Cheng, J. Shan, W. Ju, Y. Guo, and L. Zhang, "Automated breast cancer detection and classification using ultrasound images: A survey," *Pattern Recognition*, vol. 43, no. 1, pp. 299–317, Jan. 2010.

[32] M. Morrow, J. Waters, and E. Morris, "MRI for breast cancer screening, diagnosis, and treatment," *The Lancet*, vol. 378, no. 9805, pp. 1804–1811, Nov. 2011.

[33] J. G. Elmore, K. Armstrong, C. D. Lehman, and S. W. Fletcher, "Screening for breast cancer," *JAMA: the journal of the American Medical Association*, vol. 293, no. 10, pp. 1245–1256, 2005.

[34] D. Saslow, C. Boetes, W. Burke, S. Harms, M. O. Leach, C. D. Lehman, E. Morris, E. Pisano, M. Schnall, S. Sener, *et al.*, "American cancer society guidelines for breast screening with mri as an adjunct to mammography," *CA-Cancer J. Clin.*, vol. 57, no. 2, pp. 75–89, Apr. 2007.

[35] J. G. Elmore, M. B. Barton, V. M. Moceri, S. Polk, P. J. Arena, and S. W. Fletcher, "Ten-year risk of false positive screening mammograms and clinical breast examinations," *N. Engl. J. Med.*, vol. 338, no. 16, pp. 1089–1096, Apr. 1998.

[36] H. G. Welch and H. J. Passow, "Quantifying the benefits and harms of screening mammography," *JAMA Intern. Med.*, vol. 174, no. 3, pp. 448–454, 2014.

[37] D. Preston, A. Mattsson, E. Holmberg, R. Shore, N. Hildreth, and J. Boice Jr, "Radiation effects on breast cancer risk: a pooled analysis of eight cohorts.," *Radiation research*, vol. 158, no. 2, pp. 220–235, Aug. 2002.

[38] C. H. See, R. A. Abd-Alhameed, S. W. J. Chung, D. Zhou, H. Al-Ahmad, and P. S. Excell, "The design of a resistively loaded bowtie antenna for applications in breast cancer detection systems," *IEEE Trans. Antennas Propagat.*, vol. 60, no. 5, pp. 2526–2530, 2012.

[39] E. C. Fear, X. Li, S. C. Hagness, and M. A. Stuchly, "Confocal microwave imaging for breast cancer detection: Localization of tumors in three dimensions," *IEEE Trans. Biomed. Eng.*, vol. 49, no. 8, pp. 812–822, Aug. 2002.

[40] E. J. Bond, X. Li, S. C. Hagness, and B. D. Van Veen, "Microwave imaging via space-time beamforming for early detection of breast cancer," *IEEE Trans. Antennas Propagat.*, vol. 51, no. 8, pp. 1690–1705, Aug. 2003.

[41] X. Li, S. K. Davis, S. C. Hagness, D. W. Van Der Weide, and B. D. Van Veen, "Microwave imaging via space-time beamforming: Experimental investigation of tumor detection in multilayer breast phantoms," *IEEE Trans. Microwave Theory Tech.*, vol. 52, no. 8, pp. 1856–1865, Aug. 2004.

[42] M. Klemm, I. J. Craddock, J. A. Leendertz, A. Preece, and R. Benjamin, "Radar-based breast cancer detection using a hemispherical antenna array—experimental results," *IEEE Trans. Antennas Propagat.*, vol. 57, no. 6, pp. 1692–1704, Jun. 2009.

[43] M. Klemm, J. Leendertz, D. Gibbins, I. J. Craddock, A. Preece, and R. Benjamin, "Microwave radar-based differential breast cancer imaging: imaging in homogeneous breast phantoms and low contrast scenarios," *IEEE Trans. Antennas Propagat.*, vol. 58, no. 7, pp. 2337–2344, Jul. 2010.

[44] T. Yin and F. H. Ali, "Adaptive combining via correlation exploration for ultrawideband breast cancer imaging," *IEEE Antennas Wireless Propagat. Lett.*, vol. 14, pp. 587–590, Feb. 2015.

[45] X. Li and S. C. Hagness, "A confocal microwave imaging algorithm for breast cancer detection," *IEEE Microwave Wireless Compon. Lett.*, vol. 11, no. 3, pp. 130–132, Mar. 2001.

[46] Y. Xie, B. Guo, L. Xu, J. Li, and P. Stoica, "Multistatic adaptive microwave imaging for early breast cancer detection," *IEEE Trans. Biomed. Eng.*, vol. 53, no. 8, p. 1647, Aug. 2006.

[47] Y. Chen, I. J. Craddock, P. Kosmas, M. Ghavami, and P. Rapajic, "Multiple-input multiple-output radar for lesion classification in ultrawideband breast imaging," *IEEE J. Sel. Top. Sign. Proces.*, vol. 4, no. 1, pp. 187–201, Feb. 2010.

[48] E. A. Marengo, F. K. Gruber, and F. Simonetti, "Time-reversal music imaging of extended targets," *IEEE Trans. Image Processing*, vol. 16, no. 8, pp. 1967–1984, Aug. 2007.

[49] M. D. Hossain, A. S. Mohan, and M. J. Abedin, "Beamspace time-reversal microwave imaging for breast cancer detection," *IEEE Antennas Wireless Propagat. Lett.*, vol. 12, pp. 241–244, Feb. 2013.

[50] H. B. Lim, N. T. T. Nhung, E.-P. Li, and N. D. Thang, "Confocal microwave imaging for breast cancer detection: Delay-multiply-and-sum image reconstruction algorithm," *IEEE Trans. Biomed. Eng.*, vol. 55, no. 6, pp. 1697–1704, Jun. 2008.

[51] F. Yang and A. S. Mohan, "Detection of malignant breast tissues using microwave imaging," in *APMC: 2009 Asia Pacific Microwave Conference, IEEE*, pp. 397–400, IEEE, 2009.

[52] A. Shahzad, M. O'Halloran, E. Jones, and M. Glavin, "Prefiltered beamforming for early-stage breast cancer detection," *IEEE Antennas Wireless Propagat. Lett.*, vol. 12, pp. 500–503, Apr. 2013.

[53] A. Taflove and S. C. Hagness, *Computational Electrodynamics: The Finite-Difference Time-Domain Method, 3rd ed*. Boston, MA: Artech House, 2005, pp. 273–406.

[54] FCC, "Revision of Part 15 of the commissions rules regarding ultra-wideband transmission systems. FCC 02-48," 2002. [Online] Available: https://transition.fcc.gov/Bureaus/Engineering_Technology/Orders/2002/fcc02048.pdf (Last accessed in A. 2015).

[55] F. Nekoogar, *Ultra-wideband communications: fundamentals and applications*. Prentice Hall Press, 2005.

[56] C. A. Balanis, *Antenna theory: analysis and design*. John Wiley & Sons, 2012.

[57] C. E. Shannon, "Communication in the presence of noise," *Proceedings of the IRE*, vol. 37, no. 1, pp. 10–21, Jan. 1949.

[58] R. Gharpurey and P. Kinget, *Ultra wideband: circuits, transceivers and systems*. Springer, 2008.

[59] I. Güvenç, H. Arslan, *et al.*, "On the modulation options for UWB systems," in *Proceedings of the 2003 IEEE conference on Military communications-Volume II*, pp. 892–897, IEEE Computer Society, Oct. 2003.

[60] M. E. Magaña, H. Liu, and V. Venkatesan, "Performance of a Binary PPM Ultra-Wideband Communication System with Direct Sequence Spreading for Multiple Access," *Wireless Pers. Commun.*, vol. 65, no. 1, pp. 125–142, Jul. 2012.

[61] C. De Dominicis, A. Flammini, S. Rinaldi, E. Sisinni, A. Cazzorla, A. Moschitta, and P. Carbone, "High-precision UWB-based timestamping," in *Precision Clock Synchronization for Measurement Control and Communication (ISPCS), 2011 International IEEE Symposium on*, pp. 50–55, IEEE, Sep. 2011.

[62] V. Sipal, B. Allen, D. Edwards, and B. Honary, "Twenty years of ultrawideband: opportunities and challenges," *IET Commun.*, vol. 6, no. 10, pp. 1147–1162, Jul. 2012.

[63] "Advent of practical uwb localization:(r) evolution in uwb antenna research,"

[64] J. R. Reitz, F. J. Milford, and R. W. Christy, *Foundations of electromagnetic theory*. Addison-Wesley Publishing Company, 2008.

[65] X. Zhuge and A. G. Yarovoy, "A sparse aperture MIMO-SAR-based UWB imaging system for concealed weapon detection," *IEEE Trans. Geosci. Remote Sensing*, vol. 49, no. 1, pp. 509–518, Jan. 2011.

[66] S. Y. Semenov and D. R. Corfield, "Microwave tomography for brain imaging: Feasibility assessment for stroke detection," *Int. J. Antennas Propag.*, vol. 2008, Mar. 2008.

[67] P. Meaney, T. Zhou, M. Fanning, S. Geimer, and K. Paulsen, "Microwave imaging for bone fracture risk assessment," in *Proc. 2008 Appl. Computational Electromagn. Symp*, pp. 462–466, 2008.

[68] S. Y. Semenov, R. H. Svenson, A. E. Boulyshev, A. E. Souvorov, V. Y. Borisov, Y. Sizov, A. N. Starostin, K. R. Dezern, G. P. Tatsis, and V. Y. Baranov, "Microwave tomography: two-dimensional system for biological imaging," *IEEE Trans. Biomed. Eng.*, vol. 43, no. 9, pp. 869–877, Sep. 1996.

[69] S. Y. Semenov, R. H. Svenson, A. E. Bulyshev, A. E. Souvorov, A. G. Nazarov, Y. E. Sizov, V. G. Posukh, A. V. Pavlovsky, P. N. Repin, and G. P. Tatsis, "Spatial resolution of microwave tomography for detection of myocardial ischemia and infarction-experimental study on two-dimensional models," *IEEE Trans. Microwave Theory Tech.*, vol. 48, no. 4, pp. 538–544, Apr. 2000.

[70] S. Y. Semenov, R. H. Svenson, V. G. Posukh, A. G. Nazarov, Y. E. Sizov, A. E. Bulyshev, A. E. Souvorov, W. Chen, J. Kasell, and G. P. Tatsis, "Dielectrical spectroscopy of canine myocardium during acute ischemia and hypoxia at frequency spectrum from 100 kHz to 6 GHz," *IEEE Trans. Med. Imag.*, vol. 21, no. 6, pp. 703–707, Jun. 2002.

[71] A. C. Society, *Cancer facts & figures*. The Society, 2008.

[72] Canadian Cancer Society (2013). [Online]. Available:http://www.cancer.ca/en/cancer-information/cancer-101/canadian-cancer-statistics-publication/past-editions-canadian-cancer-statistics/?region=on.

[73] Breast Cancer Foundation (2007). [Online]. Available:http://bcf.org.sg. (Last accessed in Apr. 2015).

[74] S. J. Nass, I. C. Henderson, J. C. Lashof, *et al.*, *Mammography and Beyond:: Developing Technologies for the Early Detection of Breast Cancer*. National Academies Press, 2001.

[75] A. C. on Breast Cancer Screening *et al.*, "Screening for breast cancer in England: past and future," *J. Med. Screen.*, vol. 13, no. 2, pp. 59–61, Feb. 2006.

[76] V. Koukou, N. Martini, G. Fountos, P. Sotiropoulou, C. Michail, I. Valais, I. Kandarakis, and G. Nikiforidis, "Calcification Detection Optimization in Dual Energy Mammography: Influence of the X-Ray Spectra," in *XIII Mediterranean Conference on Medical and Biological Engineering and Computing 2013*, pp. 459–462, Springer, 2014.

[77] D. S. Buist, P. L. Porter, C. Lehman, S. H. Taplin, and E. White, "Factors contributing to mammography failure in women aged 40–49 years," *J. Natl. Cancer Inst.*, vol. 96, no. 19, pp. 1432–1440, 2004.

[78] M. J. Yaffe and J. G. Mainprize, "Risk of radiation-induced breast cancer from mammographic screening 1," *Radiology*, vol. 258, no. 1, pp. 98–105, Jan. 2011.

[79] A. Poulos, D. McLean, M. Rickard, and R. Heard, "Breast compression in mammography: how much is enough?," *Australasian radiology*, vol. 47, no. 2, pp. 121–126, Jun. 2003.

[80] J. G. Elmore, C. K. Wells, C. H. Lee, D. H. Howard, and A. R. Feinstein, "Variability in radiologists' interpretations of mammograms," *N. Engl. J. Med.*, vol. 331, no. 22, pp. 1493–1499, 1994.

[81] C. A. Beam, P. M. Layde, and D. C. Sullivan, "Variability in the interpretation of screening mammograms by US radiologists: findings from a national sample," *Arch. Intern. Med.*, vol. 156, no. 2, pp. 209–213, 1996.

[82] B. Bocquet, J. Van de Velde, A. Mamouni, Y. Leroy, G. Giaux, J. Delannoy, and D. Delvalee, "Microwave radiometric imaging at 3 GHz for the exploration of breast tumors," *IEEE Trans. Microwave Theory Tech.*, vol. 38, no. 6, pp. 791–793, Jun. 1990.

[83] F. Bardati and S. Iudicello, "Modeling the visibility of breast malignancy by a microwave radiometer," *IEEE Trans. Biomed. Eng.*, vol. 55, no. 1, pp. 214–221, Jan. 2008.

[84] L. V. Wang, X. Zhao, H. Sun, and G. Ku, "Microwave-induced acoustic imaging of biological tissues," *Rev. Sci. Instrum.*, vol. 70, no. 9, pp. 3744–3748, Jun. 1999.

[85] S. C. Hagness, A. Taflove, and J. E. Bridges, "Two-dimensional FDTD analysis of a pulsed microwave confocal system for breast cancer detection: Fixed-focus and antenna-array sensors," *IEEE Trans. Biomed. Eng.*, vol. 45, no. 12, pp. 1470–1479, Dec. 1998.

[86] D. B. Kopans, ""Early" breast cancer detection using techniques other than mammography," *Am. J. Roentgenol.*, vol. 143, no. 3, pp. 465–468, 1984.

[87] S. Heywang-Köbrunner, "Nonmammographic breast imaging techniques," *Curr. Opin. Radiol.*, vol. 4, no. 5, pp. 146–154, 1992.

[88] M. J. Burfeindt, J. D. Shea, B. D. Van Veen, and S. C. Hagness, "Beamforming-Enhanced Inverse Scattering for Microwave Breast Imaging," *IEEE Trans. Antennas Propagat.*, vol. 62, no. 10, pp. 5126–5132, Jul, 2014.

[89] J. De Zaeytijd, A. Franchois, C. Eyraud, and J.-M. Geffrin, "Full-wave three-dimensional microwave imaging with a regularized gauss–newton method—theory and experiment," *IEEE Trans. Antennas Propagat.*, vol. 55, no. 11, pp. 3279–3292, Nov. 2007.

[90] A. Vander Vorst, A. Rosen, and Y. Kotsuka, *RF/microwave interaction with biological tissues*, vol. 181. John Wiley & Sons, 2006.

[91] E. Fear, S. Hagness, P. Meaney, M. Okoniewski, and M. Stuchly, "Enhancing breast tumor detection with near-field imaging," *IEEE Microwave Mag.*, vol. 3, no. 1, pp. 48–56, Mar. 2002.

[92] B. Zhou, W. Shao, and G. Wang, "On the resolution of UWB microwave imaging of tumors in random breast tissue," in *Antennas and Propagation Society International Symposium, 2005 IEEE*, vol. 3, pp. 831–834, IEEE, 2005.

[93] M. Rosenstein, L. W. Andersen, and G. G. Warner, *Handbook of glandular tissue doses in mammography*. No. 8239, US Department of Health and Human Services, Public Health Service, Food and Drug Administration, Center for Devices and Radiological Health, 1985.

[94] X. Wu, G. T. Barnes, and D. Tucker, "Spectral dependence of glandular tissue dose in screen-film mammography.," *Radiology*, vol. 179, no. 1, pp. 143–148, 1991.

[95] J. Sachs, *Handbook of Ultra-wideband Short-range Sensing: Theory, Sensors, Applications*. John Wiley & Sons, 2013.

[96] S. C. Hagness, A. Taflove, and J. E. Bridges, "Three-dimensional FDTD analysis of a pulsed microwave confocal system for breast cancer detection: Design of an antenna-array element," *IEEE Trans. Antennas Propagat.*, vol. 47, no. 5, pp. 783–791, May 1999.

[97] Y. Alvarez, J. A. Martinez-Lorenzo, F. Las-Heras, and C. M. Rappaport, "An inverse fast multipole method for geometry reconstruction using scattered field information," *IEEE Trans. Antennas Propagat.*, vol. 60, no. 7, pp. 3351–3360, Jul. 2012.

[98] M. Barcellos-Hoff, "How tissues respond to damage at the cellular level: orchestration by transforming growth factor-β (TGF-β)," *Brit. J. Radiol.*, vol. Supplement_27, no. 1, pp. 123–127, Jan. 2014.

[99] E. Fear and M. Stuchly, "Microwave detection of breast cancer," *IEEE Trans. Microwave Theory Tech.*, vol. 48, no. 11, pp. 1854–1863, Nov. 2000.

[100] S. Chaudhary, R. Mishra, A. Swarup, and J. M. Thomas, "Dielectric properties of normal & malignant human breast tissues at radiowave & microwave frequencies.," *Indian J. Biochem. Biophys.*, vol. 21, no. 1, p. 76, Feb. 1984.

[101] W. T. Joines, Y. Zhang, C. Li, and R. L. Jirtle, "The measured electrical properties of normal and malignant human tissues from 50 to 900 MHz," *Med. Phys.*, vol. 21, no. 4, pp. 547–550, 1994.

[102] E. Zastrow, S. K. Davis, M. Lazebnik, F. Kelcz, B. D. Van Veen, and S. C. Hagness, "Development of anatomically realistic numerical breast phantoms with accurate dielectric properties for modeling microwave interactions with the human breast," *IEEE Trans. Biomed. Eng.*, vol. 55, no. 12, pp. 2792–2800, Dec. 2008.

[103] R. C. Conceicao, M. O'Halloran, M. Glavin, and E. Jones, "Numerical modelling for ultra wideband radar breast cancer detection and classification," *Prog. Electromagn. Res. B*, vol. 34, pp. 145–171, 2011.

[104] Y. Chen, E. Gunawan, K. S. Low, S.-C. Wang, C. B. Soh, and L. L. Thi, "Time of arrival data fusion method for two-dimensional ultrawideband breast cancer detection," *IEEE Trans. Antennas Propagat.*, vol. 55, no. 10, pp. 2852–2865, Oct. 2007.

[105] Y. Chen, E. Gunawan, K. S. Low, S.-C. Wang, C. B. Soh, and T. C. Putti, "Effect of lesion morphology on microwave signature in 2-D ultra-wideband breast imaging," *IEEE Trans. Biomed. Eng.*, vol. 55, no. 8, pp. 2011–2021, Jul. 2008.

[106] Y. Chen, I. J. Craddock, and P. Kosmas, "Feasibility study of lesion classification via contrast-agent-aided UWB breast imaging," *IEEE Trans. Biomed. Eng.*, vol. 57, no. 5, pp. 1003–1007, May 2010.

[107] K. S. Yee *et al.*, "Numerical solution of initial boundary value problems involving maxwell's equations in isotropic media," *IEEE Trans. Antennas Propagat.*, vol. 14, no. 3, pp. 302–307, 1966.

[108] W. J. Hoefer, "The transmission-line matrix method–theory and applications," *IEEE Trans. Microwave Theory Tech.*, vol. 33, no. 10, pp. 882–893, Oct. 1985.

[109] J. L. Volakis, A. Chatterjee, and L. C. Kempel, *Finite element method electromagnetics: antennas, microwave circuits, and scattering applications*. John Wiley & Sons, 1998.

[110] A. G. Hanif, T. Arima, and T. Uno, "Finite-difference frequency-domain algorithm for band-diagram calculation of 2-D photonic crystals composed of Debye-type dispersive materials," *IEEE Antennas Wireless Propagat. Lett.*, vol. 11, pp. 41–44, Mar. 2012.

[111] E. K. C. K. Y. See and Z. Liu, "Accurate and efficient evaluation of method of moments matrix based on a generalized analytical approach," *Prog. Electromagn. Res.*, vol. 94, pp. 367–382, 2009.

[112] Y. Alvarez, J. Á. Martínez, F. Las-Heras, and C. M. Rappaport, "An inverse fast multipole method for imaging applications," *IEEE Antennas Wireless Propagat. Lett.*, vol. 10, pp. 1259–1262, Nov. 2011.

[113] F. Zhen, Z. Chen, and J. Zhang, "Toward the development of a three-dimensional unconditionally stable finite-difference time-domain method," *IEEE Trans. Microwave Theory Tech.*, vol. 48, no. 9, pp. 1550–1558, Sep. 2000.

[114] A. Semlyen and B. Gustavsen, "Phase-domain transmission-line modeling with enforcement of symmetry via the propagated characteristic admittance matrix," *IEEE Trans. Power Delivery*, vol. 27, no. 2, pp. 626–631, Apr. 2012.

[115] V. Jithesh and D. Pande, "A review on computational EMI modelling techniques," in *Electromagnetic Interference and Compatibility, 2003. INCEMIC 2003. 8th International Conference on*, pp. 159–166, IEEE, Dec. 2003.

[116] M. Sharkawy, V. Demir, and A. Z. Elsherbeni, "Plane wave scattering from three dimensional multiple objects using the iterative multiregion technique based on the FDFD method," *IEEE Trans. Antennas Propagat.*, vol. 54, no. 2, pp. 666–673, Feb. 2006.

[117] D. Insana and C. M. Rappaport, "Using FDFD Technique in Two-Dimensional TE Analysis for Modeling Clutter in Wall Penetrating Radar," *Int. J. Antennas. Propag.*, vol. 2014, 2014.

[118] F. Vipiana, D. R. Wilton, and W. A. Johnson, "Advanced numerical schemes for the accurate evaluation of 4-D reaction integrals in the method of moments," *IEEE Trans. Antennas Propagat.*, vol. 61, no. 11, pp. 5559–5566, Nov. 2013.

[119] V. Rokhlin, "Rapid solution of integral equations of classical potential theory," *J. Comput. Phys.*, vol. 60, no. 2, pp. 187–207, Sep. 1985.

[120] W. C. Chew, T. J. Cui, and J. M. Song, "A FAFFA-MLFMA algorithm for electromagnetic scattering," *IEEE Trans. Antennas Propagat.*, vol. 50, no. 11, pp. 1641–1649, Nov. 2002.

[121] Y.-Q. Zhang and D.-B. Ge, "A unified FDTD approach for electromagnetic analysis of dispersive objects," *Prog. Electromagn. Res. Pier*, vol. 96, pp. 155–172, 2009.

[122] K. H. Lee, I. Ahmed, R. S. M. Goh, E. H. Khoo, E. P. Li, and T. G. G. Hung, "Implementation of the FDTD method based on lorentz-drude dispersive model on GPU for plasmonics applications," *Prog. Electromagn. Res.*, vol. 116, pp. 441–456, 2011.

[123] I. T. Rekanos and T. G. Papadopoulos, "FDTD modeling of wave propagation in cole-cole media with multiple relaxation times," *IEEE Antennas Wireless Propag. Lett.*, vol. 9, pp. 67–69, 2010.

[124] G. Mur, "Absorbing boundary conditions for the finite-difference approximation of the time-domain electromagnetic-field equations," *IEEE Trans. Electromagn. Compat.*, no. 4, pp. 377–382, Nov. 1981.

[125] Z.-P. Liao, H. Wong, B.-P. Yang, and Y. Yuan, "A transmitting boundary for transient wave analysis," *Sci. Sinica*, vol. 27, no. 10, pp. 1063–1076, 1984.

[126] J.-P. Berenger, "A perfectly matched layer for the absorption of electromagnetic waves," *J. Comput. Phys.*, vol. 114, no. 2, pp. 185–200, 1994.

[127] S. D. Gedney, "An anisotropic perfectly matched layer-absorbing medium for the truncation of FDTD lattices," *IEEE Trans. Antennas Propagat.*, vol. 44, no. 12, pp. 1630–1639, Dec. 1996.

[128] S. D. Gedney and B. Zhao, "An auxiliary differential equation formulation for the complex-frequency shifted PML," *IEEE Trans. Antennas Propagat.*, vol. 58, no. 3, pp. 838–847, Mar. 2010.

[129] P. M. Meaney, M. W. Fanning, D. Li, S. P. Poplack, and K. D. Paulsen, "A clinical prototype for active microwave imaging of the breast," *IEEE Trans. Microwave Theory Tech.*, vol. 48, no. 11, pp. 1841–1853, Nov. 2000.

[130] L. Poli, G. Oliveri, and A. Massa, "Microwave imaging within the first-order Born approximation by means of the contrast-field Bayesian compressive sensing," *IEEE Trans. Antennas Propagat.*, vol. 60, no. 6, pp. 2865–2879, Jun. 2012.

[131] T. M. Grzegorczyk, P. M. Meaney, P. A. Kaufman, R. M. di Florio-Alexander, and K. D. Paulsen, "Fast 3-D tomographic microwave imaging for breast cancer detection," *IEEE Trans. Med. Imag.*, vol. 31, no. 8, pp. 1584–1592, May 2012.

[132] A. Sabouni, "Ultra-Wideband (UWB) Microwave Tomography using Full-Wave Analysis Techniques for Heterogeneous and Dispersive Media," Ph.D. Thesis. University of Manitoba. Canada. 2011.

[133] B. Guo, Y. Wang, J. Li, P. Stoica, and R. Wu, "Microwave imaging via adaptive beamforming methods for breast cancer detection," *J. Electromagnet. Wave.*, vol. 20, no. 1, pp. 53–63, 2006.

[134] D. Byrne, M. O'Halloran, E. Jones, and M. Glavin, "Transmitter-grouping robust capon beamforming for breast cancer detection," *Prog. Electromagn. Res.*, vol. 108, pp. 401–416, 2010.

[135] M. Jalilvand, X. Li, T. Zwick, W. Wiesbeck, and E. Pancera, "UWB SAR medical imaging via broadband minimum variance distortionless response (MVDR) algorithm," in *Antennas and Propagation (EUCAP), Proceedings of the 5th European Conference on*, pp. 1268–1271, IEEE, 2011.

[136] Y. Jin, Y. Jiang, and J. M. Moura, "Time reversal beamforming for microwave breast cancer detection," in *Image Processing, 2007. ICIP 2007. IEEE International Conference on*, vol. 5, pp. V–13, IEEE, 2007.

[137] Y. Jin, J. Moura, Y. Jiang, M. Wahl, H. Zhu, and Q. He, "Breast cancer detection by time reversal imaging," in *Biomedical Imaging: From Nano to Macro, 2008. ISBI 2008. 5th IEEE International Symposium on*, pp. 816–819, IEEE, 2008.

[138] M. Sajjadieh, F. Foroozan, and A. Asif, "Breast cancer detection using time reversal signal processing," in *Multitopic Conference, 2009. INMIC 2009. IEEE 13th International*, pp. 1–5, IEEE, 2009.

[139] M. H. Sajjadieh and A. Asif, "Unsupervised time reversal based microwave imaging for breast cancer detection," in *Electrical and Computer Engineering (CCECE), 2011 24th Canadian Conference on*, pp. 001411–001415, IEEE, 2011.

[140] N. Ghavami, D. Edwards, G. Tiberi, A. Monorchio, and G. Manara, "Huygens principle based technique for microwave imaging of objects with inclusions," in *Electromagnetics in Advanced Applications (ICEAA), 2011 International Conference on*, pp. 1044–1047, IEEE, 2011.

[141] J. E. Johnson, T. Takenaka, K. A. H. Ping, S. Honda, and T. Tanaka, "Advances in the 3-D forward–backward time-stepping (FBTS) inverse scattering technique for breast cancer detection," *IEEE Trans. Biomed. Eng.*, vol. 56, no. 9, pp. 2232–2243, 2009.

[142] S. Jacobsen and Y. Birkelund, "Improved resolution and reduced clutter in ultra-wideband microwave imaging using cross-correlated back projection: Experimental and numerical results," *Journal of Biomedical Imaging*, vol. 2010, p. 20, 2010.

[143] P. Kosmas and C. M. Rappaport, "Time reversal with the FDTD method for microwave breast cancer detection," *IEEE Trans. Microwave Theory Tech.*, vol. 53, no. 7, pp. 2317–2323, Jul. 2005.

[144] R. Nilavalan, A. Gbedemah, I. Craddock, X. Li, and S. C. Hagness, "Numerical investigation of breast tumour detection using multi-static radar," *Electron. Lett.*, vol. 39, no. 25, pp. 1787–1789, Dec. 2003.

[145] M. Klemm, I. Craddock, J. Leendertz, A. Preece, and R. Benjamin, "Improved delay-and-sum beamforming algorithm for breast cancer detection," *Int. J. Antennas Propag.*, vol. 2008, Apr. 2008.

[146] X. Li, E. J. Bond, B. D. Van Veen, and S. C. Hagness, "An overview of ultra-wideband microwave imaging via space-time beamforming for early-stage breast-cancer detection," *IEEE Antennas Propagat. Mag.*, vol. 47, no. 1, pp. 19–34, Feb. 2005.

[147] M. O'Halloran, E. Jones, and M. Glavin, "Quasi-multistatic MIST beamforming for the early detection of breast cancer," *IEEE Trans. Biomed. Eng.*, vol. 57, no. 4, pp. 830–840, Apr. 2010.

[148] P. Stoica, Z. Wang, and J. Li, "Robust capon beamforming," in *Signals, Systems and Computers, 2002. Conference Record of the Thirty-Sixth Asilomar Conference on*, vol. 1, pp. 876–880, IEEE, Nov. 2002.

[149] M. Donelli, I. J. Craddock, D. Gibbins, and M. Sarafianou, "A three-dimensional time domain microwave imaging method for breast cancer detection based on an evolutionary algorithm," *Prog. Electromagn. Res. B Pier M*, vol. 18, pp. 179–195, 2011.

[150] M. Lazebnik, D. Popovic, L. McCartney, C. B. Watkins, M. J. Lindstrom, J. Harter, S. Sewall, T. Ogilvie, A. Magliocco, T. M. Breslin, *et al.*, "A large-scale study of the ultrawideband microwave dielectric properties of normal, benign and malignant breast tissues obtained from cancer surgeries," *Phys. Med. Biol.*, vol. 52, no. 20, p. 6093, Oct. 2007.

[151] M. A. Elahi, M. Glavin, E. Jones, and M. O'Halloran, "Artifact removal algorithms for microwave imaging of the breast," *Prog. Electromagn. Res. Pier*, vol. 141, pp. 185–200, 2013.

[152] A. Shahzad, M. O'Halloran, E. Jones, and M. Glavin, "A preprocessing filter for multistatic microwave breast imaging for enhanced tumour detection," *Prog. Electromagn. Res. B Pier B*, vol. 57, pp. 115–126, 2014.

[153] J. M. Sill and E. C. Fear, "Tissue sensing adaptive radar for breast cancer detection-experimental investigation of simple tumor models," *IEEE Trans. Microwave Theory Tech.*, vol. 53, no. 11, pp. 3312–3319, Nov. 2005.

[154] A. Maskooki, E. Gunawan, C. B. Soh, and K. S. Low, "Frequency domain skin artifact removal method for ultra-wideband breast cancer detection," *Prog. Electromagn. Res. Pier*, vol. 98, pp. 299–314, 2009.

[155] W. Zhi and F. Chin, "Entropy-based time window for artifact removal in UWB imaging of breast cancer detection," *IEEE Signal Processing Lett.*, vol. 13, no. 10, pp. 585–588, Oct. 2006.

[156] B. Maklad, C. Curtis, E. Fear, and G. Messier, "A skin response estimation and suppression technique for radar-based microwave breast imaging applications," in *Antennas and Propagation (EUCAP), 2012 6th European Conference on*, pp. 1772–1775, IEEE, Mar. 2012.

[157] M. Elahi, A. Shahzad, M. Glavin, E. Jones, and M. O'Halloran, "Hybrid artifact removal for confocal microwave breast imaging," *IEEE Antennas Wireless Propagat. Lett.*, vol. 13, pp. 149–152, 2014.

[158] H. Greenspan, "Super-resolution in medical imaging," *Comput. J.*, vol. 52, no. 1, pp. 43–63, 2009.

[159] J. Croteau, J. Sill, T. Williams, and E. Fear, "Phantoms for testing radar-based microwave breast imaging," in *Antenna Technology and Applied Electromagnetics and the Canadian Radio Science Meeting, 2009. ANTEM/URSI 2009. 13th International Symposium on*, pp. 1–4, IEEE, 2009.

[160] A. Mashal, F. Gao, and S. C. Hagness, "Heterogeneous anthropomorphic phantoms with realistic dielectric properties for microwave breast imaging experiments," *Microw. Opt. Techn. Let.*, vol. 53, no. 8, pp. 1896–1902, May 2011.

[161] M. J. Burfeindt, T. J. Colgan, R. O. Mays, J. D. Shea, N. Behdad, B. D. Van Veen, and S. C. Hagness, "MRI-Derived 3-D-Printed Breast Phantom for Microwave Breast Imaging Validation," *IEEE Antennas Wireless Propagat. Lett.*, vol. 11, pp. 1610–1613, Dec. 2012.

[162] N. Joachimowicz, C. Conessa, T. Henriksson, and B. Duchene, "Breast phantoms for microwave imaging," *IEEE Antennas Wireless Propagat. Lett.*, vol. 13, pp. 1333–1336, Jul. 2014.

[163] S. Hagness, A. Taflove, and J. Bridges, "Wideband ultralow reverberation antenna for biological sensing," *Electron. Lett.*, vol. 33, no. 19, pp. 1594–1595, Sep. 1997.

[164] E. Fear and M. Stuchly, "Microwave breast tumor detection: Antenna design and characterization," in *IEEE Antennas Propag. Symp. Dig.*, vol. 2, pp. 1076–1079, IEEE, 2000.

[165] M. Fernández Pantoja, S. González García, M. Hernández-López, A. Rubio Bretones, and R. Gómez Martín, "Design of an ultra-broadband V antenna for microwave detection of breast tumors," *Microw. Opt. Techn. Let.*, vol. 34, no. 3, pp. 164–166, 2002.

[166] X. Yun, E. C. Fear, and R. H. Johnston, "Compact antenna for radar-based breast cancer detection," *IEEE Trans. Antennas Propagat.*, vol. 53, no. 8, pp. 2374–2380, Aug. 2005.

[167] X. Li, M. Jalivand, Y. Sit, and T. Zwick, "A compact double-layer on-body matched bowtie antenna for medical diagnostics," *IEEE Trans. Antennas Propagat.*, vol. 62, no. 4, pp. 1808–1816, Apr. 2014.

[168] XFDTD® *Electromagnetic Solver Based on the Finite Difference Time Domain Method 7.0*, Remcom, Inc., State College, PA, 2009.

[169] "UWCEM numerical breast phantoms repository," [Online]. Available: https://uwcem.ece.wisc.edu/phantomRepository.html (Last accessed in Apr. 2015).

[170] M. O'Halloran, R. C. Conceicao, D. Byrne, M. Glavin, and E. Jones, "FDTD modeling of the breast: A review," *Prog. Electromagn. Res. B*, vol. 18, pp. 1–24, 2009.

[171] M. C. T. Weiland, "Discrete electromagnetism with the finite integration technique," *Prog. Electromagn. Res.*, vol. 32, pp. 65–87, 2001.

[172] M. R. Zunoubi, J. Payne, and W. P. Roach, "CUDA implementation of TE^z-FDTD solution of maxwell's equations in dispersive media," *IEEE Antennas Wireless Propag. Lett.*, vol. 9, pp. 756–759, Aug. 2010.

[173] R. Luebbers, F. P. Hunsberger, K. S. Kunz, R. B. Standler, and M. Schneider, "A frequency-dependent finite-difference time-domain formulation for dispersive materials," *IEEE Trans. Electromagn. Compat.*, vol. 32, no. 3, pp. 222–227, 1990.

[174] R. J. Luebbers and F. Hunsberger, "FDTD for n th-order dispersive media," *IEEE Trans. Antennas Propagat.*, vol. 40, no. 11, pp. 1297–1301, 1992.

[175] M. D. Bui, S. S. Stuchly, and G. I. Costache, "Propagation of transients in dispersive dielectric media," *IEEE Trans. Microwave Theory Tech.*, vol. 39, no. 7, pp. 1165–1172, 1991.

[176] R. Siushansian and J. LoVetri, "A comparison of numerical techniques for modeling electromagnetic dispersive media," *IEEE Microwave Guided Wave Lett.*, vol. 5, no. 12, pp. 426–428, 1995.

[177] D. F. Kelley and R. J. Luebbers, "Piecewise linear recursive convolution for dispersive media using FDTD," *IEEE Trans. Antennas Propagat.*, vol. 44, no. 6, pp. 792–797, 1996.

[178] D. M. Sullivan, "Frequency-dependent FDTD methods using z transforms," *IEEE Trans. Antennas Propagat.*, vol. 40, no. 10, pp. 1223–1230, Oct. 1992.

[179] R. M. Joseph, S. C. Hagness, and A. Taflove, "Direct time integration of maxwell's equations in linear dispersive media with absorption for scattering and propagation of femtosecond electromagnetic pulses," *Opt. Lett.*, vol. 16, no. 18, pp. 1412–1414, 1991.

[180] H. Mosallaei, "FDTD-PLRC technique for modeling of anisotropic-dispersive media and metamaterial devices," *IEEE Trans. Electromagn. Compat.*, vol. 49, no. 3, pp. 649–660, Aug. 2007.

[181] M. J. Inman, A. Z. Elsherbeni, J. G. Maloney, and B. N. Baker, "GPU based FDTD solver with CPML boundaries," in *Proc. IEEE AP-S International Symposium*, pp. 5255–5258, Jun. 2007.

[182] M.-R. Tofighi, "FDTD modeling of biological tissues cole–cole dispersion for 0.5–30 ghz using relaxation time distribution samples—novel and improved implementations," *IEEE Trans. Microwave Theory Tech.*, vol. 57, no. 10, pp. 2588–2596, Oct. 2009.

[183] M. R. Zunoubi and J. Payne, "Analysis of 3-dimensional electromagnetic fields in dispersive media using CUDA," *Prog. Electromagn. Res. M*, vol. 16, pp. 185–196, 2011.

[184] A. Shahmansouri and B. Rashidian, "GPU implementation of split-field finite-difference time-domain method for drude-lorentz dispersive media," *Prog. Electromagn. Res.*, vol. 125, pp. 55–77, 2012.

[185] K. Chun, H. Kim, H. Kim, and Y. Chung, "PLRC and ADE implementations of drude-critical point dispersive model for the FDTD method," *Prog. Electromagn. Res.*, vol. 135, pp. 373–390, 2013.

[186] W. Yu, R. Mittra, T. Su, Y. Liu, and X. Yang, *Parallel finite-difference time-domain method*. Artech House Norwood, 2006.

[187] R. N. Schneider, L. E. Turner, and M. M. Okoniewski, "Application of FPGA technology to accelerate the finite-difference time-domain (FDTD) method," in *Proc. of the ACM/SIGDA tenth international symposium on Field-programmable gate arrays*, pp. 97–105, Feb. 2002.

[188] M. Okoniewski, M. Mrozowski, and M. Stuchly, "Simple treatment of multi-term dispersion in FDTD," *IEEE Microwave Guided Wave Lett.*, vol. 7, no. 5, pp. 121–123, May 1997.

[189] J. A. Roden and S. D. Gedney, "Convolutional pml (CPML): An efficient fdtd implementation of the cfs-pml for arbitrary media," *Microw. Opt. Technol. Letters*, vol. 27, no. 5, pp. 334–338, Jun. 2000.

[190] M. Kuzuoglu and R. Mittra, "Frequency dependence of the constitutive parameters of causal perfectly matched anisotropic absorbers," *IEEE Microwave Guided Wave Lett.*, vol. 6, no. 12, pp. 447–449, Dec. 1996.

[191] J. A. LaComb, P. M. Mileski, and R. F. Ingram, "Ultra wideband surface wave communication," *Prog. Electromagn. Res. C*, vol. 8, pp. 95–105, 2009.

[192] L. Brillouin, *Wave Propagation and Group Velocity*. Academic Press, 2013.

[193] P. Kosmas, C. M. Rappaport, and E. Bishop, "Modeling with the FDTD method for microwave breast cancer detection," *IEEE Trans. Microwave Theory Tech.*, vol. 52, no. 8, pp. 1890–1897, Aug. 2004.

[194] S.-C. Kong, J. J. Simpson, and V. Backman, "ADE-FDTD scattered-field formulation for dispersive materials," *IEEE Microwave Wireless Compon. Lett.*, vol. 18, no. 1, pp. 4–6, Jan. 2008.

[195] A. C. of Radiology, A. C. of Radiology, *et al.*, "Breast imaging reporting and data system atlas (BI-RADS atlas)," *Reston, VA: American College of Radiology*, vol. 98, 2003.

[196] Y. Chen, E. Gunawan, K. S. Low, S.-C. Wang, C. B. Soh, and T. C. Putti, "Time-reversal Ultrawideband breast imaging: pulse design criteria considering multiple tumors with unknown tissue properties," *IEEE Trans. Antennas Propagat.*, vol. 56, no. 9, pp. 3073–3077, Sep. 2008.

[197] R. C. Conceicao, M. O'Halloran, M. Glavin, and E. Jones, "Comparison of planar and circular antenna configurations for breast cancer detection using microwave imaging," *Prog. Electromagn. Res.*, vol. 99, pp. 1–20, 2009.

[198] T. W. Hertel and G. S. Smith, "On the convergence of common FDTD feed models for antennas," *IEEE Trans. Antennas Propagat.*, vol. 51, no. 8, pp. 1771–1779, Aug. 2003.

[199] N. Simicevic and D. T. Haynie, "FDTD simulation of exposure of biological material to electromagnetic nanopulses," *Phys. Med. Biol.*, vol. 50, no. 2, p. 347, Jan. 2005.

[200] W. Niu, K. Hlavaty, D. Tanska, N. Tseng, J. Li, and B. Penprase, "Simulating ultra-wideband imaging for the early detection of tissue injury," in *SPIE Medical Imaging*, pp. 725813–725813, International Society for Optics and Photonics, 2009.

[201] A. Mashal, B. Sitharaman, X. Li, P. K. Avti, A. V. Sahakian, J. H. Booske, and S. C. Hagness, "Toward carbon-nanotube-based theranostic agents for microwave detection and treatment of breast cancer: Enhanced dielectric and heating response of tissue-mimicking materials," *IEEE Trans. Biomed. Eng.*, vol. 57, no. 8, pp. 1831–1834, Aug. 2010.

[202] E. Zastrow, S. C. Hagness, B. D. Van Veen, and J. E. Medow, "Time-multiplexed beamforming for noninvasive microwave hyperthermia treatment," *IEEE Trans. Biomed. Eng.*, vol. 58, no. 6, pp. 1574–1584, Jun. 2011.

[203] A. E. Souvorov, A. E. Bulyshev, S. Y. Semenov, R. H. Svenson, and G. P. Tatsis, "Two-dimensional computer analysis of a microwave flat antenna array for breast cancer tomography," *IEEE Trans. Microwave Theory Tech.*, vol. 48, no. 8, pp. 1413–1415, Aug. 2000.

[204] P. Dimbylow, "FDTD calculations of the whole-body averaged SAR in an anatomically realistic voxel model of the human body from 1 MHz to 1 GHz," *Phys. Med.Biol.*, vol. 42, no. 3, p. 479, Mar. 1997.

[205] D. W. Winters, E. J. Bond, B. D. Van Veen, and S. C. Hagness, "Estimation of the frequency-dependent average dielectric properties of breast tissue using a time-domain inverse scattering technique," *IEEE Antennas Propagat. Mag.*, vol. 54, no. 11, pp. 3517–3528, Nov. 2006.

[206] M. D. Hossain and A. S. Mohan, "Breast cancer detection in highly dense numerical breast phantoms using time reversal," in *Electromagnetics in Advanced Applications (ICEAA), 2013 International Conference on*, pp. 859–862, IEEE, Sep. 2013.

[207] M. Hossain, A. S. Mohan, *et al.*, "Beamspace time reversal maximum likelihood estimation for microwave breast imaging," in *Antennas and Propagation Society International Symposium (APSURSI), 2014 IEEE*, pp. 1921–1922, IEEE, Jul. 2014.

[208] E. Fishler, A. Haimovich, R. S. Blum, L. J. Cimini, D. Chizhik, and R. A. Valenzuela, "Spatial diversity in radars-models and detection performance," *IEEE Trans. Signal Processing*, vol. 54, no. 3, pp. 823–838, Mar. 2006.

[209] M. Klemm, I. Craddock, and A. Preece, "Contrast-enhanced breast cancer detection using dynamic microwave imaging," in *Antennas and Propagation Society International Symposium (APSURSI), 2012 IEEE*, pp. 1–2, IEEE, Jul. 2012.

[210] E. Bakken, T. S. Lande, and S. Holm, "Real time UWB radar imaging using single chip transceivers," in *Circuits and Systems (ISCAS), 2014 IEEE International Symposium on*, pp. 2461–2464, IEEE, Jun. 2014.

[211] J. Yang, J. Thompson, X. Huang, T. Jin, and Z. Zhou, "Segmented reconstruction for compressed sensing SAR imaging," *IEEE Trans. Geosci. Remote Sensing*, vol. 51, no. 7, pp. 4214–4225, Jul. 2013.

[212] S. Sun, G. Zhu, and T. Jin, "Novel Methods to Accelerate CS Radar Imaging by NUFFT," *IEEE Trans. Geosci. Remote Sensing*, vol. 53, no. 1, pp. 557 – 566, Jan. 2015.

[213] M. Leigsnering and A. M. Zoubir, "Fast wideband near-field imaging using the non-equispaced FFT with application to through-wall radar," *Proc. 19th EUSIPCO*, pp. 1708–1712, 2011.

[214] S. Kidera, T. Sakamoto, and T. Sato, "Accurate UWB radar three-dimensional imaging algorithm for a complex boundary without range point connections," *IEEE Trans. Geosci. Remote Sensing*, vol. 48, no. 4, pp. 1993–2004, Apr. 2010.

[215] Y.-S. Yoon and M. G. Amin, "High-resolution through-the-wall radar imaging using beamspace MUSIC," *IEEE Trans. Antennas Propagat.*, vol. 56, no. 6, pp. 1763–1774, Jun. 2008.

[216] T. Yin, F. H. Ali, and C. C. Reyes-Aldasoro, "A robust and artifact resistant algorithm of ultrawideband imaging system for breast cancer detection," *IEEE Trans. Biomed. Eng.*, vol. 62, no. 6, pp. 1514–1525, Jan. 2015.

Appendix A

Matlab Code of RAR Image Reconstruction Algorithm

```
function [ output_args ] = Untitled( input_args )
%% ********[Environment initialisation]********
ant_pos_cor(1,1) = {[80,39,101]};% Antenna coordinate
ant_pos_cor(1,2) = {[80,50,120]};
ant_pos_cor(1,3) = {[80,63,140]};
ant_pos_cor(1,4) = {[80,82,153]};
ant_pos_cor(1,5) = {[80,100,158]};
ant_pos_cor(1,6) = {[80,116,159]};
ant_pos_cor(1,7) = {[80,131,158]};
ant_pos_cor(1,8) = {[80,147,154]};
ant_pos_cor(1,9) = {[80,162,145]};
ant_pos_cor(1,10) = {[80,174,132]};
ant_pos_cor(1,11) = {[80,185,116]};
ant_pos_cor(1,12) = {[80,188,97]};
ant_pos_cor(1,13) = {[80,186,74]};
ant_pos_cor(1,14) = {[80,178,56]};
ant_pos_cor(1,15) = {[80,166,47]};
ant_pos_cor(1,16) = {[80,152,39]};
ant_pos_cor(1,17) = {[80,135,34]};
ant_pos_cor(1,18) = {[80,119,31]};
ant_pos_cor(1,19) = {[80,103,31]};
ant_pos_cor(1,20) = {[80,84,38]};
ant_pos_cor(1,21) = {[80,71,44]};
ant_pos_cor(1,22) = {[80,59,55]};
ant_pos_cor(1,23) = {[80,49,69]};
ant_pos_cor(1,24) = {[80,45,83]};
ant_pos_cor(1,25) = {[130,39,101]};
```

```
28 ant_pos_cor(1,26) = {[130,50,120]};
29 ant_pos_cor(1,27) = {[130,63,140]};
30 ant_pos_cor(1,28) = {[130,82,153]};
31 ant_pos_cor(1,29) = {[130,100,158]};
32 ant_pos_cor(1,30) = {[130,116,159]};
33 ant_pos_cor(1,31) = {[130,131,158]};
34 ant_pos_cor(1,32) = {[130,147,154]};
35 ant_pos_cor(1,33) = {[130,162,145]};
36 ant_pos_cor(1,34) = {[130,174,132]};
37 ant_pos_cor(1,35) = {[130,185,116]};
38 ant_pos_cor(1,36) = {[130,192,97]};
39 ant_pos_cor(1,37) = {[130,189,74]};
40 ant_pos_cor(1,38) = {[130,178,56]};
41 ant_pos_cor(1,39) = {[130,166,47]};
42 ant_pos_cor(1,40) = {[130,152,39]};
43 ant_pos_cor(1,41) = {[130,135,34]};
44 ant_pos_cor(1,42) = {[130,119,31]};
45 ant_pos_cor(1,43) = {[130,103,31]};
46 ant_pos_cor(1,44) = {[130,84,38]};
47 ant_pos_cor(1,45) = {[130,71,44]};
48 ant_pos_cor(1,46) = {[130,59,55]};
49 ant_pos_cor(1,47) = {[130,43,69]};
50 ant_pos_cor(1,48) = {[130,37,83]};
51 %********[Setting and time delay calculation]********
52 M = 48; % Number of antennas;
53 vfreespace = 2.99792458e11;% Speed of light in free space,mm/s;
54 immer_epsr = 4.3284; % Fatty-2 = immesive liquid, at center freq;
55 skin_epsr = 34.08;
56 vbre = vfreespace/sqrt(immer_epsr);% Propag. velocity in breast;
57 vskin = vfreespace/sqrt(skin_epsr); % Propag. velocity in skin;
58 skin_time = 2*1.5/vskin; basistimeslot = 1.9066e-12;
59 TotalTimeDelay = cell(1,M);% Number of time delay group;
60 cro_sec_cor_x = 95;imagerow = 130;
61 imagecol = 100;% 2D Cross-section imaging area;
62 img_row_start = 55;img_row_end = 184;
63 img_col_start = 45;img_col_end = 144;
64 timedelay = zeros(imagerow,imagecol);% Limits of imaging area;
65 for cur_ant = 1 : M% Calculate the 48 sets of theoretical
66                     %  time delay between imaging
67                     %  plane and each antenna;
68     ant_pos_cell = ant_pos_cor(1,cur_ant);
69     ant_pos_mat = cell2mat(ant_pos_cell);
70     Tx = ant_pos_mat(1,1);
71     Ty = ant_pos_mat(1,2);
```

```
72      Tz = ant_pos_mat(1,3);
73      for i = img_row_start:img_row_end
74          for j = img_col_start:img_col_end
75              d = 2*sqrt((cro_sec_cor_x - Tx)^2 +
76              (i - Ty)^2 + (j - Tz)^2);
77              temptimedelay = (d - 2*1.5)/vbre;
78              %Round-trip time delay;
79              tempx = i - 54;
80              tempy = j - 44;
81              timedelay(tempx,tempy) =  temptimedelay + skin_time;
82          end
83      end
84      TotalTimeDelay(1,cur_ant) = {timedelay};
85  end
86  %% ********[Pre-processing for artefact removal]********
87  TWNum_pusewidth = round(0.56e-9/basistimeslot);
88  Ratio_TW_Pulsewidth = 1;
89  TimeWindowNum1 = Ratio_TW_Pulsewidth*TWNum_pusewidth;
90  TimeWindowUsing = TimeWindowNum1;
91  for i = 1 : M
92      rawdata_name = ['output/A',num2str(i), '_with_E_sig','.txt'];
93      RawData = load(rawdata_name); TotalRawData(1,i) = {RawData};
94  end
95  [RawDataRowNum,b] = size(RawData);alltime =  RawData(:,1);
96  Ideal_sign = 0;%"1": Ideal; "0":Entropy.
97  if(Ideal_sign == 1)
98      run_mode = 'Ideal';TotalRawData = TotalRawData;
99  else
100     run_mode = 'Entropy';
101 %********[Entroy-based artefact removal]********
102 entropy_truncate_time1 = 0.66*1e-9;
103 entropy_truncate_time2 = 0.66*1e-9;
104 for i = 1:M
105     if(i > 24)
106         truncate_time = entropy_truncate_time2;
107     else
108         truncate_time = entropy_truncate_time1
109     end
110     truncate_time_mat_start(1,i) = truncate_time;
111 end
112 for i = 1:M
113     data = TotalRawData{1,i};
114     trucate_time = truncate_time_mat_start(i);
115     truncate_num = round(trucate_time/basistimeslot);
```

```
116         val = data(:,2);val(1:truncate_num) = 0;data(:,2) = val;
117         TotalRawData(1,i) = {data};
118     end
119     end
120     %***[Kernel calculation of pixel intensity for forming image]***
121     Intensity1 = zeros(imagerow,imagecol);% Memory allocation;
122     for i = 1: imagerow
123         for j = 1: imagecol
124             shifted_sig_mat = zeros(TimeWindowUsing,M);
125             SumofShiftedData = zeros(TimeWindowUsing,1);
126             for k = 1:M
127                 timedelaygroup = TotalTimeDelay{1,k};
128                 timedelay = timedelaygroup(i,j);
129                 RawData = TotalRawData{1,k};
130                 res = mytimeshift(RawData,timedelay,basistimeslot);
131                 s1 = res(:,2);s_truncated = s1(1:TimeWindowUsing);
132                 shifted_sig_mat(:,k) = s_truncated;
133             end
134             SumofShiftedData = sum(shifted_sig_mat,2);
135             %*********[Neighbourhood pairwise correlation]********
136             pair_nei_ind = 1;% Index initialisation;
137             for k = 1: M-1
138                 s1 = shifted_sig_mat(:,k);s2 = shifted_sig_mat(:,k+1);
139                 the_cor = mycoreff(s1,s2,TimeWindowUsing);
140                 pair_neibour_cor_mat_all(1,pair_nei_ind) = the_cor;
141                 pair_nei_ind = pair_nei_ind + 1;
142             end
143             npc_mat_all = (pair_neibour_cor_mat_all + 1)/2;
144             npc_all_sort = sort(npc_mat_all,'descend');
145             %*********[Maximum combining]*********
146             num = 0.5*length(npc_all_sort);
147             npc_all_sort_using = npc_all_sort(1:num);
148             prod_pair_nei = prod(npc_all_sort_using);
149             SumofShifted_weighted = prod_pair_nei*SumofShiftedData;
150             Intensity1(i,j) = sum(SumofShifted_weighted.^2);
151             %*************************************************
152         end
153     end
154     %********[Store imaging matrix]********
155     save('S6_RAR.mat','Intensity1');
156     end
157
158     %*****************************************
159     function re = mytimeshift(t_inputdata, t_delaytime, t_timeslot)
```

```
160  % method 1 (can only handle integral period time delay);
161
162 RawData = t_inputdata;
163 shiftedRawData = RawData;
164 [RawDataRowNum,col]=size(t_inputdata);
165 basistimeslot = t_timeslot;
166 delaynum = tempdelaytime/basistimeslot;
167 realdelaynum =  round(delaynum);% where generate the error;
168 h = dfilt.delay(realdelaynum);
169 shiftedRawData(:,1) = filter(h,RawData(:,1));
170         % shift the time delay rather than the y-value,
171         % the effect equals shift toward LEFT rather than right;
172 shiftedRawData=shiftedRawData(realdelaynum+1:RawDataRowNum,:);
173 % delete those zero of x;otherwise interpolation cannot be used;
174 n = RawDataRowNum - realdelaynum;
175 if(n > 0 | n == 0)
176     realshiftedData = shiftedRawData;
177     realshiftedData(n+1:RawDataRowNum,1)=
178     RawData(n+1:RawDataRowNum,1);
179     realshiftedData(n + 1:RawDataRowNum,2) = 0;
180 else
181     realshiftedData = zeros(RawDataRowNum,2);
182 end
183 re = realshiftedData;
184 end
185 %*****************************************
```